

## Advanced methods for Brillouin based distributed optical fiber sensors

Présentée le 14 avril 2021

Faculté des sciences et techniques de l'ingénieur  
Groupe SCI STI LT  
Programme doctoral en photonique

pour l'obtention du grade de Docteur ès Sciences

par

**Simon Adrien ZASLAWSKI**

Acceptée sur proposition du jury

Prof. C. Moser, président du jury  
Prof. L. Thévenaz, directeur de thèse  
Prof. A. Zadok, rapporteur  
Prof. M. González Herráez, rapporteur  
Prof. C.-S. Brès, rapporteuse



*"I'm a scientist and I know what constitutes proof. But the reason I call myself by my childhood name is to remind myself that a scientist must also be absolutely like a child. If he sees a thing, he must say that he sees it, whether it was what he thought he was going to see or not. See first, think later, then test. But always see first. Otherwise you will only see what you were expecting. Most scientists forget that."*

— Douglas Adams, *The Ultimate Hitchhiker's Guide to the Galaxy*

To the people I love...

# Acknowledgements

First and foremost, I would like to express my gratitude to my thesis supervisor, Prof. Luc Thévenaz, for warmly welcoming me in his laboratory and for giving me the opportunity to accomplish this PhD thesis in the best possible conditions.

I would also like to thank the members of my jury, Prof. Christophe Moser, Prof. Avi Zadok, Prof. Miguel González Herráez and Prof. Camille Sophie Brès, for accepting to review my thesis and for the time they devoted to it.

I would also like to take this opportunity to sincerely thank the people who introduced me to the fascinating world of distributed optical fiber sensors with a lot of patience when I was still a young undergraduate student asking many questions, Dr. Etienne Rochat and Dr. Sanghoon Chin, as well as the whole team at Omnisens SA who made this first encounter successful and pleasant.

During my PhD, I had the chance to meet and interact with a lot of interesting people, whether in Lausanne or abroad. My most sincere welcome thus goes to all of them, especially the members of the FINESSE network as well as the team from PHOSL, with whom I had a lot of fruitful interactions.

Naturally, I would like to express my most warmhearted thanks to all past and current teammates, as well as visiting members at GFO, and they are quite a few: Dr. Kenny Hey Tow, Pabitra Ray, Dr. Zonglei Li, Dr. Desmond Chow, Dr. Sheng Wang, Prof. Marcelo Soto, Dr. Yun Fu, Dr. Can Yao, Dr. Ana Gabriela Correa, Prof. Pingyu Zhu, Leonardo Rossi, Tiago Neves, Dr. Fan Yang, Svetlana Mashkina, Dr. Flavien Gyger, Dr. Suneetha Sebastian, Dr. Li Zhang and Malak Galal. Thank you all for making the daily life in the lab so cheerful and enjoyable.

A special thanks goes to Dr. Zhisheng Yang, with whom I spent countless hours discussing results, debugging chaotic matlab programs or struggling to assemble a complex experimental device. My PhD would simply not have been the same without his valuable input !

Lastly, I would like to thank from the bottom of my heart my family and friends for always caring for me during the past four years, and especially my beloved wife Aya, for being the most precious support I could ever have dreamed of.

*Lausanne, 20 January 2021*

Simon Zaslowski



# Abstract

After more than thirty years of continuous research and development, the performances of conventional Brillouin based distributed optical fiber sensors (DOFS) are now peaking, as they are facing fundamental barriers that restrict the power of the light injected into the fiber. For scientists, absolute limitations of this kind are hardly ever accepted as an insurmountable obstacle, rather they are considered as an additional challenge that can always be overcome by a cleverer, and often more complex apparatus. It is thus not surprising to find in the scientific literature a large diversity of reports that describe refinements brought to the conventional architectures of Brillouin based DOFS. In this thesis, we explore two entirely different ways of pushing further the capabilities of conventional Brillouin based DOFS, which are first thoroughly reviewed in a preliminary chapter devoted to depict the most fundamental aspects of this technology.

An entire chapter is dedicated to an interdisciplinary study where the formalism and methods initially developed within the theory of digital signal processing to analyze linear time-invariant systems are transposed to the case of DOFS. This methodology enables, first, to fully understand the potential improvements and limitations in terms of performances of data post-processing when applied to conventional Brillouin optical time-domain analyzers (BOTDA). Then, the concept of deconvolution is presented as a promising tool to achieve sub-metric spatial resolution measurement, which is challenging using direct methods due to the finite lifetime of acoustic phonons in the fiber. Finally, this theory is put at use to revisit the concept of optical pulse coding in BOTDA, demonstrating significant performances improvement over conventional architectures, while circumventing the many practical implementation restrictions met by other coding schemes.

The last section of this dissertation is dedicated to the study of a phenomenon known as forward stimulated Brillouin scattering (FSBS). FSBS is foreseen as a potential candidate to diversify the physical measurands that can be interrogated via DOFS, as it is highly sensitive to the acoustic boundary conditions at the glass outer boundary of the fiber. Far from having the longevity of other branches of DOFS, the performances of recently reported distributed FSBS sensing schemes are still quite poor, hence there is still a large margin for improvement. Here, the acoustic vibrations involved in FSBS are activated harmonically, and the resulting refractive index modulation is picked up by an optical pulse that acts as a pump in a conven-

tional Brillouin based sensor. First, a modified Brillouin optical time-domain reflectometer is implemented, demonstrating distributed FSBS sensing with a SR of 8 m. While displaying interesting features, this method is flawed by severe limitations, notably due to its intensity-based operating principle. We then report, for the first time to the best of our knowledge, a frequency based distributed FSBS sensing technique, that relies on the principle of serrodyne modulation. The results obtained outperform any previously documented reports, achieving a SR of 80 cm in a short section of bare single-mode fiber, and a SR of 2 m over 500 m of polyimide coated fiber.

Key words: distributed optical fiber sensor, digital signal processing, forward stimulated Brillouin scattering

# Résumé

Après plus de trente ans de recherche et développement intensifs, les performances des capteurs à fibre optique répartis (CFOR) conventionnels basés sur la diffusion Brillouin arrivent aujourd'hui à saturation, car ils se heurtent à des barrières physiques fondamentales qui limitent la puissance de la lumière injectée dans la fibre. Pour les scientifiques, les limitations de ce type ne sont presque jamais perçues comme un obstacle insurmontable, mais sont plutôt considérées comme un défi supplémentaire qui peut toujours être surmonté par un appareil au concept plus astucieux et souvent plus complexe. Il n'est donc pas surprenant de trouver dans la littérature scientifique une grande variété de rapports qui décrivent des perfectionnements apportés aux architectures conventionnelles des CFOR basé sur la diffusion Brillouin. Dans cette thèse, nous présentons deux manières complètement différentes d'améliorer les capacités des CFOR à diffusion Brillouin.

Tout d'abord, nous transposons le formalisme et les méthodes initialement développées dans le cadre de la théorie du traitement de signaux numériques afin d'analyser les systèmes linéaires et invariants dans le temps au cas des CFOR. Cette méthodologie permet d'abord de comprendre les améliorations et les limites potentielles en termes de performances du traitement des données dans les COFR à diffusion Brillouin. Le concept de déconvolution est ensuite présenté comme un outil prometteur pour effectuer des mesures avec une résolution spatiale sub-métrique, ce qui constitue un défi pour les méthodes conventionnelles en raison de la durée de vie limitée des phonons acoustiques dans la fibre. Cette théorie est ensuite utilisée afin de revisiter le concept de codage par impulsion optique dans le cadre de la technologie BOTDA, permettant une amélioration significative des performances par rapport aux architectures classiques, tout en palliant aux nombreuses contraintes pratiques rencontrées dans d'autres schémas de codage.

Enfin, nous étudions un phénomène connu sous le nom de diffusion Brillouin stimulée vers l'avant (FSBS). Très sensible aux propriétés acoustiques du matériau au contact de la fibre de verre, la FSBS est un candidat potentiel à la diversification des quantités physiques pouvant être mesurées par le biais des CFOR. Loin d'avoir la longévité d'autres technologies des CFOR, les performances des appareils de mesure FSBS documentés à ce jour sont encore assez faibles. Dans cette thèse, des ondes acoustiques sont activées de manière harmonique, et la modulation de l'indice de réfraction qui en résulte est captée par une impulsion optique qui agit comme une pompe dans un capteur Brillouin classique. Tout d'abord, un réflectomètre



optique Brillouin modifié est mis en œuvre, permettant une mesure de la diffusion FSBS répartie avec une résolution spatiale de 8 m. Bien que possédant des caractéristiques intéressantes, cette méthode présente de sérieux défauts, notamment en raison de son principe de fonctionnement basé sur une détection d'intensité optique. Nous présentons ensuite, pour la première fois à notre connaissance, une technique de détection FSBS distribuée basée sur la fréquence, et qui repose sur le principe de la modulation serrodyne. Les résultats obtenus sont meilleurs que tous les rapports établis précédemment, atteignant une résolution spatiale de 80 cm dans une courte section de fibre monomode, et une résolution spatiale de 2 m dans 500 m de fibre revêtue de polyimide.

Mots clefs : capteur à fibre optique réparti, traitement numérique de signaux, diffusion Brillouin stimulée vers l'avant

# Contents

<b>Acknowledgements</b>	<b>i</b>
<b>Abstract (English/Français)</b>	<b>iii</b>
<b>1 Introduction</b>	<b>1</b>
<b>2 Fundamentals</b>	<b>5</b>
2.1 Optical fibers . . . . .	5
2.1.1 Manufacturing process . . . . .	5
2.1.2 Characteristics of single-mode optical fibers . . . . .	7
2.2 Optical fibers as electromagnetic waveguides . . . . .	8
2.2.1 Maxwell and the wave equation . . . . .	8
2.2.2 Optical modes . . . . .	9
2.2.3 Fundamental mode . . . . .	11
2.3 Scattering mechanisms in optical fibers . . . . .	13
2.3.1 Rayleigh scattering . . . . .	14
2.3.2 Raman scattering . . . . .	17
2.3.3 Spontaneous Brillouin scattering . . . . .	19
2.3.4 Stimulated Brillouin scattering . . . . .	24
2.4 Distributed optical fiber sensing . . . . .	29
2.4.1 Spatial resolution . . . . .	29
2.4.2 Signal-to-noise ratio . . . . .	30
2.4.3 Acquisition time . . . . .	31
2.4.4 Sensing range . . . . .	32
2.4.5 Brillouin optical time-domain reflectometry . . . . .	33
2.4.6 Brillouin optical time-domain analysis . . . . .	35
<b>3 Digital signal processing applied to distributed optical fiber sensing</b>	<b>39</b>
3.1 Basic concepts of digital signal processing . . . . .	40
3.1.1 Linearity, time-invariance and convolution . . . . .	40
3.1.2 The continuous-time Fourier transform . . . . .	41
3.1.3 The sampling theorem and the discrete-time Fourier transform . . . . .	42
3.1.4 The discrete Fourier transform . . . . .	44
3.1.5 Distributed optical fiber sensors as LTI systems . . . . .	45

3.2	Noise reduction in Brillouin optical time-domain analyzers . . . . .	46
3.2.1	Noise as a random process . . . . .	46
3.2.2	Noise sources in BOTDA . . . . .	47
3.2.3	Curve fitting and experimental uncertainty . . . . .	48
3.2.4	Noise aliasing and digital filtering . . . . .	50
3.2.5	A note on the 2-D post-processing of BOTDA measurements . . . . .	52
3.3	Short spatial resolution retrieval . . . . .	55
3.3.1	Acoustic lifetime and spatial resolution . . . . .	55
3.3.2	Convolution and deconvolution . . . . .	56
3.3.3	Performances improvement evaluation . . . . .	58
3.3.4	Artifacts mitigation . . . . .	59
3.3.5	Sub-meter spatial resolution . . . . .	60
3.4	Genetic-optimised aperiodic coding . . . . .	61
3.4.1	Challenges of optical pulse coding . . . . .	62
3.4.2	Optical pulse coding based on deconvolution . . . . .	62
3.4.3	The noise scaling factor . . . . .	63
3.4.4	Coding gain . . . . .	64
3.4.5	Optimization of the coding sequence: spectrum management . . . . .	67
3.4.6	Robustness to EDFA gain saturation . . . . .	68
3.4.7	Experimental results . . . . .	69
<b>4</b>	<b>Distributed forward stimulated Brillouin scattering sensing</b>	<b>71</b>
4.1	Acoustic waves propagation in optical fibers . . . . .	72
4.1.1	The elastic waves equation . . . . .	72
4.1.2	The potentials method . . . . .	73
4.1.3	Separation of variables . . . . .	74
4.1.4	Boundary conditions . . . . .	75
4.1.5	The frequency equation . . . . .	75
4.1.6	Purely radial modes . . . . .	76
4.2	Forward stimulated Brillouin scattering . . . . .	77
4.2.1	Wave coupling in FSBS . . . . .	78
4.2.2	Efficiency of FSBS: modal dependency . . . . .	79
4.2.3	Sensing properties of FSBS . . . . .	80
4.2.4	The impact of coating . . . . .	82
4.2.5	FSBS in harmonic regime . . . . .	85
4.3	Distributed FSBS measurement using broadband BOTDR . . . . .	87
4.3.1	Harmonic phase modulation . . . . .	87
4.3.2	Experimental setup . . . . .	89
4.3.3	Experimental Results . . . . .	91
4.3.4	Discussion . . . . .	94
4.4	Distributed FSBS sensing based on serrodyne modulation . . . . .	94
4.4.1	Operating principle . . . . .	94

4.4.2	Experimental setup . . . . .	97
4.4.3	Acquisition process . . . . .	98
4.4.4	Numerical simulations . . . . .	99
4.4.5	Pulses synchronization . . . . .	100
4.4.6	Remote distributed FSBS sensing in bare fiber . . . . .	102
4.4.7	Accumulated effects in fully distributed FSBS sensing . . . . .	106
4.4.8	Fully distributed FSBS sensing in polyimide coated fiber . . . . .	107
4.4.9	Discussion . . . . .	110
<b>5</b>	<b>Conclusions and Perspectives</b>	<b>111</b>
<b>A</b>	<b>Solution of the acoustic wave equation in cylindrical coordinates</b>	<b>115</b>
A.1	Useful relationships . . . . .	115
A.1.1	Problem Geometry . . . . .	115
A.1.2	Nabla operations in cylindrical coordinates . . . . .	116
A.1.3	Useful vector calculus identities . . . . .	116
A.1.4	Bessel functions properties . . . . .	116
A.1.5	Strain-displacement relations . . . . .	117
A.1.6	Stress-strain relations . . . . .	117
A.1.7	Boundary conditions . . . . .	117
A.2	The acoustic wave equation in cylindrical coordinates . . . . .	118
A.2.1	Homogeneous equation . . . . .	118
A.2.2	The potentials methods . . . . .	118
A.2.3	The gauge invariance principle . . . . .	119
A.2.4	Separation of variables . . . . .	119
A.2.5	Displacement, stress and strain . . . . .	121
A.2.6	Boundary conditions . . . . .	123
A.2.7	The matrix form and the frequency equation . . . . .	124
A.2.8	Longitudinal-radial modes . . . . .	125
A.2.9	Purely radial acoustic modes . . . . .	126
A.3	Acoustic modes in a coated fiber . . . . .	127
A.3.1	Displacement field . . . . .	127
A.3.2	Frequency equation of purely radial modes . . . . .	128
<b>B</b>	<b>Distributed FSBS sensing: numerical simulations</b>	<b>131</b>
<b>C</b>	<b>List of publications</b>	<b>133</b>
	<b>Bibliography</b>	<b>142</b>
	<b>Curriculum Vitae</b>	<b>143</b>



# 1 Introduction

Brillouin scattering describes the interaction of light with sound. While both light and sound fall under the denomination of "waves", one might wonder how such disparate objects can influence one another. This fascinating physical mechanism, which was observed and studied for the first time almost a century ago by Léon Brillouin [1], is made possible and efficient in a suitable medium, through which both waves might exchange energy. It turns out that optical fibers are a well-suited platform to observe, manipulate and of course harness information from Brillouin scattering, or any other suitable scattering mechanism. By designing proper optical interrogation techniques, the mechanical or thermodynamic properties of an optical fiber can be retrieved all along its length, a process known as distributed optical fiber sensing (DOFS). Far from being confined to a purely experimental environment such as a laboratory, this technology is now widely used in diverse real-life applications. Optical fibers are routinely embedded in all sorts of civil engineering structures, such as bridges, dams, pipelines and many others, providing a fully distributed monitoring system that is equivalent to a constellation of individual point sensors [2].

Nowadays, distributed optical fiber sensors encompass a broad variety of techniques that, depending on their operating principle, all yield different performances in terms of key specifications inherent to DOFS. Some methods are well suited to operate on very long distances (tens of kilometers) with moderate spatial resolution (meter range) while others exhibit high sensitivity to e.g temperature (mK) and/or deliver spatially resolved information with extremely sharp resolution (mm). Generally speaking, there is no method that outperforms all others in every single aspect, hence some techniques are more suited to certain configurations than others, depending on the considered requirements (sensing range, spatial resolution, precision, cost, etc.). In this thesis, we focus on DOFS that rely on Brillouin scattering. Moreover, we shall restrict our analysis to time-domain techniques, which operate in their most conventional implementation by injecting a single optical pulse into the sensing fiber and measuring the corresponding backscattered response.

The first mention of a Brillouin based sensor was made in 1989 by Horiguchi *et. al*, and was labelled as Brillouin optical time-domain analysis (BOTDA) [3]. As BOTDA requires access to

both ends of the fiber, a single-end alternative was shortly investigated, yielding the so-called Brillouin optical time-domain reflectometry (BOTDR) technique in 1993 [4]. Nowadays, that is roughly thirty years after these pioneering works, these two techniques are now facing fundamental limitations imposed by the triggering of non-linear effects which restrict the amount of optical power to be launched in the fiber. While classical implementations of BOTDA and BOTDR are not expected to spontaneously and significantly see major performances improvement, there are yet many creative and ingenious strategies to be explored in order to benefit further from these technologies. This dissertation presents some advanced methods of Brillouin based DOFS, and is structured in three main chapters that cover the following topics:

- Chapter 2 covers the fundamentals of distributed optical fiber sensing, starting with a description of optical fibers. This includes their manufacturing process, the basic light guiding mechanism of single-mode fibers as well as a description of the various scattering mechanisms occurring in glass-made fibers. Finally, it provides with some background knowledge on the characteristics of distributed optical fiber sensing, notably describing a typical implementation of a BOTDR as well as a BOTDA.
- Chapter 3 presents an interdisciplinary study that merges knowledge from the theory of digital signal processing with DOFS and revolves around the concept of linear time-invariant (LTI) systems. After a mandatory introduction on this topic, one turn to analyze in details how post-processing impacts the data delivered by a conventional BOTDA. More specifically, a fundamental limit on the reduction of the experimental uncertainty is drawn, under the strict restriction of preserving the initial spatial resolution of the sensor. The concept of deconvolution is then put at use in two remarkable applications. First, one illustrates how to access, via post-processing, the sharp spatial resolution information contained in a coarser spatial resolution measurement, showing promising results to achieve sub-meter distributed sensing. Finally, a novel form of optical pulse coding (OPC) is presented. While showing similar performances improvement with respect to other existing coding techniques, this method brings a solution to the many practical difficulties encountered so far in any reported implementation of OPC, and that severely hindered the potential of this fantastic technique.
- Chapter 4 is devoted to an emerging field of study that analyzes an opto-acoustic interaction known as forward stimulated Brillouin scattering (FSBS). While this phenomenon has been documented for the first time in optical fibers as early as 1985 under the denomination of guided wave acoustic Brillouin scattering [5], it recently drew a significant interest within the fiber optic sensing community due to its potential to diversify the sensing capabilities of DOFS [6]. Since this interaction involves acoustic waves that are guided by the optical fiber, this chapter begins with a theoretical study that describes the main features of the acoustic modes exhibited by a single-mode fiber. The interaction itself (FSBS) is then thoroughly described, pinpointing aspects most relevant to the topic of interest here, i.e. sensing. We then present two experimental setups

---

aiming at measuring FSBS in a spatially-resolved way. Both techniques rely on activating pure-tone acoustic waves in the fiber by launching a powerful activating optical pulse, followed by a second reading pulse that acts as a pump in a dedicated backscattered based time-of-flight interrogation technique. Early results obtained via a modified BOTDR are first provided, achieving a spatial resolution of 8 m in a section of ~ 30 m of bare fiber located at the remote end of a ~400 m long conventional fiber. Finally, a frequency-based technique relying on serrodyne modulation is presented, achieving a spatial resolution of only 80 cm in a remote distributed sensing configuration, and of 2 m in a ~500 m long fully sensitive polyimide coated fiber, showing major improvement with respect to previous reports [7, 8].





## 2 Fundamentals

This chapter depicts the fundamental features of distributed optical fiber sensing (DOFS). This technology takes advantage of the massive growth in terms of development, manufacturing and usage of optical fibers at a global scale, owing to their formidable data transmission potential in an era revolving around telecommunication. It appears therefore natural to offer first a brief description of optical fibers, as they are the host of the intricate physical mechanisms that enable performing distributed sensing. Since all these effects stem from the information carrier propagating in optical fibers, i.e. light, the latter is then treated as an electromagnetic wave within the formalism of Maxwell's equations. We then mention the three main types of scattering processes occurring in an optical fiber, on which all of DOFS rely, with a strong emphasis on Brillouin scattering, which occupies a central position in this thesis. Finally, we provide with general aspects related to distributed sensing, enumerating parameters used as specifications that enable classifying and comparing DOFS.

### 2.1 Optical fibers

Optical fibers are mostly known to have revolutionized cabled telecommunication, outperforming in every aspect wired transmission over metallic cables. Besides delivering information with subsequent throughput, optical fibers are in addition a fantastic platform for sensing applications. An in-depth understanding on this topic requires some preliminary knowledge on the structure of optical fibers, which is tightly related to their manufacturing process. We therefore start by providing general information related to optical fiber manufacturing, pinpointing notions relevant to the topic of sensing.

#### 2.1.1 Manufacturing process

Optical fibers rely on an effect known as *waveguiding*, which was demonstrated for light by Jean-Daniel Colladon and Jacques Babinet as early as 1842 [9] by trapping sunlight into a bent water jet via total internal reflection. More than 100 years later, Kao *et al.* theoretically

demonstrated the potential use of glass-based optical fibers for long-haul communication by analyzing the main sources of optical loss in glass [10], predicting that attenuation could be brought down below 20 dB/km. Through intensive research lead over more than half a century, optical attenuation could be lowered in silica-based optical fibers by several orders of magnitude, modern fibers exhibiting attenuation levels so low, i.e. 0.17 dB/km at a wavelength of 1550 nm, that they are approaching the fundamental limit imposed by Rayleigh scattering [11]. Nowadays, optical fibers encompass an extremely diverse portfolio following the massive development of micro-structured fibers in the last three decades [12]. The fibers used in the framework of this thesis are amongst the most conventional ones, and are known as single-mode fibers (SMF). This designation refers to the waveguiding mechanism these fibers rely on, as will be explained in section 2.2.

Silica-based SMFs are manufactured following a two step process. First, a magnified version of the target fiber is fabricated by a vapor deposition process [2], i.e depositing a mixture of pure silica ( $\text{SiO}_2$ ) and dopants, e.g. germania ( $\text{GeO}_2$ ) or boron oxide ( $\text{B}_2\text{O}_3$ ), in concentric layers, ending up with a glass cylinder exhibiting the same refractive index profile and aspect ratio as the targeted SMF. This oversized fiber is called a preform, and is later drawn to proper dimensions following the (simplified) procedure depicted in Fig.2.1 The preform is first heated

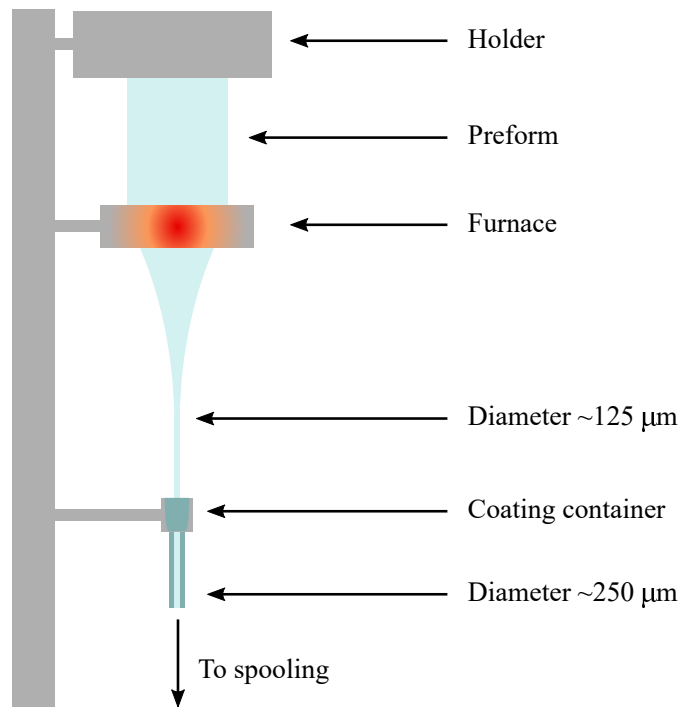


Figure 2.1 – Optical fiber drawing from a preform. Here, only the main steps are described, while in reality the entire process requires precise control and regulation.

to high temperature using a furnace, which softens the glass until it starts to drop, shrinking in diameter while retaining its cross-sectional structure. The fiber is elongated until it reaches its target diameter (125 μm for most SMFs) and is immediately dipped in a coating solution that

protects the fiber and improves its mechanical robustness. The most commonly used coating material for SMFs is acrylate, which is usually applied in a dual layer of  $62.5\ \mu\text{m}$ , bringing the total fiber diameter to  $250\ \mu\text{m}$ . The inner layer is softer while the outer layer is usually more rigid. The issues encountered later on in chapter 4 respective to acrylate as a coating material are mostly due to the softer inner layer.

Overall, the entire optical fiber manufacturing chain is extremely demanding, both in terms of material purity and geometrical uniformity. Nevertheless, thanks to the technology at disposal nowadays as well as decades of improving know-how, commercially available single-mode fibers remarkably satisfy stringent requirements even over several tens of kilometers. To illustrate this, and as it will come of great interest in chapter 4 of this thesis, typical tolerances on the physical dimensions of conventional SMFs are about  $\pm 1\ \mu\text{m}$  for the glass diameter ( $125\ \mu\text{m}$ ) and about  $\pm 5\ \mu\text{m}$  for the coating diameter ( $250\ \mu\text{m}$ )<sup>I</sup>.

### 2.1.2 Characteristics of single-mode optical fibers

Following the procedure described in section 2.1.1, conventional single-mode fibers (SMFs) end up exhibiting the structure shown in Fig.2.2. The optical fiber itself, i.e. the glass-rod, is

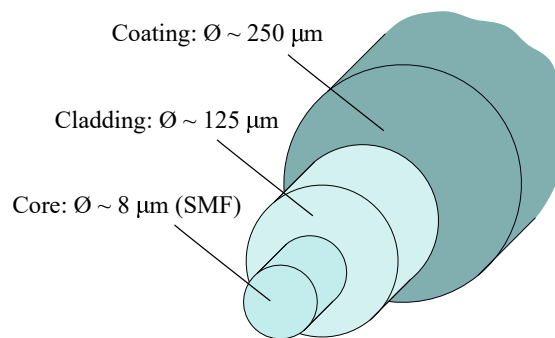


Figure 2.2 – Typical structure of a single-mode fiber (not to scale).

constituted of two distinct regions called core and cladding, respectively. Note that core and cladding are forming a single piece of glass and are not physically dissociated as the figure might suggest, rather they delimit distinct regions with different optical properties. Thanks to the introduction of dopants in the preform manufacturing process, the refractive index of either the core and/or the cladding might be increased or lowered with respect to pure silica. In SMFs, light is guided by total internal reflection, which requires for the refractive index of the core to be slightly higher than the one in the cladding. The refractive index difference for SMFs,  $\Delta n$  is typically in the order of 0.3%-0.8% [13] which results from design requirements regarding the waveguiding performances of the fiber (see section 2.2 for more details). Note that while we described here the structure of a step-index fiber, i.e. the refractive index in the core and the cladding are different but uniform in each region, other types of refractive index profiles are possible to achieve optical waveguiding, notably graded-index fibers which exhibit

<sup>I</sup>These values are made available by fiber manufacturers, e.g. Corning® (<https://www.corning.com>)

a well-defined refractive index distribution from the core to the glass boundary [13].

The role of the coating is fundamental, but unrelated to the optical properties of the fiber. It provides the entire structure with mechanical robustness by sealing the fiber from air exposure, as the glass would otherwise turn brittle and too delicate to handle directly, let alone be used in any practical application. Usually, optical fibers are further protected by one or several additional layers, in which case the fiber is usually referred to as an optical fiber cable. The most widely used coating material is undoubtedly acrylate, but other materials such as polyimide or carbon are routinely used depending on the target application and/or the environment hosting the fiber. In the later chapters of this dissertation (see chapter 4), significant attention will be drawn to the coating material used in the sensing fibers considered, as it plays a central role in the mechanical behavior of the fiber in terms of acoustic modes propagation.

## 2.2 Optical fibers as electromagnetic waveguides

The waveguiding mechanism in single-mode optical fibers is typical of dielectric waveguides, and is described based on the formalism of Maxwell's equations. While the overall approach remains superficial, an emphasis is put on key aspects particularly relevant to opto-acoustic interactions.

### 2.2.1 Maxwell and the wave equation

Light waveguiding in optical fibers is classically described by the formalism of electromagnetism, which was unified in 1862 by James Clerk Maxwell in a set of relations known as Maxwell's equations. Maxwell's equations are an extremely powerful tool, that enable describing plethora of complex electromagnetic phenomena. They read [14, 15, 16]

$$\nabla \times \mathcal{E} = -\frac{\partial \mathcal{B}}{\partial t} \quad (2.1)$$

$$\nabla \times \mathcal{H} = \frac{\partial \mathcal{D}}{\partial t} + \mathcal{J} \quad (2.2)$$

$$\nabla \cdot \mathcal{D} = \rho \quad (2.3)$$

$$\nabla \cdot \mathcal{B} = 0 \quad (2.4)$$

where  $\mathcal{E}$  and  $\mathcal{D}$  are the electric field and the electric flux density, respectively,  $\mathcal{H}$  and  $\mathcal{B}$  are the magnetic field and the magnetic flux density, respectively,  $\rho$  is the density of free charges and  $\mathcal{J}$  is the current density. While equations (2.1)-(2.4) in their fundamental form are extremely general, we shall restrict ourselves here to the specific case of optical fibers. The material is therefore assumed to be non-magnetic, isotropic and homogeneous (by region) in addition to be free of charges. This implies that we may set  $\mathcal{J} = \mathbf{0}$  in (2.2) and  $\rho = 0$  in (2.3). Furthermore,

we may write

$$\mathcal{D} = \epsilon_0 \mathcal{E} + \mathcal{P} \quad (2.5)$$

$$\mathcal{B} = \mu_0 \mathcal{H} \quad (2.6)$$

where  $\epsilon_0$  is the vacuum permittivity,  $\mathcal{P}$  is the induced electric polarization and  $\mu_0$  is the vacuum permeability. Then, by making use of equations (2.1)-(2.6) and after some simplifications [14, 15] we end up with

$$\nabla^2 \mathcal{E} - \frac{1}{c_0^2} \frac{\partial^2 \mathcal{E}}{\partial t^2} = \mu_0 \frac{\partial^2 \mathcal{P}}{\partial t^2} \quad (2.7)$$

where  $c_0 = (\epsilon_0 \mu_0)^{-1/2}$  is the speed of light in vacuum. Equation (2.7) is known as the wave equation, and enables to describe a large variety of linear and nonlinear effects in optical fibers or any other media. An essential aspect that needs to be considered when solving (2.7) lies in the form taken by the polarization field  $\mathcal{P}$  on the right-hand side of the wave equation. As of now, and in order to understand the basic waveguiding mechanism of an optical fiber, it is sufficient to assume that  $\mathcal{P}$  is linear with respect to the electric field  $\mathcal{E}$ . We thus write

$$\mathcal{P} = \epsilon_0 \chi \mathcal{E} \quad (2.8)$$

where  $\chi$  is the electric susceptibility. Note that equation (2.8) implies that the medium is linear and non-dispersive. The refractive index  $n$  is defined as

$$n = \sqrt{1 + \chi} \quad (2.9)$$

such that we end up with

$$\nabla^2 \mathcal{E} - \frac{n^2}{c_0^2} \frac{\partial^2 \mathcal{E}}{\partial t^2} = 0 \quad (2.10)$$

which is the form of the wave equation that will be used in the following section.

### 2.2.2 Optical modes

The wave equation in the form given in (2.10) is linear in terms of the electric field  $\mathcal{E}$  because dimensional and temporal derivatives are linear operators. In this case, it is usually simpler to solve equation (2.10) in the frequency domain by taking its Fourier transform, yielding [14]

$$\nabla^2 \tilde{\mathcal{E}} + \omega^2 \frac{n^2}{c_0^2} \tilde{\mathcal{E}} = 0 \quad (2.11)$$

which is known as Helmholtz equation, in which  $\omega$  denotes the angular frequency and  $\tilde{\mathcal{E}}$  is the Fourier transform of the electric field  $\mathcal{E}$ . Equation (2.11) is then solved in cylindrical

coordinates  $(r, \theta, z)$ , as the latter are far more suited than cartesian coordinates given the geometry of an optical fiber (the  $z$ -axis is aligned with the fiber axis). Equation (2.11) is quite cumbersome to solve directly due to the vectorial nature of the electric field  $\tilde{\mathcal{E}}$ . The derivation can fortunately be made more straightforward by remembering that the components of the electric field are related by Maxwell's equations (2.1)-(2.4) in the first place, hence we only need to solve for one component of  $\tilde{\mathcal{E}}$  and one component of  $\tilde{\mathcal{H}}$ . Note that the derivation of the solution for the magnetic field is extremely similar to the one shown here, hence is of little added interest and will not be explicitly performed. Equation (2.11) when restricted to the  $z$ -component of the electric field  $\tilde{E}_z$  in cylindrical coordinates reads

$$\frac{\partial^2 \tilde{E}_z}{\partial r^2} + \frac{1}{r} \frac{\partial \tilde{E}_z}{\partial r} + \frac{1}{r^2} \frac{\partial^2 \tilde{E}_z}{\partial \theta^2} + \frac{\partial^2 \tilde{E}_z}{\partial z^2} + n^2 k_0^2 \tilde{E}_z = 0 \quad (2.12)$$

where  $k_0 = \omega/c_0$  is the wavevector in vacuum. Like many partial differential equations, (2.12) is traditionally solved by the method of separation of variables, i.e. we express the solution as a product of variables, each depending on a single parameter

$$\tilde{E}_z = W(\omega) R(r) e^{im\theta} e^{i\beta z} \quad (2.13)$$

where  $i$  denotes the imaginary number,  $m$  is an integer and  $\beta$  is known as the propagation constant. Note that  $W(\omega)$  is a frequency-dependent scaling factor and could only be determined through normalization by knowing e.g. the amount of optical power at a given frequency, hence it is not treated further in the derivation. Inserting (2.13) into (2.12) and dividing by  $\tilde{E}_z$  yields

$$\frac{\partial^2 R}{\partial r^2} + \frac{1}{r} \frac{\partial R}{\partial r} + \left( n^2 k_0^2 - \beta^2 - \frac{m^2}{r^2} \right) R = 0 \quad (2.14)$$

Equation (2.14) is a most classical equation which naturally arises due to the cylindrical nature of the problem. It is known as Bessel's equation, and assumes solutions in the form of Bessel functions. The form of the solution is yet highly dependent on the term  $n^2 k_0^2 - \beta^2$ , more particularly on its sign. The latter is influenced by the value of the refractive index  $n$ , which takes two distinct values in the core ( $n_{co}$ ) and the cladding ( $n_{cl}$ ). The waveguiding mechanism in single-mode step index fibers requires that  $n^2 k_0^2 > \beta^2$  in the core, and  $n^2 k_0^2 < \beta^2$  in the cladding. As a consequence, and for an optical fiber with a core radius  $a$ ,  $R(r)$  takes the following form

$$r \leq a \quad R(r) = A J_m(pr) + B Y_m(pr) \quad (2.15)$$

$$r \geq a \quad R(r) = C I_m(qr) + D K_m(qr) \quad (2.16)$$

where  $J_m$  and  $Y_m$  denote  $m$ th order Bessel functions of the first and second kind, respectively,  $I_m$  and  $K_m$  denote  $m$ th order modified Bessel functions of the first and second kind, respectively, while  $A$ ,  $B$ ,  $C$  and  $D$  are integration constants. The parameters  $p$  and  $q$  are defined as

to be real valued, i.e.

$$p = \sqrt{n_{\text{co}}^2 k_0^2 - \beta^2} \quad (2.17)$$

$$q = \sqrt{\beta^2 - n_{\text{cl}}^2 k_0^2} \quad (2.18)$$

Equations (2.15) and (2.16) can be immediately simplified due to the very disparate nature of the various Bessel functions in presence. In the core, we may set  $B = 0$  as  $Y_m$  diverges when  $r$  approaches 0. In the cladding,  $I_m$  are exponentially growing functions of  $r$ , hence we may similarly set  $C = 0$ . The remaining integration constants  $A$  and  $D$  are scaling parameters and may be merged in the amplitude response parameter  $W(\omega)$ , as they do not provide any insight regarding the form of the solution. The derivation continues with the application of the appropriate boundary conditions, which follow directly from Maxwell's equations [16]. The boundary conditions state that the tangential components of the fields ( $\mathcal{E}$  and  $\mathcal{H}$ ) as well as the normal components of the flux densities ( $\mathcal{D}$  and  $\mathcal{B}$ ) must be continuous through the interface of two dielectric materials. The whole procedure is lengthy, and offers no particular relevant information, hence we directly provide the final result, known as the frequency equation or dispersion relation [14]

$$\left[ \frac{J'_m(pa)}{pJ_m(pa)} + \frac{K'_m(qa)}{qK_m(qa)} \right] \left[ \frac{J'_m(pa)}{pJ_m(pa)} + \frac{n_{\text{cl}}^2}{n_{\text{co}}^2} \frac{K'_m(qa)}{qK_m(qa)} \right] = \left( \frac{m\beta k_0 (n_{\text{co}}^2 - n_{\text{cl}}^2)}{an_{\text{co}} p^2 q^2} \right)^2 \quad (2.19)$$

where the prime indicates the first order derivative with respect to the argument of the functions. Generally speaking, and for a given value of  $m$ , there exist several values of  $\beta$  that satisfy (2.19), usually designated as  $\beta_{mn}$ . Thus, the complete solution for a given fiber ( $a$ ,  $n_{\text{co}}$ ,  $n_{\text{cl}}$ ) at a specified wavelength ( $k_0$ ) breaks down into a set of discrete independent solutions, known as modes. Each mode is thus characterized by a given propagation constant  $\beta_{mn}$  and a specific field distribution. Equation (2.19) is a very general one, that applies to any step-index fiber configuration. It can fortunately be greatly simplified when dealing with single-mode fibers, which have the particularity to exhibit a very low refractive index difference  $\Delta n$ . Notice that we assumed here that the fiber cladding diameter is infinite, i.e. we do not take into account the cladding/coating (or cladding/air) interface. While this is fundamentally speaking wrong, this assumption is perfectly reasonable as explicated in the following section.

### 2.2.3 Fundamental mode

The analysis presented here relies on a key simplification known as the weakly guiding approximation [11, 13], which is valid only when  $n_{\text{co}} \approx n_{\text{cl}}$ . In all generality, the modes described in the previous section can be classified into several categories, which usually are related to their field distribution. For instance, we may define TM modes which stand for transverse magnetic modes where  $H_z = 0$ , as well as TE modes where similarly  $E_z = 0$ . Hybrid modes refer to all other modes having six non-zeros components ( $E_r$ ,  $E_\theta$ ,  $E_z$ ,  $H_r$ ,  $H_\theta$ ,  $H_z$ ). In the weakly guided approximation, hybrid modes are further divided in two categories known as EH and HE. As



the refractive index difference reduces, several modes that were clearly dissociated tend to degenerate, i.e. they end up satisfying the same frequency equation, at least to a very good approximation [13]. Quite remarkably, by adding up the spatial distributions of all modes sharing an identical propagation constant  $\beta$ , we end up with a new series of modes in which the light is linearly polarized [11]. These fictive modes, i.e. in reality they are a combination of the fiber real modes, are labelled as  $LP_{ml}$  ( $m \geq 0, l \geq 1$ ) and are associated with simplified versions of the frequency equation (2.19), which are summarized in table 2.1 [13]. Prior to

$LP_{ml}$ mode ( $l \geq 1$ )	Modes combination	Frequency equation
$LP_{0l}$	$HE_{1l}$	$\frac{J_0(pa)}{pJ_1(pa)} = \frac{K_0(qa)}{qK_1(qa)}$
$LP_{1l}$	$TE_{0l} + TM_{0l} + HE_{2l}$	$\frac{J_1(pa)}{pJ_0(pa)} = -\frac{K_1(qa)}{qK_0(qa)}$
$LP_{2l}$	$EH_{m-1,l} + HE_{m+1,l}$	$\frac{J_m(pa)}{pJ_{m-1}(pa)} = -\frac{K_m(qa)}{qK_{m-1}(qa)}$

Table 2.1 – Categorization of LP modes and associated frequency equation

draw fundamental conclusions related to LP modes, we first introduce the parameter  $V$  known as the normalized frequency

$$V^2 = a^2(p^2 + q^2) = a^2 k_0^2 (n_{co}^2 - n_{cl}^2) \quad (2.20)$$

which enables to define the cutoff condition of a given mode, that is determining whether the mode is being guided or not. This is achieved by letting  $q \rightarrow 0$  (hence  $V \rightarrow ap$ ) in the frequency equations provided in table 2.1, which yields the following conditions [13]

$$m = 0 \quad \frac{J_0(V)}{VJ_1(V)} \rightarrow \infty \quad (2.21)$$

$$m \geq 1 \quad \frac{J_m(V)}{VJ_{m-1}(V)} \rightarrow -\infty \quad (2.22)$$

that enable classifying the different LP modes according to the order in which they are being guided. The first mode of all is the  $LP_{01}$ , which corresponds to the solution  $V = 0$  in (2.21). The value  $V = 0$  implies that this mode is *always* guided, hence it is referred to as the fundamental mode. The next mode to be guided is the  $LP_{11}$ , which corresponds to the first zero of  $J_0(V)$ , that is  $V \approx 2.405$ . The next guided modes are the  $LP_{02}$  and  $LP_{21}$  modes, where  $V \approx 3.832$  corresponds to the second zero of  $J_1(V)$  ( $V = 0$  is the first zero) and so on. Practically speaking, this implies that in order to secure a single-mode operation, one should maintain  $V < V_c = 2.405$ . There is however a trade-off, as setting  $V$  much lower than  $V_c$  would have disastrous impacts on the waveguiding properties of the fiber. Indeed, a lower value of  $V$  results in the mode being less confined to the core, that is a larger fraction of the optical power travels in the cladding, making it more sensitive to bending loss [17], such that  $V$  is usually set close to  $V_c$ . The fundamental mode shape radial profile  $R(r)$  follows the Bessel functions defined in (2.15)

for the core, and in (2.16) for the cladding. The mode shape is in practice often approximated by a Gaussian function, i.e.

$$R(r) \approx \exp\left(-\frac{r^2}{w^2}\right) \quad (2.23)$$

and the matching is excellent, as depicted in Fig.2.3 for  $V = 2.4$ . The beam waist  $w$  is to a first

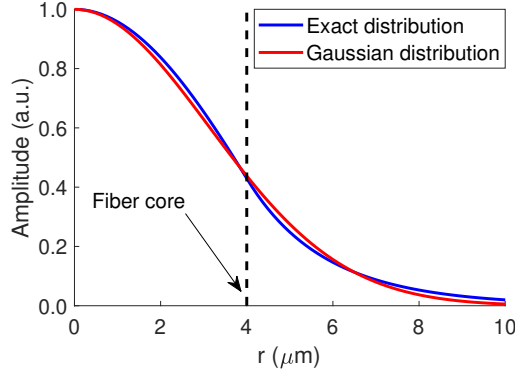


Figure 2.3 – Fundamental mode ( $LP_{01}$ ) radial profile for  $V = 2.4$  and a fiber core radius of  $a = 4 \mu\text{m}$ .

order approximation given by the core radius  $a$ , yet a more precise value might be obtained from the following empirical expression, which is fairly accurate for values of  $V$  ranging from 1.2 to 2.4 [18]

$$\frac{w}{a} \approx 0.65 + 1.619V^{-3/2} + 2.879V^{-6} \quad (2.24)$$

In this case, the beam waist is  $w \approx 4.4 \mu\text{m}$ . It appears from Fig.2.3 that the power of the fundamental mode (the square of the curves displayed) travels in both core and cladding. This behavior is typical of dielectric waveguides, where the light is not confined to a given region but rather spreads over the entire structure. Notice that while most of the amplitude vanishes at a distance  $\sim 10 \mu\text{m}$  from the core, the cladding extends up to  $125 \mu\text{m}$ , i.e. it is safe to consider the cladding as infinite in all previous derivations. The shape of the fundamental mode will turn extremely important in latter chapters on forward stimulated Brillouin scattering (FSBS), as this interaction relies on the surface overlap between acoustic and optical modes of the fiber.

### 2.3 Scattering mechanisms in optical fibers

When light is injected into an optical fiber, a fraction of its energy is continuously returned to its emitting point due to different scattering processes. This backscattered light provides information on the local condition of the fiber, as all scattering processes rely on the fiber optomechanical or thermodynamic properties. The three major classes of scatterings occurring in

in an optical fiber are depicted in Fig. 2.4. Rayleigh scattering arises due to density fluctuations

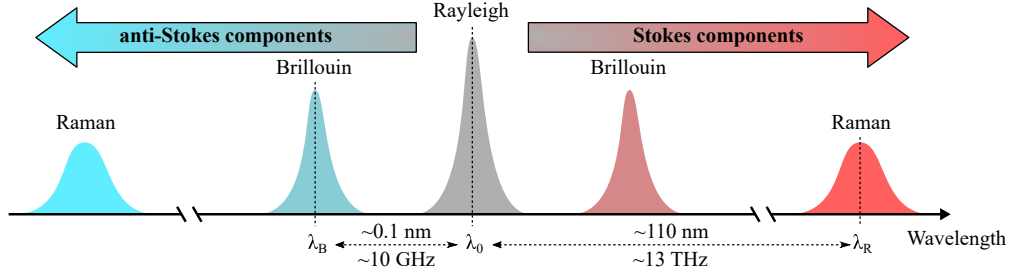


Figure 2.4 – Scattering processes in optical fibers at a wavelength ~1550 nm.

in the medium, and is well known to be the main reason why the sky appears blue. It is labelled as *elastic* scattering, because the scattered light does not experience any frequency shift. In optical fibers, Rayleigh scattering is far stronger than Brillouin or Raman scattering in terms of scattering efficiency. Both Brillouin and Raman scattering are *inelastic* scatterings, i.e. the scattered light experiences a frequency shift with respect to the carrier frequency of the incident light. In both cases, the backscattered light comprises a red-shifted and a blue-shifted components, known as Stokes and anti-Stokes components, respectively. Brillouin and Raman scattering share similarities in the nature of the scattering process, but exhibit very distinct behaviors. Raman scattering results from molecular scattering, yielding a broadband spectrum, far shifted from the incident light central wavelength (~110 nm or ~13 THz for a central wavelength of ~1550 nm). The frequency shift in Brillouin scattering, which involves material displacement in the form of acoustic waves, is several orders of magnitude lower (~0.1 nm or ~10 GHz for a central wavelength of ~1550 nm), and the spectrum of the scattered light is far narrower than for Raman scattering owing to a strict phase matching requirement.

### 2.3.1 Rayleigh scattering

Rayleigh scattering results from the interaction between an incident electromagnetic field and particles much smaller than the light wavelength [19, 20]. Through dimensional considerations, lord Rayleigh was able as early as 1871 to predict that the intensity of light scattered by a particle much smaller than the wavelength is inversely proportional to the fourth power of the wavelength  $\lambda$  [21]. For a single particle presenting a polarizability  $\alpha$ , the ratio of scattered intensity  $I_s$  over incident intensity  $I_i$  reads

$$\frac{I_s}{I_i} = \frac{1}{\lambda^4} \frac{16\pi^4 \sin^2(\varphi) \alpha^2}{R^2} \quad (2.25)$$

where  $\varphi$  denotes the angle between the input polarization (linear) orientation and the direction of the scattering and  $R$  is the distance from the scatterer to the observer. In optical fibers, the "particles" initiating Rayleigh scattering are actually density fluctuations frozen in the fiber structure during manufacturing, as well as material composition variations due to inhomogeneous doping [11] (see section 2.1.1). The angular dependency of Rayleigh scatter-

ing (2.25) implies that only a certain fraction of it will be recaptured by the fiber and guided back towards the source, as pictured in Fig.2.5. While the amount of density fluctuations

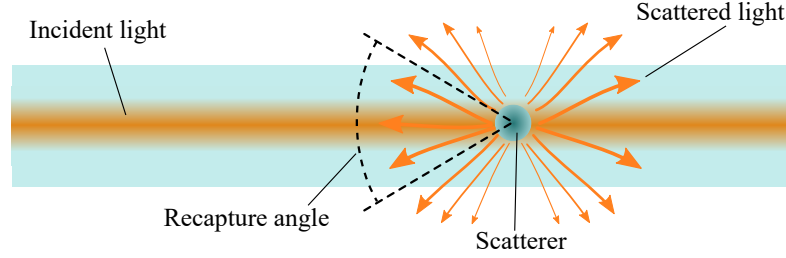


Figure 2.5 – Illustration of Rayleigh scattering in optical fibers.

has been significantly alleviated over time by dedicated research, it will never be possible to entirely suppress them in silica-based fibers, due to the amorphous nature of glass. Therefore, Rayleigh scattering imposes a hard limit to the loss achievable in standard single-mode fibers. The  $\lambda^{-4}$  dependency of Rayleigh scattering drove the telecommunication industry to operate towards higher wavelengths, ultimately settling at  $\lambda \approx 1550$  nm where material absorption starts to dominate [14]. At this wavelength, Rayleigh scattering amounts to a loss of  $\sim 0.15$  dB/km, which is nearly reached by modern commercially available fibers<sup>II</sup>. Following these considerations, Rayleigh scattering was exploited at a very early stage to evaluate the loss over entire optical links, and is still widely used nowadays both in laboratory as well as in industrial environment. The first experimental implementation of what would later be known as an optical time-domain reflectometer (OTDR) was demonstrated in 1976 by *Barnoski et al.* [22].

#### Incoherent optical time-domain reflectometry

An incoherent OTDR operates by launching incoherent light in the form of an optical pulse in a given fiber or fiber link, i.e. comprising two or more cascaded optical fibers, and measuring the returning power as a function of time. By time-of-flight evaluation, the time-dependent information can be accurately mapped to a distance-dependent trace, and the power backscattered from a given position by Rayleigh scattering  $P_R(z)$  is given by [11]

$$P_R(z) = P_0 \alpha_s(\lambda, z) B_c(\lambda, z) \frac{W}{2} e^{-2\alpha z} \quad (2.26)$$

where  $P_0$  is the pulse peak power,  $\alpha_s$  is the scattering coefficient,  $B_c$  is the recapture coefficient,  $W$  is the pulse width and  $\alpha$  is the attenuation coefficient. The two factors 2 in (2.26) are inherent to single-end access optical reflectometers. The factor 2 halving the pulse width  $W$  is omnipresent in distributed sensing technologies, and is due to the counter-propagating nature of the two signals in presence, i.e. the forward travelling pulse and the backward propagating scattering (see section 2.4.1). The factor 2 in the exponential attenuation term is due to the round-trip experienced by the light, i.e. the pulse undergoes the fiber attenuation until a given

<sup>II</sup>For instance, see the SMF-28 ULL by Corning® which certifies loss lower than 0.17 dB/km

position  $z$ , and the backscattered signal is again attenuated during its propagation back to the detection system. A typical response of an incoherent OTDR is shown in Fig.2.6.a).

### Sensing based on coherent Rayleigh scattering

Rayleigh scattering also has a strong potential for sensing applications when the incoherent light source used in conventional OTDR is replaced with a highly coherent one, i.e. a narrow-linewidth laser. The working principle is exactly the same as for incoherent OTDR, except this time the detected signal exhibits a jagged-like pattern owing to the multiple interferences between the signals emitted by individual scatterers within the pulse width, as shown in Fig.2.6.b). This behavior was predicted as early as 1984 [23], but was considered

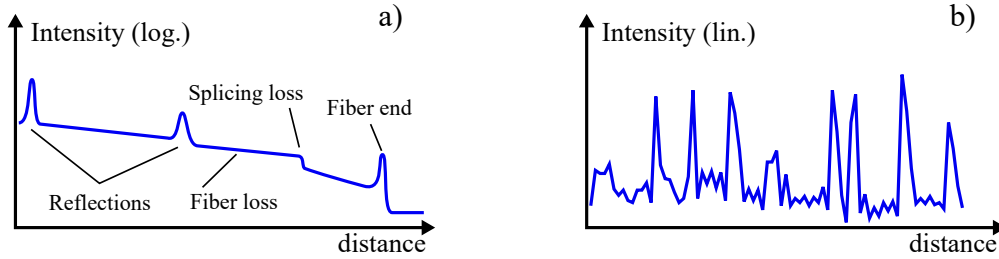


Figure 2.6 – Typical response of incoherent OTDR (a) and  $\Phi$ -OTDR (b).

at that time as a disruptive effect to the normal operation of conventional OTDR. Although *a priori* chaotic, the typical pattern of the so called phase-OTDR or  $\Phi$ -OTDR is repeatable provided that the experimental conditions remain unchanged. Since the trace is determined by interferometric process, it turns out that it is extremely sensitive to any change in the fiber mechanical properties. This high sensitivity was first exploited in an intrusion sensor [24], where even tenuous vibrations could be detected owing to the high sensitivity of the system. The sensitivity of  $\Phi$ -OTDR based systems is better understood by pointing out that the phase of an optical signal at a given frequency  $\nu$  varies with distance  $z$  accordingly to the magnitude of its wavevector  $k$  as

$$kz = \frac{2\pi n(\epsilon, T)\nu}{c_0} z \quad (2.27)$$

where the dependency of the refractive index  $n$  on strain  $\epsilon$  and temperature  $T$  is emphasized. Note that practically speaking, temperature changes mainly impact on the refractive index  $n$ , while strain ( $\epsilon$ ) has a much larger contribution on the propagated distance  $z$  due to fiber elongation/contraction. Many  $\Phi$ -OTDRs operate by scanning the frequency of the interrogating light source, which as seen from (2.27) can compensate for variations in the phase  $kz$  due to strain and/or temperature changes. The sensitivity of  $\Phi$ -OTDR systems is thus usually defined as the ratio between the amplitude of the frequency excursion  $\Delta\nu$  required to compensate for a shift of one degree or one micro-strain  $\mu\epsilon$ . Typical values lie approximately one thousand

times higher than Brillouin based systems [2], i.e.

$$\frac{\Delta\nu}{\Delta T} \approx -1.3 \text{ GHz/K} \quad (2.28)$$

$$\frac{\Delta\nu}{\Delta\epsilon} \approx -150 \text{ MHz}/\mu\epsilon \quad (2.29)$$

### 2.3.2 Raman scattering

Raman scattering refers to the scattering of light with vibrational modes of the molecules within a given medium [11, 14, 15, 20]. The interaction, reported for the first time in 1928 by Raman [25], is usually described using a quantum-mechanical approach, as shown in Fig.2.7.a). The frequency shift of the Stokes and anti-Stokes branches of Raman scattering

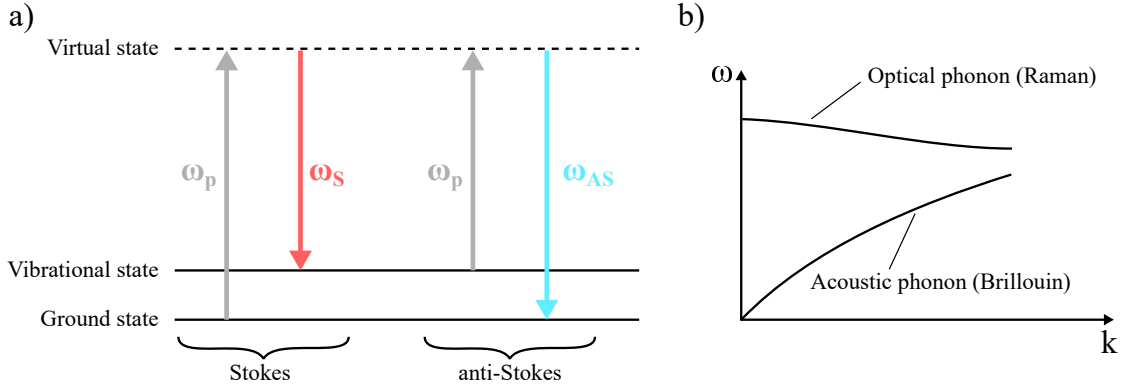


Figure 2.7 – a) Energy diagram of Raman scattering. b) Dispersion diagram of optical and acoustic phonons.

can be understood by looking at the energy diagram shown in Fig.2.7.a). In the former case, the molecule is in the ground state, and transits to a higher energy vibrational state through a virtual state of even higher energy by absorbing a pump photon  $\omega_p$ . The energy balance is brought by the emission of a photon with lower frequency  $\omega_s$ , explaining the red-shift observed in Stokes scattering. If the molecule is already in a excited (vibrational) state, a complementary process may occur where the transition this time leads to the generation of a photon of higher energy (blue shifted)  $\omega_{AS}$ . A similar approach may be envisioned for Brillouin scattering (see details in section 2.3.3), yet the two mechanisms are inherently different due to the properties of the phonons involved in the process. This is depicted in Fig.2.7.b) [11], which shows the energy-momentum relation of optical phonons, involved in Raman scattering, and acoustic phonons, involved in Brillouin scattering. In the first case, the phonon may exhibit high energy ( $\omega$ ) with zero momentum ( $k$ ), while in the second case, the dispersion diagram shows a radically different behavior as a vanishing momentum yields zero energy. As detailed in the upcoming section, this implies that Brillouin scattering can only occur under strict phase matching, which ensures that energy and momentum are conserved during the interaction. This requirement is largely relaxed for Raman scattering, because the phonons

involved show similar energy levels over a broad range of momentum, which implies that a wide variety of optical waves will be able to satisfy the rules of energy and momentum conservation. This explains why the observed Raman spectrum in optical fiber is so broad, as it extends over ~40 THz at a wavelength of 1550 nm [14].

### Raman based distributed sensing

Raman scattering was exploited in pioneer works to achieve distributed temperature sensing as early as 1985 [26]. The operating principle of distributed Raman sensors relies on the thermal activation of optical phonons in the fiber, which follows the Bose-Einstein distribution [11]

$$\bar{n} = \left( e^{\frac{h\Omega}{kT}} - 1 \right)^{-1} \quad (2.30)$$

where  $\bar{n}$  is the average number of phonon at frequency  $\Omega$  and temperature  $T$ , while  $h$  and  $k$  denote Planck and Boltzmann constants, respectively. Since a phonon is annihilated in the anti-Stokes process, the scattering is proportional to  $\bar{n}$ , while the generation of a new phonon during the Stokes process implies that the scattering is proportional to  $\bar{n} + 1$  [11]. For Raman scattering, the average number of thermally activated phonons is quite low, owing to the large energy  $\Omega$  involved in the process. Indeed, injecting  $\Omega = 13$  THz and  $T = 300$  K in (2.30) yields  $\bar{n} \approx 0.14$ . Distributed Raman sensing then operates by acquiring the power of the anti-Stokes  $P_{AS}$  and the Stokes waves  $P_S$ , and evaluating their ratio as

$$R_{A,S} = \frac{P_{AS}}{P_S} \propto \frac{\bar{n}}{\bar{n} + 1} = e^{-\frac{h\Omega}{kT}} \quad (2.31)$$

The sensitivity of Raman sensors at room temperature, i.e. the normalized variation of (2.31) with respect to  $T$  is about [2]

$$\frac{1}{R_{A,S}} \frac{\Delta R_{A,S}}{\Delta T} \approx 0.74\% / K \quad (2.32)$$

While quite straightforward to implement, Raman distributed sensors face two major performances limitations. First, the low amount of backscattered light often requires the use of multimode fibers in order to increase the captured power, which in turns limit the maximum sensing range due to inter-modal dispersion, that is due to the different propagation velocity of the modes guided at the probing wavelength. Second, the measurement described by (2.31) is an intensity measurement, hence will be impaired by wavelength dependent loss that will not be properly alleviated by the ratio operation performed in (2.31) due to the large spectral separation between the Stokes and the anti-Stokes waves.

### 2.3.3 Spontaneous Brillouin scattering

Brillouin scattering accounts for one of the light-scattering mechanisms observable in an optical fiber, and was described as early as 1922 by Léon Brillouin [1]. It originates from the interaction of light with density fluctuations induced by the propagation of acoustic waves in the fiber [11, 14, 15, 20]. The high optical intensity resulting from the tight confinement of light in optical fibers combined to ultra-low propagation loss make this type of waveguide propitious to the triggering of Brillouin scattering even at moderate input power. This phenomenon was however described and observed way before the advent of optical fibers, such that many approaches focus on modeling Brillouin scattering in bulk media, without taking into account the impact of the guiding structure. Although such description predicts accurately most of the features of Brillouin scattering in optical fibers, it fails to model the impact induced by the guided propagation of acoustic waves on the scattered optical signal. In particular, guided acoustic waves enable Brillouin scattering to occur in the forward direction, a behavior prohibited in bulk opto-acoustic media. This specific mechanism is known as forward stimulated Brillouin scattering (FSBS) and is thoroughly addressed in chapter 4.

#### Density waves

Classically, Brillouin scattering is modeled by two sets of wave equations governing the evolution of density fluctuations and light (2.7) in a given material. The density wave equation takes the following form.

$$\frac{\partial^2 \Delta \rho}{\partial t^2} - \Gamma \nabla^2 \frac{\partial \Delta \rho}{\partial t} - V_a^2 \nabla^2 \Delta \rho = 0 \quad (2.33)$$

Here,  $\Delta \rho$  describes the deviation of the density from its average value  $\rho_0$ , which is assumed to remain constant in both space and time,  $\Gamma$  is the acoustic damping coefficient and  $V_a$  is the acoustic velocity of longitudinal waves. In such conditions, equation (2.33) is decoupled from the optical wave equation (2.7). This is perfectly reasonable, given that in spontaneous regime the incident light should by definition not influence the scattering process. Equation (2.33) is solved assuming a solution in the form of a plane wave depending on position  $\mathbf{r}$  and time  $t$  as

$$\Delta \rho(\mathbf{r}, t) = \text{Re} \left\{ Q e^{i(\mathbf{q} \cdot \mathbf{r} - \Omega_A t)} \right\} \quad (2.34)$$

where  $Q$  is the acoustic amplitude,  $\mathbf{q}$  is the wavevector and  $\Omega_A$  is the acoustic angular frequency. Injecting (2.34) into (2.33) yields

$$\Omega_A = -i \frac{\Gamma_B}{2} + \sqrt{\Omega_0^2 - \left( \frac{\Gamma_B}{2} \right)^2} \quad (2.35)$$



where only the positive square root was retained as it carries a physical meaning.  $\Omega_0$  is the system natural frequency defined as

$$\Omega_0 = V_a |\mathbf{q}| \quad (2.36)$$

and  $\Gamma_B$ , the acoustic decay rate, is related to the phonon lifetime  $\tau_B$  as [27]

$$\Gamma_B = \tau_B^{-1} = \left( |\mathbf{q}|^2 \Gamma \right) \quad (2.37)$$

Injecting (2.35) into (2.34) yields

$$\Delta \rho(\mathbf{r}, t) = e^{-\Gamma_B t/2} \text{Re} \left\{ Q e^{i(\mathbf{q} \cdot \mathbf{r} - \Omega_B t)} \right\} \quad (2.38)$$

which corresponds to a damped harmonic wave with

$$\Omega_B = \sqrt{\Omega_0^2 - \left( \frac{\Gamma_B}{2} \right)^2} \quad (2.39)$$

### Additional polarization

At first glance, there seems to be no influence from the density wave equation (2.33) on the electromagnetic wave equation (2.7), yet such relation is required for light scattering to occur. The origin of spontaneous Brillouin scattering lies in a physical phenomenon called photoelasticity, which refers to the change in the optical properties of a given medium in response to mechanical deformations. It can be expressed as [15, 20]

$$\Delta \chi = \frac{\gamma_e}{\rho_0} \Delta \rho \quad (2.40)$$

where  $\gamma_e$  is the electrostrictive constant and  $\Delta \chi$  indicates a change in electric susceptibility. As a consequence of the induced susceptibility change  $\Delta \chi$ , the polarization defined in (2.8) acquires an additional term  $\mathcal{P}_{\text{spt}}$ , i.e.

$$\mathcal{P} = \epsilon_0 \mathcal{E} (\chi + \Delta \chi) = \mathcal{P}_{\text{lin}} + \mathcal{P}_{\text{spt}} \quad (2.41)$$

The first term on the right-hand side of (2.41),  $\mathcal{P}_{\text{lin}}$ , yields the contribution to the linear refractive index (2.9) while the second term is found by injecting (2.40) and (2.38) into (2.41)

$$\mathcal{P}_{\text{spt}} = \frac{\epsilon_0 \gamma_e}{2 \rho_0} e^{-\Gamma_B t/2} \text{Re} \left\{ Q E_0 e^{i[(\mathbf{k}_i + \mathbf{q}) \cdot \mathbf{r} - (\omega_i + \Omega_B) t]} + \overline{Q} E_0 e^{i[(\mathbf{k}_i - \mathbf{q}) \cdot \mathbf{r} - (\omega_i - \Omega_B) t]} \right\} \quad (2.42)$$

where  $\overline{Q}$  designates the complex conjugate and we assumed a harmonic incident electric field  $\mathcal{E}(\mathbf{r}, t)$  of the form

$$\mathcal{E}(\mathbf{r}, t) = \text{Re} \left\{ E_0 e^{i(\mathbf{k}_i \cdot \mathbf{r} - \omega_i t)} \right\} \quad (2.43)$$

where  $E_0$ ,  $\mathbf{k}_i$  and  $\omega_i$  are the amplitude, wavevector and angular frequency of the electric field, respectively.

#### Phase matching

The additional polarization (2.42) is linear with respect to the incident optical wave and contains two distinct contributions. The first term, leading to anti-Stokes scattering, exhibits a wavevector equal to  $\mathbf{k}_i + \mathbf{q}$  and oscillates at a frequency  $\omega_i + \Omega_B$ , whereas the second term corresponds to Stokes scattering, which wavevector and frequency are given by  $\mathbf{k}_i - \mathbf{q}$  and  $\omega_i - \Omega_B$ , respectively. In order to represent valid solutions to the wave equation, the newfound components must exhibit the typical dispersion of an optical wave.

$$\mathbf{k}_S = \mathbf{k}_i - \mathbf{q} \quad (2.44a)$$

$$\omega_S = \omega_i - \Omega_B = |\mathbf{k}_S| \frac{c_0}{n} \quad (2.44b)$$

$$\mathbf{k}_{aS} = \mathbf{k}_i + \mathbf{q} \quad (2.45a)$$

$$\omega_{aS} = \omega_i + \Omega_B = |\mathbf{k}_{aS}| \frac{c_0}{n} \quad (2.45b)$$

Equations (2.44) and (2.45) state conservation of energy and momentum in spontaneous Brillouin scattering, as depicted in Fig.2.8. This representation of Brillouin scattering enables

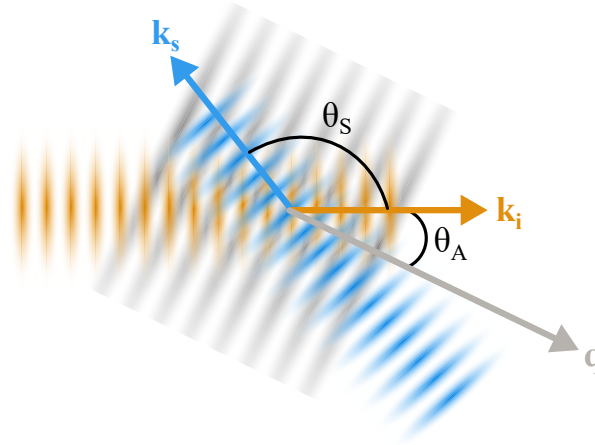


Figure 2.8 – Three waves interaction satisfying phase-matching condition in Brillouin scattering. The wavevectors denote the incident optical wave  $\mathbf{k}_i$ , the scattered wave  $\mathbf{k}_s$  and the acoustic wave  $\mathbf{q}$ .

to interpret the frequency shift experienced by the Stokes and anti-Stokes components as a Doppler shift resulting from the scattering of the incident light by a moving Bragg grating. Indeed, the frequency shift amounts to  $\Omega_B$ , which turns proportional to the velocity of acoustic waves in the fiber, as evidenced later on in equation (2.49). In the Stokes case, the incident optical field propagates in the same direction as the acoustic wave, such that the scattered field carrier frequency gets down-shifted. On the other hand, anti-Stokes scattering corresponds to the scattering of light by a grating moving against the incident optical field, hence increasing

the frequency of the scattered signal. Alternatively, Brillouin scattering may also be addressed following the quantum-mechanical approach used to describe Raman scattering in section 2.3.2. The major difference lies in the fact that due to the large momentum carried by acoustic waves (see Fig.2.7.b), the interaction requires this time a strict phase-matching as given by equations (2.44) and (2.45).

### Brillouin frequency shift

In order to simplify relations (2.44) and (2.45), one may observe that while optical frequencies lie above a hundred THz, the acoustic frequencies considered here are known *a posteriori* to amount to several GHz only. It is thus safe to assume that

$$\omega_S \approx \omega_{aS} \approx \omega_i \quad (2.46)$$

Therefore, (2.44b) and (2.45b) imply

$$|\mathbf{k}_i| \approx |\mathbf{k}_{aS}| \approx |\mathbf{k}_S| \quad (2.47)$$

such that either  $(\mathbf{k}_i, \mathbf{k}_S, \mathbf{q})$  or  $(\mathbf{k}_i, \mathbf{k}_{aS}, \mathbf{q})$  form the sides of an isosceles triangle. Using the cosine rule or any similar method, one retrieves

$$|\mathbf{q}| = 2|\mathbf{k}_i| \sin\left(\frac{\theta_s}{2}\right) \quad (2.48)$$

where  $\theta_s$  denotes the angle between  $\mathbf{k}_i$  and either  $\mathbf{k}_S$  or  $\mathbf{k}_{aS}$  (see Fig.2.8). We first neglect the influence of damping by setting  $\Gamma_B = 0$  in (2.39), yielding

$$\Omega_B = \Omega_0 = |\mathbf{q}| V_a \quad (2.49)$$

The acoustic frequency is finally given by

$$\nu_B = \frac{\Omega_B}{2\pi} = \frac{2V_a n}{\lambda} \sin\left(\frac{\theta_s}{2}\right) \quad (2.50)$$

where  $\lambda = \omega_i / (2\pi c_0)$  is the optical wavelength. Equation (2.50) shows that Brillouin scattering in bulk media is a directional process, i.e. its properties depend on the scattering angle. A most important consideration is that there is no forward scattering component, a statement that will be overruled when taking into account the acoustic waveguiding properties of the fiber in chapter 4.2. The acoustic wavevector is largest for fully backward scattering, that is for  $\theta_s = \pi$ . In optical fibers, light propagation is constrained along the optical axis, such that Brillouin scattering may be either fully forward ( $\theta = 0$ ) or backward ( $\theta = \pi$ ). The value of (2.50) when  $\theta = \pi$  is referred to as the Brillouin frequency shift (BFS)

$$\nu_B = \frac{2V_a n}{\lambda} \quad (2.51)$$

#### Brillouin based sensing

For standard single mode optical fibers,  $\nu_B$  lies usually between 9 GHz and 11 GHz. The exact value depends on multiple parameters, including the presence of dopant in the core and/or the cladding as well as the fabrication process, such that even two fibers fabricated in similar conditions by the same manufacturer might exhibit different BFS. In Brillouin based sensors, evaluation of the BFS provides information about whether the optical fiber is being subject to mechanical deformation or temperature change. This can be explained by observing that  $\nu_B$  depends on the mechanical properties of the fiber through  $V_a$  and  $n$ , although the latter contribution is negligible compared to the former. Indeed, the acoustic velocity  $V_a$  depends directly on the medium density, which will inevitably vary should the fiber be elongated, compressed or subject to a temperature change. For conventional SMFs at a wavelength of  $\sim 1550$  nm, the sensitivities, that is the shift in BFS  $\Delta\nu_B$  per degree  $T$  change or micro-strain  $\mu\epsilon$  read

$$\frac{\Delta\nu_B}{\Delta T} \approx 1 \text{ MHz/K} \quad (2.52)$$

$$\frac{\Delta\nu_B}{\Delta\mu\epsilon} \approx 50 \text{ kHz}/\mu\epsilon \quad (2.53)$$

Note that compared to (2.28) and (2.29), these values are roughly three orders of magnitude lower.

#### Acoustic damping

We now consider the impact of acoustic loss in our study. Taking into account a non-zero acoustic damping rate  $\Gamma_B$ , the temporal exponential decay described in (2.42) is analyzed in the frequency domain by means of a Fourier transform, yielding the following scattered intensity  $I_s$  [20]

$$I_s \propto \frac{1}{(\Delta\omega^2 - \Omega_0^2)^2 + \Gamma_B^2 \Delta\omega^2} \quad (2.54)$$

where  $\Delta\omega$  indicates the frequency shift with respect to the natural frequency, i.e.  $\Delta\omega = \omega - \omega_i$ . Equation (2.54) has two implications on the abovementioned results. First, and although this is negligible in all cases considered in the framework of this thesis, the value of the Brillouin shift (2.51) is now determined by  $\Delta\omega_{\max} = \sqrt{\Omega_0^2 - \Gamma_B^2}/2$ . Second, the linewidth of the resonance defined in (2.54), that is its full-width at half maximum (FWHM) is

$$\Delta\nu_B = \frac{\Gamma_B}{2\pi} = \frac{1}{2\pi\tau_B} \quad (2.55)$$

In conventional single-mode fibers at  $\lambda \approx 1550$  nm,  $\tau_B$  is approximatively equal to 6 ns, hence  $\Delta\nu_B \approx 27$  MHz [11].

### 2.3.4 Stimulated Brillouin scattering

Stimulated Brillouin scattering (SBS) differs from its spontaneous counterpart on one major aspect; it is a nonlinear phenomenon. It arises from a positive feedback loop involving two complementary physical effects known as photo-elasticity and electrostriction [14, 15]. While photo-elasticity (also known as the elasto-optic effect) refers to the variation of refractive index induced by density changes, electrostriction leads to an increase of material density in a dielectric when subject the latter experiences an intense electric field [15]. The entire process is depicted in Fig.2.9. Note that SBS is only possible provided that acoustic phonons

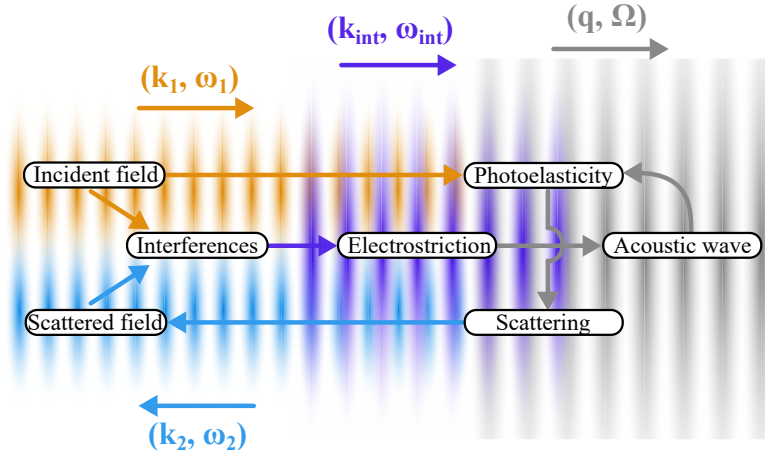


Figure 2.9 – Positive feedback loop in stimulated Brillouin scattering. The wavevectors denote two counter-propagating optical waves optical wave  $(\mathbf{k}_1$  and  $\mathbf{k}_2$ ), the resulting interference pattern  $(\mathbf{k}_{int})$  as well as the acoustic wave  $\mathbf{q}$ , each associated to the corresponding angular frequency.

are generated in the interaction, hence the scattered wave refers to the Stokes wave. The Stokes wave grows due to the scattering of the incident wave against the moving grating induced by the acoustic wave (via photo-elasticity). The intensity pattern resulting from the interference between the incident and scattered fields lead, through electrostriction, to the generation of acoustic waves that add up constructively to the vibrations already present. As a consequence, both the scattered field as well as the acoustic wave grow at the expense of the incident field.

#### Density waves driven by light

While the effect of photo-elasticity, that is the influence of acoustic waves on light scattering, was taken into account by the additional polarization (2.42), considering electrostriction requires to slightly modify the density wave equation given in (2.33). More specifically, we introduce a driving term on the right-hand side of the equation, yielding [15]

$$\frac{\partial^2 \Delta \rho}{\partial t^2} - \Gamma \nabla^2 \frac{\partial \Delta \rho}{\partial t} - V_a^2 \nabla^2 \Delta \rho = -\frac{1}{2} \epsilon_0 \gamma_e \nabla^2 \langle \mathcal{E} \cdot \mathcal{E} \rangle \quad (2.56)$$

where  $\epsilon_0$  is the vacuum permittivity and the brackets indicate a time average operation. The physical meaning behind (2.56) is clear. In stimulated regime, the density waves are driven by the second order dimensional derivative of the time-averaged intensity  $\langle \mathcal{E} \cdot \mathcal{E} \rangle$ . The efficiency of this simulation depends on the electrostrictive coefficient  $\gamma_e$ . Note that the electric field  $\mathcal{E}$  in (2.56) refers to the total electric field in presence, i.e. it is given by the sum of the incident electric field and the scattered electric field.

### Three waves interaction

In order to simplify the description of SBS, we consider that the incident and scattered optical waves are linearly polarized along the same axis. Therefore, we limit the analysis to scalar quantities, written as

$$\mathcal{E}_1 = \text{Re} \{E_1\} = \text{Re} \left\{ A_1(z, t) e^{i(k_1 z - \omega_1 t)} \right\} \quad (2.57)$$

$$\mathcal{E}_2 = \text{Re} \{E_2\} = \text{Re} \left\{ A_2(z, t) e^{i(-k_2 z - \omega_2 t)} \right\} \quad (2.58)$$

$$\Delta \rho(z, t) = \text{Re} \left\{ Q(z, t) e^{i(qz - \Omega t)} \right\} \quad (2.59)$$

where  $E_1$  and  $E_2$  denote the complex fields associated with  $\mathcal{E}_1$  and  $\mathcal{E}_2$ , respectively. Note that in our definition,  $\mathcal{E}_2$  is counterpropagating with respect to  $\mathcal{E}_1$  which is expected from (2.50). Notice also that we denoted the acoustic angular frequency by the free parameter  $\Omega$ , as here the frequency of the acoustic wave is imposed by the frequency difference of the optical waves involved in the interaction. In this configuration, we assumed that the two optical waves are externally generated and sent into the fiber, which is known as a Brillouin amplifier. SBS might as well originate from noise, i.e. by sending only a single optical wave into the fiber, which is known as a Brillouin generator [15].

### Acoustic waves at steady-state

The scalar product of the total electric field appearing on the right-hand side of (2.56) yields

$$\mathcal{E} \cdot \mathcal{E} = \text{Re} \{E_1\}^2 + \text{Re} \{E_2\}^2 + \frac{1}{2} \text{Re} \{E_1 E_2\} + \frac{1}{2} \text{Re} \{E_1 \bar{E}_2\} \quad (2.60)$$

and the bar denotes once more the complex conjugate. Equation (2.60) contains various terms oscillating at different frequencies. Due to the time-averaging operation performed in (2.56), all components oscillating at optical frequencies vanish. Furthermore, and in order to end up with a driving term that is phase-matched to the acoustic wave in presence (2.59), only the last term on the right hand-side of equation (2.60) is retained in the remaining of the derivation. Given the scalar approach adopted, the Laplacian operator in (2.56) reduces to a second order derivative against  $z$ . Eventually, we end up with

$$-\frac{1}{2} \epsilon_0 \gamma_e \nabla^2 \langle \mathcal{E} \cdot \mathcal{E} \rangle = \frac{1}{4} \epsilon_0 \gamma_e q^2 \text{Re} \left\{ A_1(z, t) \bar{A}_2(z, t) e^{i(qz - \Omega t)} \right\} \quad (2.61)$$

where we have assumed phase-matching by defining  $q = k_1 + k_2 \approx 2k_1 \approx 2k_2$  and  $\Omega = \omega_1 - \omega_2$ . Following the derivation performed in [15], we end up neglecting all temporal and spatial derivatives when explicitly writing down (2.56), i.e. we assume steady state. Following (2.49), we express  $\Omega_0 = q^2 V_a$ , inject (2.61) into (2.56) and end up with

$$Q = \frac{1}{4} \frac{\epsilon_0 \gamma_e q^2 A_1(z, t) \bar{A}_2(z, t)}{(\Omega_0^2 - \Omega^2 - i\Omega\Gamma_B)} \quad (2.62)$$

which defines the amplitude of the acoustic wave  $Q$  at steady-state.

### Additional polarization

Computation of the additional polarization  $\mathcal{P}_{\text{stim}}$  in stimulated Brillouin scattering is performed in a manner similar to the derivation of (2.42) for the spontaneous case. This time however, the electric field  $\mathcal{E}$  is the total electric field resulting from the addition of the two counter-propagating waves  $\mathcal{E}_1$  and  $\mathcal{E}_2$ . Explicitly,

$$\mathcal{P}_{\text{stim}} = \frac{\epsilon_0 \gamma_e}{\rho_0} \text{Re} \left\{ Q e^{i(qz - \Omega t)} \right\} \text{Re} \{ E_1 + E_2 \} \quad (2.63)$$

and all wave parameters are defined in (2.57) to (2.59). Explicit derivation of (2.63) yields to four different terms, only two of which are phase-matched with either  $\mathcal{E}_1$  or  $\mathcal{E}_2$  and are retained in further derivation, i.e.

$$\mathcal{P}_{\text{stim}} = \frac{\epsilon_0 \gamma_e}{2\rho_0} \left[ \text{Re} \left\{ Q A_2 e^{i(k_1 z - \omega_1 t)} \right\} + \text{Re} \left\{ \bar{Q} A_1 e^{i(-k_2 z - \omega_2 t)} \right\} \right] \quad (2.64)$$

### The slowly varying envelope approximation

We make a brief digression at this stage of the derivation to introduce a well known relationship that will enable to simplify greatly the upcoming results, and is known as the slowly varying envelope approximation [14, 15]. It is expressed as follows

$$\left| \frac{\partial A(z, t)}{\partial t} \right| \ll |\omega| |A(z, t)| \quad (2.65)$$

$$\left| \frac{\partial A(z, t)}{\partial z} \right| \ll |k| |A(z, t)| \quad (2.66)$$

where  $A$ ,  $k$  and  $\omega$  refer to the amplitude, wavevector and angular frequency, respectively, of any wave (optical or acoustic). Relations (2.65) and (2.66) state that the amplitude of a given wave varies slowly over a few cycles, both in time and distance. The practical implication will be to get rid of higher order derivatives, providing an approximate solution of reasonable complexity.

### Coupled amplitude equations

The total electric field  $\mathcal{E}$  as well as the additional polarization (2.64) consist of two terms, each associated with a given optical wave  $\mathcal{E}_1$  and  $\mathcal{E}_2$ . We thus end up with two equations after their injection in the wave equation (2.7), which are simplified following the slowly varying envelope approximation, yielding

$$\frac{\partial A_1}{\partial z} + \frac{n}{c_0} \frac{\partial A_1}{\partial t} = i \frac{\omega \gamma_e Q A_2}{4nc\rho_0} \quad (2.67)$$

$$-\frac{\partial A_2}{\partial z} + \frac{n}{c_0} \frac{\partial A_2}{\partial t} = i \frac{\omega \gamma_e \tilde{Q} A_1}{4nc\rho_0} \quad (2.68)$$

We may now introduce the solution found for the acoustic amplitude (2.62). Assuming steady-state by making temporal derivatives vanish, one end up with

$$\frac{dA_1}{dz} = i \frac{\epsilon_0 \omega q^2 \gamma_e^2}{8nc_0 \rho_0} \frac{A_1 |A_2|^2}{(\Omega_0^2 - \Omega^2 - i\Omega\Gamma_B)} \quad (2.69)$$

$$\frac{dA_2}{dz} = -i \frac{\epsilon_0 \omega q^2 \gamma_e^2}{8nc_0 \rho_0} \frac{A_2 |A_1|^2}{(\Omega_0^2 - \Omega^2 + i\Omega\Gamma_B)} \quad (2.70)$$

which now define a set of coupled equations. The form taken by these equations enables to derive a new set of equations ruling the evolution of the optical intensities of the two waves involved in SBS [15].

### Coupled intensity equations

The intensity  $I$  associated with a plane wave of amplitude  $E_0$  propagating in a medium with refractive index  $n$  is by definition

$$I = \frac{c_0 n \epsilon_0}{2} |E_0|^2 \quad (2.71)$$

which enables to derive coupled equations for the intensities  $I_1$  and  $I_2$  of the optical waves as

$$\frac{dI_1}{dz} = \frac{c_0 n \epsilon_0}{2} \left( A_1 \frac{d\bar{A}_1}{dz} + \bar{A}_1 \frac{dA_1}{dz} \right) \quad (2.72)$$

$$\frac{dI_2}{dz} = \frac{c_0 n \epsilon_0}{2} \left( A_2 \frac{d\bar{A}_2}{dz} + \bar{A}_2 \frac{dA_2}{dz} \right) \quad (2.73)$$

which can be explicitly obtained by inserting (2.69) and (2.70) into (2.72) and (2.73). In doing so, we assume that the frequency difference between the optical waves is close to the natural Brillouin frequency shift, i.e. we assume  $\Omega \approx \Omega_0$ , yielding the following approximation

$$(\Omega_0^2 - \Omega^2)^2 \approx 4\Omega^2 (\Omega_0 - \Omega)^2 \quad (2.74)$$



which enables to express (2.72) and (2.73) as

$$\frac{dI_1}{dz} = -gI_1I_2 \quad (2.75)$$

$$\frac{dI_2}{dz} = -gI_1I_2 \quad (2.76)$$

where  $g$  is the Brillouin gain spectrum (BGS). The latter exhibits a Lorentzian lineshape

$$g = g_0 \frac{(\Gamma_B/2)^2}{(\Omega_0 - \Omega)^2 + (\Gamma_B/2)^2} \quad (2.77)$$

and  $g_0$  is the Brillouin gain, given by

$$g_0 = \frac{\gamma_e^2 \omega^2}{nV_a c_0^3 \rho_o \Gamma_B} \quad (2.78)$$

and amounts approximately to  $1.4 \times 10^{-11}$  m/W in standard single-mode fibers at 1550 nm. This value was evaluated using  $\gamma_e \approx 0.902$ ,  $\rho_0 \approx 2210$  kg/m<sup>3</sup> and  $V_a \approx 6000$  m/s [14]. Sensing platforms relying on SBS use exactly the same principle as for spontaneous Brillouin scattering, i.e. the device aims at evaluating the value of the Brillouin frequency shift  $\Omega_0$  at every position along the fiber. As will be discussed in section 2.4.6, time-domain based approaches require for one of the waves  $I_1$  and  $I_2$  to be much smaller than the other, i.e. enabling to decouple equations (2.75) and (2.76). Before concluding this section, let us notice that so far no identity

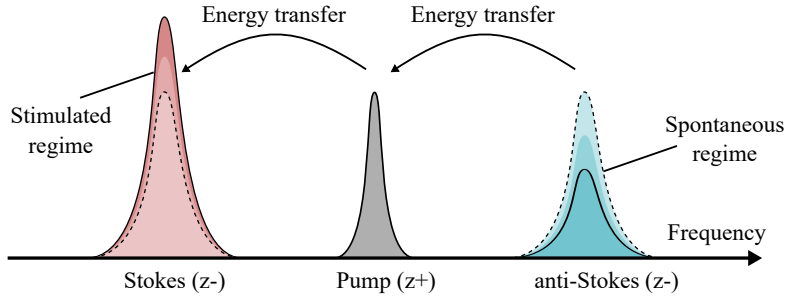


Figure 2.10 – Energy transfer in stimulated Brillouin scattering. The pump is counter-propagating with respect to the Stokes and anti-Stokes waves.

has been put on the two intensities  $I_1$  and  $I_2$ , simply we assumed that  $I_1$  is co-propagating with the acoustic wave whereas  $I_2$  experiences a counter-propagating motion. Therefore, while equation (2.75) describes the attenuation undergone by  $I_1$ , equation (2.76) implies that  $I_2$  experiences amplification, i.e. energy is transferred from  $I_1$  to  $I_2$ , that is from the wave of higher frequency to the wave of lower frequency. Consider now a Brillouin generator scenario, i.e. a single optical wave, referred to as the pump, is launched into an optical fiber. At low input power, that is lower than the SBS critical power [14], the pump generates a spontaneous backscattered Stokes and anti-Stokes waves. As the pump power grows and SBS starts to take place, it appears that  $I_1$  might either play the role of the pump and  $I_2$  the one of the Stokes

wave, or  $I_1$  might take the role of the anti-Stokes wave and  $I_2$  the one of the pump. This dual process yields a unidirectional energy transfer as depicted in Fig.2.10. Note that this remains valid if the optical waves are externally generated and sent counter-propagating in the fiber, i.e. a signal located within the Stokes (anti-Stokes) BGS will experience gain (loss).

## 2.4 Distributed optical fiber sensing

In this section, we will provide with general notions on distributed optical fiber sensors (DOFS), restricting the scope of the discussion to time-domain methods that operate by sending an optical impulse into the fiber and acquiring a specific backscattered signal. While all parameters presented here are valid for most time-domain DOFS, the analysis is articulated around Brillouin based sensors, which were used to acquire all the results reported in this dissertation.

### 2.4.1 Spatial resolution

Spatial resolution (SR) is a key parameter in distributed optical fiber sensors (DOFS), as it defines the minimum distance between two independent events that can be fully distinguished. It also specifies the minimum length of an event, such as e.g. a temperature change, which magnitude can be fully evaluated by the sensor (or to 90% of its value depending on the definition [2]). In time-domain based DOFS, the spatial resolution is intricately related to the width  $W$  of the pulse sent into the fiber. The counter-propagating motion of the interrogating pulse, usually referred to as the pump, and the backscattered signal bringing back the information to the end user introduces a factor two in the relationship, such that the spatial resolution ends up being only half of the spatial extent covered by the pump, as explained in Fig.2.11.

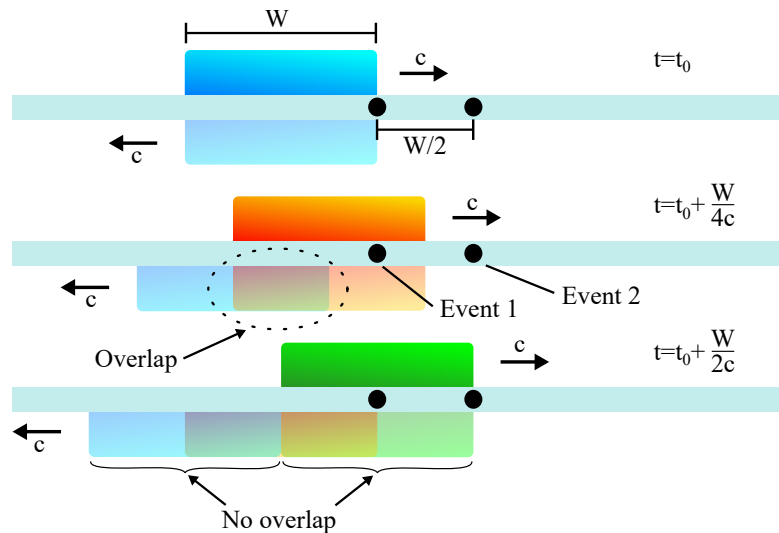


Figure 2.11 – Illustration of spatial resolution in time-domain based distributed optical fiber sensors.

We consider an optical fiber comprising two events (labelled as 1 and 2) separated by a distance equivalent to half of the pulse width  $W$ . At any time, due to e.g. Brillouin scattering, part of the pump pulse energy is sent backwards into the fiber towards the emitting point of the pulse. Both the pump and the backscattered signal travel at the group velocity of light at the given wavelength, denoted  $c$ . At a given time  $t_0$ , the leading edge of the pulse sees the first event, hence the backscattered signal (in blue) already contains information related to that event. After a delay corresponding to a quarter of the pulse duration, part of the newly generated backscattered signal (in orange) overlaps with the previous emission due to the finite propagation speed of the signals in the fiber. Therefore, part of the energy emitted at  $t_0$  and at  $t_0 + W/(4c)$  end up reaching the detector at the same time, mixing the information from both locations. In order to avoid any information overlap, it is therefore sufficient for the pulse to propagate on a distance equal to only half of its width, i.e. the backscattered signal emitted at  $t_0 + W/(2c)$  is totally dissociated from the one generated at  $t_0$ . As a consequence, the information on the second event does not mix with the information acquired for the first event. The spatial resolution of a pulse based interrogator is thus

$$\text{SR} = \frac{W}{2} \quad (2.79)$$

where  $W$  is the pulse width in meters. As will become clearer in section 2.4.2, the spatial resolution of a given sensor is always compromised by other criteria, such as the sensing distance. Overall, one would like to reduce the pulse width as much as possible, hence achieve extremely sharp spatial resolution. However, this comes at the expense of energy, as the shorter the pulse, the lower the backscattered signal, which in turns restricts the range of the sensor. In DOFS, all parameters are interconnected, such that it is generally speaking not possible to improve on one aspect without degrading on another.

### 2.4.2 Signal-to-noise ratio

Signal-to-noise ratio (SNR) is a very general concept, that describes the quality of a measurement by evaluating the ratio of information, quantified by the signal power  $P_s$ , to the level of detrimental fluctuations of the measurand induced by noise  $P_n$ , i.e.

$$\text{SNR} = \frac{P_s}{P_n} \quad (2.80)$$

While this definition of SNR is intuitive and formal, accurate evaluation of the noise and signal powers in practical applications is not that straightforward. As will be explained in sections 2.4.5 and 2.4.6, Brillouin sensors operate by retrieving a bell-shaped curve known as the Brillouin gain spectrum (BGS, see section 2.3.4) at each fiber location, as shown in Fig. 2.12. The SNR is thus more conveniently evaluated by proceeding to repeated measurements in identical conditions, typically five as in Fig. 2.12, and operate the following ratio

$$\text{SNR} = \frac{\mu}{\sigma} \quad (2.81)$$

where  $\mu$  and  $\sigma$  are the mean value and standard deviation of the BGS value at resonance (maximum value), evaluated based on successive acquisitions. The SNR is a crucial parameter

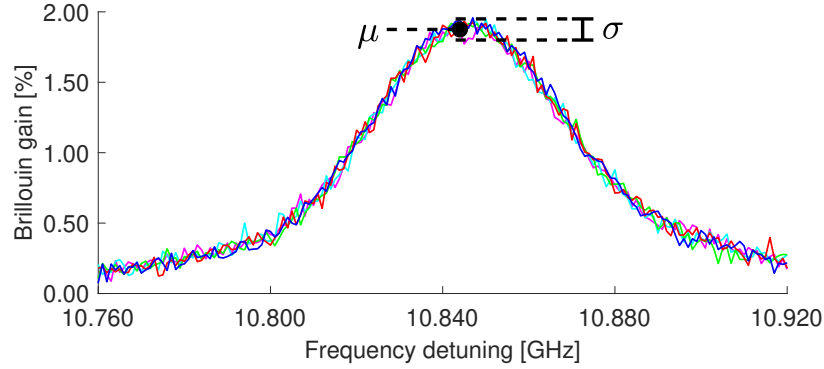


Figure 2.12 – 5 consecutive BGS measurements in reproducible conditions enabling evaluating the signal-to-noise ratio. The unit of the y-axis (%) is intrinsic to the method used to acquire the data, known as Brillouin optical time-domain analysis (BOTDA, see section 2.4.6).

for any acquisition system. For the case of Brillouin based sensors, the SNR can be shown to be inversely proportional to the experimental uncertainty on e.g. the measured temperature [28]. In time-domain based distributed optical fiber sensors (DOFS), the SNR is to a large extent determined by the pulse energy and the noise characteristics of the photodetector at the receiver side. For a given noise level, the SNR is thus entirely driven by the pulse energy, which for a rectangular pulse amounts to a product between its width and its peak power. As explained in section 2.4.1, the pulse width is usually set to meet a specific spatial resolution. The pulse peak power can be increased only up to a certain amount, which is determined by the onset of nonlinear effects, typically modulation instability (MI) in conventional single-mode fibers [29]. As a consequence, conventional Brillouin based DOFS are now hitting fundamental barriers, that define ultimate performances, provided that the noise is properly tackled [30]. The optimization of a given setup as well as solutions to improve the performances of Brillouin based DOFS will be given in chapter 3.

### 2.4.3 Acquisition time

The acquisition time, quite naturally, defines the total amount of time required to perform a given measurement while matching with certain requirements. The systems considered in this dissertation rely on a frequency scanning, i.e. the Brillouin gain spectrum (BGS, as shown in Fig.2.12) at each fiber location, which is stored in a 2-D matrix, is reconstructed by concatenating a series of 1-D traces acquired at different frequencies. At each frequency, the acquisition is averaged  $N_{\text{avg}}$  times, an operation that is mandatory in DOFS due to the weak backscattered optical power. Overall, for a frequency scanning performed on  $N_{\text{freq}}$  points, the

acquisition time  $T$  is

$$T = N_{\text{freq}} \left( \tau_{\text{switch}} + N_{\text{avg}} \frac{2L}{c} \right) \quad (2.82)$$

where  $L$  is the fiber length and  $c$  is the speed of light in the fiber. The parameter  $\tau_{\text{switch}}$  is introduced to account for a delay in the switching time between two successive frequencies due e.g. to the stabilization of the considered device. This amounts usually to  $\sim 1$  ms and the factor  $\tau_{\text{switch}}$  is dominant in short fibers. The transit time given by  $2L/c$  accounts for the time required for the pump pulse to reach the fiber end and for the backscattered signal to return, i.e. a return trip to the fiber far end. This waiting time is mandatory as to prevent sending a second pulse in the fiber while the information from the remote end is still on its way to the detector. For a fiber of length  $L = 50$  km, the return trip effectuated by light is  $\sim 0.5$  ms, hence the factor  $N_{\text{avg}} 2L/c$  turns dominant in long fibers, since the averaging number  $N_{\text{avg}}$  is usually set to several thousands. Note that equation (2.82) defines the ideal acquisition time, which is usually not reached due to instrumental limitations in the acquisition system. It also enables putting light on another trade-off related to the signal-to-noise ratio (SNR), as doubling the averaging  $N_{\text{avg}}$  will result in a noise reduction factor of  $\sqrt{2}$ , yet this will double the acquisition time as evidenced in (2.82). This shows that improving the performances of a given sensor by increasing the averaging number to a large amount is often not a suitable solution, as it would lead to significantly longer measurement times.

### 2.4.4 Sensing range

The sensing range defines the maximum distance that can be interrogated by a given sensor. It generally has to be trade-off with all abovementioned parameters. The main factor limiting the sensing range is the fiber attenuation  $\alpha$ , which imposes an exponential decay on the pulse power as it travels down the fiber. In reflectometry, where only a pulse is sent into the fiber, the detected signal  $P_{\text{det}}(z)$  as a function of distance can be expressed as

$$P_{\text{det}}(z) = P_0 e^{-2\alpha z} \quad (2.83)$$

where  $P_0$  is the power measured at the fiber entrance and the factor two accounts once more for a return trip in the fiber. Attenuation in optical fibers is often expressed in dB/km, by computing the following ratio

$$10 \log_{10} \left( \frac{P_{\text{det}}(z)}{P_0} \right) = 10 \log_{10} (e^{-2\alpha z}) = -2z 10 \log_{10} (e) \alpha = -2\alpha_{\text{dB}} z \quad (2.84)$$

Typically,  $\alpha_{\text{dB}} \approx 0.2$  dB/km, and a 3 dB loss is equivalent to a loss of half of the initial power  $P_0$ . If we again consider a fiber of  $L = 50$  km, the signal measured at the fiber far end is 20 dB weaker than  $P_0$ , which translates in linear scale to a factor 100. This immediately signifies that the signal-to-noise ratio (SNR) at the fiber remote end is one hundred times lower than at the fiber beginning. This explains why most specifications of commercially

available DOFS have to be met at a given distance. In addition to the massive difference in SNR between the fiber ends, the dynamic range of the photodetector in use must be also properly designed as to accurately measure signals with different orders of magnitude. As will be seen in section 2.4.6, this requirement can be relaxed when exploiting stimulated Brillouin scattering (SBS), as the attenuation factor in the exponential decay of the power is halved with respect to reflectometers relying on spontaneous scattering processes. Moreover, this two-way attenuation is also compensated for in Brillouin optical time-domain reflectometry (BOTDR), owing to the coherent detection process used to measure the backscattered signal, as elaborated in the upcoming section.

### 2.4.5 Brillouin optical time-domain reflectometry

Brillouin optical time-domain reflectometry (BOTDR) was first proposed in 1993 [4] as a single-access alternative to Brillouin optical time-domain analysis (BOTDA, see section 2.4.6), which requires launching light simultaneously from both ends of the fiber. BOTDR usually relies on optical heterodyne detection, which is well suited to detect low amplitude signals such as e.g. spontaneous Brillouin scattering. Consider two monochromatic optical signals, linearly polarized along the same axis. They are represented by their electric field denoted

$$\mathcal{E}_{\text{sig}} = \text{Re} \{E_{\text{sig}}\} = \text{Re} \{A_{\text{sig}} e^{i\omega_{\text{sig}} t}\} \quad (2.85)$$

$$\mathcal{E}_{\text{LO}} = \text{Re} \{E_{\text{LO}}\} = \text{Re} \{A_{\text{LO}} e^{i\omega_{\text{LO}} t}\} \quad (2.86)$$

where LO stands for local oscillator. Heterodyne detection operates by measuring the intensity of the beat signal between  $\mathcal{E}_{\text{sig}}$  and  $\mathcal{E}_{\text{LO}}$ , i.e.

$$I \propto |E_{\text{sig}} + E_{\text{LO}}|^2 = I_{\text{sig}} + I_{\text{LO}} + 2\sqrt{I_{\text{sig}} I_{\text{LO}}} \cos[(\omega_{\text{sig}} - \omega_{\text{LO}})t] \quad (2.87)$$

The two low-frequency contributions ( $I_{\text{sig}}$  and  $I_{\text{LO}}$ ) are usually filtered out, such that the last term on the right-hand side of (2.87) remains. This interference term oscillates at the frequency difference between the signal frequency and the LO ( $\omega_{\text{sig}} - \omega_{\text{LO}}$ ) and is proportional to the square root of the product of the intensities of the two signals. This feature is extremely convenient as it enables to compensate for a low intensity signal by mixing it with a strong local oscillator, which is usually the case in BOTDR. Additionally, this square root dependency also enables to counteract the double-path loss described by (2.83), i.e. the factor 2 in the exponential vanishes, which implies that the requirement on the dynamic range of this system is much reduced compared to a direct detection scheme.

A typical implementation of a BOTDR is shown in Fig. 2.13 and operates as follows. The coherent light emitted by a laser source is split in two branches by a coupler. The upper branch is dedicated to shape the continuous-wave (CW) light from the laser into a rectangular pump pulse (in green), amplify it and launch it in the fiber under test (FUT). This is achieved by an intensity modulator, here a semiconductor optical amplifier (SOA) driven by a pulse

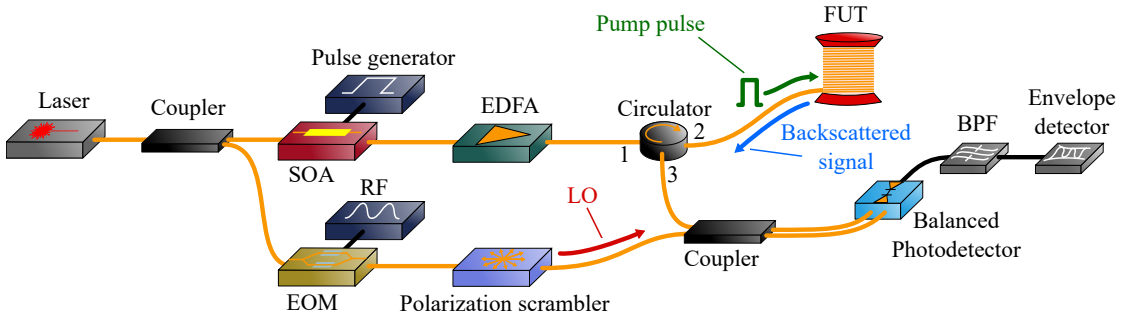


Figure 2.13 – Typical implementation of a BOTDR. The abbreviations stand for: SOA - semiconductor optical amplifier, EDFA - Erbium doped fiber amplifier, RF - Radiofrequency, EOM - electro-optic modulator, FUT - fiber under test, BPF - bandpass filter, LO - local oscillator.

generator. If required, the pulse might be further amplified by an erbium doped fiber amplifier (EDFA) before its injection in the FUT through a circulator. This circulator is also responsible to pick up the signal backscattered by the pump (in blue), and mix it with the local oscillator (LO) generated in the lower branch of the setup (in red). The LO is generated from the same light source as the pump, and comprises two sidebands induced by an electro-optic modulator (EOM), which is driven at extinction by a radio frequency (RF) generator operating at a tunable frequency  $f_{\text{RF}}$ . Each sideband is thus frequency shifted with respect to the laser carrier frequency  $\nu_0$  by  $f_{\text{RF}}$ , as shown in Fig. 2.14.

The polarization scrambler plays a central role in the interferometric process taking place at the photo-detector level and described by (2.87). Indeed, owing to the usage of conventional single-mode fibers, the polarization state of the backscattered signal is random at each fiber location [11]. Therefore, the detected beating signal turns dependent on the instantaneous polarization states of the LO and the backscattered signal, which is random and prone to vary over time, and thus requires proper polarization management, which can be implemented by using e.g. a polarization scrambler. Overall, and without polarization compensation, the measured intensity will exhibit sharp and large transitions. The role of the scrambler is thus to alleviate this detrimental perturbation by averaging out the contributions from a multitude of different, random polarization states of the LO.

The signal delivered by the photodetector is not monochromatic, i.e. it results from the convolution between the LO and the fiber Brillouin gain spectrum (BGS). Note that the latter is in addition usually larger than the fundamental BGS described in section 2.3.3 due to the spectral broadening induced by the finite pump pulse width [31]. The role of the bandpass filter (BPF) is twofolds. First, it filters out any unwanted DC component in the signal due e.g. to a slight unbalance between the amplitudes of the waves sent into the photodetector (balanced detection). Second, it enables sampling the BGS by letting energy flow only through a very narrow frequency band. The magnitude of this signal that oscillates at the BPF central frequency is finally delivered by an envelope detector. The detection process is detailed in Fig. 2.14, showing the transition from the optical domain to the electrical domain after

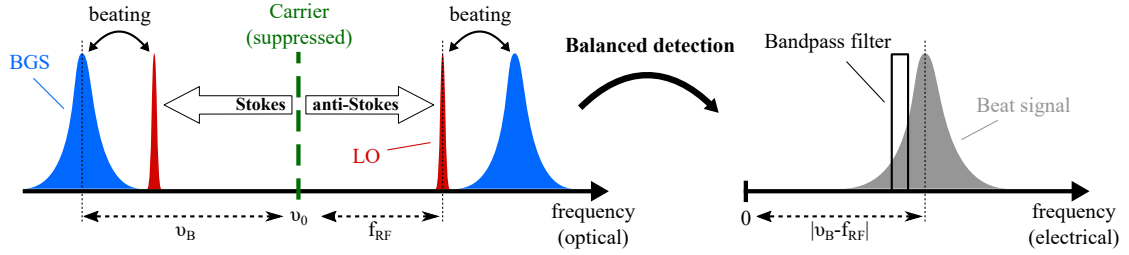


Figure 2.14 – Heterodyne detection of spontaneous Brillouin scattering using balanced detection. The LO frequency is set close to the fiber Brillouin frequency shift  $\nu_B$ , such that the beating signal, once converted to the electrical domain, can be sampled by a narrow bandpass filter.

balanced detection. The gain spectrum can be retrieved by scanning  $f_{RF}$ , thus sweeping the electrical beat signal (in gray) through the bandpass filter seen on the right-hand side of the figure.

#### 2.4.6 Brillouin optical time-domain analysis

Initially, Brillouin optical time-domain analysis (BOTDA) was proposed as an alternative to optical time-domain reflectometry based on incoherent Rayleigh scattering, i.e. the technique aimed at evaluating the loss experienced by a signal propagating in an optical fiber [3]. Its potential ability to perform distributed strain and temperature measurements was quickly understood, the first reports being published shortly after the first mention of the technique [32, 33]. BOTDA relies on stimulated Brillouin scattering (SBS), and operates by sending an optical pulse from one end of the fiber, known as the pump, and a continuous-wave signal from the other end, referred to as the probe. If the frequency difference between pump and probe is close to the fiber Brillouin frequency shift (BFS), energy transfer occurs and the probe experiences either amplification (if the probe frequency is lower than the pump) or attenuation (if the probe frequency is higher than the pump), as depicted in Fig. 2.15. The first scenario is

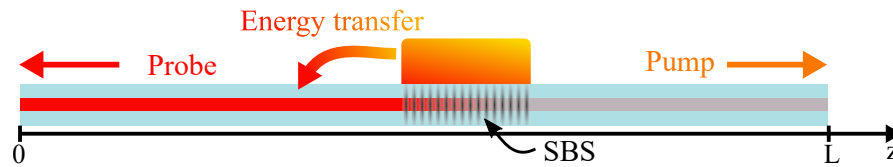


Figure 2.15 – Operating principle of a BOTDA, involving an optical pulse (pump) and a counterpropagating CW wave (probe).

known as Brillouin gain, as opposed to Brillouin loss in the second case. After its interaction with the pump, the amplified (or attenuated) probe proceeds in the fiber, eventually reaching the photodetector. A time acquisition of the probe intensity thus enables to retrieve local information about the energy transfer occurring all along the fiber. Notice that we depicted a unidirectional energy transfer in Fig. 2.15, as if no energy was transferred from the probe



to the pump, in apparent contradiction with equations (2.75) and (2.76). This is known as the undepleted pump approximation [14, 15], and relies on the fact that the pump is larger than the probe by several orders of magnitude. For instance, in long range BOTDA where the fiber length exceeds 20 km, the pump power is capped to ~200 mW (23 dBm) by modulation instability [29] while the probe power is usually maintained below 50  $\mu$ W (-13 dBm) [34], in order to avoid the so-called pump-depletion effect, which defines a scenario where the energy transfer between pump and probe is too severe. Note that the requirement on the probe power is nowadays relaxed to 250  $\mu$ W (-6 dBm) by sending a dual-sideband probe signal into the fiber [35].

Consider now a Brillouin gain configuration, i.e. the intensity  $I_1$  and  $I_2$  in equations (2.75) and (2.76) refer to the pump and the Stokes wave, respectively. They are therefore respectively labelled as  $I_{pu}$  and  $I_{pr}$  for the sake of clarity. The evolution of their intensity is described in a three steps process.

- 1 Before interacting, pump and probe are injected from both ends of a fiber of length  $L$ . Assuming they only experience the fiber attenuation  $\alpha$ , their intensity reads

$$I_{pu}(z_-) = I_{pu}(0)e^{-\alpha z} \quad (2.88)$$

$$I_{pr}(z_-) = I_{pr}(L)e^{-\alpha(L-z)} \quad (2.89)$$

where the minus subscript indicates that SBS did not take place yet.

- 2 During SBS, we make use of the undepleted pump approximation, i.e. we assume that the powerful pump pulse is unaffected by the interaction, hence we write

$$\frac{dI_{pu}}{dz} = 0 \quad (2.90)$$

which implies that  $I_{pu}(z_-) = I_{pu}(z_+) = I_{pu}(z)$ . Assuming that the energy transfer is constant over the pulse width  $W$ , solving of equation (2.76) yields

$$I_{pr}(z_+) = I_{pr}(z_-)e^{gI_{pu}(z)W} \quad (2.91)$$

- 3 After interacting with the pump, the probe proceeds down the fiber towards the photoreceiver. The detected intensity is thus

$$I_{det}(z) = I_{pr}(z_+)e^{-\alpha z} \quad (2.92)$$

Finally, injecting (2.88), (2.89) and (2.91) into (2.92) yields

$$I_{det}(z) = I_{pr}(L)e^{-\alpha L}\exp(g(z, \Delta\nu)I_{pu}(0)e^{-\alpha z}W) \quad (2.93)$$

where we emphasized the dependency of the Brillouin gain on both distance  $z$  and on the frequency detuning between pump and probe  $\Delta\nu$ . Equation (2.93) comprises two distinct

contributions. The first one corresponds to the probe intensity at the detector without SBS interaction, hence we rename it

$$I_{DC} = I_{pr}(L)e^{-\alpha L} \quad (2.94)$$

The second one within the exponential function is labelled as the Brillouin linear gain  $G(z, \Delta\nu)$ , enabling to express (2.93) as

$$I_{det}(z) = I_{DC}e^{G(z, \Delta\nu)} \quad (2.95)$$

By evaluating  $I_{DC}$ , the linear Brillouin amplification denoted  $G(z, \Delta\nu)$  can be retrieved by the following normalization procedure [36]

$$G(z, \Delta\nu) = g(z, \Delta\nu)I_{pu}(0)e^{-\alpha z}W = \ln\left(\frac{I_{det}(z)}{I_{DC}}\right) \quad (2.96)$$

The linear Brillouin gain  $G(z, \Delta\nu)$  is the quantity that any BOTDA pursues to evaluate. Since it is directly proportional to the Brillouin gain  $g(z, \Delta\nu)$ , it provides with identical knowledge on the spectral shape of the Brillouin gain spectrum (BGS). In conventional single-mode fibers,  $G(z, \Delta\nu)$  is in the order of a few percent, as exemplified in Fig.2.12. Notice that  $G(z, \Delta\nu)$  is directly proportional to the pulse width  $W$ <sup>III</sup>, hence broadening the spatial resolution by increasing  $W$  will yield a higher gain as a consequence from a larger energy transfer. Note also that the  $G(z, \Delta\nu)$  only fades with distance at a rate  $e^{-\alpha z}$ , i.e. the exponential attenuation is only half the one of reflectometers operating in direct detection (2.83).

A practical implementation of a BOTDA, that shares many similarities with a Brillouin optical time-domain reflectometer (BOTDR), is shown in Fig.2.16. The upper branch of the setup

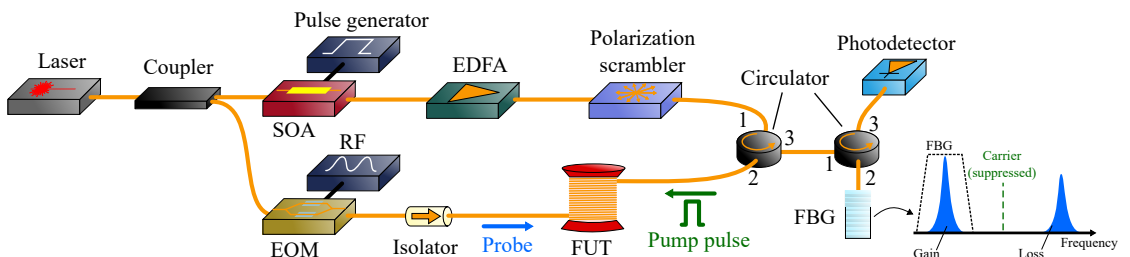


Figure 2.16 – Typical implementation of a BOTDA. The abbreviations stand for: SOA - semiconductor optical amplifier, EDFA - erbium doped fiber amplifier, RF - radiofrequency, EOM - electro-optic modulator, FUT - fiber under test, FBG - fiber Bragg grating.

is once more dedicated to produce a high intensity rectangular pulse by shaping the light of the laser source using an intensity modulator, here a semiconductor optical amplifier (SOA) driven by a pulse generator. An erbium doped fiber amplifier (EDFA) might be used to increase the pump power if required. The probe branch mostly consists of an electro-optic modulator

<sup>III</sup>This is an approximation, as in reality the Brillouin gain fades rapidly when the pulse width approaches the acoustic phonon lifetime, as explicated in section 3.3

(EOM) driven at extinction by an RF modulator at a frequency  $f_{\text{RF}}$ , producing a double side band carrier suppressed continuous-wave (CW) signal. The probe flows into the fiber under test (FUT), meeting with the pulse propagating in the opposite direction, which is stopped by an optical isolator, preventing it from perturbing the operational conditions of the EOM. After its propagation in the FUT, one of the two sidebands of the probe is filtered out by a narrowband fiber Bragg grating before detection by a photodetector, as illustrated by the inset. In this example, the FBG is set as to filter out the anti-Stokes wave, i.e. the device operates in gain mode. Switching to loss mode is extremely straightforward, as it suffices to either tune the FBG (if possible) to filter out the Stokes wave, or change the laser wavelength to achieve the same result. Notice that in this configuration, the effect of pump depletion mentioned earlier is virtually suppressed, because the side-band that is not being detected helps replenishing the pump energy during SBS interaction.

In BOTDA, no additional filtering is required after detection due to the use of a narrow linewidth laser source that serves as an optical fiber during the SBS energy transfer. The Brillouin gain spectrum (BGS) all along the fiber is probed by scanning the EOM frequency  $f_{\text{RF}}$  accordingly, similarly to the case of BOTDR. Note that the requirements on the photodetector for a BOTDA are radically different from the ones for a BOTDR, as the signal detected here consists of a strong DC ( $I_{\text{DC}}$ ), which is being slightly amplified by the pump pulse (a few percents only). Finally, notice that due to SBS relying on the interference pattern between pump and probe, the polarization scrambler is once more devoted to average out fading effects due to random variations of polarization states of the two waves.

### 3 Digital signal processing applied to distributed optical fiber sensing

Digital signal processing (DSP) is a fundamental field of study that provides with the tools and algorithms necessary to transform and analyze digital signals. By definition, a signal consists in any physical quantity, which variations with respect to a given variable such as time or distance are not random but carry some meaningful, underlying information [37]. The distinction between a signal and a *digital* signal, is that the former often refers to analog signals, which are continuous variables depending on continuous value parameters, whereas the latter imply that the data consists in a discrete series of finite precision values that may be stored on any digital memory. Except in rare cases, most signals encountered nowadays eventually end up becoming digital through an important operation known as digitization, which consists in assigning a single value to a continuously varying variable within a certain interval of the free parameter it depends on, often time [38]. This scenario actually applies to *any* type of distributed optical fiber sensor (DOFS), which irremediably end up digitizing the analog signal delivered by an optical receiver. Due to its omnipresence in DOFS and more generally in any scientific field of research, DSP is routinely used to process the raw data provided by a given sensor in order to extract in a most efficient manner the targeted information. Quite naturally, this processing operation is usually tailored to a specific application, and certain algorithms or DSP techniques became standards to deal with the data delivered by a particular DOFS. While this often yields good results, one have to be careful as to not reduce DSP to a set of algorithms or to a series of steps to be taken blindly in order to process a specific data.

In this chapter, we explore how the theory of DSP, restricted to linear time-invariant (LTI) systems, can be used to optimize the performances of a Brillouin optical time-domain analyser (BOTDA). Furthermore, and by making use of very general methodologies, we will show that proper post-processing offers other advantages. First, we will detail how to achieve flexible spatial resolution, resolving information with a shorter spatial resolution than defined by the pulse width. Finally, we will address the topic of optical pulse coding, which consists in sending a well-defined sequence of pulse into the fiber before decoding the measured response to outperform conventional single pulse systems. All these results yet require to become familiar with certain concepts of DSP, which are presented in an introductory theoretical part.

### 3.1 Basic concepts of digital signal processing

This section aims at introducing several key concepts of digital signal processing (DSP) which find later on an application in the framework of distributed optical fiber sensing (DOFS). Because an entire thesis would not be sufficient to address every possible aspect related to DSP, we will restrict ourselves to techniques and algorithms that can be described by a linear time-invariant system (LTI). This assumption is the cornerstone of every single result presented in this chapter.

#### 3.1.1 Linearity, time-invariance and convolution

Linear time-invariant (LTI) systems or filters are mathematical objects that can be described by a linear convolution operation [37, 38]. The demonstration presented here closely follows the one presented in [39]. So far, we deal with analog signals, i.e. we assume  $x(t)$  is a real-valued function depending on a continuous and real-valued parameter  $t$ . An LTI system is modelled as an operator  $L$  that modifies  $x(t)$  while satisfying to the requirements of linearity and time-invariance. We also introduce the Dirac impulse  $\delta(t)$ , also known as delta function (although formally it is not a function), which is used to characterize any LTI system. The response of an LTI system to a Dirac is known as the impulse response, often labelled  $h(t)$  [37, 38, 39]

$$h(t) = L[\delta(t)] \quad (3.1)$$

The Dirac also exhibits the following property

$$x(t) = \int_{-\infty}^{+\infty} x(u)\delta(t-u)du \quad (3.2)$$

which enables characterizing the behavior of any LTI system by its impulse response (3.1). To do so, we rely on our definition and exploit the fact that the operator  $L$  is linear, i.e.

$$L[x(t)] = \int_{-\infty}^{+\infty} x(u)L[\delta(t-u)]du \quad (3.3)$$

Now, since the operator is also time-invariant, and using (3.1) we may write

$$L[x(t)] = \int_{-\infty}^{+\infty} x(u)h(t-u)du = \int_{-\infty}^{+\infty} h(u)x(t-u)du = x(t) * h(t) \quad (3.4)$$

which shows that the effect of any LTI operator  $L$  on a signal  $x(t)$  may be described by a linear convolution between the signal and the impulse response of the system  $h(t)$ . This conclusion is fundamental, as it will enable to model the response of many distributed optical fiber sensors (DOFS) by means of their impulse response  $h(t)$ . While the temporal response of a given sensor is eventually the desired quantity as it can be mapped to a distance-map information via a time of flight evaluation, many operations are performed in the frequency domain by

means of the Fourier transform. While these concepts are well known, they are prerequisites to introduce more specific concepts related to digital signal processing.

#### 3.1.2 The continuous-time Fourier transform

The Fourier transform operation might be seen as the orthogonal projection of a function  $x(t)$  on a vector-space which eigenvectors are complex exponentials  $e^{i\omega t}$ , where  $\omega$  is the angular frequency. This can be seen by evaluating the response of a complex exponential to a linear time-invariant (LTI) operator  $L$  characterized by an impulse response  $h(t)$ , i.e.

$$L[e^{i\omega t}] = \int_{-\infty}^{+\infty} h(u) e^{i\omega(t-u)} du = e^{i\omega t} \int_{-\infty}^{+\infty} h(u) e^{-i\omega u} du = e^{i\omega t} \hat{h}(\omega) \quad (3.5)$$

and we recognize the eigenvalue  $\hat{h}(\omega)$  as the Fourier transform of  $h(t)$ . The definition of the Fourier transform can be extended to any function  $x(t)$  belonging to the space of finite energy function  $\mathcal{L}^2(\mathbb{R})$  [39], and we can write the following Fourier transform pair, which we will refer to specifically as the continuous-time Fourier transform (CTFT)

$$\hat{x}(\omega) = \int_{-\infty}^{+\infty} x(t) e^{-i\omega t} dt \quad (3.6)$$

$$x(t) = \frac{1}{2\pi} \int_{-\infty}^{+\infty} \hat{x}(\omega) e^{i\omega t} d\omega \quad (3.7)$$

We will now provide two fundamental results without demonstration. The first one, known as Plancherel formula, states the conservation of energy as

$$\int_{-\infty}^{+\infty} |x(t)|^2 dt = \frac{1}{2\pi} \int_{-\infty}^{+\infty} |\hat{x}(\omega)|^2 d\omega \quad (3.8)$$

Finally, the convolution theorem states that

$$z(t) = x(t) * y(t) \xleftrightarrow{\text{CTFT}} \hat{z}(\omega) = \hat{x}(\omega) \hat{y}(\omega) \quad (3.9a)$$

$$z(t) = x(t)y(t) \xleftrightarrow{\text{CTFT}} \hat{z}(\omega) = \frac{1}{2\pi} \hat{x}(\omega) * \hat{y}(\omega) \quad (3.9b)$$

and is a central theorem in the theory of signal processing. It translates the fact that a complex operation such as a convolution integral can be achieved by computing the Fourier transform of the two functions independently, multiplying them and finally taking the inverse Fourier transform of the result. Filtering operations are often far more intuitive when transposed to the frequency domain, where the removal of certain frequencies can be more easily understood than by direct inspection of the convolution operation in the time domain.

### 3.1.3 The sampling theorem and the discrete-time Fourier transform

All results presented so far were obtained considering continuous-time functions of continuous-valued parameters. While some results will be exploited as such, one must also fully understand how the mathematical tools and objects that are integral operations and continuous-valued functions can be transposed to a world where every information is reduced to a series of bits stored in a computer. This transition is mandatory as to adequately process the data delivered by a distributed optical fiber sensor (DOFS), provided that the latter may be described as a linear time invariant (LTI) system. We will comment on that statement shortly on.

Consider now a real-valued continuous time signal  $x(t)$ . The mathematical operation that enables to transit from a continuous-time signal to a discrete-time signal is known as sampling, and can be defined as [37, 38, 39]

$$x[m] \triangleq x(mT) \quad (3.10)$$

where  $m$  is a positive integer,  $T$  is the time interval between two samples and the square brackets emphasize that  $x[m]$  is a discrete-time signal. An important observation is that the samples  $x[m]$  are now disconnected from any temporal basis provided by  $t$ , in other words  $x[m]$  consists in a series of values stored in a 1-D vector. This will yield the concept of normalized frequency, as explained here below. A question naturally arising when sampling a signal is about the appropriate sampling rate or sampling frequency defined as

$$f_s = \frac{1}{T} \quad (3.11)$$

To determine this, we will consider that the sampling operation described in (3.10) is equivalent to multiply  $x(t)$  with a Dirac comb  $\delta_T(t)$ , i.e. an infinite set of Diracs separated by a time interval  $T$

$$\delta_T(t) = \sum_{m=-\infty}^{+\infty} \delta(t - mT) \quad (3.12)$$

which assumes the following Fourier transform with respect to frequency  $f = \omega/2\pi$

$$\hat{\delta}_T(f) = f_s \sum_{m=-\infty}^{+\infty} \delta(f - mf_s) \quad (3.13)$$

The Fourier transform of a comb with a period of  $T$  is thus another comb but with a period  $f_s$  in the frequency domain. According to the convolution theorem (3.9), the sampling operation (multiplication) transposed to the frequency domain yields a convolution between the Fourier transform of  $x(t)$  and the newly found Dirac comb, or explicitly

$$x[m] = x(t)\delta_T \quad \longleftrightarrow \quad \hat{x}_m(f) = \hat{x}(f) * \hat{\delta}_T(f) \quad (3.14)$$

where  $\hat{x}_m(f)$  is the Fourier transform of  $x[m]$  and consists of infinite replica of the spectrum of

the initial continuous-time signal  $x(t)$  (scaled by  $f_s$ ), as illustrated in Fig.3.1. The fundamental

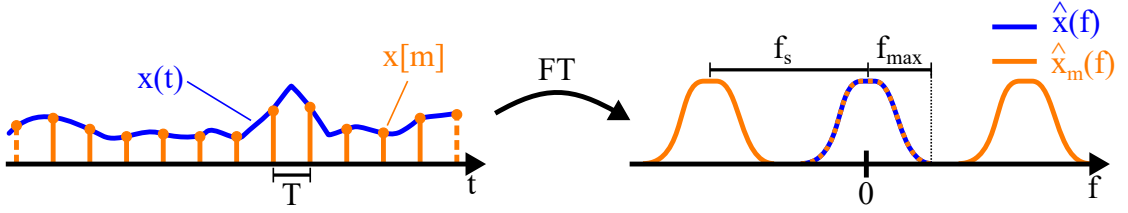


Figure 3.1 – Effect of sampling on the (normalized) spectrum of the signal  $x(t)$ .

principle of the sampling theorem is that one should avoid any spectral overlap between the replica of the original spectrum  $\hat{x}(f)$ , a phenomenon known as *aliasing*. This is mandatory in order to perfectly reconstruct the original signal. To secure this, it clearly appears from Fig.3.1 that the frequency extent of the signal being sampled  $x(t)$  should not exceed half of the sampling frequency, or reversely, the sampling frequency should be at least twice larger than the maximum frequency of the signal  $f_{\max}$

$$f_s \geq 2f_{\max} \quad (3.15)$$

The samples  $x[m]$  are now properly defined mathematically as to reflect the data resulting from the digitization of an analog signal. Notice however that we are still stuck with a continuous-valued function when moving on to the frequency domain. This operation is known as the *discrete-time* Fourier transform (DTFT), and is not to be confused with the *discrete* Fourier transform (DFT) detailed in the following section. The DTFT and its inverse are computed as follows

$$\hat{x}(\Omega) = \sum_{m=0}^{N-1} x[m] e^{-im\Omega} \quad (3.16)$$

$$x[m] = \frac{1}{2\pi} \int_{-\pi}^{+\pi} \hat{x}(\Omega) e^{im\Omega} d\Omega \quad (3.17)$$

where  $N$  is the number of samples in  $x[m]$  and  $\Omega$  is the normalized angular frequency defined as

$$\Omega = 2\pi F = \frac{\omega}{f_s} \quad (3.18)$$

where  $F$  is the normalized frequency and  $\Omega$  is expressed in [radian/sample]. The concept of normalized frequency naturally arises from the discarding of the temporal information when sampling the signal, i.e there is no explicit time variable in (3.16), although implicitly the samples are acquired at precise time-stamps ( $x[m] = x(mT)$ ). Note that since  $m$  is an integer, the periodicity of the DTFT is immediately highlighted in (3.16), and the period is equal to  $2\pi$  (or 1 in terms of normalized frequency  $F$ ). This explains why in the inverse DTFT (3.17), the integral is carried over the fundamental interval ranging from  $[-\pi, \pi]$ . The DTFT is a sort of hybrid transform, lying midway between the continuous-time Fourier transform (CTFT),



which relates two continuous-valued signals, and the DFT, which as we will see operates between two discrete signals. As in the case of the CTFT, a relationship stating the energy conservation exists and is given by

$$\sum_{m=0}^{N-1} |x[m]|^2 = \frac{1}{2\pi} \int_{-\pi}^{+\pi} |\hat{x}(\Omega)|^2 d\Omega \quad (3.19)$$

Notice that the integration interval in the normalized frequency domain is again  $[-\pi, \pi]$ . The convolution theorem yields

$$z[m] = x[m] * y[m] \xleftrightarrow{\text{DTFT}} \hat{z}(\Omega) = \hat{x}(\Omega) \hat{y}(\Omega) \quad (3.20a)$$

$$z[m] = x[m] y[m] \xleftrightarrow{\text{DTFT}} \hat{z}(\Omega) = \frac{1}{2\pi} \hat{x}(\Omega) \circledast \hat{y}(\Omega) \quad (3.20b)$$

where  $\circledast$  designates a *circular* convolution operation, which is similar in all aspects to the *linear* convolution defined in (3.4), except that in this case the integration interval corresponds to one period of the two signals (both periodic of period  $2\pi$ ), conventionally one uses  $[-\pi, \pi]$ . The distinction between the linear and circular convolution is critical, because it may cause a lot of confusion when processing any numerical data.

### 3.1.4 The discrete Fourier transform

The discrete-time Fourier transform (DTFT) is not an adequate tool to process data with, as its frequency domain representation cannot be reduced to a set of discrete values. This issue is circumvented by sampling the DTFT, yielding the following definition of the discrete Fourier transform (DFT) and its inverse

$$\hat{x}[k] = \sum_{m=0}^{N-1} x[m] e^{-i \frac{2\pi km}{N}}, \text{ where } 0 \leq k \leq N-1 \quad (3.21)$$

$$x[m] = \frac{1}{N} \sum_{k=0}^{N-1} \hat{x}[k] e^{i \frac{2\pi km}{N}} \quad (3.22)$$

where both sequences contain the same number of samples  $N$ . The DFT is a fantastic tool to analyze the frequency content of signals after their digitization, especially thanks to fast Fourier transform (FFT) algorithms, which designate efficient implementations of (3.21) and (3.22) when  $N$  equals a power of 2 [37]. A most fundamental aspect when dealing with the DFT, is that every signal is now to be considered as periodic of period  $N$ . While this may seem counter-intuitive at first, it is perfectly reasonable when taking into account the effect induced by sampling in section 3.1.3. As a reminder, sampling of a continuous-time signal  $x(t)$  led to infinite replica of its initial spectrum after computation of the Fourier transform of  $x[m]$ , i.e. the Fourier transform of a digital signal is periodic. It seems thus natural that sampling the continuous-valued spectrum delivered by the DTFT yields in turn a periodic signal in the temporal domain. Therefore, any Fourier operation performed via the DFT must consider

that the original signals are periodic, of period  $N$ . This is evidenced by the form taken by the convolution theorem, i.e.

$$z[m] = x[m] \overset{N}{\circledast} y[m] \xleftrightarrow{\text{DFT}} \hat{z}[k] = \hat{x}[k] \hat{y}[k] \quad (3.23a)$$

$$z[m] = x[m] y[m] \xleftrightarrow{\text{DFT}} \hat{z}[k] = \frac{1}{N} \hat{x}[k] \overset{N}{\circledast} \hat{y}[k] \quad (3.23b)$$

where all convolution operations are now circular convolutions defined as

$$x[m] \overset{N}{\circledast} y[m] = \sum_{m'=0}^{N-1} x[m'] y[\langle m - m' \rangle_N] \quad (3.24)$$

and the brackets  $\langle \rangle_N$  denote the modulo operation. Finally, the Plancherel theorem reads

$$\sum_{m=0}^{N-1} |x[m]|^2 = \frac{1}{N} \sum_{k=0}^{N-1} |\hat{x}[k]|^2 \quad (3.25)$$

#### 3.1.5 Distributed optical fiber sensors as LTI systems

Before proceeding with experimental results, it is important to understand which distributed optical fiber sensors (DOFS) fall within the definition of a linear time-invariant system (LTI) and which do not. Time-invariance is normally assumed in DOFS because one usually considers that the experimental conditions do not vary during the acquisition time. The key criterion to discriminate whether the methodology developed here above applies to a given DOFS is thus linearity. To provide with a counter-example,  $\Phi$ -OTDR (see section 2.3.1) cannot be described by an LTI system, because the response of the system is highly non-linear. Brillouin optical time-domain reflectometry (BOTDR, see section 2.4.5) is also not directly an LTI system due to the usage of coherent detection, that yields a response proportional to the square root of the intensity. In this case, one could still retrieve an LTI response by squaring the measured signal, but significant problems would arise due to cross-terms involving the signal and the additive white Gaussian noise (AWGN) at detection. On another hand, the LTI description fits both incoherent Rayleigh scattering optical time-domain reflectometry (OTDR), Raman OTDR as well as Brillouin optical time-domain analysis (BOTDA), which all exhibit a response linearly proportional to the optical intensity. All results reported in the following sections were obtained for BOTDA, but could be transposed for the case of either incoherent OTDR or Raman OTDR.

## 3.2 Noise reduction in Brillouin optical time-domain analyzers

Most of the results presented in this section were published in the following article [30]<sup>1</sup>. We analyze here the data delivered by a Brillouin optical time-domain analyser (BOTDA) with the perspective of optimizing the final experimental uncertainty making use of digital signal processing (DSP) methodologies. We first begin by describing the data acquisition process in a BOTDA with an emphasis on notions that are relevant from a point of view of signal processing theory such as a description of the noise sources encountered in a conventional BOTDA. We then address the issue of curve fitting and how it impacts the experimental uncertainty. Finally, we will show how to attain optimal performances in single-pulse configuration, raising important issues regarding the usage of digital filtering, especially with respect to 2-D algorithms.

### 3.2.1 Noise as a random process

A given measurement performed by any sensor is unavoidably corrupted by noise. In many applications, including the configurations of distributed optical fiber sensors (DOFS) considered here, the noise can be modelled as an additive white Gaussian noise (AWGN), that is the noisy acquired signal  $x_n(t)$  is expressed as

$$x_n(t) = x(t) + n(t) \quad (3.26)$$

where  $x(t)$  is the noise-free signal and  $n(t)$  designates noise. Here we must emphasize that  $x(t)$  and  $n(t)$  are very different by nature, as  $x(t)$  designates a *deterministic* signal while  $n(t)$  is a *random* signal, that is  $n(t)$  is actually a single realisation of a random process  $N(t)$ . While  $n(t)$  is evidenced to be additive by the model defined by (3.26), the notions of white noise and Gaussian noise are inherent to the statistical properties of the signal. A noise is Gaussian if its probability density function is Gaussian with zero mean, that is

$$N(t) \sim \mathcal{N}(0, \sigma) \quad (3.27)$$

and  $\sigma$  designates the standard deviation of the normal distribution  $\mathcal{N}$ . The term *white* refers to the power spectral density (PSD)  $\Gamma_{nn}(f)$  of the noise, i.e. the distribution of power with respect to frequency  $f$ , which is constant and infinite, explicitly

$$\Gamma_{nn}(f) = \sigma^2 \quad (3.28)$$

and the fact that it equals the square of the standard deviation of (3.27) is clarified hereafter. If one assumes that the random process is stationary [37], the autocorrelation function  $\gamma_{nn}(\tau)$  of

---

<sup>1</sup>@2020 IEEE. Reprinted, with permission from S. Zaslowski, Z. Yang and L. Thévenaz, On the 2-D Post-Processing of Brillouin Optical Time-Domain analysis, J. Light. Technol. 38 (14), 3723-3736 (2020), doi = 10.1109/JLT.2020.2967091

the noise and its PSD form a continuous-time Fourier transform (CTFT) pair, i.e.

$$\gamma_{nn}(\tau) = \int_{-\infty}^{+\infty} \Gamma_{nn}(f) e^{i2\pi f\tau} df = \sigma^2 \delta(\tau) \quad (3.29)$$

and the fact that  $\gamma_{nn}(\tau)$  is proportional to a Dirac follows from (3.28). For a zero-mean signal, the value of the autocorrelation at  $\tau = 0$  is equal to the variance of the considered random process. An AWGN thus shows a uniform PSD equal to  $\sigma^2$  over the entire spectrum (3.28). In the time-domain, this translates by a complete uncorrelation between successive samples (3.29). Note that we only consider continuous-valued variables, as we shall detail the impact of sampling on noise in section 3.2.4.

#### 3.2.2 Noise sources in BOTDA

An example of a Brillouin optical time-domain analyzer (BOTDA) acquisition as well as its decomposition following the model of additive white Gaussian noise (AGWN) defined by (3.26) is shown in Fig.3.2. The noisy signal  $x_n(t)$  (which we assume to be continuous although it

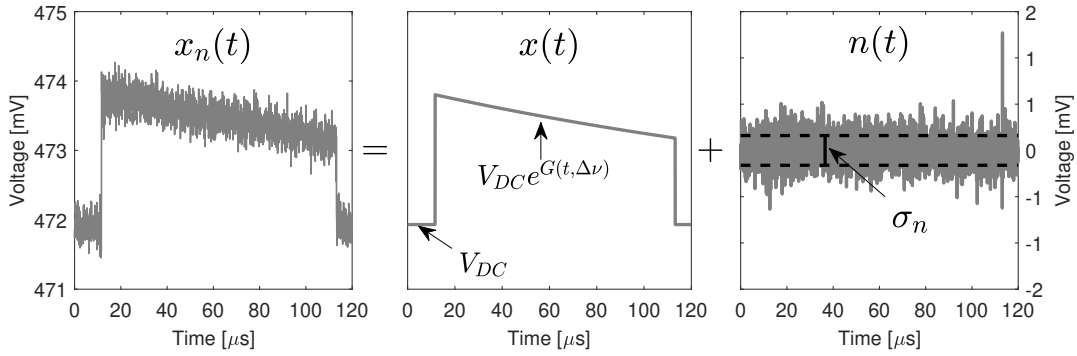


Figure 3.2 – Modelling of a BOTDA acquisition in time domain ( $x_n(t)$  and  $x(t)$  share the same y-axis).

is actually sampled) can be broken down into a pure signal  $x(t)$  and a single realisation of a random process, i.e. an AWGN  $n(t)$  with standard deviation  $\sigma_n$ . The trace  $x(t)$  is typical of a BOTDA, where the desired information given by the linear Brillouin gain  $G(z, \Delta\nu)$  (2.96) is contained in a small amplitude modulation (here about 2 mV) on top of a large DC signal ( $\sim 472$  mV).

While a complete study on the noise sources in BOTDA is out of the scope of this dissertation, we still provide with general information on the most common ones for the sake of completeness. For an in-depth analysis including the optimization of the signal-to-noise ratio (SNR) by acting on the system optical design, we refer the interested reader to [40]. In BOTDA, and more generally speaking in most optical acquisitions systems, the most commonly found sources of noise are shot noise and thermal noise [16]. Shot noise originates from the discrete nature of light carriers (photons) as well as electrons that build up the electric current involved in the

measurement process. The contribution to the variance due to shot noise on the measured voltage  $V$  is [40]

$$\sigma_{\text{sh}}^2 = 2R_L q V B_{\text{det}} \quad (3.30)$$

where  $R_L$  is the resistive load that enables the transimpedance gain (photocurrent conversion into a voltage),  $q$  is the elementary charge and  $B_{\text{det}}$  is the detection bandwidth. Thermal noise finds its origin in the thermally activated motion of electric charges in resistive elements and is thus a direct function of the absolute temperature  $T$ . It can be expressed as

$$\sigma_{\text{th}}^2 = 4k_B T R_L B_{\text{eq}} \quad (3.31)$$

where  $k_B$  is Boltzmann's constant and  $B_{\text{eq}}$  is the equivalent noise bandwidth. The fact that the two bandwidths considered in (3.30) and (3.31) are in practice different is due to the architecture of most photoreceivers, which very likely include a post-amplification step after the transimpedance conversion that adds to the overall thermal noise [40]. Note that  $B_{\text{eq}}$  is usually not provided by photoreceiver manufacturers hence needs proper calibration in well optimized system. The total noise of the system is finally characterized by the following standard deviation

$$\sigma_n = \sqrt{\sigma_{\text{sh}}^2 + \sigma_{\text{th}}^2} \quad (3.32)$$

Note that shot noise is directly proportional to the signal power, hence it is usually negligible at low optical powers whereas thermal noise is power-independent and its contribution remains identical regardless of the power at input of the photoreceiver.

#### 3.2.3 Curve fitting and experimental uncertainty

The amount of noise in any receiving system is irrelevant as such, and needs to be compared to the level of the signal being measured in order to draw conclusions regarding the quality of the acquisition, yielding the notion of signal-to-noise ratio (SNR), which is detailed in section 2.4.2. While SNR is indeed a valid metric in Brillouin optical time domain analysis (BOTDA), the precision of a measurement is preferably defined by the uncertainty on the Brillouin frequency shift (BFS, see section 2.3.3). The BFS, usually labelled  $\nu_B$ , is extracted from the BOTDA measurement via a curve fitting process, or similar. The target here is not to find the ultimate BFS extraction algorithm delivering the lowest experimental uncertainty, a topic which has been thoroughly addressed in [41], rather one aims at drawing attention to critical aspects inherent to this procedure. Curve fitting in BOTDA is spatial-resolution (SR) dependent, because the pump pulse spectrum shapes the measured Brillouin gain spectrum (BGS) through a convolution operation performed in the frequency domain [31]. We rely here on quadratic fitting to extract the BFS, i.e. we fit in the least square sense a parabola to the upper part of the BGS, as illustrated in Fig.3.3. Since quadratic fitting requires a prior estimate of the BFS to deliver accurate results [41], the noisy BGS (in blue) is first smoothed using a

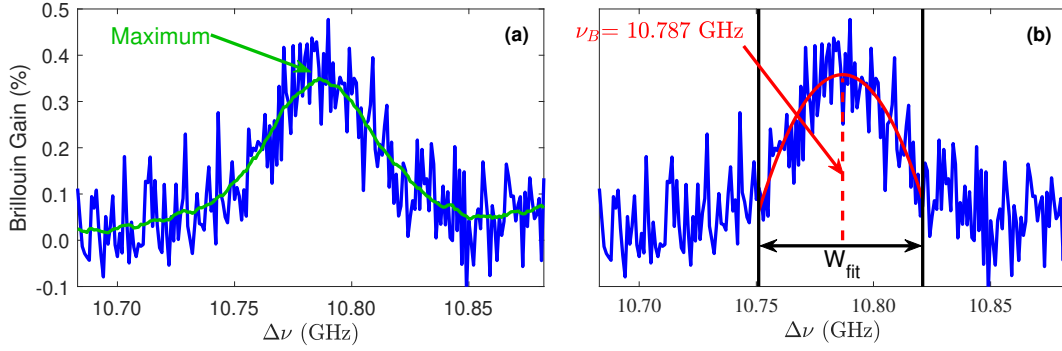


Figure 3.3 – Quadratic fitting in a BOTDA with 2 m SR. The maximum value found from a moving average filter in (a) is used to restrict the number of samples used in the quadratic fitting operation performed in (b).

moving average filter or any similar low-pass filter. The peak frequency of this filtered curve (in green) is then used as the center position of a windowing operation of width  $W_{\text{fit}}$  that restricts the number of samples involved in the quadratic fitting operation (in red), which ultimately delivers the BFS  $\nu_B$ .

A valid question arising from this fitting procedure is how to optimize the width of the window  $W_{\text{fit}}$ . Intuitively, taking into account a larger number of samples should provide with a better estimate, as evidenced by the following relationship [28]

$$\sigma_B = \frac{1}{\text{SNR}} \sqrt{\frac{3\delta\Delta\nu_B}{8\sqrt{2}(1-\eta)^{3/2}}} \quad (3.33)$$

where  $\sigma_B$  is the uncertainty on  $\nu_B$ , SNR is defined in (2.81),  $\delta$  is the frequency scanning step in the BOTDA measurement,  $\Delta\nu_B$  is the BGS full width at half maximum (FWHM) and  $\eta$  defines the number of points involved in the fitting process. More specifically, for a normalized BGS which values range from 0 to 1, only samples greater or equal to  $\eta$  are retained. Equation (3.33) is not intended to provide with an accurate numerical value, as it was derived assuming that the true data is also a parabola. However, it provides with some meaningful insight on the dependency on the experimental uncertainty of the BGS width ( $\Delta\nu_B$ ), the frequency scanning step ( $\delta$ ) and more importantly of the SNR, the latter being inversely proportional to  $\sigma_B$ . With these considerations in mind, the impact of the fitting window width  $W_{\text{width}}$  on  $\sigma_B$  was assessed by performing repeated BOTDA measurements at 1 m, 2 m and 5 m SR and different SNR levels, explicitly 3 dB, 6 dB and 9 dB. The corresponding uncertainty  $\sigma_B$  as a function of  $W_{\text{fit}}$  is shown in Fig.3.4.

Generally speaking, the uncertainty lowers when the fitting window widens. The improvement is yet limited because the BGS in its full extent is never a parabola, i.e. there is an ideal fitting window size. As evidenced by the curves shown in Fig.3.4, the impoverishment of the experimental uncertainty due to an oversized window is moderate, but the increase

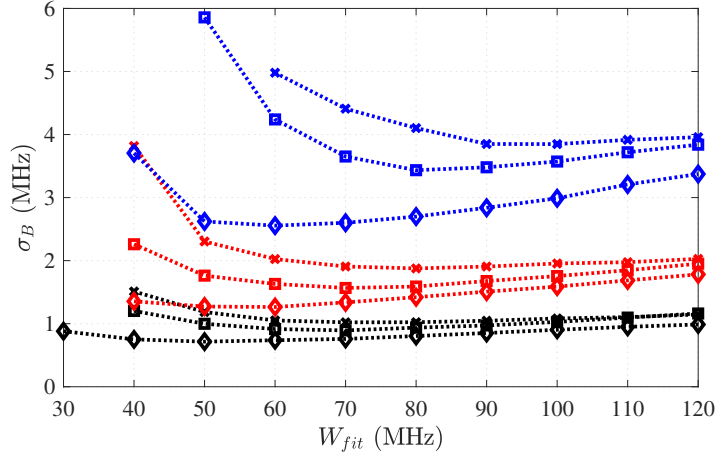


Figure 3.4 – Experimental uncertainty  $\sigma_B$  for different spatial resolutions - 1 m ( $\cdots \times \cdots$ ), 2 m ( $\cdots \square \cdots$ ) and 5 m ( $\cdots \diamond \cdots$ ) - and different SNR levels - 3 dB (blue), 6 dB (red) and 9 dB (black).

in  $\sigma_B$  turns highly critical when  $W_{\text{fit}}$  decreases below a certain value. This is particularly pronounced at low SNR, e.g. considering the results for a spatial resolution of 2 m and an SNR of 3 dB (blue, squares). Notice that a simple adjustment of the fitting window from 50 MHz to 80 MHz enables almost halving the experimental uncertainty, illustrating the importance of carefully optimizing the digital signal processing (DSP) algorithms used to analyze the raw data delivered by a BOTDA. We draw the reader's attention on the fact that a fitting window of 50 MHz at 2 m SR does operate poorly at low SNR, but does not constitute *a priori* an inconceivable choice, given that the BGS FWHM approximately equals 50 MHz (see Fig.3.3). A good way of validating the behavior of any curve-fitting algorithm would be to observe whether the inverse proportionality between SNR and  $\sigma_B$  is respected. Notice that this is indeed the case in Fig.3.4 for a SR of 2 m and  $W_{\text{fit}}=80$  MHz, that is the uncertainty at 6 dB SNR ( $\sim 1.6$  MHz) is roughly half the uncertainty at 3 dB SNR ( $\sim 3.4$  MHz), while this relationship no longer holds when  $W_{\text{fit}}=50$  MHz ( $\sim 1.8$  MHz at 6 dB SNR compared to  $\sim 5.9$  MHz at 3 dB SNR).

### 3.2.4 Noise aliasing and digital filtering

We now address the impact of sampling on noise. We will see that sampling also has an influence on the digital signal processing (DSP) operations that might be undertaken as to improve the quality of the measurements by reducing noise. Recalling section 3.1.3, undersampling of a deterministic signal  $x(t)$  might lead to information loss and signal distortion as a consequence from spectral overlap (see Fig.3.1). Since noise is a random process and therefore cannot be represented by a signal exhibiting a well-defined Fourier transform, it is legitimate to wonder about the consequences of a violation of the sampling theorem when considering noise. It turns out that noise experiences a frequency folding similar to a signal, only that it involves the noise power spectral density (PSD)  $\Gamma_{nn}(f)$  rather than a direct Fourier transform [42].

In order to grasp the implications of that statement, we will now consider a situation where the sampling frequency  $f_s$  is sufficiently high to avoid signal aliasing, but is not necessarily adjusted as to prevent noise aliasing. This scenario, which is illustrated in Fig.3.5, is commonly encountered in BOTDA and other distributed optical fiber sensors (DOFS), because the signal bandwidth is essentially dictated by the pulse width, which is flexible, while the photoreceiver is unique and its bandwidth is usually designed as to accommodate for the sharpest achievable SR. The noise considered is assumed to be white, hence its PSD is uniform and amounts to

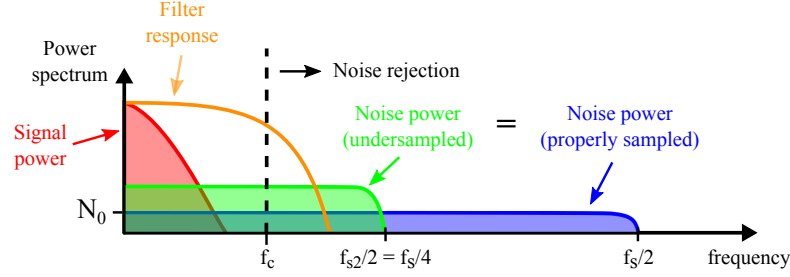


Figure 3.5 – Impact of improperly setting the acquisition system sampling frequency leading to noise aliasing.

a value of  $N_0$  when properly sampled, i.e. the noise extent is limited to  $f_s/2$  and the total noise power in this case is thus  $N_0 f_s$ , considering a two-sided spectrum integration. This also implies that the noise variance is equal to  $\sigma_n^2 = N_0 f_s$ . If we now consider a sampling frequency  $f_{s2} = f_s/2$ , noise aliasing occurs and the upper-half of the noise PSD folds back over the lower frequency band. Because we are dealing with noise, the noise power adds up *linearly*, and the sampled noise PSD is now twice larger but occupies a frequency extent twice narrower. As a consequence, the total noise power is conserved, and the noise variance remains  $\sigma_n^2 = N_0 f_s$ . This implies that, as long as no digital filtering operation is involved, noise aliasing will have no impact on the signal-to-noise ratio (SNR), and consequently the experimental uncertainty  $\sigma_B$  will remain unchanged.

Noise aliasing yet severely hinders the potential of noise-reduction algorithm, for instance a low-pass filter as exemplified here. This is illustrated in Fig.3.5 by the fact that the signal power is evidently independent of the sampling frequency, and therefore so is the cutoff frequency of the digital low-pass filter  $f_c$ . The latter should be set larger than the frequency extent of the signal, in order to avoid any distortion or information loss. Consequently, the filter will let any power at frequencies lower than  $f_c$  go through unaffected while highly suppressing any signal power above  $f_c$ . In the case of noise aliasing, the noise PSD exhibits a higher magnitude in a reduced frequency band, hence the fraction of noise power effectively suppressed by the filter is less than for a properly sampled signal, i.e. the improvement on the SNR is diminished.

This was experimentally demonstrated by performing repeated BOTDA measurements at 5 m spatial resolution, enabling illustrating this effect more clearly by reducing the signal bandwidth to ~20 MHz. The measured  $\sigma_B$  along the fiber is shown in Fig.3.6 for a sampling frequency of 200 MHz (blue), 100 MHz (red) and 50 MHz (black). Notice how the experimental



uncertainty remains identical in all cases despite being sampled at significantly different frequencies  $f_s$ . If unprocessed, the experimental data thus do not suffer from an insufficient sampling rate as long as signal aliasing is avoided. Now, let us observe the impact of filtering

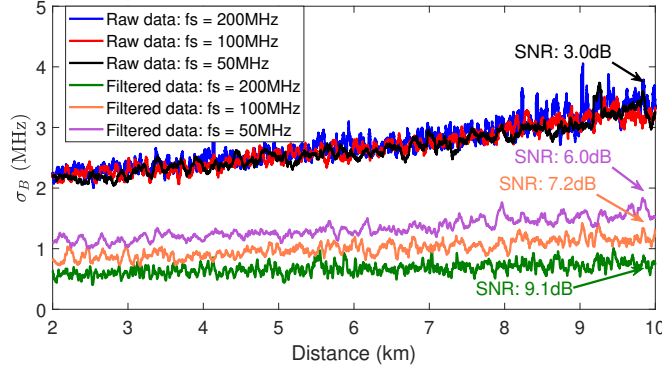


Figure 3.6 – Impact of noise aliasing on experimental uncertainty for raw and filtered data. The green, orange and purple curves originate from the same data set as the blue, red and black curves, respectively, but were numerically filtered with a Gaussian filter.

the raw data, associated to the blue, red and black curves, with a numerical Gaussian filter of fixed bandwidth, yielding the experimental uncertainty profiles depicted in green, orange and purple, respectively. The SNR at the fiber end, that is at a distance of 10 km, are indicated in Fig.3.6. When applying a digital low-pass filter on the data, the SNR improvement reduces by a factor 2 (from 6 dB improvement to 3 dB improvement) when reducing the sampling frequency by a factor 4, in agreement with the square root dependency between noise variance and the noise standard deviation used in our definition of SNR (2.81). This demonstrates the critical need of adjusting the sampling frequency  $f_s$  to the noise bandwidth rather than the signal bandwidth in order to fully harness the potential of digital filters, or to reduce the overall system bandwidth using e.g. an analog filter before proceeding to the sampling operation.

#### 3.2.5 A note on the 2-D post-processing of BOTDA measurements

A Brillouin optical time domain analyser (BOTDA) measurement consists in a series of 1-D traces, concatenated to form a 2-D matrix holding the value of the Brillouin gain at every position  $z$  and every frequency detuning  $\Delta\nu$ . In order to clarify later descriptions, the 1-D traces being concatenated are labelled as Brillouin gain profiles (BGP), as opposed to Brillouin gain spectra (BGS), which refer to the sets of Brillouin gain value versus  $\Delta\nu$  at a fixed distance (see Fig.3.7). So far, we discussed noise reduction along a single dimension of this data matrix, i.e. by filtering each acquisition performed at a fixed  $\Delta\nu$ . Recently, there has been an outburst of interest for 2-D signals processing algorithms, including techniques developed in the field of image processing to improve the performances of BOTDA measurements by significantly enlarging their signal-to-noise ratio (SNR) [43, 44]. Unfortunately, and despite numerous publications claiming performances improvement, this SNR enhancement is illusory and

does not contribute to lower the experimental uncertainty by the same amount, as should be the case according to equation (3.33). The confusion arising from the discrepancy between an apparently measurable SNR improvement and a dissimilar  $\sigma_B$  reduction can be lifted by means of a separable 2-D Gaussian numerical filter.

A 2-D Gaussian filter is completely defined by two parameters that define its spread in both dimensions, conveniently labelled as  $\sigma_{\text{BGP}}$  and  $\sigma_{\text{BGS}}$  to match with the denomination used to characterize the BOTDA matrix. The values taken by  $\sigma_{\text{BGP}}$  and  $\sigma_{\text{BGS}}$  depend both on the pulse width, the former via its temporal (or dimensional) spread and the latter via its frequency extent. In order to introduce some flexibility in the design of the 2-D Gaussian filter, we allow some degrees of freedom by introducing two tuning parameters denoted  $k_{\text{BGP}}$  and  $k_{\text{BGS}}$ , respectively, yielding the following definitions

$$\sigma_{\text{BGP}} = \frac{W_{\text{pulse}}}{k_{\text{BGP}} \Delta t} \quad (3.34)$$

$$\sigma_{\text{BGS}} = \frac{\Delta \nu_B}{k_{\text{BGS}} \delta} \quad (3.35)$$

where  $W_{\text{pulse}}$  and  $\Delta t$  designate the pulse temporal width and the sampling interval, respectively, while  $\Delta \nu_B$  and  $\delta$  are the BGS full width at half maximum (FWHM) and the frequency scanning step, respectively. The 2-D kernel of the numerical Gaussian filter  $f_G$  is defined as

$$f_G[m, n] = \frac{1}{2\pi\sigma_{\text{BGP}}\sigma_{\text{BGS}}} e^{-\frac{m^2}{2\sigma_{\text{BGP}}^2} - \frac{n^2}{2\sigma_{\text{BGS}}^2}} = \underbrace{\frac{1}{\sqrt{2\pi}\sigma_{\text{BGP}}} e^{-\frac{m^2}{2\sigma_{\text{BGP}}^2}}}_{f_{\text{BGP}}[m]} \underbrace{\frac{1}{\sqrt{2\pi}\sigma_{\text{BGS}}} e^{-\frac{n^2}{2\sigma_{\text{BGS}}^2}}}_{f_{\text{BGS}}[n]} \quad (3.36)$$

where  $0 \leq m \leq N_{\text{BGP}}$ ,  $0 \leq n \leq N_{\text{BGS}}$ , and  $N_{\text{BGP}}$  and  $N_{\text{BGS}}$  denote the number of samples in distance and in frequency detuning, respectively. In writing (3.36), we highlighted the separability property of the Gaussian filter which allows to break down its effect along each dimension of the BOTDA matrix independently by means of the 1-D filters  $f_{\text{BGP}}$  and  $f_{\text{BGS}}$  [39]. The effect of 2-D filtering on BOTDA measurements is assessed by following the procedure depicted in Fig.3.7. First, the SNR and experimental uncertainty  $\sigma_B$  are evaluated on raw data,

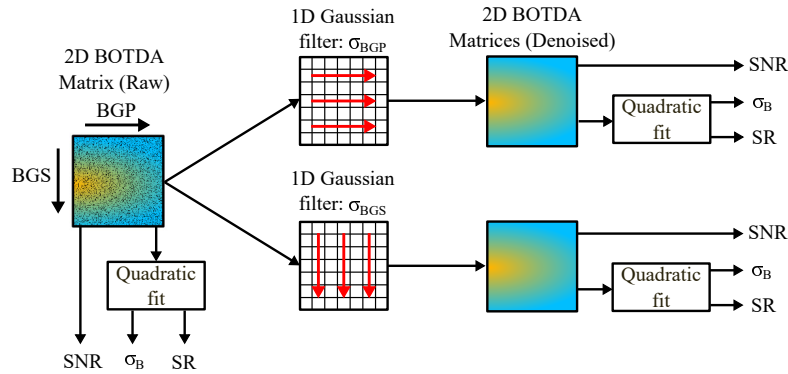


Figure 3.7 – Evaluation of the impact of 2-D filtering on BOTDA measurement.

i.e. before digital filtering. The same data set is then filtered on one hand by  $f_{BGP}$  and on the other hand by  $f_{BGS}$ , before proceeding in each case to evaluate once more both SNR and  $\sigma_B$ . While a reduction of the experimental uncertainty is desirable, it must not be performed at the expense of other metrics of the BOTDA, in particular the processed data should not exhibit a lower spatial resolution (SR) than the raw data. This is verified by analyzing the Brillouin frequency shift (BFS) profile at a transition, realized in practice by immersing a section of fiber (here 5 m long) in warm water, creating a hotspot, usually near the fiber end. The raw data designated in Fig.3.7 consists in a BOTDA matrix for which the SNR at the fiber end is 3 dB, corresponding to an experimental uncertainty of  $\sigma_B = 3.49$  MHz. The BFS profiles after filtering are shown in Fig.3.8, and the experimental SR is evaluated by comparing the results with a reference profile acquired at high SNR (12 dB). Fig.3.8.(a) shows the evaluated

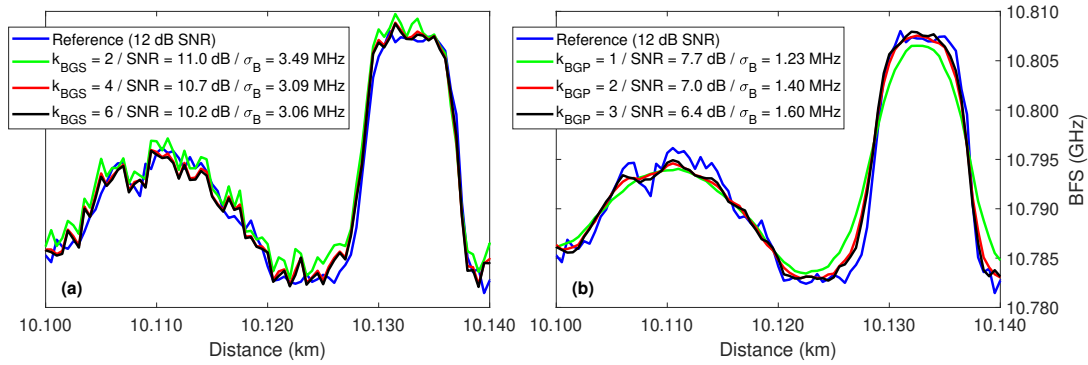


Figure 3.8 – Evaluation of potential spatial resolution degradation due to 1-D filtering. The raw data, i.e. before applying any numerical filter, exhibits an SNR of 3 dB for an experimental uncertainty of  $\sigma_B = 3.49$  MHz.

BFS profiles after filtering along each BGS, and varying the filter strength by tuning  $k_{BGS}$  between 2 and 6. Overall, the SNR improvement appears to be very large, i.e. from 3 dB (raw data) up to 11 dB, corresponding to an 8 dB improvement. However, the experimental uncertainty  $\sigma_B$  barely decreases when compared to the raw data (3.49 MHz), in apparent total contradiction with equation (3.33). In addition, the BFS profile seems unaffected by the filtering operation, disregard of the filter strength. The reason for this lies in the curve fitting operation described in 3.2.3. Fundamentally, fitting a smooth curve over a noisy data set can be seen as finding the optimal low-frequency trend, i.e. a sort of low-pass filtering operation. It is actually mathematically equivalent, given that polynomial curve fitting may be described by a dedicated class of filters known as Savitzky-Golay filters [45]. Therefore, any noise reduction algorithm, being a simple Gaussian filter or a more advanced 2-D image processing algorithm, will be redundant with respect to the curve fitting operation used to extract the BFS from the BGS, and this includes any apparent SNR improvement. Notice for instance that the inverse proportionality between SNR and  $\sigma_B$  in (3.33) was derived assuming statistical independence between the samples, a condition which is violated by any denoising algorithm operating along each BGS or in 2D.

On a conclusive note, notice that in the case of Fig.3.8.(b), the SNR improvement, although moderate, is this time accompanied by a consistent reduction in  $\sigma_B$ . Moreover, one observes a clear deterioration of the experimental spatial resolution as the filter strength increases for lower values of  $k_{BGP}$ . This classical trade-off between SNR (or equivalently experimental uncertainty) and SR that was described in sections 2.4.1 and 2.4.2, naturally shows up here due to the filtering operation. This implies that one may improve the experimental uncertainty *a posteriori*, provided that one can afford to downgrade the sensor spatial resolution. Remarkably, the complementary operation, that is improving the SR at the expense of a poorer SNR is also achievable, and is described in the following section.

### 3.3 Short spatial resolution retrieval

Most of the results presented in this section were published in the following article [46]<sup>II</sup>. In most distributed optical fiber sensors (DOFS), spatial resolution (SR) is often regarded as a key specification, as a finer SR is equivalent with a higher density of information or a larger number of sensing points. Here, we illustrate how to achieve shorter SR in Brillouin optical time domain analyzers (BOTDA) by proper post-processing of the acquired data. Despite the appearance of unwanted numerical artifacts, the technique presented here is straightforward to implement and enables overcoming some of the challenges specific to achieving short SR in Brillouin based sensors. Moreover, it proves to significantly reduce the experimental uncertainty at short SR compared to a conventional BOTDA that would operate at the targeted spatial resolution.

#### 3.3.1 Acoustic lifetime and spatial resolution

In a most direct approach, the simplest way to enhance the spatial resolution (SR) of a given distributed optical fiber sensor (DOFS) operating in a time-domain approach is to reduce the width of the optical pulse launched into the fiber. As mentioned in sections 2.4.1 and 2.4.2, this improvement in the SR of the sensor is accompanied by a poorer precision due to the lower energy of the backscattered signal. Note that since the pulse peak power is limited by the onset of nonlinear effects such as modulation instability [29], the SR-SNR trade-off is unavoidable, and the purpose here is not to provide with a general solution applicable to any time-domain based DOFS. The discussion here is centered around BOTDA, for which the penalty of using a narrow optical pulse is more severe once the pulse width approaches the phonon acoustic lifetime in silica (~6 ns, see section 2.3.3). Indeed, below ~11 ns, corresponding roughly to a spatial resolution of 1 m, the peak Brillouin gain turns highly non-linear with respect to the pulse width [31]. This implies that shortening the pulse width by e.g. a factor 2 will not yield to a response 2 times poorer, but maybe 4 or 6 times worse depending on the initial pulse

<sup>II</sup>@2020 OSA. Reprinted, with permission from S. Wang, Z. Yang, S. Zaslawski and L. Thévenaz, Short spatial resolution retrieval from a long pulse Brillouin optical time-domain analysis trace, Opt. Lett. 45 (15), 4152-4155 (2020), doi = 10.1364/OL.397101

width, although the pulse energy is indeed halved. While more advanced time-domain based approaches [47, 48, 49] have been proposed to circumvent this difficulty, they all come at the cost of a degradation in other key specifications of the sensor, e.g. the acquisition time. Here we base our technique on the model developed in the previous section, i.e. we operate a conventional BOTDA and rely on post-processing to extract the short SR information from the response provided by a longer optical pulse.

#### 3.3.2 Convolution and deconvolution

We proceed one step further in the linear time-invariant (LTI) model developed in section 3.2.1 and used to describe the response of an LTI DOFS such as a BOTDA. More specifically, we focus our attention on the pure signal response  $x(t)$  appearing in equation (3.26) by taking into account the effect of the pump pulse, denoted  $p(t)$ . Explicitly, the temporal BOTDA response  $r_p(t)$  at a given frequency detuning  $\Delta\nu$  reads

$$r_p(t) = p(t) * h(t) + n(t) \quad (3.37)$$

where  $h(t)$  is the fiber intrinsic impulse response. Equation (3.37) states that the acquired trace in time-domain results from the *linear* convolution between the fiber response and the pump pulse, which is assumed to be rectangular and of duration  $T_p$ . Furthermore, the pump pulse itself might be seen as resulting from the linear convolution between a shorter pulse  $s(t)$  of duration  $T_s$  and a series of Diracs separated by a time interval  $T_s$ . In order to take into account the transient response of stimulated Brillouin scattering (SBS) in our model, each Dirac is weighted by an exponential envelope  $e(t)$  that depends on the acoustic lifetime in silica  $\tau_B$  as illustrated in Fig.3.9, that is [27]

$$e(t) = 1 - e^{-\frac{t}{2\tau_B}} \quad (3.38)$$

Eventually, the pump pulse  $p(t)$  is expressed as

$$p(t) = s(t) * d(t) = s(t) * [e(t)\delta_{T_s}(t) (u(t) - u(t - T_p))] \quad (3.39)$$

where  $\delta_{T_s}(t)$  denotes a Dirac comb (see section 3.1.3) and  $u(t)$  is the Heaviside step function which is used to act as a rectangular window of duration  $T_p$ .

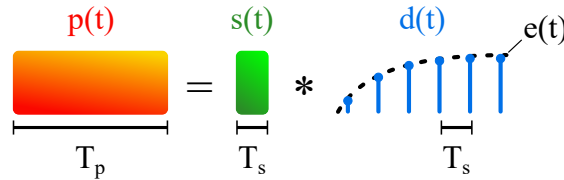


Figure 3.9 – Representation of a BOTDA pump pulse  $p(t)$  as a series of shorter pulses  $s(t)$ .

Equations (3.37) and (3.39) describe the response of the sensor in the optical regime, i.e. before

acquisition. The sampling frequency requires now to take into account the targeted spatial resolution defined by  $T_s$  rather than the used pump pulse duration  $T_p$ . Notice that without surprise, this also implies to dimension the photodetector bandwidth accordingly.

The numerical short pulse response, denoted  $r_s[m]$  is now recovered from the properly sampled long pulse trace  $r_p[m]$  in the frequency domain. Before proceeding further in the derivation, it is important to mention that since all calculations are carried out by means of the discrete Fourier transform (DFT, see section 3.1.4), the multiplications performed in the frequency domain correspond in practice to circular convolutions in the time domain. While this has no impact in the present case because circular and linear convolution are here equivalent, greater care will have to be taken when considering optical coding described in the following section. From (3.37) and (3.39), the DFT of  $r_p[m]$  reads

$$\hat{r}_p[k] = \hat{s}[k] \hat{d}[k] \hat{h}[k] + \hat{n}[k] \quad (3.40)$$

and the short pulse response  $r_s[m]$  is made available by performing the following inverse DFT operation

$$r_s[m] = \text{IDFT} \left\{ \frac{\hat{r}_p[k]}{\hat{d}[k]} \right\} = s[m] * h[m] + \text{IDFT} \left\{ \frac{\hat{n}[k]}{\hat{d}[k]} \right\} \quad (3.41)$$

also known as deconvolution. From (3.41), it appears that the short spatial resolution response given by  $s[m] * h[m]$  can always be perfectly recovered in theory. This is not entirely true in practice and yields minor artifacts in the reconstructed signal at abrupt transitions, as detailed in section 3.3.4. As will be lengthy discussed in the section devoted to optical coding, the second term on the right-hand side of equation (3.41) is critical, as it might lead to severe noise amplification due to the division operation performed in the frequency domain. Assuming additive white Gaussian noise (AWGN, see section 3.2.1), and an initial noise variance of  $\sigma_p^2$ , the scaled noise exhibits a variance  $\sigma_s^2$  given by

$$\sigma_s^2 = \frac{\sigma_p^2}{N} \sum_{k=0}^{N-1} \frac{1}{|\hat{d}[k]|^2} \quad (3.42)$$

The noise scaling factor  $Q$  is thus determined by the acoustic envelope (3.38) and is defined as the increase in the noise standard deviation, i.e.

$$Q = \frac{\sigma_s}{\sigma_p} = \sqrt{\frac{1}{N} \sum_{k=0}^{N-1} \frac{1}{|\hat{d}[k]|^2}} \approx 1.5 \quad (3.43)$$

This noise amplification needs to be taken into account when evaluating the benefits of the technique compared to a conventional BOTDA operating with a pulse of duration  $T_s$ .

### 3.3.3 Performances improvement evaluation

The model developed in the previous section is compared, by means of numerical simulations and experimental data, to the response of a conventional BOTDA. Despite the noise enhancement factor described in (3.43), the proposed technique is expected to perform significantly better than a direct measurement at short spatial resolution due to the removal of the exponential envelope in the deconvolution operation (3.41). Notice that the pure signal in the retrieved trace  $r_s[m]$  is given by  $s[m] * h[m]$ , i.e. the linear convolution between the short pulse and the fiber impulse response. Consequently, the Brillouin gain spectrum (BGS) is the multiplication between the fundamental Brillouin resonance, that is approximatively a Lorentzian function with a full-width at half maximum (FWHM) of  $\sim 27$  MHz (see section 2.3.3) and the pulse spectrum.

The shape of the measured resonance is thus expected to be dominated by the fundamental BGS, and hence is expected to be as narrow as  $\sim 27$  MHz disregard of the targeted SR. This implies that compared to a conventional BOTDA acquisition that suffers from significant spectral broadening at short SR [31], the retrieved BGS is expected to be narrower and peak higher, as confirmed by the numerical simulations results shown in Fig.3.10.(a). Taking into account the constant noise enhancement factor (3.43), both signal-to-noise ratio (SNR) and experimental uncertainty  $\sigma_B$  still highly benefit from the procedure as evidenced in Fig.3.10.(b). The improvement in experimental uncertainty is especially high for spatial resolutions below 1 m.

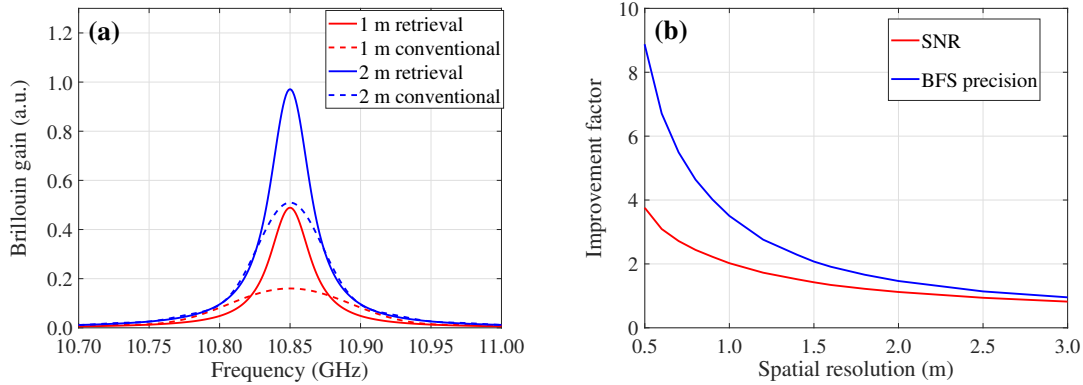


Figure 3.10 – (a). Comparison between the BGS acquired from a conventional BOTDA and the short spatial resolution retrieval method developed here. (b) performance improvement in terms of SNR and experimental uncertainty on the BFS ( $\sigma_B$ ).

These theoretical predictions are then challenged with experimental data, and the results are shown in Fig.3.11. The fiber under test is approximately 50 km long, and is first measured by a conventional BOTDA with a spatial resolution of 6 m, corresponding to a pump pulse width of 60 ns. Fig.3.11.(a) shows the retrieved BGS with a spatial resolution of 2 m inside and outside a 2 m long hotspot placed at the fiber remote end. Accordingly to the model



developed here above, the BGS observed are indeed far narrower than for a conventional BOTDA operating directly at a SR of 2 m, i.e. the full-width at half maximum (FWHM) of the measured resonances is  $\sim 34$  MHz, and can be compared to the 50 MHz wide BGS shown e.g. in Fig.3.3 for a conventional BOTDA. The experimental uncertainty on the Brillouin frequency shift (BFS) along the fiber is shown in Fig.3.11.(b), both for the proposed method (from 6 m to 2 m and 1 m) and for a conventional BOTDA operating at 2 m and 1 m. As anticipated from Fig.3.10.(b), the improvement is about 1.56 for 2 m and 3.5 for 1 m, in excellent agreement with our theoretical prediction.

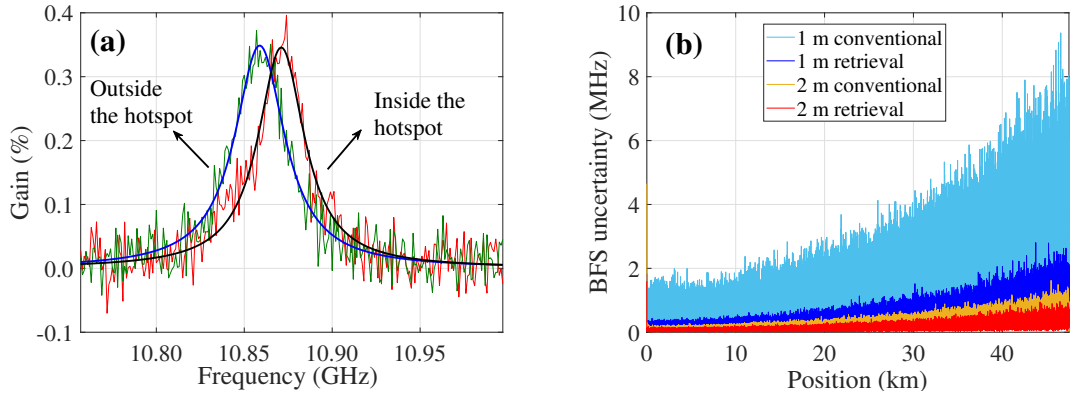


Figure 3.11 – (a) BGS retrieved inside and outside of a 2 m hotspot with a retrieved SR of also 2 m. (b) Experimental uncertainty between the proposed method and a conventional BOTDA.

#### 3.3.4 Artifacts mitigation

Despite a significant improvement in terms of experimental uncertainty compared to a conventional BOTDA operating at short SR, the Brillouin frequency shift (BFS) profile reconstructed with the technique developed here above might display distortions at sharp transitions. These artifacts, which are illustrated in Fig.3.12.(a), are the consequence from the definition of the temporal acoustic envelope defined in (3.38), which is only true at resonance, i.e. when the frequency detuning between pump and probe matches the fiber BFS [27]. Off-resonance, the Brillouin gain exhibits an oscillatory behavior before settling to its steady-state value, hence the acoustic envelope used in our model is not fully representative of the response of the system, leading to distortions in the retrieved signal after deconvolution.

Empirically, these artifacts were measured to be no larger than 3 MHz, which is usually not an issue in most configurations. In addition, these distortions were only observed before a sharp transition in the BFS profile (see section 3.3.5), thus are not degrading the entire measurement. Furthermore, and since they originate from the transient regime of the Brillouin interaction, they are dependent on the initial width of the long pulse used in the acquisition, as exemplified in Fig.3.12.(a) for an initial pulse width of 60 ns and 120 ns. If undesired, these numerical artifacts might thus be alleviated by averaging the contributions of two measurements from



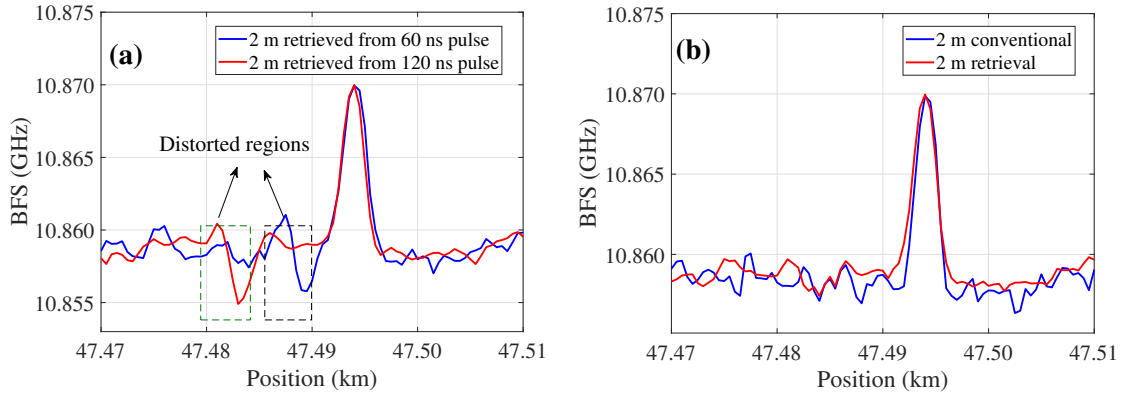


Figure 3.12 – (a) Numerical artifacts before a sharp transition in the fiber BFS at a hotspot. (b) Compensation of these artifacts by averaging the two profiles shown in (a).

two different spatial resolution, as shown in Fig.3.12.(b). The tradeoff to achieve a more accurate measurement is thus to double the measurement time.

Following these results, a recent study addressed in more depth the source of these artifacts [50]. Since the main reason for the presence of the observed BFS distortions lies in the discrepancy between the expected transient response of SBS (assumed to be exponential) and the actual transient response of SBS (oscillatory and dependent on the underlying BFS distribution), the idea presented in [50] relies on performing a deconvolution operation on a differential pulse-pair (DPP) measurement (see hereafter), thus effectively suppressing the contribution from the transient in the measured response. While this is a more elegant and rigorous way of recovering a distortion free BFS, this again comes with the requirement to perform an additional measurement. Eventually, it is a matter of choice for the end user to go for a simpler implementation subject to mild distortions or for a slightly more complex setup that delivers an artifact-free response.

### 3.3.5 Sub-meter spatial resolution

Finally, the proposed technique is challenged to perform in the sub-meter range, starting from a spatial resolution of 4 m, corresponding to a pulse width of 40 ns. Measurements are conducted on a ~10 km long fiber comprising a 20 cm long hotspot at its remote end. The data is compared to the one acquired by a differential pulse-pair (DPP) technique [48], which consists in performing two distinct BOTDA measurements at two slightly different pulse widths (here 42 ns and 40 ns) and subtracting them before processing the result. Note that in DPP, two measurements are mandatory while the technique presented here only requires a single measurement, provided that one can afford the presence of the numerical artifacts described in the previous section. The BFS profiles provided by the two techniques are shown in Fig.3.13.(a).

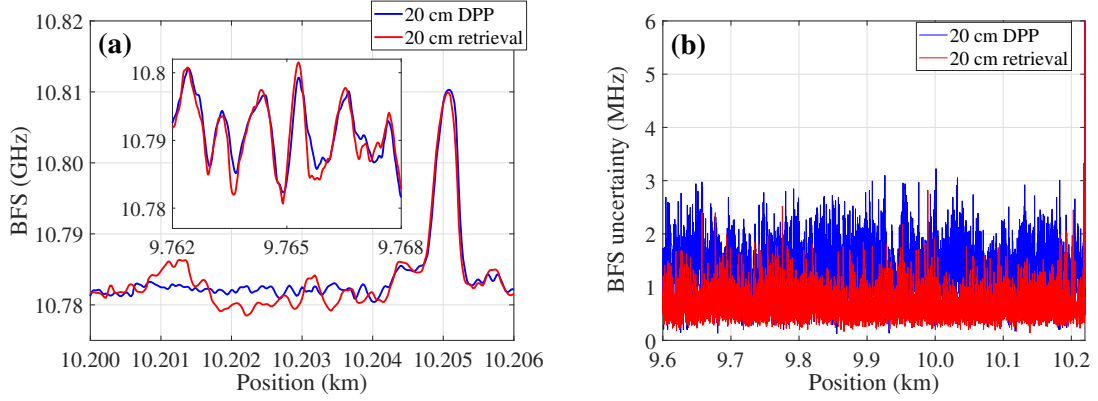


Figure 3.13 – (a) BFS profile between a DPP method and the proposed technique with a target SR of 20 cm. The pulse widths in the DPP operation are 42 ns and 40 ns while the pulse width of the proposed method is 40 ns. (b) corresponding experimental uncertainty.

Despite minor distortions, the BFS profiles are matching very well, demonstrating the capabilities of the technique for sharp resolution sensing. In addition, the inset in Fig.3.13.(a) shows that the two techniques yields very similar results even when the BFS varies rapidly along the fiber, i.e. without detrimental artifacts. In addition to a halved measurement time, the proposed approach also performs better in terms of experimental precision, as demonstrated in Fig.3.13.(b), showing a  $\sim 1.7$  reduction in BFS uncertainty. This improvement is mostly attributed to the subtraction operation performed in DPP, which is sensitive to polarization fading effects [51].

### 3.4 Genetic-optimised aperiodic coding

Most of the results presented in this section were published in the following article [52]<sup>III</sup>. Here, we rely one more time on the methodology of linear time-invariant (LTI) systems to develop an optical pulse coding method based on deconvolution. We first begin by introducing the general concept of coding, emphasizing on its interest but also on the many difficulties encountered so-far. Second, we present a solution that operates accordingly to the concept of deconvolution, i.e. a very straightforward approach that yet requires the use of sophisticated algorithms borrowed from the field of genetics. Finally, we present some experimental results based on Brillouin optical time-domain analysis (BOTDA) that demonstrate the validity of the method.

<sup>III</sup>@2020. Reprinted, with permission from X. Sun, Z. Yang, X. Hong, S. Zaslawski, S. Wang, M. A. Soto, X. Gao, J. Wu and L. Thévenaz, Genetic-optimised aperiodic code for distributed optical fibre sensors, Nat. Commun. 11, 5774 (2020), doi = 10.1038/s41467-020-19201-1

### 3.4.1 Challenges of optical pulse coding

Originally, pulse coding was developed for RADAR applications, which operate similarly to many time-domain based distributed optical fiber sensors [53]. Optical pulse coding (OPC) is a very general concept that does not only apply to BOTDA, although we will restrict the scope of the analysis developed here below to this technique. OPC consists in sending in the optical fiber a sequence of pulses, and decoding the information contained in the acquired trace that results from a mixture of the individual responses produced by each pulse, as illustrated in Fig.3.14. OPC rapidly arose as a promising candidate to effectively improve

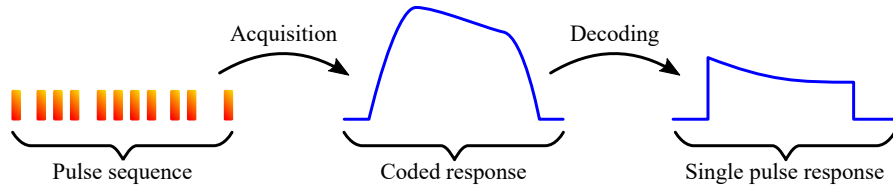


Figure 3.14 – Concept of optical pulse coding.

the performances of many distributed optical fiber sensors (DOFS), by circumventing the limitations imposed on the power of the optical waves launched in the fiber, i.e. in BOTDA the pump pulse power is limited by the onset of modulation instability (MI) [29], and the probe might trigger detrimental non-local effects if not kept below a certain threshold [35].

The first adaptation of pulse coding to an incoherent optical time-domain reflectometer (OTDR) goes back as early as 1987 [54], while the first mention of OPC for BOTDA was demonstrated much later in 2010 [55]. Although conceptually of great interest, OPC is yet facing a series of practical difficulties that hinder its potential as a pure improvement over conventional single-pulse based BOTDAs. A first major limitation lies in the additional acquisition and processing time inherent to the existing codes, i.e. Golay coding requires to launch 4 pulse sequences in the fiber [56], while in Simplex coding the number of launched sequences has to be equal to the number of codewords [55]. More importantly, both methods are highly dependent on the power uniformity of the sequence launched in the fiber to perform efficiently and without distortions, which is impossible to secure without adding to the setup complexity due to the uneven amplification brought by erbium doped fiber amplifiers (EDFA) over such a long and non-uniform signal [36]. In this section, we illustrate how to create pulse sequences with unique spectral properties, that enable launching a single pulse train in the fiber, and decoding the corresponding response with negligible added time, bringing a solution to the two major issues enounced previously.

### 3.4.2 Optical pulse coding based on deconvolution

The coding procedure developed in this section relies on the concept of deconvolution. Following a description very similar to (3.37), the digitized response of a Brillouin optical time-

domain analyzer (BOTDA)  $r_c[m]$  can be generalized to

$$r_c[m] = \underbrace{d[m] * p[m]}_{c[m]} * h[m] + n[m] \quad (3.44)$$

where  $c[m]$  is the coded pulse sequence,  $p[m]$  is the sampled pulse shape,  $h[m]$  is the fiber impulse response and  $n[m]$  represents a digitized additive white Gaussian noise (AWGN). The term  $d[m]$  is equal to a Dirac in case the system operates in single-pulse configuration, or is a series of weighted-amplitude Diracs that represent the coding sequence. The processing is performed in the frequency domain by means of the discrete Fourier transform (DFT), which has to be evaluated for each signal on the total number of points resulting from the two convolution operations performed in (3.44) and denoted  $N$ . In order to retrieve the single-pulse response, a deconvolution operation similar to (3.41) is performed, yielding

$$r_s[m] = \text{IDFT} \left\{ \frac{\hat{r}_c[k]}{\hat{d}[k]} \right\} = p[m] * h[m] + \text{IDFT} \left\{ \frac{\hat{n}[k]}{\hat{d}[k]} \right\} \quad (3.45)$$

which enables once more to perfectly retrieve the single-pulse response  $p[m] * h[m]$ . Unlike the short-spatial retrieval method presented in section 3.3, the noise term on the right-hand side of (3.45) is highly critical. Indeed, with no prior requirement on the coding sequence, it is hardly conceivable to anticipate and/or quantify any performance improvement as one might just as well magnify the noise by a significant amount instead of reducing it. In order to benefit from this coding and decoding procedure, the pulse sequence and more specifically its spectral behavior need to be rigorously tailored by making use of a devoted genetic algorithm. The reasons behind these conclusions are thoroughly developed in the following sections.

### 3.4.3 The noise scaling factor

The effect of the decoding process on noise is evaluated by means of the power spectral density (PSD). Here, we assume that the noise is wide-sense stationary, thus enabling to assess its statistical properties from a single observation. Following the conclusions drawn in section 3.2.1, the initial noise variance (before decoding) is estimated from the auto-correlation function  $\gamma_{nn}[m]$  as follows [37]

$$\sigma_n^2 = \gamma_{nn}[0] = \frac{1}{N} \sum_{m=0}^{N-1} |n[m]|^2 \quad (3.46)$$

By making use of Plancherel's theorem (3.25) we rewrite (3.46) as

$$\sigma_n^2 = \frac{1}{N^2} \sum_{k=0}^{N-1} |\hat{n}[k]|^2 \quad (3.47)$$

Assuming an additive white Gaussian noise (AWGN), the PSD is defined to be uniform over the entire frequency range, i.e.

$$|\hat{n}[k]|^2 = K/N \iff \sigma_n^2 = \frac{K}{N^2} \quad (3.48)$$

where  $K$  is a constant. The variance of the decoded noise denoted  $\sigma_d^2$ , which corresponds to the right-most term on the right-hand side of equation (3.45), is given by

$$\sigma_d^2 = \frac{1}{N^2} \sum_{k=0}^{N-1} \left| \frac{\hat{n}[k]}{\hat{d}[k]} \right|^2 = \frac{K}{N^3} \sum_{k=0}^{N-1} \left| \frac{1}{\hat{d}[k]} \right|^2 = \frac{\sigma_n^2}{N} \sum_{k=0}^{N-1} \left| \frac{1}{\hat{d}[k]} \right|^2 \quad (3.49)$$

where we made use of (3.47) and (3.48). It then follows that the initial noise is either attenuated or magnified according to the value of the noise scaling factor  $Q$  defined as

$$Q = \frac{\sigma_d^2}{\sigma_n^2} = \frac{1}{N} \sum_{k=0}^{N-1} \left| \frac{1}{\hat{d}[k]} \right|^2 \quad (3.50)$$

$Q$  is thus entirely defined by the coding sequence  $d[n]$  through a complex relationship that involves the inverse of its PSD. In order to minimize  $Q$ , one would require to find a sequence composed of a series of 1 and 0 (see upcoming section), which spectral properties would yield a low value of  $Q$ . To the best of our knowledge, this problem is way too complex to be solved analytically, hence the search for proper sequences is to be carried through dedicated algorithms. At this stage, initiating a search process would yield no conclusive results due to the lack of any *a priori* information on the structure of the coding sequence. For instance, one could ask what is the fraction of 1 with respect to the sequence length, i.e. how many 1 should we place in a sequence of  $N$  elements? The answer to this question can be found by thoroughly analyzing (3.50).

#### 3.4.4 Coding gain

In deriving (3.50), we considered the discrete Fourier transform (DFT) performed over  $N$  points, i.e. the total acquired number of points. In reality, the coding sequence  $d[m]$  corresponds to the upsampled version of another sequence denoted  $u[m]$ , as explicated in Fig.3.15. The signal  $u[m]$  consists is a series of 1 and 0 that characterize entirely the coding sequence, such that all spectral properties of  $d[m]$  can be inferred from  $u[m]$ , and this for two reasons. First, the zero-padding operation required in the DFT operation does not provide with any additional information although it enables interpolating the discrete spectrum on a finer grid [37]. Second, the DFT of the upsampled sequence  $\hat{d}[k]$  consists in a series of replica of  $\hat{u}[k]$ , as proved here after. Notice that the upsampling operation can be formally expressed as

$$d[m] = \sum_{m'=0}^{N_u-1} u[m'] \delta[m - m'N_x] \quad 0 \leq m \leq N_d - 1 \quad (3.51)$$

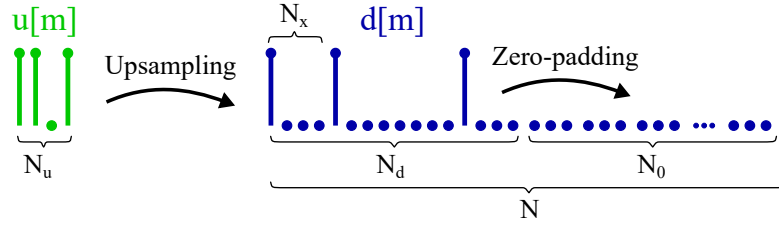


Figure 3.15 – Generation of a coding sequence of  $N_d$  elements from an  $N_x$  upsampling of an initial sequence  $u[m]$ . The sequence is further padded with  $N_0$  zeroes before computing its DFT over  $N$  acquired points.

yielding

$$\hat{d}[k] = \sum_{m=0}^{N_d-1} \sum_{m'=0}^{N_u-1} u[m'] \delta[m - m'N_x] e^{-i2\pi m \frac{k}{N_d}} = \sum_{m'=0}^{N_u-1} u[m'] e^{-i2\pi m' \frac{k}{N_u}} \quad (3.52)$$

where  $0 \leq k \leq N_d - 1$  and we used the relationship  $N_d/N_x = N_u$ . Note that although (3.52) may be at first mistaken for the Fourier transform of  $u[m]$ , the fact that the value of  $k$  goes beyond  $N_u$  results in periodic replica of the original FFT  $\hat{u}[k]$ . The  $Q$  factor defined in (3.50) may thus equivalently be expressed as

$$Q = \frac{1}{N_u} \sum_{k=0}^{N_u-1} \left| \frac{1}{\hat{u}[k]} \right|^2 \quad (3.53)$$

We now analyze in greater details (3.53) by dissociating the contribution from the DC component  $k = 0$ . Following the definition of the DFT (3.21), we find

$$|\hat{u}[0]|^2 = \left| \sum_{m=0}^{N_u-1} u[m] \right|^2 = F_E^2 \quad (3.54)$$

where we defined the energy enhancement factor  $F_E$  as the total number of ones in the sequence, as illustrated in Fig. 3.16. The physical meaning behind  $F_E$  is clear, as each one

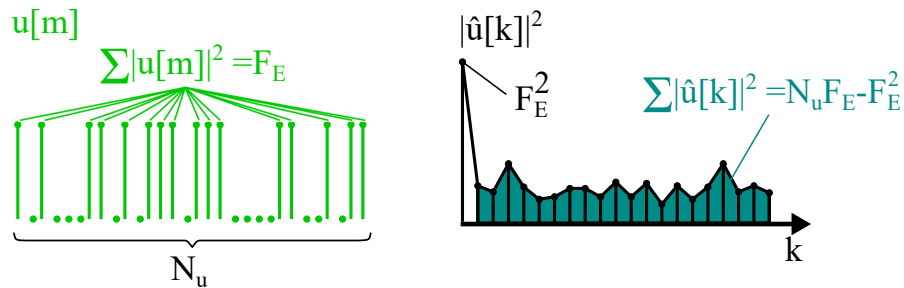


Figure 3.16 – Spectral properties of the coding sequence based on energy conservation.

corresponds to the emission of a pulse in the sequence. We thus express the noise scaling

factor (3.53) as

$$Q = \frac{1}{N_u} \left( \frac{1}{F_E^2} + \sum_{m=1}^{N_u-1} \left| \frac{1}{\hat{u}[k]} \right|^2 \right) \quad (3.55)$$

Next, we apply the Cauchy-Schwarz inequality to the partial sum in (3.55) yielding

$$\left( \sum_{m=1}^{N_u-1} \left| \frac{1}{\hat{u}[k]} \right|^2 \right) \left( \sum_{m=1}^{N_u-1} |\hat{u}[k]|^2 \right) \geq \left| \sum_{m=1}^{N_u-1} \frac{|\hat{u}[k]|^2}{|\hat{u}[k]|^2} \right|^2 = (N_u - 1)^2 \quad (3.56)$$

Furthermore, and making use of Plancherel formula (3.25), we may write

$$\sum_{m=1}^{N_u-1} |\hat{u}[k]|^2 = N_u F_E - F_E^2 \quad (3.57)$$

which allows us deriving the following inequality

$$Q \geq \frac{1}{N_u F_E^2} + \frac{(N_u - 1)^2}{N_u^2 F_E - F_E^2 N_u} \quad (3.58)$$

We now relate the sequence length  $N_u$  to the total number of ones in the sequence, i.e. the energy enhancement factor  $F_E$ , via

$$M = \frac{N_u}{F_E} \quad (3.59)$$

yielding

$$Q \geq \frac{1}{M F_E^3} + \frac{(M F_E - 1)^2}{M F_E^3 (M - 1)} \quad (3.60)$$

Furthermore, we make the reasonable assumption that  $M F_E \gg 1$ , i.e. the coding sequence is expected to provide a substantial energy enhancement, yielding

$$Q \geq \frac{M}{F_E (M - 1)} \quad (3.61)$$

Here, let us recall that since  $Q$  was defined as the increase of the noise variance (3.50), and since the decoding process yields the single pulse response without distortion (3.45), the so-called coding gain  $G_c$  can be defined as the decrease in the noise standard deviation, thus being consistent with the definition of signal-to-noise ratio (SNR) conventionally adopted (2.81), i.e.

$$G_c = \sqrt{\frac{1}{Q}} \leq \sqrt{\frac{F_E (M - 1)}{M}} \quad (3.62)$$

In evaluating the performances of the coding technique, it is interesting to compare the coding gain  $G_c$  to the reference coding gain provided by other methods such as simplex or Golay

coding, i.e.  $G_r = \sqrt{F_E/2}$ . This is achieved by computing the following coding ratio

$$R_G = \frac{G_c}{G_r} \leq \sqrt{\frac{2(M-1)}{M}} \quad (3.63)$$

### 3.4.5 Optimization of the coding sequence: spectrum management

In optimizing the gain delivered by the coding sequence, the parameter  $M$ , that defines the number of 1 with respect to the length of the coding sequence (3.59), is of outermost importance. For a given energy enhancement factor  $F_E$ , that is a fixed number of 1 or equivalently a fixed number of optical pulses in the sequences, a larger value of  $M$  corresponds to an overall longer sequence. From (3.63), it appears that the theoretical upper bound of the coding gain increases as  $M$  gets larger, eventually saturating at a value  $\sqrt{2}$  larger than the reference coding gain. While this is true to some extent (see Fig.3.17.(a)), one should not forget that equations (3.62) and (3.63) define *inequalities*, hence a coding gain of  $\sqrt{2}G_r$  when  $M$  gets large only defines an upper bound value. This upper bound can only be met provided that the sequence power spectral density (PSD) is perfectly flat, according to the Cauchy-Schwarz inequality (3.56). Indeed, the Cauchy-Schwarz inequality yields the considered bandwidth squared  $(N_u - 1)^2$ , hence the sequence PSD and its inverse should cancel each other out to meet the equality. Therefore, setting only a few ones in an otherwise empty sequence would have disastrous repercussions on the shape of the PSD, severely hindering the actual coding gain. Intuitively, a signal composed in such a way would essentially be concentrated at low frequencies, i.e. many spectral bands would be close to 0, leading to a large noise enhancement in the decoding process.

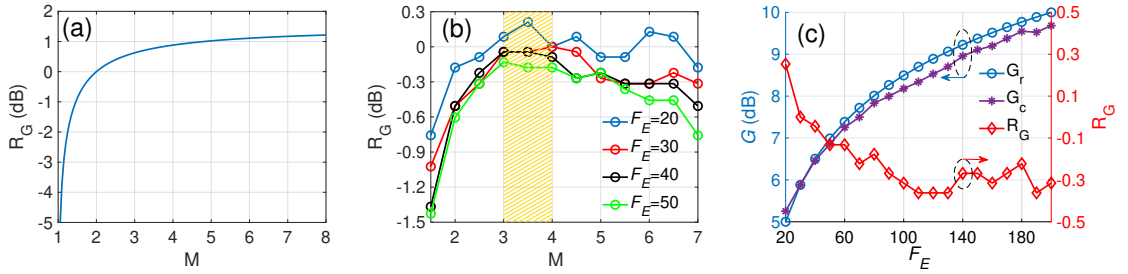


Figure 3.17 – (a) Coding ratio defined in (3.63). (b) Actual coding ratio delivered by the genetic algorithm search. (c) Coding gain and coding ratio for  $M = 3$ .

Fig.3.17.(a) shows the evolution of the coding ratio (3.63) as a function of  $M$ , exhibiting a rapidly growing trend that ends up saturating at value of  $\sqrt{2}$ . The coding gain  $R_G$  of numerical sequences delivered by a distributed genetic algorithm<sup>IV</sup> for various values of  $F_E$  and as a function of  $M$  is shown in Fig.3.17.(b). As expected, the coding ratio grows as  $M$  gets larger, yet starts decaying again for values larger than 4. Empirically, it turns out that  $M$  should be

<sup>IV</sup>The genetic algorithm is not detailed here, as one focuses here in elaborating the general principles of the method rather than the specific tools used to put it in practice. A detailed description can be found in [52].



between 3 and 4 as to optimize the coding gain, yielding a good trade-off between potential gain and achievable gain. Finally, Fig.3.17.(c). demonstrates the performances of the proposed technique compared to the reference gain, applicable e.g. for simplex coding. Overall, the difference in performances is minor (less than 0.5 dB), and negligible in most practical cases. Furthermore, and as mentioned in section 3.4.1, conventional coding schemes only operate at specific code lengths, while the coding technique developed here is entirely flexible. This aspect is critical in optimizing instruments for any experimental conditions.

One could wonder whether the use of a dedicated algorithm based on genetic search is justified in order to find good coding sequences. To answer to this question, Fig.3.18.(a) illustrates the result from a 10-hour search, where over 100 millions of coding sequences exhibiting an enhancement factor  $F_E = 40$  and  $M = 3$  were randomly generated. The red line in the figure illustrates the theoretical coding gain  $\sqrt{F_E/2} \approx 4.47$ . Even with such a massive data-set generated, the search fails to produce a single sequence coming close enough to the theoretical gain  $G_r$ , as evidenced in Fig.3.18.(b). In comparison, the distributed genetic search algorithm enables finding a sequence with  $G_c = 4.35$  in approximately 2 hours.

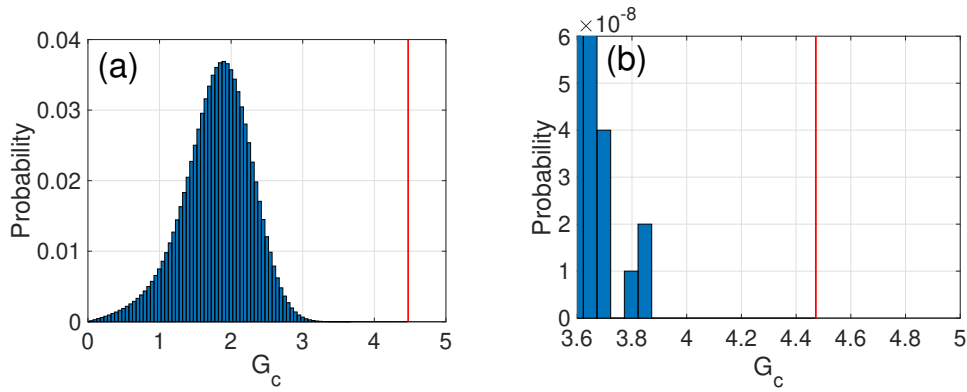


Figure 3.18 – (a) Probability distribution of  $G_c$  by brute-force searching. (b) Zoom on values ranging from 3.6 to 5.

#### 3.4.6 Robustness to EDFA gain saturation

As mentioned in section 3.4.1, conventional optical pulse coding (OPC) techniques suffer from distortions induced by erbium doped fiber amplifiers (EDFA) on the pulse sequence. The reason for this is that the mathematical relations exploited in the decoding process are very sensitive to any perturbation, especially for Golay coding [36]. In the proposed method, EDFA induced distortions can be modelled as a multiplicative signal in the convolution operation (3.44), yielding a convolution operation in the sequence power spectral density (PSD). This trend can be accurately anticipated based on EDFA specification and implemented in the model by defining a calibrated envelope signal, as illustrated in Fig.3.19. Actually, all results presented in this section take into account EDFA saturation via this calibrated envelope in

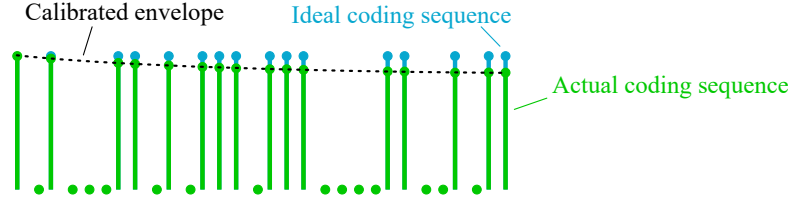


Figure 3.19 – Inclusion of EDFA gain saturation in the model.

the sequence searching process, demonstrating the robustness of the method as well as its suitability to operate in a conventional Brillouin optical time-domain analyzer (BOTDA) without hardware modification. In practical implementations, the pulse sequence distorted by the EDFA should be measured, in order to retrieve the actual envelope to be used in the deconvolution operation (3.45).

### 3.4.7 Experimental results

To demonstrate the feasibility of the proposed technique, experimental measurements were performed on a 100 km long sensing fiber with a spatial resolution (SR) of 2 m (and later on 1 m). The fiber includes a hotspot at its remote end, achieved by placing a section of ~2 m in a temperature controlled bath. The energy enhancement factor  $F_E$  is adjusted to be ~40, in order to avoid excessive noise at the fiber remote end (see discussion here after), yielding a theoretical coding gain of  $G_c = 6.2$  dB. The coded BOTDA response is compared to a single pulse BOTDA acquisition, both averaged 1024 times, and a reference measurement is performed with 17795 averages, corresponding to the same signal-to-noise ratio (SNR) improvement as the one delivered by coding ( $10\log_{10}\sqrt{17795/1024} = 6.2$  dB). Fig.3.20.(a) shows the acquired pulse sequence  $c[m]$  as well as the retrieved coding sequence made of weighted Diracs  $d[m]$ , evaluated by measuring the peak power of each pulse in the sequence. Fig.3.20.(b) displays the measured Brillouin gain at resonance, either directly acquired or resulting from the deconvolution operation in the case of the genetic-optimised (GO) coding, i.e. the proposed technique. Visually, the trace suffers no distortion, as the exponential trend is perfectly recovered. However, the trace (red) appears much thicker at the fiber beginning than the reference (black), revealing a poorer SNR.

This is confirmed in Fig.3.20.(c), which displays the measured SNR (in dB) for all three acquisitions along the fiber length. Increasing the number of averages naturally results in a uniform SNR enhancement all along the fiber, while in the case of coding, the SNR at the fiber beginning is actually lower than for the single-pulse case with 1024 averages. This feature is intrinsic to any coding technique and is related to the increase in noise due to gain-dependent noise sources, including polarization noise and beating noise<sup>V</sup>. Indeed, while most noise sources are negligible in single-pulse configuration due to the moderate Brillouin gain (e.g. 2.5% here), the accumulated gain due to a sequence of pump pulse (e.g. here 40, corresponding to a total gain

<sup>V</sup>See the supplementary note 3 of reference [52] for more details.

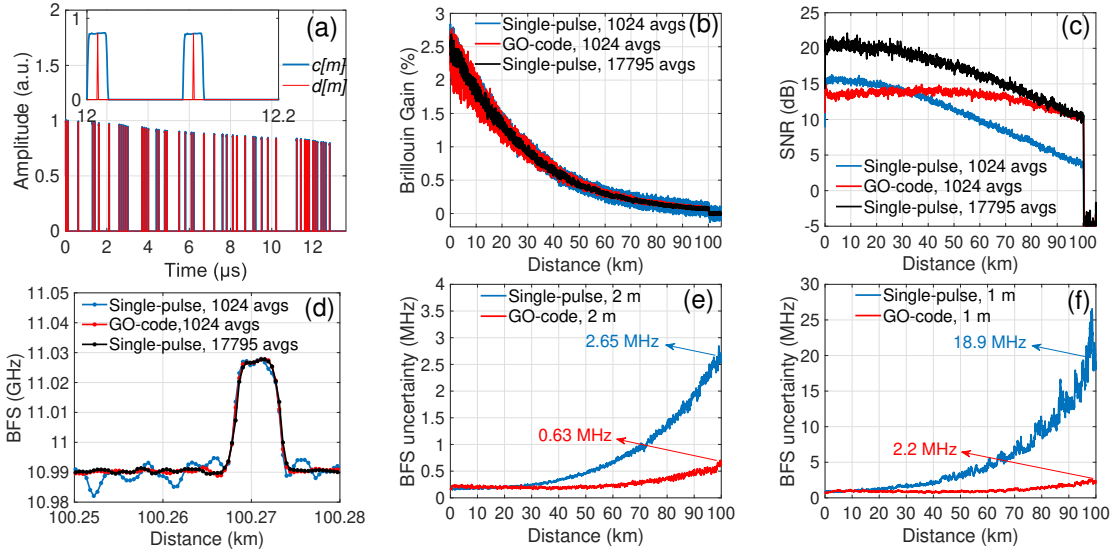


Figure 3.20 – (a) Acquired pulse sequence and coding sequence (normalized). (b) Brillouin gain at resonance. (c). Signal-to-noise ratio (SNR). (d) Brillouin frequency shift (BFS) at hotspot location. (e) Experimental uncertainty with 2 m SR. (f) Experimental uncertainty with 1 m SR.

of 100%) severely amplifies these phenomena. Note that this limiting factor is included in the design of the pulse sequence and sets a hard constraint on the targeted energy enhancement factor  $F_E$ . Nevertheless, the SNR reached by the GO-code at the fiber remote end matches the one of the reference, demonstrating a significant performance improvement. Moreover, the SNR decrease in the first section of the fiber is usually not an issue in most applications, given that the resulting SNR is still sufficiently high (here above 10 dB), which secures an excellent experimental uncertainty.

The GO-code is then shown to preserve the experimental spatial resolution, as evidenced in Fig.3.20.(d) showing the Brillouin frequency shift (BFS) profile at the hotspot. As discussed in section 3.2, the most valuable metric in BOTDA (besides spatial resolution preservation) is the BFS uncertainty, displayed in Fig.3.20.(e). Notice that in spite of SNR penalty at the fiber beginning, the experimental uncertainty is still very low ( $<0.5$  MHz) over the first two-third of the fiber length, and reaches a value of 0.63 MHz at the fiber remote end (red). Compared to the single-pulse case (2.65 MHz, blue), this is equivalent to a 4.2 fold improvement, or equivalently an increase of 6.2 dB, in excellent agreement with the theoretically predicted value. The benefits of optical pulse coding (OPC) are most impactful in scenarios where the original performances are low, i.e. starting from a poor SNR. This is illustrated in Fig.3.20.(f), showing the experimental uncertainty for a single pulse BOTDA measurement with a SR of 1 m acquired on the same fiber, as well as the BFS uncertainty delivered by GO-coded BOTDA ( $F_E = 200$ ,  $G_c = 9.3$  dB). In this case, the BFS uncertainty in single-pulse configuration (18.9 MHz) translates for instance into a temperature uncertainty of  $\sim 18.9$  °C, while the coded BOTDA delivers an uncertainty of only 2.2 MHz (or 2.2 °C). The BFS uncertainty reduction is this time a factor 8.6, perfectly matching the theoretical coding gain of 9.3 dB.

## 4 Distributed forward stimulated Brillouin scattering sensing

Forward stimulated Brillouin scattering (FSBS) refers to an opto-mechanical interaction involving light and guided acoustic waves, hence it was initially labelled as guided acoustic waves Brillouin scattering (GAWBS). The denomination "FSBS" is to some extent more insightful than "GAWBS", as it emphasizes on the main characteristics of this interaction, that is the light scattering occurs in the forward direction only. The first report of FSBS in optical fibers goes back as early as 1985 [5], where it was described as an additional noise source for optical signals. Interestingly, some of the features inherent to FSBS were documented some 15 years before in order to observe the acoustic modes of a cylindrical rod [57] or to model birefringence effects in a Nd:YAG rod laser [58]. The phenomenon was further studied in coming years, describing effects related to its polarization [59] as well as its bandwidth [60]. FSBS was later on studied in photonic crystal fibres to achieve coherent stimulated phonon oscillation [61, 62].

Recently, FSBS drew substantial interest within the optical fiber sensing community, as it was successfully demonstrated to perform liquid sensing by exploiting its dependency on the acoustic impedance difference at the interface between two media [6]. Quite remarkably, the light remains confined to the fiber core, i.e. the optical fiber operates in nominal conditions, while the acoustic vibrations carry information from the fiber outer surface back to the core. So far, FSBS based sensing faces two major difficulties:

- 1 The lack of any backscattered signal prevents direct distributed measurement of FSBS. This intrinsic difficulty has been circumvented as of now by measuring the backscattered response of an auxiliary signal, which experiences energy transfer due to FSBS [8, 63, 64].
- 2 The acrylate coating of conventional optical fibers greatly dampens acoustic waves, drastically diminishing the efficiency of FSBS. This issue can be addressed by either removing the fiber coating, but this makes it impractical owing to the fragility of the glass rod, or by making use of another, more adapted coating material such as polyimide.

Distributed FSBS sensing is still at an early stage of research, hence it is poorly performing compared to other mature DOFS techniques. It is yet highly attractive due to its potential to diversify the physical parameters measurable by DOFS, as it is not limited to sense quantity having a direct impact on light propagation, such as temperature or strain in Brillouin optical time-domain analysis (BOTDA). There is thus still a large margin for improvement, and this chapter is dedicated to take a step into that direction. In order to understand the benefits and limitations of FSBS, we first need to present a description of its physical properties, starting with a study of acoustic waves propagation in optical fibers. We then discuss the potential of FSBS for sensing, and enumerate aspects that are critical in most applications. Finally, we introduce an original concept for distributed FSBS sensing based on serrodyne modulation [65, 66].

### 4.1 Acoustic waves propagation in optical fibers

As seen in chapter 2, optical fibers are manufactured as to be efficient waveguides for electromagnetic waves, i.e. light. They are also perfectly capable of supporting the propagation of acoustic waves, as evidenced by the presence of Brillouin scattering, described in sections 2.3.3 and 2.3.4. An accurate description of forward stimulated Brillouin scattering (FSBS) requires a more adequate theory than the density-wave equation used to characterize backward Brillouin scattering (2.33). FSBS is studied in the framework of the theory of linear elasticity [67, 68, 69] by solving the corresponding wave equation in cylindrical coordinates. Here the analysis is kept succinct, showing only major steps in the derivation, while the detailed procedure can be found in Appendix A.

#### 4.1.1 The elastic waves equation

We consider first the optical fiber to be a plain rod of radius  $a$ , which corresponds to the case where the fiber has been stripped of its protective coating. The geometry of the problem is shown in Fig.4.1 in cylindrical coordinates. The following equation is valid for a linear and

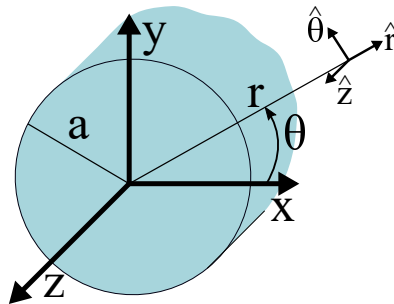


Figure 4.1 – Problem geometry in cylindrical coordinates  $(r, \theta, z)$  as defined from Cartesian coordinates  $(x, y, z)$  where  $a$  represents the fiber radius.

isotropic elastic material

$$\mu \nabla^2 \mathbf{U} + (\lambda + \mu) \nabla (\nabla \cdot \mathbf{U}) - \rho \frac{\partial^2 \mathbf{U}}{\partial t^2} = \mathbf{0} \quad (4.1)$$

where  $\mathbf{U}$  is the displacement field vector, and  $\lambda$  and  $\mu$  are Lamé first and second parameters, respectively. In the framework of linear elasticity, one always requires the knowledge on two independent mechanical constants, such as the Lamé parameters here. Although they are naturally related to the wave equation, the Lamé parameters are not necessarily physically meaningful (except for  $\mu$  which designates the shear modulus), nor familiarly encountered when discussing the mechanical properties of a material. Fortunately, it is always possible to derive all other mechanical parameters from two independent ones, for instance

$$\lambda = \frac{E\sigma}{(1+\sigma)(1-2\sigma)} \quad (4.2)$$

$$\mu = \frac{E}{2(1+\sigma)} \quad (4.3)$$

where  $E$  is the Young's modulus and  $\sigma$  designates Poisson's ratio. In its form, the acoustic wave equation (4.1) shares some similarities with respect to the electromagnetic wave equation (2.7). Quite remarkably, and as will be shown hereafter, the cylindrical geometry of the problem also results in solution exhibiting a radial dependency depending on Bessel functions. We now turn to the solving of equation (4.1) in cylindrical coordinates.

#### 4.1.2 The potentials method

Solving of the wave equation is based on the potentials method, i.e. we express the displacement field as [67]

$$\mathbf{U} = \nabla \psi + \nabla \times \boldsymbol{\Psi} \quad (4.4)$$

where  $\psi$  is a dilatational potential (scalar) and  $\boldsymbol{\Psi}$  is an equivoluminal vector potential. Injecting (4.4) into (4.1) yields two decoupled equations

$$V_d^2 \nabla^2 \psi - \frac{\partial^2 \psi}{\partial t^2} = 0 \quad (4.5)$$

$$V_s^2 \nabla^2 \boldsymbol{\Psi} - \frac{\partial^2 \boldsymbol{\Psi}}{\partial t^2} = 0 \quad (4.6)$$

where  $V_d$  and  $V_s$  are the dilatational waves and shear waves velocity, respectively, defined as

$$V_d = \sqrt{\frac{\lambda + 2\mu}{\rho}} \quad (4.7)$$

$$V_s = \sqrt{\frac{\mu}{\rho}} \quad (4.8)$$

where  $\rho$  is the material density. In silica,  $V_d \approx 5996$  m/s while  $V_s \approx 3740$  m/s [6]. Before proceeding further in solving equations (4.5) and (4.6) in cylindrical coordinates, we introduce the following relationship

$$\nabla \cdot \Psi = F(r, \theta, z) \quad (4.9)$$

where  $F$  designates an arbitrary function. The fact that  $F$  can be any function is known as the gauge invariance principle. Indeed, in deriving (4.6) one comes across the following relationship

$$\nabla (\nabla \cdot (\nabla \times \Psi)) = \nabla \times (\nabla (\nabla \cdot \Psi)) = \nabla \times (\nabla F) = \mathbf{0} \quad (4.10)$$

which equals  $\mathbf{0}$  due to fundamental vectorial calculus identities. In solving for appropriate boundary conditions to the problem, we shall make use of the additional degree of freedom brought by (4.9) to greatly simplify the calculations.

### 4.1.3 Separation of variables

The potential equations (4.5) and (4.6) are solved again using the approach of the separation of variables. We make the following *Ansatz*

$$\psi = f(r) \cos(n\theta) \cos(\gamma z - \omega t) \quad (4.11)$$

$$\Psi_r = g_r(r) \sin(n\theta) \sin(\gamma z - \omega t) \quad (4.12)$$

$$\Psi_\theta = g_\theta(r) \cos(n\theta) \sin(\gamma z - \omega t) \quad (4.13)$$

$$\Psi_z = g_z(r) \sin(n\theta) \cos(\gamma z - \omega t) \quad (4.14)$$

where  $\Psi_r$ ,  $\Psi_\theta$  and  $\Psi_z$  designate the three components of  $\Psi$ ,  $n$  is a positive integer,  $\gamma$  is the propagation constant and  $\omega$  is the angular frequency. The radial dependency  $f$ ,  $g_r$ ,  $g_\theta$  and  $g_z$  are found by injecting equations (4.11) to (4.14) into (4.5) and (4.6). It turns out that both  $f$  and  $g_z$  obey the same Bessel equation, that is

$$f(r) = A J_n(\alpha r) \quad (4.15)$$

$$g_z(r) = B_3 J_n(\beta r) \quad (4.16)$$

where  $A$  and  $B_3$  are integration constants while  $\alpha$  and  $\beta$  are given by

$$\alpha^2 = \frac{\omega^2}{V_d^2} - \gamma^2 \quad (4.17)$$

$$\beta^2 = \frac{\omega^2}{V_s^2} - \gamma^2 \quad (4.18)$$

The two remaining function  $g_\theta$  and  $g_z$  need to be addressed simultaneously. They both yield again Bessel equations in the form

$$g_r - g_\theta = 2B_1 J_{n+1}(\beta r) \quad (4.19)$$

$$g_r + g_\theta = 2B_2 J_{n-1}(\beta r) \quad (4.20)$$

Here, we invoke the gauge invariance principle (4.9) to define  $F$  such that

$$g_r = -g_\theta \quad (4.21)$$

which yields  $B_2 = 0$  and

$$g_r = B_1 J_{n+1}(\beta r) \quad (4.22)$$

#### 4.1.4 Boundary conditions

Now that the form of the radial dependency of the given eigenfunctions is known, we turn to apply the corresponding boundary conditions to our problem. Here we consider the classical stress-free boundary condition, in which the stress at the outer surface of the cylinder is assumed to vanish. This condition corresponds to the case of a bare section of optical fiber exposed to air, as will be better understood in the following section on sensing.

$$\sigma_{rr}|_{r=a} = 0 \quad (4.23a)$$

$$\sigma_{r\theta}|_{r=a} = 0 \quad (4.23b)$$

$$\sigma_{rz}|_{r=a} = 0 \quad (4.23c)$$

The boundary conditions (4.23) are usually expressed in matrix form, that is

$$CB = \begin{pmatrix} C_{11} & C_{12} & C_{13} \\ C_{21} & C_{22} & C_{23} \\ C_{31} & C_{32} & C_{33} \end{pmatrix} \begin{pmatrix} A \\ B_1 \\ B_3 \end{pmatrix} = \begin{pmatrix} 0 \\ 0 \\ 0 \end{pmatrix} \quad (4.24)$$

and the coefficients  $C_{ij}$  of the matrix can be found in Appendix A.

#### 4.1.5 The frequency equation

According to Cramer's rule, the only way to avoid the trivial solution  $A = B_1 = B_3 = 0$  in (4.24) is to impose the following condition, known as the frequency equation or the dispersion relation



$$|C| = 0 \quad (4.25)$$

As such, equation (4.25) is a very general one that provides a global solution to the problem considered. Similar to the frequency equation for optical waves (2.19), it can be factorized into a set of discrete solutions known as modes. The dominant parameter in the modal classification is the azimuthal parameter  $n$ , which defines the symmetry of revolution of the considered mode displacement profile. For instance, setting  $n = 0$  yields on one side the family of purely torsional modes, as well as the family of longitudinal-radial modes (see Appendix A). Notice that for each set of parameters, there is an infinite number of solutions as a consequence from the oscillatory nature of the Bessel functions involved in the frequency equation (4.25).

#### 4.1.6 Purely radial modes

In single-mode fibers (SMF), only torsional-radial modes with  $n = 2$ , denoted  $TR_{2m}$  and purely radial modes with  $n = 0$ , denoted  $R_{0m}$ , are involved in Forward stimulated Brillouin scattering (FSBS) [5]. The reason for this lies in the azimuthal symmetry of the electrostrictive driving force, which exhibits two distinct contributions, one showing a purely radial symmetry while the other shows a two-fold azimuthal symmetry [70]. Note that this assumption is invalidated in multi-core fibers, for which other families of torsional-radial modes might be involved [71]. Interestingly, *Sittig et al* already mentioned in 1970 that  $TR_{2m}$  modes exhibit birefringence at the center of a glass cylindrical rod, hence showing a potential for light phase modulation [57].

In practical applications involving SMFs,  $TR_{2m}$  modes are far less efficient than  $R_{0m}$  modes [60], hence they are not considered further in the remaining of this document. In FSBS, the opto-mechanical coupling takes place between two co-propagating light-waves, therefore the differential wave-vector, i.e. the acoustic wave-vector alongside the fiber axis, is extremely small. Assuming  $n = 0$  and  $\gamma = 0$  in (4.25) yields the following factorization

$$|C| = -C_{23}C_{11}C_{32} = 0 \quad (4.26)$$

where the terms  $C_{11}$  and  $C_{23}$  are associated with purely longitudinal modes and purely torsional modes, respectively, and are thus not taken into account. The term  $C_{32}$  yields the well-known dispersion relation for purely radial modes

$$\frac{2\alpha}{a}J_1(\alpha a) - \beta^2 J_0(\alpha a) = 0 \quad (4.27)$$

where  $\alpha$  and  $\beta$  are given by equations (4.17) and (4.18), respectively. (4.27) is the characteristic equation that enable to determine the frequency of purely-radial modes. The frequencies  $f_m$  of the 10 first modes for an SMF of radius  $a = 62.5 \mu\text{m}$ , with a density  $\rho = 2200 \text{ kg/m}^3$ , a Young's modulus of  $73 \times 10^9 \text{ Pa}$  and a Poisson ratio of  $\sigma = 0.17$  are given in Table.4.1

$f_m$ [MHz]	30.2	81.7	130.2	178.3	226.3	274.1	322.0	369.8	417.7	465.5
-------------	------	------	-------	-------	-------	-------	-------	-------	-------	-------

Table 4.1 – Frequencies of purely radial modes (from  $R_{01}$  to  $R_{010}$ ).

Finally, the displacement profile of purely radial modes is entirely given by the radial component of displacement  $U_r$  as

$$U_r(r) = K J_1(\alpha r) \quad (4.28)$$

where  $K$  is an integration constant. The displacement profile of several acoustic modes are compared with the fundamental mode profile of a single-mode fiber (see section 2.2.3) in Fig.4.2. With increasing mode order, the number of lobes within a given profile gets larger,

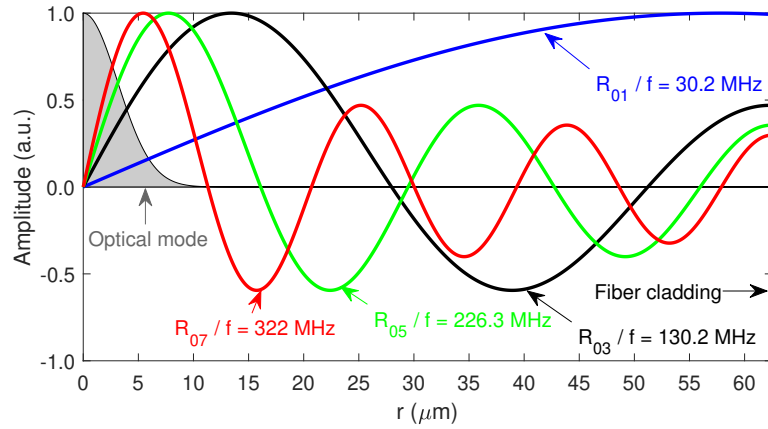


Figure 4.2 – Modes profiles of purely-radial modes  $R_{01}$ ,  $R_{03}$ ,  $R_{05}$  and  $R_{07}$  together with the optical mode profile of a single-mode fiber, normalized to unity.

and the energy starts shifting toward the fiber core. As discussed in section 4.2.2, this behavior defines the efficiency of FSBS, which is low for low-order modes due to a poor spatial overlap between acoustic and optical mode profiles.

## 4.2 Forward stimulated Brillouin scattering

We now discuss forward stimulated Brillouin scattering (FSBS) in details, articulating the analysis around the sensing potential of this effect in single-mode fibers. We first revisit the wave-coupling interaction described for backward stimulated Brillouin scattering (SBS) in section 2.3.4, evidencing the forward nature of the scattering as well as its mode-dependent efficiency when considering the guided acoustic waves described in the previous section. We then describe the sensing mechanism behind FSBS before proceeding to analyze the influence of the fiber coating on the interaction, a topic of paramount importance for any realistic practical application.

### 4.2.1 Wave coupling in FSBS

In the classical theory of Brillouin scattering, the scattering is essentially backward, as imposed by a strict phase matching between the optical and acoustic waves in presence. Forward scattering cannot occur because of the dispersion relation of the considered acoustic wave, which is assumed to be linear (see section 2.3.3). The situation is entirely different for forward stimulated Brillouin scattering (FSBS), as the purely radial modes described in section 4.1.6 exhibit a highly non-linear dispersion relation. Formally speaking, purely radial modes cease to exist as soon as the acoustic wavevector  $\gamma$  (4.11) - (4.14) vanishes, and join a larger class of modes known as longitudinal-radial modes (see Appendix A). Yet, and for the magnitude of propagation considered, it is perfectly reasonable to still use the denomination of purely radial modes  $R_{0m}$ . Nevertheless, the dispersion relation for  $R_{0m}$  modes is described by the Pochhammer-Cree equation, which was discovered as early as 1876 by Pochhammer [72] and independently later by Chree in 1889 [73], and is given by

$$\frac{2\alpha}{a} J_1(\alpha a) J_1(\beta a) (\beta^2 + \gamma^2) - J_0(\alpha a) J_1(\beta a) (\beta^2 - \gamma^2)^2 - 4\gamma^2 \alpha \beta J_0(\beta a) J_1(\alpha a) = 0 \quad (4.29)$$

Equation (4.29) is extremely complex, and numerous mathematical workarounds to analyze it were found before having the availability of sufficient computational power [74, 75]. The dispersion curves of the first ten  $R_{0m}$  modes are shown in Fig.4.3, together with the dispersion curve of the optical wave involved in FSBS.

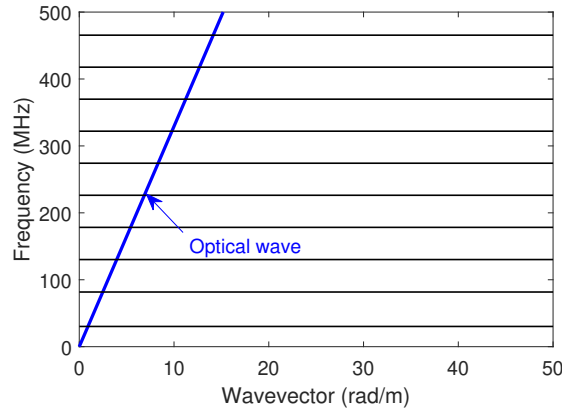


Figure 4.3 – Dispersion relation of the ten first purely radial modes near cutoff ( $\gamma = 0$ ) compared to the dispersion relation of an optical wave.

Owing to their different nature, optical waves and acoustic waves evolved in entirely different regimes. While light exhibits a linear dispersion, acoustic waves involved in FSBS are barely past cutoff, hence their dispersion curve is nearly flat. The phase-matching condition stating the conservation of momentum (wavevector) and energy (frequency) is thus largely relaxed compared to backward SBS, and is very similar to Raman scattering (hence it was labelled Raman-like scattering in [61]). Indeed, for two co-propagating light waves exhibiting

a frequency difference of  $\Delta\omega$ , phase matching is achieved provided that

$$\frac{\Delta\omega}{2\pi} = f_m \quad (4.30)$$

where  $f_m$  is given by equation (4.27) or equivalently (4.29) when letting  $\gamma = 0$ .

#### 4.2.2 Efficiency of FSBS: modal dependency

As evidenced by Fig.4.3, there is a large number of acoustic modes naturally involved in forward stimulated Brillouin scattering (FSBS) in a conventional single-mode fiber (SMF). The scattering efficiency is however highly mode-dependent. The scattering efficiency of FSBS was already derived in [70] and later on thoroughly revisited in a series of publications devoted to FSBS sensing in both SMF and multi-core fibers (MCF) by *Zadok et al.* from Bar-Ilan university in Tel Aviv [6, 7, 71, 76]. Physically speaking, FSBS manifests, via electrostriction and photoelasticity, as a mode and frequency dependent refractive index perturbation  $\Delta n_{\text{FSBS}}^{(m)}$ . At a resonant frequency  $f_m$ , this refractive index change is given by [7]

$$\Delta n_{\text{FSBS}}^{(m)} = \frac{P(f_m)}{32\pi n^2 c_0 \rho} \frac{Q_{\text{ES}}^{(m)} Q_{\text{PE}}^{(m)}}{f_m \Gamma_m} \quad (4.31)$$

where  $P(f_m)$  is the optical power at frequency  $f_m$ ,  $n$  is the refractive index,  $c_0$  is the speed of light in vacuum and  $\Gamma_m$  is the acoustic damping rate, which will be thoroughly discussed hereafter. The terms  $Q_{\text{ES}}^{(m)}$  and  $Q_{\text{PE}}^{(m)}$  designate overlap integrals associated with electrostriction and photoelasticity, respectively [70]. The electrostriction overlap integral is equal to

$$Q_{\text{ES}}^{(m)} = (a_1 + 4a_2)2\pi \int_0^a E_N(r) \frac{dE_N(r)}{dr} U_N^{(m)}(r) r dr \quad (4.32)$$

where  $m$  designates the mode number. In (4.32),  $E_N(r)$  is the normalized optical wave electric field profile (2.23), which we assume here to be Gaussian as described in section 2.2.3 and  $U_N^{(m)}$  is the  $m$ th normalized acoustic mode displacement profile (4.28). The normalization is performed such that the integrated power (the absolute squared value of the field) is unitary. The two constants  $a_1$  and  $a_2$  are related to the elasto-optic constants  $P_{11}$  ( $= 0.121$  for fused silica) and  $P_{12}$  ( $= 0.27$  for fused silica) via [70]

$$a_1 = -n^4 (P_{11} - P_{12}) \quad (4.33)$$

$$a_2 = -n^4 P_{12} \quad (4.34)$$

and  $\epsilon_0$  is the vacuum permittivity. The photo-elastic integral yields

$$Q_{\text{PE}}^{(m)} = \left( \frac{a_1}{2} + a_2 \right) 2\pi \int_0^a |E_N(r)|^2 \left( \frac{dU_N^{(m)}}{dr} + \frac{U_N^{(m)}}{r} \right) r dr \quad (4.35)$$

Quite remarkably, and for the case of a single-mode fiber considered here, the two integrals  $Q_{ES}^{(m)}$  and  $Q_{PE}^{(m)}$ , which are both frequency-dependent, yield almost identical results when normalized to unity with respect to their maximum output. The influence from  $Q_{ES}^{(m)}$  and  $Q_{PE}^{(m)}$  as well as the  $1/f$  dependency on  $\Delta n_{FSBS}^{(m)}$  are illustrated in Fig. 4.4. The overall efficiency (blue

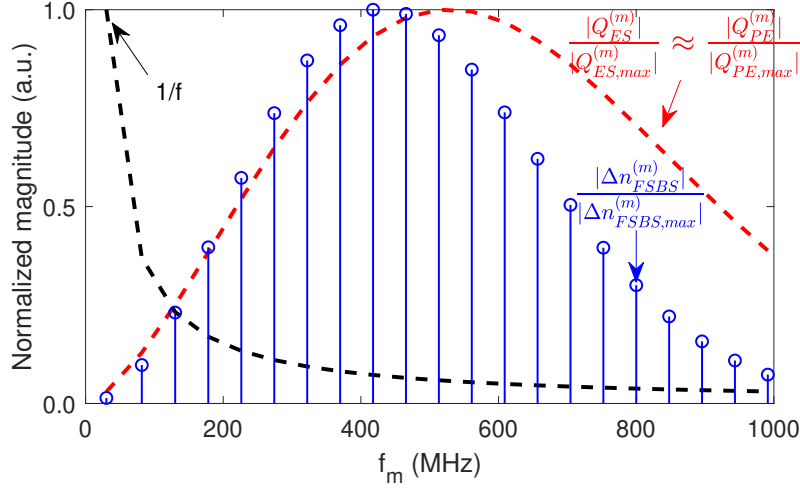


Figure 4.4 – Normalized FSBS induced refractive index change as a function of frequency.

line) is small for low-order modes, as a consequence from the poor spatial overlap between optical and acoustic modes evidenced in Fig. 4.2. As the frequency increases, the higher concentration of acoustic energy towards the fiber core yields a larger overlap, hence the overall efficiency increases despite the  $1/f$  trend. Past a certain mode (here the 9<sup>th</sup> mode at a frequency of ~417 MHz), both the overlap integral as well as the  $1/f$  contribution tend to lower the FSBS efficiency. The overlap integral eventually diminishes because past a certain point, the optical field end up averaging out contributions from positive and negative acoustic lobes, i.e. the overall refractive index modulation yields 0 [60]. As will be seen later on, this mode-dependent efficiency is critical in the design of any experimental setup aiming at performing distributed FSBS sensing.

### 4.2.3 Sensing properties of FSBS

So far, we left out the feature of forward stimulated Brillouin scattering (FSBS) most interesting to this dissertation, i.e. its potential for sensing. From the very first measurements of FSBS, it was understood that conventional fiber coating such as acrylate ended up acting as a damper for acoustic waves [5]. Acoustic damping in this case originates from acoustic radiation at the fiber-coating interface, very similarly to the optical loss produced by a semi-reflective surface on a light wave. An interesting paper published as early as 1993 [60] documents this effect in single-mode fibers (SMF), emphasizing at the time on torsional-radial ( $TR_{2m}$ ) modes. In this report, two conclusions are drawn which are highly relevant to our study on distributed FSBS sensing. First, the acoustic damping is mode-selective, and is far more severe for modes

displaying a large displacement profile near the fiber cladding as the acoustic radiation is in that case significant. Second, the observed resonance, and especially the measure of the linewidth of each resonance with respect to frequency cannot be explained by acoustic damping. Instead, the author concludes that the measured spectra result from the overlap of multiple individual resonances exhibiting slightly different resonant frequencies. We shall come back to these two aspects in the following section, and discuss their practical implication on experimental measurements.

Similarly to a soft material such as acrylate, surrounding a section of bare fiber with a fluid will end up having a similar effect on acoustic waves [60]. Formally speaking, the effect of the fluid on the propagation of acoustic waves in the fiber is modelled by modifying the stress-free boundary condition (4.23a) at the fiber-fluid interface [77]

$$\sigma_{rr}|_{r=a} = -p(a) \quad (4.36)$$

where  $p$  designates the fluid pressure. Assuming a negligible axial wavevector ( $\gamma = 0$ ), the following expression can be found [7]

$$\sigma_{rr}|_{r=a} = \omega Z^{(flu)} \frac{H_0\left(\omega/V_d^{(flu)}\right)}{H_1\left(\omega/V_d^{(flu)}\right)} U_r(a) \quad (4.37)$$

where  $\omega$  is the angular frequency,  $Z^{(flu)}$  and  $V_d^{(flu)}$  are the acoustic impedance of the fluid and the longitudinal wave velocity in the fluid, respectively, while  $H_m$  designates the  $m$ th order Hankel function. Note that in this case, the term corresponding to  $\sigma_{rr}$  is to be included in the boundary condition matrix  $C$ , and the frequency equation (4.25) is solved by including an imaginary part to the frequency, i.e. [7]

$$\omega \longrightarrow \omega + i\Gamma \quad (4.38)$$

and  $\Gamma$  is the corresponding damping rate. About twenty years later, it was understood that measuring the radiation loss of acoustic waves provided with information on the acoustic impedance of the fluid in which the fiber is immersed. The first report of liquid sensing using FSBS was made in 2016 by *Antman et al.* [6], where the authors successfully discriminated between water and ethanol. Indeed, for a bare single-mode fiber of radius  $a$ , the acoustic damping rate due to radiation loss can be expressed as

$$\Gamma = \frac{V_d^{(fib)}}{2a} \ln \left( \left| \frac{Z^{(fib)} - Z^{(flu)}}{Z^{(fib)} + Z^{(flu)}} \right| \right) \quad (4.39)$$

where  $Z^{(fib)}$  and  $V_d^{(fib)}$  are the acoustic impedance of the fiber and the longitudinal wave velocity in the fiber, respectively. Equation (4.39) shows that the damping rate depends on the (normalized) acoustic impedance difference between the two media. In order to provide with some order of magnitudes, the acoustic impedance of silica is  $\sim 13.2 \times 10^6 \text{ kg}/(\text{m}^2\text{s})$  while

for air it is only  $\sim 416 \text{ kg}/(\text{m}^2\text{s})$  [6], yielding a damping rate of only  $\sim 2\pi \times 0.5 \text{ kHz}$ . Acoustic waves are thus extremely long-lived when the fiber is exposed to air, which behaves as a high quality acoustic cavity. The case is entirely different when the fiber is immersed in a fluid, e.g. ethanol, which displays an acoustic impedance of  $\sim 0.95 \times 10^6 \text{ kg}/(\text{m}^2\text{s})$ , corresponding to an acoustic damping rate of  $\sim 2\pi \times 1.1 \text{ MHz}$ . FSBS measurement setups thus aim at evaluating this damping rate, and if possible in a spatially resolved way. Before stepping into considerations regarding the practical implementation of a dedicated setup, we mention some critical aspects related to the fiber coating.

### 4.2.4 The impact of coating

In most distributed optical fiber sensing (DOFS) applications, the fiber coating is important, for instance it should be adapted when considering *in situ* applications instead of laboratory experiments, but the choice of a given coating is not expected to profoundly modify the behavior of the system. In FSBS sensing, the choice of a given coating is a major design parameter to be taken into account as it affects the waveguiding mechanism of the acoustic vibrations involved in the process. As mentioned already in early works [5, 60], the widely used acrylate coating is not a suitable choice for proper FSBS sensing, as its mechanical properties and thickness make it act as an acoustic damper that severely attenuates acoustic waves. Recently, the use of polyimide was foreseen as a promising alternative due to its better acoustic impedance matching with silica, as well as being coated in thin layers [78, 79]. We will see that, despite delivering indeed good performances in terms of acoustic sensing, the impact of polyimide coating (in fact, any coating) is to be deeply considered in experiments. A coated fiber may be represented by the geometry depicted in Fig.4.5, where the glass rod

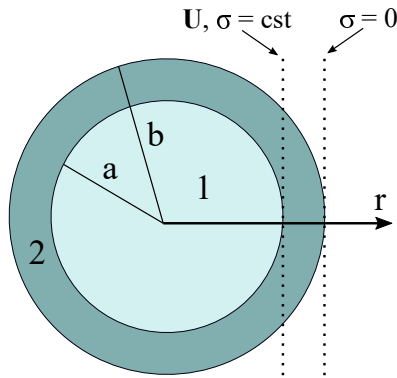


Figure 4.5 – Cross-section of a coated fiber.

of radius  $a$  is surrounded by a protective layer of outer radius  $b$ . Label 1 designates the silica glass while label 2 refers to the coating. Propagation of acoustic waves in such structures have been intensively studied in the field of acoustics [80, 81]. When exposed to air, the boundary conditions include continuity at the cladding-coating interface in addition to the stress-free requirement on the fiber surface, i.e.

$$U_r^{(1)}|_{r=a} = U_r^{(2)}|_{r=a} \quad (4.40a)$$

$$\sigma_{rr}^{(1)}|_{r=a} = \sigma_{rr}^{(2)}|_{r=a} \quad (4.40d)$$

$$\sigma_{rr}^{(2)}|_{r=b} = 0 \quad (4.40g)$$

$$U_\theta^{(1)}|_{r=a} = U_\theta^{(2)}|_{r=a} \quad (4.40b)$$

$$\sigma_{r\theta}^{(1)}|_{r=a} = \sigma_{r\theta}^{(2)}|_{r=a} \quad (4.40e)$$

$$\sigma_{r\theta}^{(2)}|_{r=b} = 0 \quad (4.40h)$$

$$U_z^{(1)}|_{r=a} = U_z^{(2)}|_{r=a} \quad (4.40c)$$

$$\sigma_{rz}^{(1)}|_{r=a} = \sigma_{rz}^{(2)}|_{r=a} \quad (4.40f)$$

$$\sigma_{rz}^{(2)}|_{r=b} = 0 \quad (4.40i)$$

The frequency equation of the general problem is now described by a  $9 \times 9$  matrix, which reduces to a  $3 \times 3$  matrix for purely radial modes (see Appendix A.3 for more details). Due to the added boundary conditions (4.40) compared to a bare fiber, some acoustic modes turn out to be extremely sensitive to any variation in cladding or coating diameter. To illustrate this, let us evaluate the cutoff frequency of purely radial modes in a bare fiber when the cladding radius is varied by  $\pm 1 \mu\text{m}$ . The parameters for silica are  $\rho^{(Si)} = 2200 \text{ kg/m}^3$ ,  $E^{(Si)} = 73 \times 10^9 \text{ Pa}$  and  $\sigma^{(Si)} = 0.17$ . The results are shown in Fig.4.6.(a), which displays the relative frequency

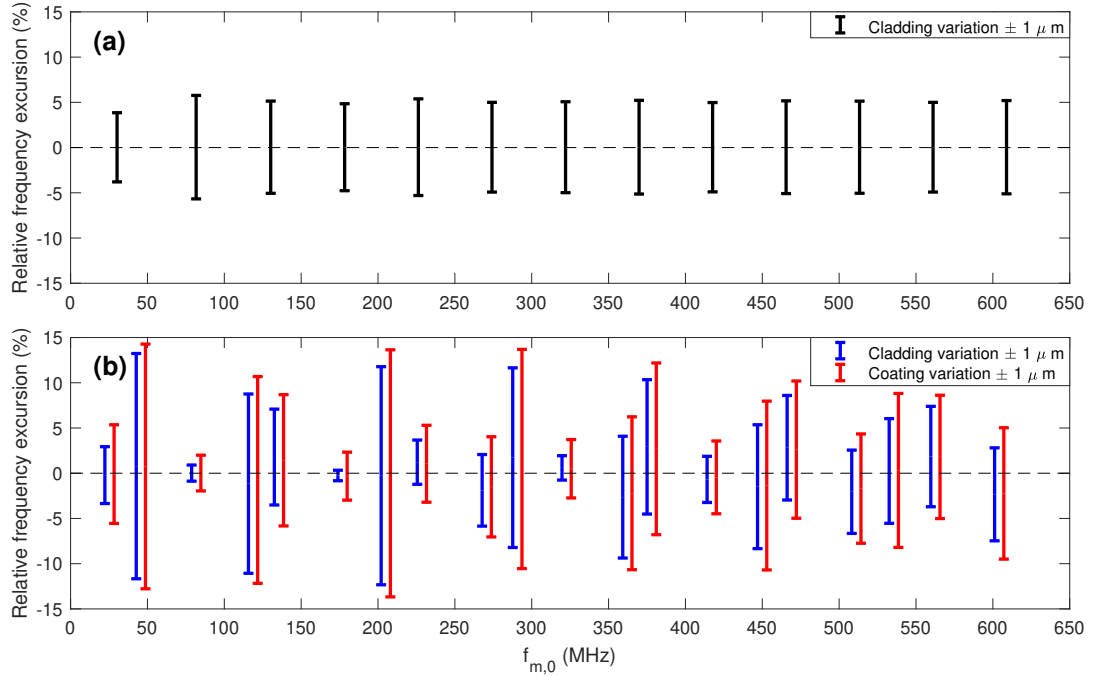


Figure 4.6 – Relative frequency excursion of  $R_{0m}$  modes when the fiber cladding and/or coating exhibits non-uniformities in the order of  $1 \mu\text{m}$  for a bare fiber (a) and a polyimide coated fiber (b).

excursion compared to a nominal radius of  $a_0 = 62.5 \mu\text{m}$  corresponding to a conventional single-mode fiber (SMF). The relative frequency shift is more or less mode independent and amounts to about 5% of the mode nominal cutoff frequency. Note that this implies that the absolute frequency excursion grows linearly with frequency, i.e. higher order modes exhibit larger frequency variations induced by cladding non-uniformities. The same calculation is shown in Fig.4.6.(b) for a coated SMF with an identical nominal cladding radius of  $a_0 = 62.5 \mu\text{m}$  and a nominal coating thickness of  $10 \mu\text{m}$ , yielding an external coating radius of  $b_0 = 72.5 \mu\text{m}$ . The parameters for polyimide are  $\rho^{(Po)} = 1420 \text{ kg/m}^3$ ,  $E^{(Po)} = 2.5 \times 10^9 \text{ Pa}$  and



$\sigma^{(Po)} = 0.34$ <sup>I</sup>. As evidenced in the figure, some modes exhibit a severe frequency deviation when either the cladding or the coating radius is slightly modified ( $\pm 1 \mu\text{m}$ ) while other show very little sensitivity. To understand this, let us compare the displacement profile of two consecutive modes, i.e.  $R_{06}$  and  $R_{07}$ , the former showing very little sensitivity while the later exhibits a massive relative frequency excursion of nearly 15%. The (normalized) displacement distributions of both modes are shown in Fig.4.7

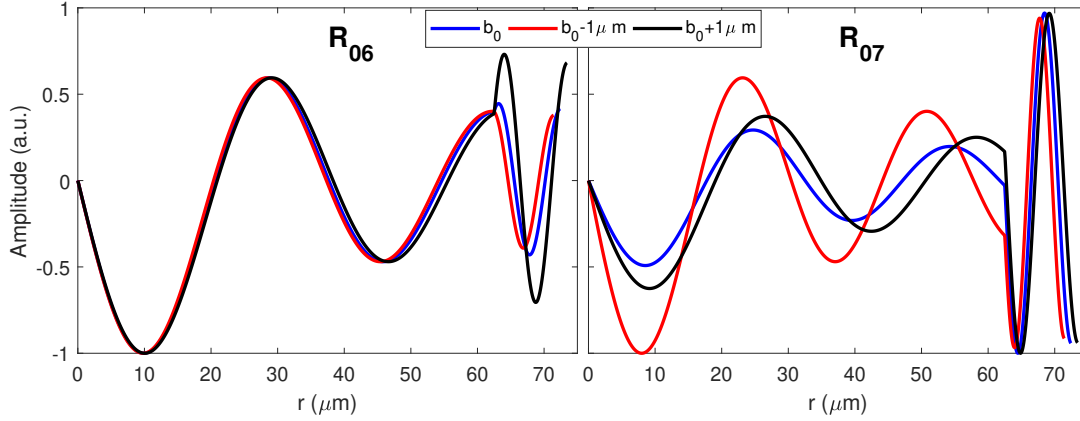


Figure 4.7 – Normalized displacement profile of the 6<sup>th</sup> and 7<sup>th</sup> purely radial mode in a coated fiber for a coating thickness varying of  $\pm 1 \mu\text{m}$ .

The major difference between these two modes is that a much larger fraction of acoustic energy is present within the coating in the case of the  $R_{07}$  mode compared to the case of the  $R_{06}$  mode. Consequently, the displacement distribution for the 6<sup>th</sup> mode is almost entirely imposed by its contribution in the fiber, i.e. the mode shape in the fiber barely varies when the coating diameter is modified. The situation is reversed for the 7<sup>th</sup>, which shows an almost identical displacement distribution within the coating but exhibits massively different behaviours in the fiber. In addition to possible large frequency excursions, different acoustic modes exhibit different damping rates when immersed in a liquid [7], as the acoustic energy radiation exclusively depends on the displacement amplitude at the boundary with the external environment [60]. It turns out that the acoustic damping rate of some modes is far more sensitive to cladding and/or coating non-uniformities than others, yet this is far more challenging to anticipate without in-depth studies of the fiber under test, as greatly discussed in [7]. As will be detailed in section 4.4, selection of an acoustic mode in our case is fully determined by experimental conditions, hence there is unfortunately no possibility to deliberately select an acoustic mode displaying good acoustic properties. Since the fiber condition cannot be known *a priori*, proper measurements will require dedicated calibration to deliver accurate results.

<sup>I</sup>The values for polyimide can be found here: <http://www.mit.edu/~6.777/matprops/polyimide.htm>

### 4.2.5 FSBS in harmonic regime

Due to the lack of any backscattered light, performing distributed FSBS sensing was not a straightforward task but was ingeniously achieved by measuring the backscattered response of optical waves which experienced energy transfer due to FSBS, either via OTDR [64] or BOTDA [52, 63]. We focus here on the second approach, in which acoustic waves are induced via electrostriction by a strong pulse which is intensity modulated following a sinusoidal pattern. By modifying the wave equation accordingly, the behavior of an optical fiber can be related to a forced damped harmonic oscillator. This has profound consequences on the implementation of dedicated FSBS sensing systems presented in the last sections of this chapter.

Formally speaking, the analysis developed here is only valid for the case of a bare fiber. However, the temporal response of the system is expected to be entirely identical for a coated fiber, the only difference lying in the modes displacement profiles, frequencies as well associated damping rates which are parameters to the model. This assumption is further corroborated by experimental results in section 4.4. The acoustic wave equation (4.1) is thus modified as follows

$$\mu \nabla^2 \mathbf{U} + (\lambda + \mu) \nabla (\nabla \cdot \mathbf{U}) - \rho \frac{\partial^2 \mathbf{U}}{\partial t^2} - 2\rho \Gamma \frac{\partial \mathbf{U}}{\partial t} = \mathbf{D} \quad (4.41)$$

where we introduced a fictitious term that accounts for acoustic energy dissipation through the damping rate coefficient  $\Gamma$  [68] and  $\mathbf{D}$  represents a driving term induced by FSBS. Assuming harmonic acoustic wave activation, the driving term takes the form

$$\mathbf{D} = -A_d J_1(\alpha r) \cos(\omega_d t) \hat{\mathbf{r}} \quad (4.42)$$

which corresponds to purely radial modes in a bare fiber or which describes the displacement profile of purely radial modes in a coated fiber when restricted to the fiber itself (the glass). We denote  $\omega_d = 2\pi f_d$  and  $f_d$  is the driving frequency,  $\hat{\mathbf{r}}$  is a unit vector oriented along the r-axis and the minus sign is introduced for later convenience. Note that the displacement amplitude  $A_d$  could be formally calculated based on the analysis developed in section 4.2.2 but considering only the contribution from electrostriction [70, 71]. However, we are interested here in the functional dependency of the acoustic displacement subject to a harmonic activation, hence we synthesize its amplitude in a constant-value parameter denoted  $A_d$  so far. The parameter  $\alpha$  is to be slightly modified to include the contribution from attenuation, i.e.

$$\alpha = \sqrt{\frac{\omega^2 + \Gamma^2}{V_d^2}} \quad (4.43)$$

where  $\omega = \omega_d$  in driven regime, and  $V_d$  is the longitudinal wave velocity (4.7). We assume that

a single-mode is activated, thus we make the following *Ansatz* regarding the solution

$$\mathbf{U}_d = AJ_1(\alpha r) \cos(\omega_d t - \theta) \hat{\mathbf{r}} \quad (4.44)$$

where  $A$  is the amplitude of displacement, and  $\theta$  is an additional phase term. Injecting (4.42) and (4.44) into (4.41) yields

$$\cos(\omega_d t - \theta) (\omega_d^2 - \omega_0^2) + 2\Gamma\omega_d \sin(\omega_d t - \theta) = \frac{A_d}{A} \cos(\omega_d t) \quad (4.45)$$

where we have introduced the oscillator undamped resonance frequency, i.e.

$$\omega_0 = \alpha V_d \quad (4.46)$$

which corresponds to the absence of acoustic loss modelled by setting  $\Gamma = 0$  in (4.43). Equation (4.45) is identical to the one of a forced damped harmonic oscillator. It assumes the following solution

$$A = \frac{A_d}{\sqrt{(\omega_0^2 - \omega_d^2)^2 + 4\Gamma^2\omega_d^2}} \quad (4.47)$$

$$\theta = \tan^{-1} \left( \frac{2\omega_d\Gamma}{\omega_0^2 - \omega_d^2} \right) \quad (4.48)$$

which is represented graphically in Fig.4.8. The amplitude response is close to a Lorentzian

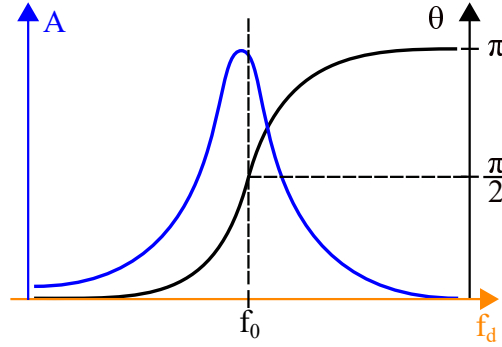


Figure 4.8 – Amplitude  $A$  and phase  $\theta$  response of FSBS induced acoustic waves in a bare fiber in harmonic regime.

and peaks at a value slightly lower than the undamped frequency  $f_0$ , although in practice the difference is completely negligible. The solution derived so far corresponds to the steady-state response in *driven* regime, that is the optical field responsible to induce acoustic waves is still present. However, in practical cases, this situation is to be avoided in order to prevent cross-phase modulation between this activating field and another optical wave used to probe the FSBS resonance [14, 15]. We will thus consider that once reaching steady-state, the activation is to be abruptly interrupted, leading the system to oscillate freely until the acoustic vibrations vanish. The governing equation in this case is still (4.41), only this time the driving term is

set to  $\mathbf{D} = 0$ . This equation is now solved taking as initial condition the very last input from the driven regime, i.e. we assume continuity in the solution. However, in the absence of any external driving force, the acoustic cavity, that is the fiber, now oscillates at its natural frequency, which is entirely determined by its mechanical and dimensional parameters, as derived in section 4.1. The free-running refractive index perturbation, is thus found to be

$$\Delta n_{fr}(t) = A \cos(\omega_m t - \theta) \quad (4.49)$$

where  $\omega_m$  is the angular frequency of the  $m^{\text{th}}$  purely radial mode activated. Here we emphasize that  $\omega_m$  does not equal  $\omega_d$ , but is the mode frequency closest to  $\omega_d$ . Note that the amplitude response  $A$  was derived considering the displacement field, whereas equation (4.49) describes the corresponding refractive index change. However, the two are proportionally related via the photo-elastic overlap integral defined in (4.35) [71]. We can therefore merge all proportionality constants into  $A_d$  in (4.47), and relate it to (4.31), yielding

$$A_d = \frac{P(f_m) Q_{\text{ES}}^{(m)} Q_{\text{PE}}^{(m)}}{8n^2 c_0 \rho} \quad (4.50)$$

With this quite complete picture of the phenomenon, we now turn our attention to experimental setups that enable probing the FSBS resonance in a spatially-resolved manner.

## 4.3 Distributed FSBS measurement using broadband BOTDR

Most of the results presented in this section were published in the following proceedings [46]<sup>II</sup>. One critical aspect regarding distributed forward stimulated Brillouin scattering (FSBS) measurement is the need to resort to a double-scanning process, either to scan both the FSBS as well as the backward SBS resonances in Brillouin based approaches [52, 63], or to average the contribution from coherent Rayleigh scattering when probing FSBS using an incoherent optical time domain reflectometer (OTDR) [64]. This limitation has the major consequence of significantly extending the overall acquisition time. In this section, we present one way to circumvent this difficulty by making use of Brillouin optical time-domain reflectometry (BOTDR), associated with a large bandwidth electrical filter.

### 4.3.1 Harmonic phase modulation

The core principle to achieve distributed FSBS sensing based on harmonic sensing is illustrated in Fig. 4.9. A strong "activating" pulse, modulated in intensity at a frequency  $f_d$  precedes a second "reading" pulse that experiences refractive index modulation from the decaying acoustic wave induced via FSBS. Note that the two pulses temporal profiles are strictly sepa-

<sup>II</sup>@2019 SPIE. Reprinted, with permission from S. Zaslowski, Z. Yang, S. Wang and L. Thévenaz, Distributed forward stimulated Brillouin scattering measurement using broadband BOTDR, Seventh European Workshop on Optical Fibre Sensors (11199), 323-326 (2019), doi = 10.1117/12.2540011

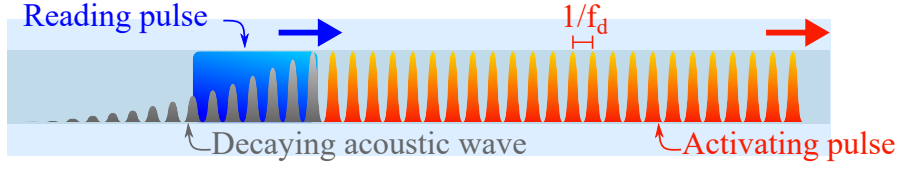


Figure 4.9 – Basic principle of distributed FSBS sensing relying on harmonic activation.

rated in order to avoid any unwanted cross-phase modulation [63, 82]. The driving frequency  $f_d$  is set as to probe a given acoustic mode  $f_m$ . The selection of the most suitable mode is fiber and experiment dependent, and is largely influenced by the mode-dependent FSBS efficiency described in section 4.2.2. In this experiment, the reading pulse width  $W$  is assumed to be far larger than the acoustic wave period  $1/f_m$ , such that many periods are contained within the reading pulse duration. Furthermore, the effect of the additional phase (4.48) is neglected, and averaged out in practice owing to the working principle of the experimental layout. Consequently, the reading pulse experiences phase modulation as it propagates in the fiber [63]

$$\Delta\phi(f_d, z, t) = \frac{2\pi}{\lambda} \int_0^z \Delta n(f_d, z') \cos[\omega_m(z')t] dz' \quad (4.51)$$

where  $\omega_m = 2\pi f_m$ ,  $\lambda$  is the reading pulse wavelength and  $z$  is the position in the fiber. As evidenced from equation (4.51), the forward nature of FSBS implies that the local effects experienced by the pulse during its propagation in the fiber accumulate, such that one will eventually require to resort to a differentiation operation to retrieve the local response. Equation (4.51) also emphasizes that the free-running frequency of the selected acoustic mode  $f_m$  is position dependent, as it might differ slightly from one location to another following the variations in cladding diameter, as seen in section 4.2.4. Here, we assume that this variation is negligible with respect to the integral operation performed in (4.51), hence we define the accumulated phase-shift  $\Delta\phi_{\text{acc}}$  as follows

$$\Delta\phi(f_d, z, t) = \cos(\omega_m t) \frac{2\pi}{\lambda} \int_0^z \Delta n(f_d, z') dz' = \cos(\omega_m t) \Delta\phi_{\text{acc}}(f_d, z, t) \quad (4.52)$$

The perturbed electric field of the reading pulse might be expressed in complex notation as

$$E_{\text{read}}(f_d, z, t) = A(z, t) e^{i[kz - \omega t + \Delta\phi(f_d, z)]} \quad (4.53)$$

where  $A(z, t)$  is the field amplitude,  $k$  is the wavevector and  $\omega$  is the carrier angular frequency. We now make use of the Jacobi-Anger expansion to obtain

$$E_{\text{read}}(f_d, z, t) = A(z, t) \sum_{n=-\infty}^{\infty} i^n J_n[\Delta\phi_{\text{acc}}(f_d, z)] e^{i[kz + t(n\omega_m - \omega)]} \quad (4.54)$$

where  $J_n$  denotes the  $n$ th order ordinary Bessel function of the first kind. Equation (4.54) yields the well known result associated to harmonic phase or frequency modulation, that

is the presence of sidebands located at multiple of the modulating frequency ( $n\omega_m$ ) apart from the carrier frequency. The evolution of the amplitude of each sideband, including the component oscillating at the carrier frequency corresponding to  $n = 0$ , follows the associated Bessel function. Consequently, the intensity of each sideband, labelled as  $I_n$ , is a function of  $J_n^2$ . By using the well-known recurrence relation typical of Bessel functions (see Appendix A)

$$\frac{2n}{x} J_n(x) = J_{n-1}(x) + J_{n+1}(x) \quad (4.55)$$

the accumulated FSBS induced phase change can be evaluated by measuring the intensity of the first three sidebands as

$$\Delta\phi_{\text{acc}}(f_d, z) = \frac{2\sqrt{I_1}}{\sqrt{I_0} + \sqrt{I_2}} \quad (4.56)$$

Finally, the local FSBS response is obtained after numerical differentiation of  $\Delta\phi_{\text{acc}}(f_d, z)$ .

#### 4.3.2 Experimental setup

The procedure described in the previous section was originally implemented by using Brillouin optical time-domain analysis (BOTDA, see section 2.4.5) [63]. Each sideband intensity would be evaluated by measuring the Brillouin gain spectrum (BGS) around the carrier frequency, that is  $I_0$ , as well as around  $I_1$  and  $I_2$ . The overall process thus required to perform a complete BOTDA acquisition three times, for each scanned FSBS frequency  $f_d$ . The BOTDA scanning is mandatory in order to keep track of the BGS maximum value since the Brillouin frequency shift (BFS) might vary along the fiber due to strain even when the fiber temperature is maintained constant. The workaround presented here relies on Brillouin optical time domain reflectometry (BOTDR, see section 2.4.5), and the experimental setup is depicted in Fig.4.10. In this early experiment, the activating pulse was not fully optimized, hence we do not describe

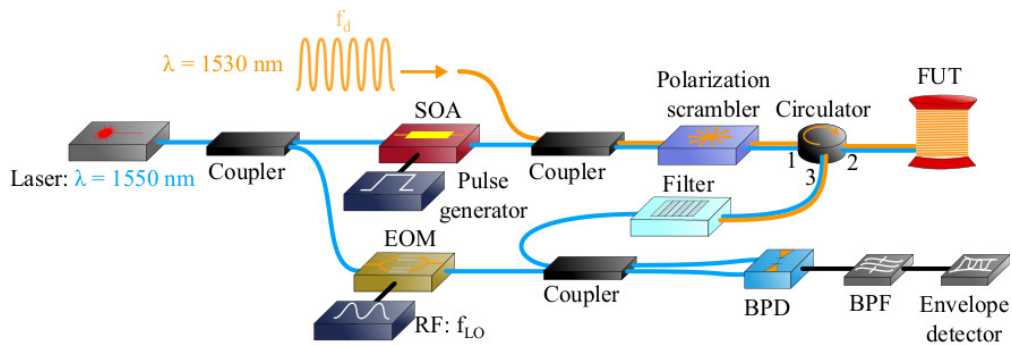


Figure 4.10 – Distributed FSBS measurement setup based on broadband BOTDR. The blue path denotes the BOTDR, while the orange path shows the injection of the activating pulse in the setup. The abbreviations stand for: SOA - semiconductor optical amplifier, EOM - electro-optic modulator, RF - radio frequency, FUT - fiber under test, BPD - balanced photo-detector, BPF - bandpass filter.

its generation in details, as it will be done in the following section. The blue path depicts a conventional BOTDR (see Fig.2.13, in section 2.4.5), where the light from a laser operating at 1550 nm is used to generate, on one branch, a pump pulse (the reading pulse) by making use of a semiconductor optical amplifier (SOA) driven by a pulse generator, and on the other branch, a local oscillator (LO) by driving an electro-optic modulator at extinction (carrier suppression mode) with a pure tone radio-frequency (RF) signal at a frequency  $f_{LO}$ . The polarization scrambler is used to simultaneously average out polarization-induced intensity variations in the BOTDR at detection as well as the contribution from torsional-radial modes in the FSBS interaction [6]. The filter enables filtering out the strong backscattered signal due to the activating pulse. The major difference with a conventional BOTDR lies in the design of the bandpass filter (BPF) located at the balanced photodetector (BPD) output, and which is detailed here after.

In a BOTDR setup aiming at performing distributed sensing based on backward Brillouin scattering, the electrical BPF is designed as to finely sample the fiber BGS by letting energy flow only through a narrow frequency band (see section 2.4.5). Here, the approach is entirely opposite, as the filter in use should capture the entire BGS at once, as illustrated in Fig.4.11. This way, the signal at the BPF output after coherent detection is proportional to the BGS

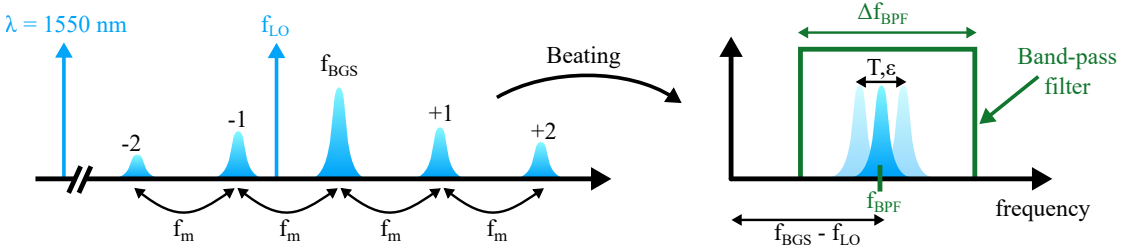


Figure 4.11 – Coherent detection in broadband BOTDR. The BPF bandwidth is such that the entire energy carried by the BGS around each sideband is entirely captured by the filter, even under moderate temperature/strain.

integrated energy, which in turns is proportional to the sideband intensity in the phase-modulation process described in the previous section. Note that additionally, and provided that the fiber BFS is more or less uniform over its entire length, a sufficiently broad BPF will capture the entire BGS despite the latter undergoing slight frequency excursions due to temperature and/or strain. This makes this setup temperature and/or strain insensitive, provided that the BFS deviation are such that the BGS remains at all time entirely within the BPF pass-band. The acquisition is performed as follows. First, the LO frequency  $f_{LO}$  is set such that the beating from the BGS associated to the fundamental sideband ( $I_0$ ) equals the BPF central frequency, i.e.  $f_{BGS} - f_{LO} = f_{BPF}$ . Then, the LO frequency is either upshifted or downshifted by  $f_m$  to measure the first order sideband  $I_1$ , and later on  $I_2$  following the same procedure.

Overall, both the filter bandwidth as well as its central frequency should be carefully adjusted in order to secure a proper operation by avoiding any cross-talk from the beating between

the LO and other sidebands than the one considered. While only two higher order sidebands are represented in Fig.4.11, the frequency modulation can become sufficiently large such that higher order sidebands should also be considered, especially if the interaction length turns significant due to the accumulative nature of FSBS. One possible solution would be to set the LO frequency far higher or far lower than the entire modulated spectrum (sidebands included), but this would shift the BPF central frequency to higher values, implying to employ a photodetector with a larger bandwidth.

#### 4.3.3 Experimental Results

The setup described in Fig.4.10 was used to perform distributed FSBS sensing with a spatial resolution (reading pulse half width) of 8 m. First of all, the capability of the bandpass filter (BPF) to effectively capture the entire Brillouin gain spectrum (BGS) needs to be assessed. The BPF has a bandwidth of  $\Delta f_{\text{BPF}} = 100$  MHz which is centered around  $f_{\text{BPF}} = 550$  MHz. A prior measurement is realized in the absence of the activating pulse, scanning the local oscillator (LO) frequency  $f_{\text{LO}}$  from 10 GHz to 10.6 GHz, the results of which are shown in Fig.4.12 The

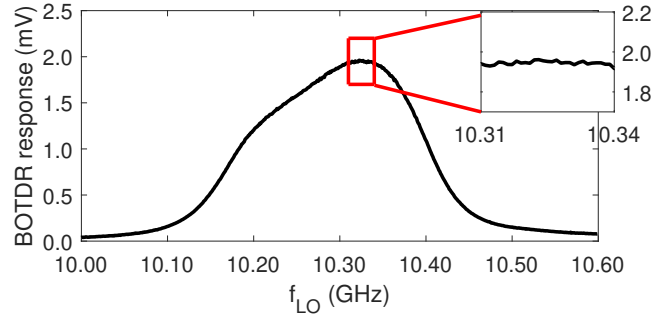


Figure 4.12 – Broadband BOTDR response as a function of  $f_{\text{LO}}$ .

filter shape reveals to be asymmetric as it was realized by cascading a low-pass filter and a high-pass filter. Nevertheless, the inset in Fig.4.12 illustrates a suitable operating region of ~30 MHz, over which the BOTDR response is uniform. From this preliminary measurement, it turns out that the LO ideal frequency is 10.322 GHz, i.e.  $f_{\text{LO}}$  is set to that value in order to measure  $I_0$ .

We now turn to actual FSBS sensing, activating the 8<sup>th</sup> purely radial mode at a frequency  $f_m \approx 370$  MHz. The fiber under test (FUT) is made of a section of ~30 m of bare fiber, which coating has been chemically removed in order to enable FSBS sensing (see section 4.2), located after a section of ~400 m of conventional coated fiber and followed by another section of roughly 100 m of coated fiber. The fibers are all conventional single-mode fibers (SMF) with a cladding radius of ~62.5  $\mu\text{m}$ . In this dissertation, we refer to this configuration as *remote* distributed sensing as opposed to *fully* distributed sensing, because only a short section of fiber respective to the entire sensor length is actually sensitive. Moreover, and as will be further discussed in upcoming sections, achieving fully distributed FSBS sensing is a more challenging



task, because one then need to carefully handle the amount of accumulated effects resulting from the forward scattering process.

Fig.4.13.(a) shows the measured sidebands as a function of distance. The transition from a coated section of fiber to the bare fiber is clearly visible from the figure, and illustrates the severe acoustic damping induced by the acrylate coating. Fig.4.13.(b) depicts the retrieved

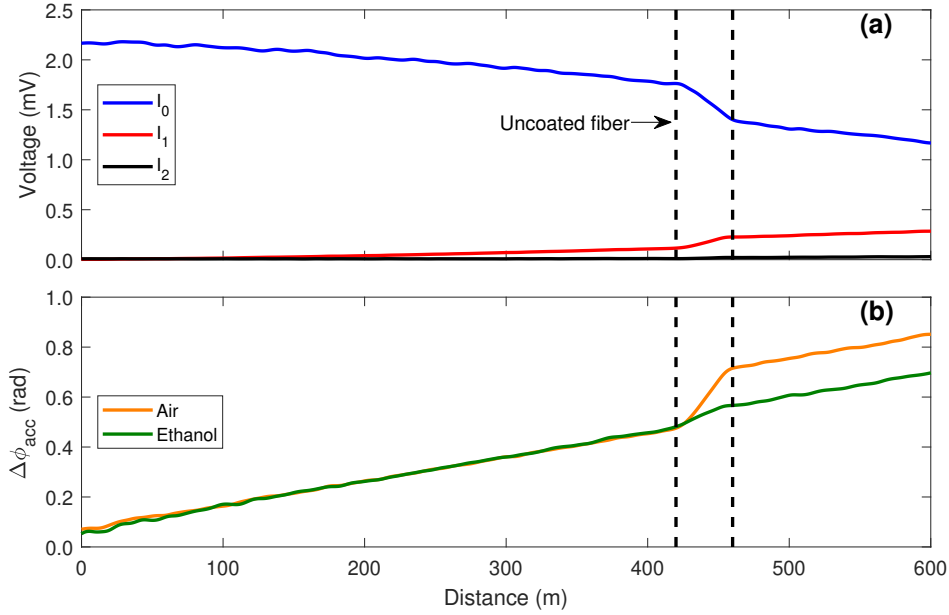


Figure 4.13 – (a) Sidebands intensities as a function of distance. (b) Retrieved accumulated phase shift.

accumulated phase shift  $\Delta\phi_{acc}$ , estimated from combining the measured sidebands intensities according to (4.56). The orange line shows the case where the bare fiber is exposed to air while the green curve shows the response once the bare fiber is immersed in ethanol, illustrating once more the effect of acoustic damping induced this time by the fluid. Note that in retrieving  $\Delta\phi_{acc}$ , fiber attenuation and other common loss mechanisms are compensated and do not influence the result (4.56). However, one major issue with this procedure is that the signal-to-noise ratio (SNR) of the measured  $\Delta\phi_{acc}$  relies on the amplitude of  $I_1$ , which is vanishing at the fiber beginning, i.e. before FSBS could take place, such that the sensor exhibits a dead-zone. This also implies that the SNR is position dependent.

The local FSBS response is now evaluated by performing numerical differentiation, and is given in terms of refractive index modulation amplitude, that is we compute the following value [63]

$$\Delta n(f_d, z) = \frac{\lambda}{2\pi} \frac{\Delta\phi(f_d, z) - \Delta\phi(f_d, z - \text{SR})}{\text{SR}} \quad (4.57)$$

where SR stands for spatial resolution (here 8 m). Local refractive index changes are shown in

Fig.4.14.(a) in terms of distance for  $f_d = 370$  MHz, and in Fig.4.14.(b) in terms of  $f_d$  at a location within the section of bare fiber. The results emphasize the impossibility of achieving proper

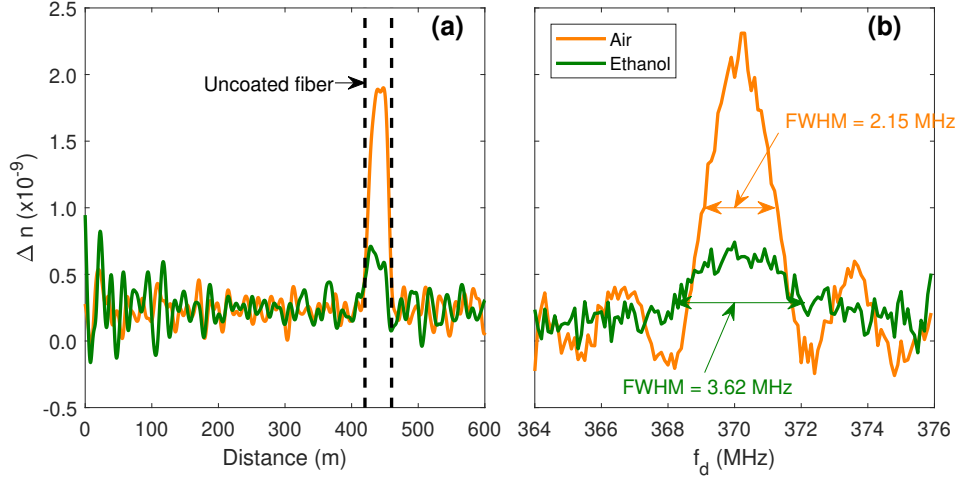


Figure 4.14 – Local FSBS induced refractive index change against (a) distance and (b) driving frequency.

FSBS sensing in acrylate coated fiber, the response being almost ten times weaker when compared to a bare fiber. Notice indeed that the response outside of the bare fiber in Fig.4.14.(a) is not centered around 0, but around a small value (here  $\sim 0.2 \times 10^{-9}$ ). Notice also how the SNR improves over the first  $\sim 200$  m of coated fiber due to the increase of  $I_1$ , as evidenced by the trace thickness. The measured FSBS resonances corresponding to air and ethanol are displayed in Fig.4.14.(b). The resonance in ethanol is significantly broadened compared to the one in air. Here, we refrain from fitting a theoretical curve to the experimental data, due to the lack of a well-detailed model. Indeed, the measured resonances are substantially distorted with respect to the true underlying FSBS response, and this for two reasons.

First, the finite activating pulse width (here 400 ns) yields a convolution operation between the fundamental FSBS resonance and the pulse power spectral density, which is especially detrimental when the FSBS resonance is narrow, that is in air. Indeed, theoretical calculations show that the acoustic damping rate when the fiber is exposed to air should yield a resonance of only a few kHz, while the spectrum measured here has a full width at half maximum (FWHM) of  $\sim 2$  MHz. Second, and as evidenced by the analysis performed in section 4.2.4, variations in the fiber cladding diameter yield to excursions in the FSBS resonance frequency, which in turn might induce a spectral broadening due to the overlap from many resonances with different central frequencies. The amplitude and scale of such non-uniformities are difficult to assess *a priori*, hence we refrain from assigning an associated damping rate  $\Gamma$  to the measured response.

### 4.3.4 Discussion

Despite representing an interesting proof of concept for single-scan distributed FSBS sensing, the method presents many drawbacks that hinder its potential for further development. First of all, the harmonic phase-modulation model neglects the frequency variations induced by fiber non-uniformities, making it intrinsically incomplete. Second, the mathematical operations required to extract the information are not a suitable option, because 1) the sensing region exhibits a blind zone at the fiber beginning and 2) the SNR varies along the fiber. Second, this method can only work for moderate modulation depth, as the oscillating nature of Bessel functions would yield further complications in the data processing in case of strong modulation, i.e. the SNR would drop to 0 at locations corresponding to zeroes of the Bessel function associated to  $I_1$ . Third, the design of the bandpass filter can become quite cumbersome if higher-order sidebands are taken into account and/or if the spatial resolution decreases (which would broaden the BGS), which would consequently strengthen the requirement on the BPF bandwidth. Fourth, and as all methods reported so far to the best of our knowledge, the method developed here is intensity-based, hence is more severely impacted by all sorts of noise sources than e.g. frequency-based methods, such as the one described in the following section.

## 4.4 Distributed FSBS sensing based on serrodyne modulation

Most of the results presented in this section were published in the following article [83]<sup>III</sup>. We present here a novel approach to achieve distributed forward stimulated Brillouin scattering (FSBS) based on serrodyne modulation, which consists in applying a linear phase shift over an optical signal, typically by generating a sawtooth waveform, resulting in a frequency translation [66, 84]. Although the method requires a double scanning process, it enables circumventing most of the drawbacks enumerated in section 4.3.4, which are inherent to intensity-based techniques based on harmonic phase modulation. The proposed technique was used to perform both remote distributed FSBS sensing as well as fully distributed FSBS sensing with unprecedented spatial resolution compared to previous works [7, 52, 63, 64]. Before presenting and analyzing the results obtained, we begin this section with an explanation of the method operating principle, followed by a presentation of the experimental setup.

### 4.4.1 Operating principle

The technique operating principle relies on the model developed in section 4.2.5. The idea is similar to the previous section, only this time the reading pulse width is made shorter than the acoustic wave period. This way, instead of experiencing harmonic phase modulation, the reading pulse undergoes a net frequency shift proportional to the induced acoustic wave

---

<sup>III</sup>@2021 OSA. Reprinted, with permission from S. Zaslowski, Z. Yang and L. Thévenaz, Distributed optomechanical fiber sensing based on serrodyne analysis, *Optica* 8 (3), 388-395 (2021), doi = 10.1364/OPTICA.414457

amplitude as elaborated here below. We consider an optical fiber as a concatenation of cylindrical acoustic cavities, which are brought to oscillation by launching an optical pulse, the so-called activating pulse, which intensity is harmonically modulated at the driving frequency  $f_d$ . At a given fiber location  $z_0$ , the FSBS induced refractive index perturbation is

$$\Delta n(\omega_d, z_0, t) = A(\omega_d, z_0) \cos[\omega_d t - \theta(\omega_d, z_0)] \quad (4.58)$$

where  $A$  and  $\theta$  are given in (4.47) and (4.48) and are illustrated on the right-hand side of Fig.4.15, where  $A_d$  is given in (4.50). We now consider the impact of the decaying acoustic wave (light blue) on a reading pulse (red) that follows the activating pulse with a delay  $\Delta t$ , as illustrated in Fig. 4.15. Here, the additional phase-lag appearing in the forced damped

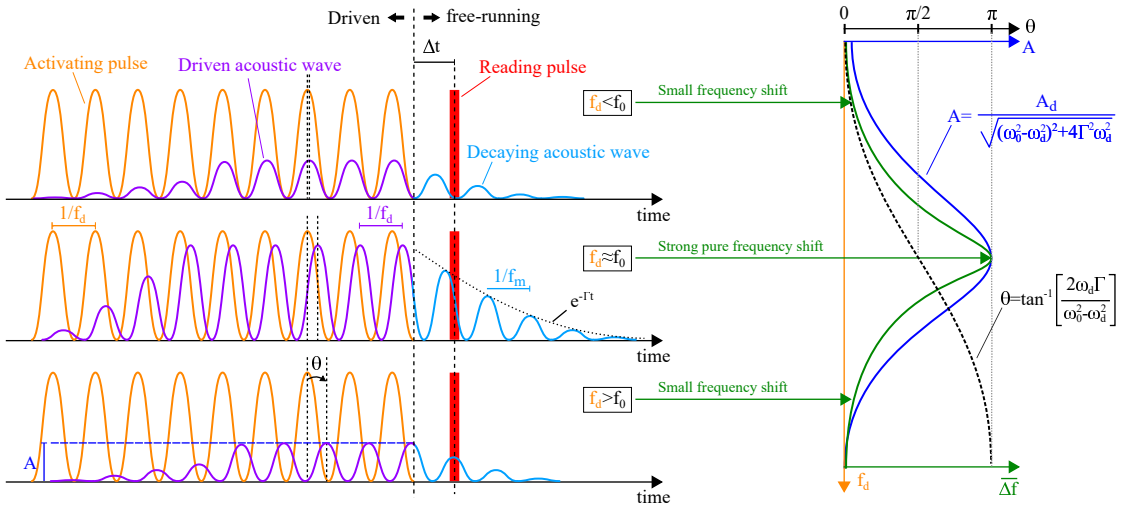


Figure 4.15 – Acoustic and optical waves temporal profiles at a given fiber location.

harmonic oscillator model is of critical importance, as elaborated here after. The phase shift induced on the reading pulse can be expressed as

$$\Delta\phi(\omega_d, z_0, t) = \frac{2\pi}{\lambda} A(\omega_d, z_0) \cos[\omega_m(t - \Delta t) - \theta(\omega_d, z_0)] \quad (4.59)$$

where  $\lambda$  is the reading pulse wavelength and  $\omega_m = 2\pi f_m$  where  $f_m$  is the frequency of the  $m^{\text{th}}$  acoustic mode. In the following demonstration, the time delay  $\Delta t$  is assumed to be set such that  $\omega_m \Delta t$  is an integer multiple of  $2\pi$  thus (4.59) describes a cosine function. As detailed hereafter, this yields a one-sided FSBS resonance, which is ideal in terms of sensing performances. We shall come back on the impact that a change of  $\Delta t$  has on the experiment working principle in section 4.4.5.

We are now interested in determining the frequency experienced by the pulse due to the additional phase profile (4.59), and which is represented by the green curve on the right-hand side of Fig.4.15. As seen from the figure, the measured resonance, that is the effective frequency shift  $\Delta f$  of the reading pulse against the driving frequency  $f_d$ , is narrower than the

pure amplitude response  $A$ . To intuitively understand this, let us consider two distinct cases:

- 1  $f_d$  is far-off resonance, i.e.  $f_d \ll f_m$  or  $f_d \gg f_m$ . The former case is associated to  $\theta = 0$ , that is source and response are in-phase, while the latter case yields  $\theta = \pi$ , i.e. source and response are out of phase. In such situation, (4.59) might be well approximated by a Taylor's expansion as

$$\Delta\phi(\omega_d, z_0, t) \approx \frac{2\pi}{\lambda} A(\omega_d, z_0) \left(1 - \frac{\omega_m^2 t^2}{2}\right) \quad (4.60)$$

and the instantaneous frequency shift experienced by the pulse is

$$\Delta f(\omega_d, z_0, t) = \frac{1}{2\pi} \frac{d\Delta\phi(\omega_d, z_0, t)}{dt} = \frac{A(\omega_d, z_0)}{\lambda} 4\pi^2 f_m^2 t \quad (4.61)$$

which is characteristic of a linear frequency chirp that broadens the pulse spectrum without impacting its carrier frequency. Formally, this can be expressed as the average frequency shift over the pulse duration  $W$ , i.e.

$$\overline{\Delta f}(\omega_d, z_0) = \frac{1}{W} \int_{\Delta t - W/2}^{\Delta t + W/2} \Delta f(\omega_d, z_0, t) dt = 0 \quad (4.62)$$

Note that in order for (4.62) to be true, the pulse width  $W$  needs to be sufficiently narrow, such that the limited development (4.60) is accurate enough. Therefore, far-off resonance, the frequency shift induced on the reading pulse is greatly diminished due to the contribution of the additional phase-lag  $\theta$ .

- 2  $f_d$  is at resonance, i.e.  $f_d = f_m$ , which corresponds to the case  $\theta = \pi/2$ , and (4.59) yield a sinusoidal function. Consequently, the limited expansion of  $\Delta\phi$  yields

$$\Delta\phi(\omega_d, z_0, t) \approx \frac{2\pi}{\lambda} A(\omega_d, z_0) \omega_m t \quad (4.63)$$

which corresponds to the following instantaneous frequency shift

$$\Delta f(\omega_d, z_0, t) = \frac{1}{2\pi} \frac{d\Delta\phi(\omega_d, z_0, t)}{dt} = \frac{A(\omega_d, z_0)}{\lambda} 2\pi f_m \quad (4.64)$$

and the net frequency shift experienced by the reading pulse is

$$\overline{\Delta f}(\omega_d, z_0) = \frac{1}{W} \int_{\Delta t - W/2}^{\Delta t + W/2} \Delta f(\omega_d, z_0, t) dt = \frac{A(\omega_d, z_0)}{\lambda} 2\pi f_m \quad (4.65)$$

At resonance, the pulse experiences thus a pure frequency shift.

Notice that the two cases considered are furthermore scaled by the amplitude response  $A(\omega_d, z_0)$ , which reaches a minimum in case 1) and a maximum in case 2). Based on this analy-

sis, it can be understood that as  $f_d$  is scanned across a given FSBS resonance  $f_m$ , the frequency shift experienced by the reading pulse  $\overline{\Delta f}(\omega_d, z_0)$  will describe a bell-shaped curve that is narrower than  $A(\omega_d, z_0)$ . Fortunately, the measured response  $\overline{\Delta f}(\omega_d, z_0)$  can be univocally mapped back to the underlying amplitude response  $A(\omega_d, z_0)$  as elaborated here after, hence measuring  $\overline{\Delta f}(\omega_d, z_0)$  provides with a mean to evaluate the acoustic damping rate  $\Gamma$  all along the sensing fiber. To the best of our knowledge, this is the first time that a distributed FSBS sensing technique relies on evaluating a frequency shift rather than measuring the energy exchange between optical tones. Despite requiring additional experimental complexity, this method enables to deliver results with unprecedented spatial resolution (SR).

##### 4.4.2 Experimental setup

The experimental setup is built around a conventional Brillouin optical time-domain analyzer (BOTDA) and is shown in Fig.4.16. The two lasers operate at  $\sim 1550$  nm, but are spectrally

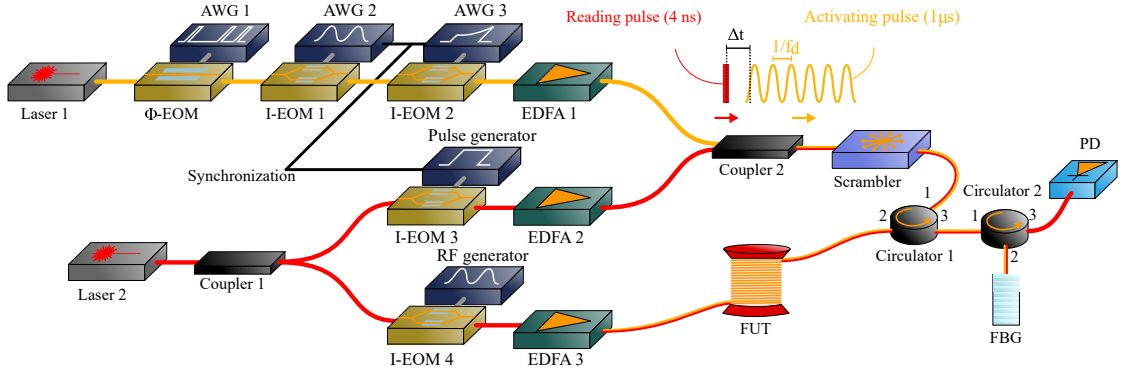


Figure 4.16 – Experimental setup showing the optical path of the activating pulse (orange) and the reading pulse (read). The abbreviations stand for: AWG - arbitrary waveform generator, EOM - electro-optic modulator, EDFA - erbium doped fiber amplifier, RF - radio frequency, FUT - fiber under test, FBG - fiber Bragg grating, PD - photodetector

parted  $\sim 3$  nm from each other. The orange path depicts the generation of a long rectangular activating pulse modulated in intensity. First, the continuous-wave (CW) light from laser 1 is phase-modulated by a phase electro-optic modulator ( $\Phi$ -EOM) driven by an arbitrary waveform generator (AWG) which is loaded with a pseudo-random bit sequence (PRBS). The purpose of this operation is to broaden the activating pulse spectrum via frequency dithering in order to increase the threshold of non-linear effects, especially backward stimulated Brillouin scattering (SBS) that may arise within the activating pulse itself. The sinusoidal intensity modulation is to be taken more carefully as in the previous setup (see Fig.4.10), because each reading pulse needs to meet the exact same refractive index pattern on each individual acquisition. This problem is tackled by driving the intensity EOM 1 (I-EOM) with AWG 2, which is loaded with a sinusoidal signal at frequency  $f_d$  enabling a precise control of the harmonic wave phase. Then, the activating pulse is shaped by I-EOM 2, which is driven by AWG 3 loaded with a  $1 \mu\text{s}$  long pre-distorted pulse shape that is designed to anticipate the

distortion induced by the saturation of the following erbium doped fiber amplifier (EDFA 1), and eventually delivering an activating pulse with uniform power all over its duration.

The red path is a conventional BOTDA (see Fig.2.16), which operates by splitting the light from laser 2 in pump (upper part) and probe (lower part) branches by coupler 1. The pump, i.e. the reading pulse, is generated by I-EOM 3 driven by a pulse generator and amplified by EDFA 2 before coupling it with the activating pulse. The reading pulse duration is subject to an important trade-off between FSBS efficiency and BOTDA performance. Actually, in order to satisfy all equations derived in section 4.4.1, the reading pulse width should be small with respect to the acoustic wave period  $1/f_m$ . In the fibers measured here, FSBS is most efficient at frequencies ranging between ~300 MHz and ~400 MHz (see Fig.4.4 for instance). Yet, this would constraint the reading pulse to be typically shorter than 1 ns, for which the BOTDA response is dramatically low due to the phonon acoustic lifetime in silica fibers [31]. We shall see that the FSBS amplitude is actually capped in our experiment due to non-local effects, hence we can afford to slightly diminish its efficiency. Ideal experimental conditions were found by setting the reading pulse width to 4 ns, and activating acoustic waves at frequencies around 130 MHz.

The probe consists in a double-sideband carrier suppressed CW signal, which is obtained by driving I-EOM 4 at extinction with a radio frequency (RF) generator at a frequency  $f_{RF}$ . EDFA 3 amplifies the probe before its injection in the fiber under test (FUT), which ensures reaching maximum signal-to-noise ratio (SNR) at detection [40]. The sinusoidal pattern imposed on the activating pulse as well as its gating signal together with the reading pulse require precise synchronization, as evidenced by the black wire shown in the figure. This temporal adjustment is necessary as to secure a well defined and stable time delay  $\Delta t$  between the two pulses. After combining the two paths through coupler 2, the presence of a polarization scrambler enables to simultaneously average out polarization fading effects in the BOTDA as well as the contribution from torsional-radial modes in the FSBS process. After its propagation through the FUT, and before its detection by a 350 MHz photo-detector (PD), the probe sees one of its sideband rejected by a fiber Bragg grating (FBG), which also enables filtering out any strong backscattered emission from the activating pulse that might distort the measurement.

### 4.4.3 Acquisition process

Although the main distributed sensing is Brillouin optical time-domain analysis (BOTDA), the acquisition process is reconsidered in order to adapt it to forward stimulated Brillouin scattering (FSBS) sensing. The procedure is illustrated in Fig.4.17. Fig.4.17.(a) shows the pulses sequence as they are launched into the sensing fiber. The activating pulse is only present every second pulse acquisition, thus the frequency change induced by FSBS only affects every second acquisition, as illustrated in Fig.4.17.(b) which depicts the net effect of FSBS on the measured Brillouin gain at a fixed probe frequency  $f_{RF}$  as well as the corresponding acquisition window. Note that this ensures that only temperature and/or strain changes occurring within

#### 4.4. Distributed FSBS sensing based on serrodyne modulation

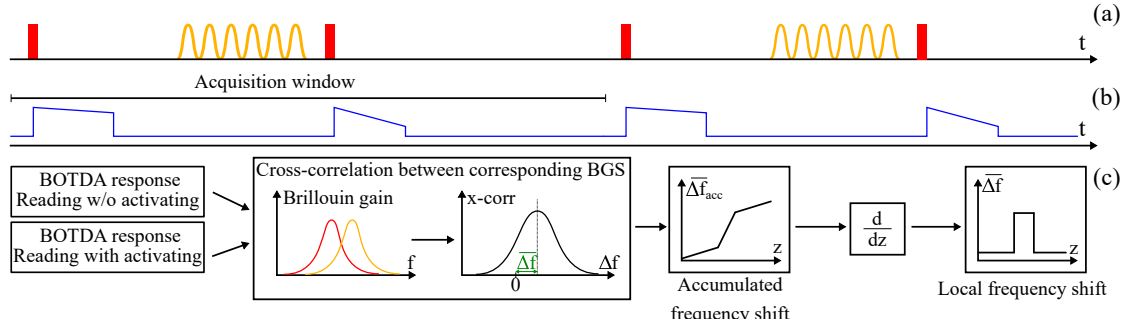


Figure 4.17 – (a) Pulses sequence launched in the fiber. (b) Brillouin gain at a given probe frequency  $f_{RF}$  illustrating the portion of signal acquired. (c) Post-processing yielding the local frequency shift experienced by the reading pulse due to FSBS.

the time interval between two reading pulses (here a few tens of  $\mu s$ ) can effectively influence the measurement, which can be safely neglected here.

The data processing is detailed in Fig. 4.17.(c). After acquisition, the two BOTDA measurements are compared with each other by performing a cross-correlation between the corresponding Brillouin gain spectra (BGS) at each fiber position. The cross-correlation maximum yields the accumulated frequency shift along the fiber  $\Delta f_{acc}$  at a given driving frequency  $f_d$ , which is finally differentiated against distance to retrieve the local frequency shift experienced by the pulse and denoted  $\Delta f$ . Note that unfortunately, one resort once more to a double frequency scanning process, i.e. one for the FSBS resonance and another for the BOTDA.

##### 4.4.4 Numerical simulations

Throughout the following sections, we shall compare experimental results with numerical simulations that reproduce the behavior of our experimental apparatus, a detailed pseudo-code implementation of which can be found in Appendix B. The numerical simulation is performed as follows:

- The fiber is modelled as a concatenation of resonances, defined by three parameters  $A_d(z)$ ,  $f_0(z)$  and  $\Gamma(z)$ .
- At each fiber position, the FSBS induced additional phase profile  $\Delta\phi(\omega_d, z, t)$  (4.59) is evaluated without approximation. The finite activating pulse duration is taken into account by performing a convolution operation between the FSBS resonance defined by equations (4.47) and (4.48) and a normalized sinc function corresponding to the activating pulse width.
- This phase profile then increments the previously calculated phase profile in order to account for the accumulative nature of FSBS.
- The accumulated phase profile is then impinged on the reading pulse.



- The pure Brillouin gain spectrum (BGS) as well as the FSBS modified BGS are evaluated as the convolution between the fundamental BGS and the reading pulse power spectral density (PSD) [85].
- The cross-correlation between the two BGS is evaluated, and the frequency corresponding to its maximum value is stored in a matrix that corresponds to the accumulated frequency shift experienced by the pulse along the fiber due to FSBS.

The benefit of performing such simulations is twofold. First, it validates the theoretical model developed in section 4.2.5. Second, it enables evaluating the damping rate  $\Gamma$  in actual distributed FSBS measurements. Before delivering results related to sensing, we investigate on the consequences of varying the time delay  $\Delta t$  between the activating and the reading pulse (4.59) on the experiment operating principle.

### 4.4.5 Pulses synchronization

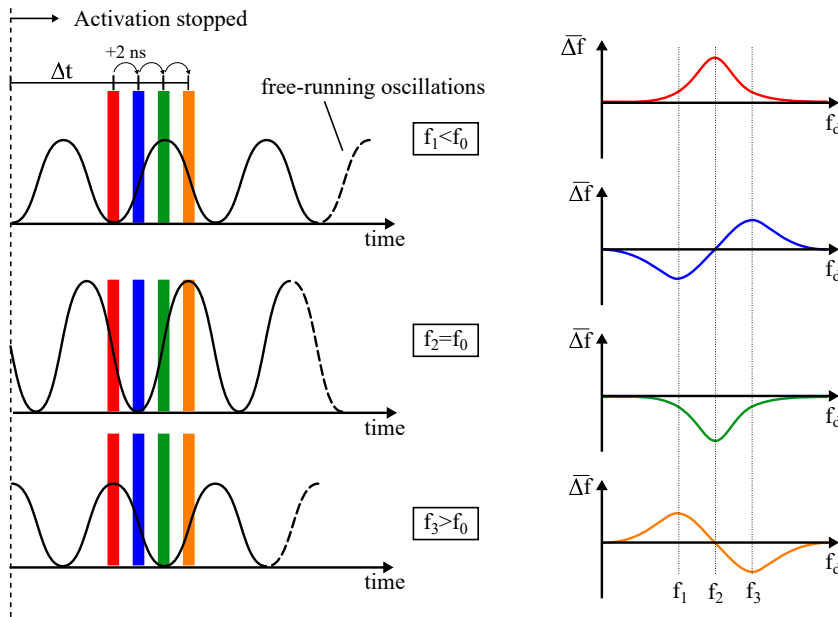


Figure 4.18 – Impact of an added time-shift between the reading pulse and the activating pulse on the retrieved FSBS resonance.

In this section, we explore how the temporal delay  $\Delta t$  between activating and reading pulses can be seen as an additional degree of freedom in the experimental design. Moreover, and for the sensing applications in which we are most interested here, this value needs to be precisely adjusted as to deliver optimized results. In this experiment, the acoustic wave frequency is assumed to be roughly equal to 130 MHz, yielding an acoustic period in the order of 8 ns. Fig. 4.18, depicts the measured FSBS response for different time delays  $\Delta t$ . The figure reproduces some of the features shown in Fig. 4.15, but focuses on the free-running oscillation.

#### 4.4. Distributed FSBS sensing based on serrodyne modulation

Notice for instance that the effect of acoustic damping is not shown here for the sake of simplicity. The left-hand side of the figure shows four different reading pulses experiencing the free-running acoustic field from the cavity, while the right-hand side depicts the corresponding retrieved responses. The red pulse (associated with the uppermost response), corresponds to the case presented in Fig.4.15, while subsequent pulses (by order blue, green and orange) are each time delayed by 2 ns, corresponding roughly to  $\frac{1}{4}$  of a period ( $f_0 \approx 130$  MHz). As shown in the right-hand side of the figure, the retrieved FSBS responses turns asymmetric with respect to  $f_0$  when the reading pulse is delayed by a quarter of a period (2 ns) with respect to its initial delay  $\Delta t = \Delta \tau_{\max}$ , and flips over when delayed by half a period (4 ns) with respect to  $\Delta t$ .

The behavior predicted in Fig.4.18 is experimentally demonstrated by performing remote distributed FSBS measurements in a section of  $\sim 30$  m of bare fiber located at the remote end of a  $\sim 200$  m section of coated conventional single-mode fiber (SMF). The experimental parameters used for this measurement are synthesized in Table.4.2.

Activating pulse (width/power)	1 $\mu$ s / $\sim 3$ W
Reading pulse (width/power)	4 ns / $\sim 1$ W
Probe power (per sideband)	$\sim 700$ mW
$f_{\text{RF}}$ (start/interval/# steps)	10.3 GHz / 10 MHz / 100
$f_d$ (start/interval/# steps)	128.5 MHz / 100 kHz / 40
Averaging	300

Table 4.2 – Parameters in the experiment dedicated to measure the impact of a change in the temporal delay between activating and reading pulses. Optical powers are measured at the FUT input.

All optical powers are adjusted as to maximize the signal-to-noise ratio (SNR) while securing the absence of detrimental non-linear effects such as backward amplified spontaneous Brillouin scattering for the activating pulse [52], and modulation instability (MI) for the reading pulse [29]. After acquiring the Brillouin gain response, each trace is digitally filtered by means of a Gaussian filter with a bandwidth of 20 MHz, yielding here a spatial resolution (SR) of 5 m. Note that this post-processing operation enables at the same time to improve the experimental SNR by reducing additive white Gaussian noise (AWGN, see Chapter 3), but also because the accumulated response due to FSBS is far larger over 5 m than the initial SR (40 cm). Notice that in this experiment, one do not seek at reaching high performances, hence the averaging is kept low (300) and the BOTDA frequency scanning step is coarse (10 MHz). The results are displayed in Fig.4.19, where the colors of the different resonances shown are matching the ones displayed in Fig.4.18.

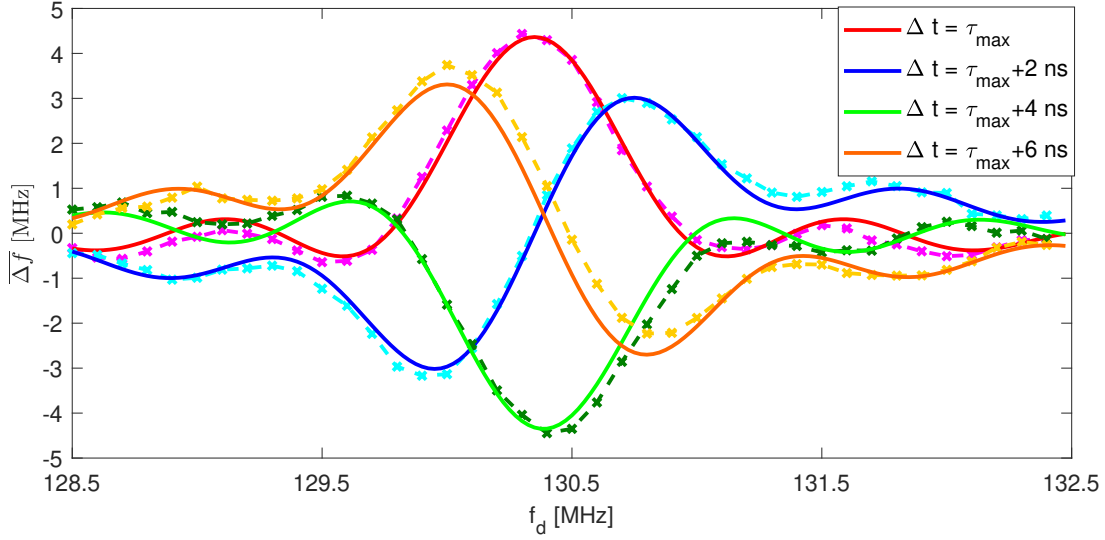


Figure 4.19 – Measured FSBS resonance (x-markers) compared to numerical simulations (solid lines).

The matching between the numerical simulations (solid lines) and the experimental data (x-markers) is excellent, especially in finer features such as the sidelobes, which are induced by the finite duration of the activating pulse (see Supplement B.). We emphasize that all acquisitions are rigorously identical, except for an additional time-shift of 2 ns of the reading pulse between each case. While no specific application is targeted here, the results shown here demonstrate a high flexibility to induce a bipolar frequency shift on a pulse obtained by delaying either the activation or the reading pulse, or by operating at a frequency either below or above the FSBS resonant frequency. Finally, notice that the discrepancies between the observed resonances and the theoretical curves are very likely to originate from variations in the fiber cladding diameter, resulting in a non-uniform FSBS resonance profile, as elaborated hereafter.

#### 4.4.6 Remote distributed FSBS sensing in bare fiber

The results presented here are obtained in the same fiber as in the previous section, i.e. FSBS is only efficiently activated in a ~30 m long section of bare fiber located after ~200 m of conventional SMF. The selected acoustic mode is the 3<sup>rd</sup> purely radial mode, at a frequency  $f_m \approx 130$  MHz. The delay between activating and reading pulses is carefully adjusted as to maximize the system response, and the experimental parameters are provided in Table 4.3. Note that compared to the previous setup (see Table 4.2), the acquisition time is significantly longer due to a finer frequency scan in the BOTDA acquisition (4 MHz instead of 10 MHz) and a larger averaging (4096 instead of 300). Each acquisition is this time digitally filtered by a Gaussian filter with a bandwidth of ~125 MHz, yielding a final spatial resolution (SR) of 80 cm. While the employed pulse width would potentially allow reaching a spatial resolution of 40 cm,

#### 4.4. Distributed FSBS sensing based on serrodyne modulation

Activating pulse (width/power)	1 $\mu$ s / ~3 W
Reading pulse (width/power)	4 ns / ~1 W
Probe power (per sideband)	~700 mW
$f_{RF}$ (start/interval/# steps)	10.3 GHz / 4 MHz / 250
$f_d$ (start/interval/# steps)	128.5 MHz / 100 kHz / 40
Averaging	4096

Table 4.3 – Parameters to remotely measure FSBS in a single-mode fiber. Optical powers are measured at the FUT input.

this requirement would yield an exaggerated acquisition time, hence it was decided to lower the experimental SR to 80 cm, which still outperforms the latest reported results [52].

Fig.4.20 illustrates the procedure described in Fig.4.17. Fig.4.20.(a) shows the 2-D map of the measured Brillouin gain in the fiber under test (FUT) without activation, while the black curve depicts the corresponding Brillouin frequency shift (BFS). The two fibers, that is the coated fiber as well as the bare segment, are discernible due to their different intrinsic BFS. Fig.4.20.(b) enables observing the effect of the presence of the activating pulse when the

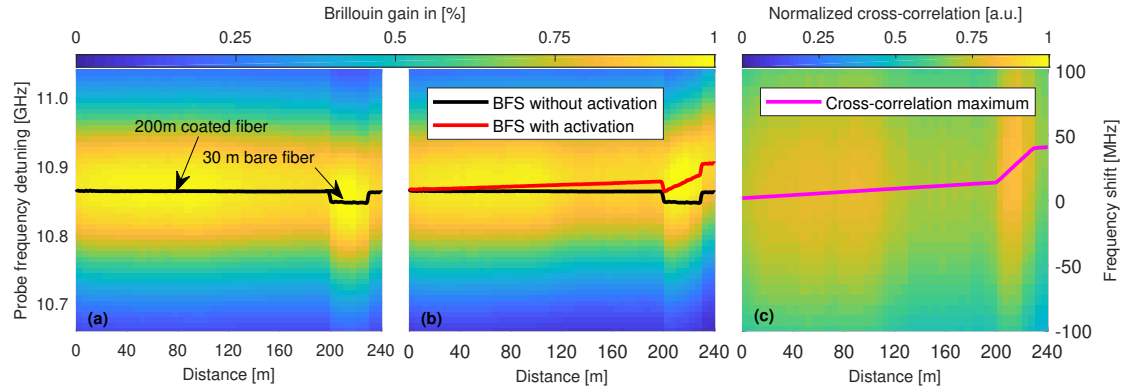


Figure 4.20 – 2-D map of the Brillouin gain response without (a) and with activating pulse (b). (c) 2-D map of the cross-correlation performed columnwise between (a) and (b).

driving frequency is within the fiber FSBS resonance ( $f_d = 130.4$  MHz). Notice that FSBS is not entirely extinguished in the coated SME, but its effect is significantly weaker than in the bare fiber segment, which displays a ~40 MHz shift over ~30 m of fiber. Finally, Fig.4.20.(c) shows a 2-D map of the cross-correlation operation performed columnwise between Fig.4.20.(a) and Fig.4.20.(b) while the magenta line depicts the accumulated shift  $\overline{\Delta f}_{acc}$ .

We now analyze the FSBS resonance after performing the required differentiation operation described in Fig.4.17. The segment of bare fiber is first exposed to air (as in Fig.4.20) and is

later on immersed in ethanol. Fig.4.21.(a) shows the local frequency shift  $\overline{\Delta f}$  at a fixed driving frequency ( $f_d = 130.4$  MHz) near the fiber end. The effect of acoustic damping due to ethanol is clearly visible, as the signal amplitude drops by a factor  $\sim 5$  when the fiber is immersed in the fluid. The signal remains nevertheless well above the noise floor, which is quantified in Fig.4.21.(b) that shows the experimental uncertainty as the standard deviation on the retrieved frequency shift  $\sigma_{\overline{\Delta f}}$ , and which was evaluated by performing 5 repeated measurements. The

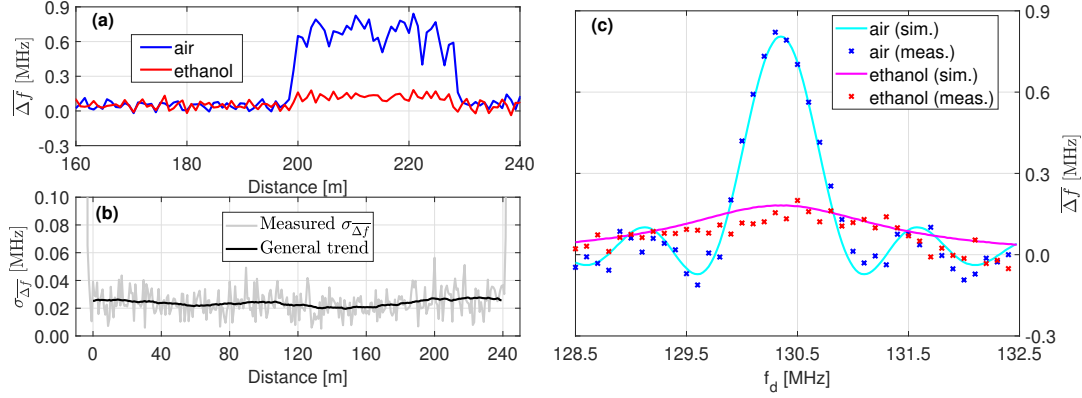


Figure 4.21 – (a) Local FSBS response  $\overline{\Delta f}$  for  $f_d = 130.4$  MHz when the section of fiber is exposed to air (blue) or immersed in ethanol (red). (b) Uncertainty on the measured frequency shift. (c) Retrieved FSBS resonance in the middle of the segment of bare fiber.

experimental uncertainty being found to be lower than 0.03 MHz over the entire fiber, the sharp signal variations observed in Fig.4.21.(a) cannot be explained by noise. It turns out that these abrupt changes in the signal amplitude originate from non-uniformities in the FSBS central resonance profile, as shown later on in Fig.4.22. Fig.4.21.(c) compares the measured resonances in air and ethanol (x-markers) with the results obtained from the simulations described in Appendix B.

In air, the resonance width is almost entirely determined by the activating pulse width (1  $\mu$ s, corresponding to 1 MHz). Yet the fine structure of the observed resonance, such as sidelobes, is still dependent on the underlying damping rate. In air, the acoustic radiation loss ( $\Gamma_r \approx 2\pi \times 0.5$  kHz [6]) contributes very little to the effective damping rate denoted  $\Gamma_e$ , which also includes bulk material acoustic damping ( $\Gamma_m \approx 2\pi \times 3$  kHz [86]) as well as geometrical non-uniformities such as cladding diameter variation, as discussed in section 4.2.4, and strain non-uniformity  $\Gamma_n$ . This last parameter is difficult to estimate without *a priori* information, hence it requires dedicated calibration. Overall, the effective damping rate  $\Gamma_e = \Gamma_r + \Gamma_m + \Gamma_n$  delivering the most accurate fitting of the experimental resonance is found to be equal to  $2\pi \times 80$  kHz. This implies that cladding and/or strain variations only amount to  $2\pi \times 76.5$  kHz over 80 cm, which is remarkably low as further elaborated in Fig.4.22. This ensures that in the case of ethanol, most of the contribution to the total damping rate comes from the acoustic radiation loss which amounts to  $\Gamma_r = 2\pi \times 1.1$  MHz [6]. The theoretical curve (in magenta) in Fig.4.21.(c) using this value shows good agreement with the experimentally measured

resonance.

In order to complement these results, Fig.4.22.(a) provides with a 2-D map of the retrieved frequency shift in the section of bare fiber. As evidenced from the figure, the non-uniformity of the FSBS resonance frequency  $f_m$  is indeed responsible for the signal amplitude variations depicted in Fig.4.21.(a). These fluctuations are confirmed to be intrinsic to the fiber and not the experimental method by swapping the fiber ends and repeating the measurement. Fig.4.22.(b) shows a perfect match between this additional measurement and the initial

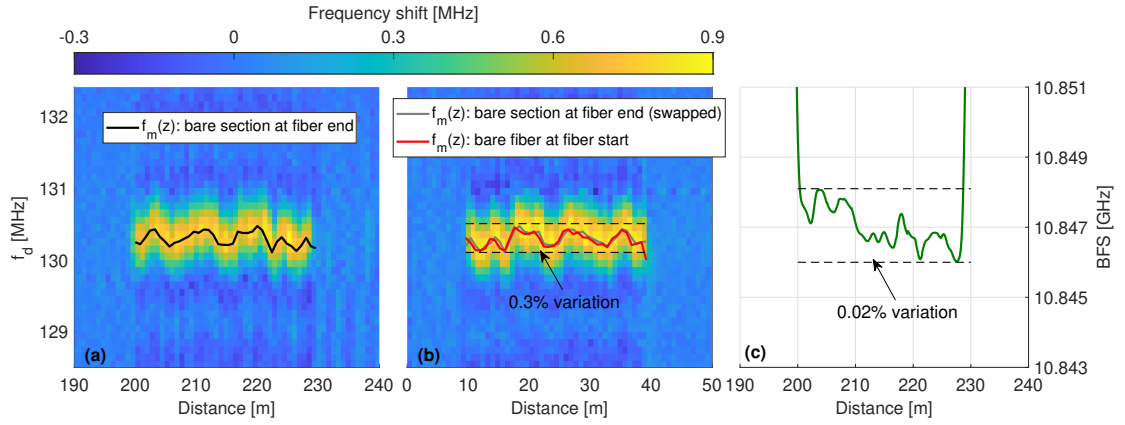


Figure 4.22 – (a) 2-D map of the reconstructed FSBS resonance in the bare fiber. (b) Same as in (a) but with swapped fiber ends. (c) Brillouin frequency shift (BFS) profile in the bare fiber.

acquisition performed in Fig.4.22.(a) once mirrored. The observed 0.3% variation in the resonance frequency  $f_m$  are mostly attributed to cladding non-uniformities, especially given that the non-uniform strain profile along the fiber produces relative BFS variations one order of magnitude lower (0.02%), hence this contribution can be largely ruled out [87]. These observations yields two important conclusions for any sensing application. First, the effective damping rate  $\Gamma_e$  needs to be properly calibrated all along the fiber, as different underlying  $f_m$  profiles might yield entirely different values of  $\Gamma_n$ . Notice for instance how a value of  $\Gamma_n = 2\pi \times 76.5$  kHz was attributed to the measured resonance in Fig. 4.21.(c), while the overall observed  $f_m$  variation amounts to 400 kHz (0.3% of ~130 MHz). This also implies that sensors with coarser spatial resolutions will inevitably results in broader observed FSBS resonances, as corroborated by previous reports [52, 63, 64, 88]. It is worth mentioning that, in addition, this technique also enables to resolve changes in the fiber cladding diameter with such a sharp spatial resolution (80 cm). It can therefore potentially be used to assess imperfections in the physical dimensions of optical fibers or even waveguides, provided that the spatial resolution can be reduced down to a sufficient extent.

#### 4.4.7 Accumulated effects in fully distributed FSBS sensing

We now address the problem of achieving fully distributed forward stimulated Brillouin scattering (FSBS) sensing in a polyimide coated fiber. The benefit of using polyimide instead of acrylate lies in the better impedance matching between silica (the fiber itself) and the coating, yielding to improved performances in terms of FSBS activation while preserving the fiber mechanical robustness. Due to the accumulative nature of FSBS, that is the increase in the phase modulation experienced by the reading pulse with distance, one must now evaluate whether the integrated effect will lead to unwanted consequences, such as signal distortion. To the best of our knowledge, this topic has not been addressed yet in the literature, mostly due to the fact that distributed FSBS sensing is an emerging field of research, and also because most results reported actually correspond to remote distributed FSBS sensing [52, 63, 64]. Fully distributed FSBS sensing in polyimide coated fiber has been presented in a recent work [7], yet the aforementioned issue has not been discussed.

The study conducted hereafter is specific to the technique employed here, yet the general conclusions are believed to apply to any distributed FSBS sensing scheme, since they all rely on the same physical process. We analyze the effect of varying the activating pulse power in a 500 m long fiber, which replicates the polyimide fiber used in the corresponding experiments (see section 4.4.8). Following the procedure utilized in the study of non-local effects in Brillouin optical time-domain analysis (BOTDA) [35], we simulate a worst case scenario where the accumulated effect is most detrimental, i.e. we consider that the first 490 m of fiber are perfectly uniform ( $f_m = 130.5$  MHz) while the last 10 m show a slightly shifted FSBS resonance ( $f_m = 130.3$  MHz).

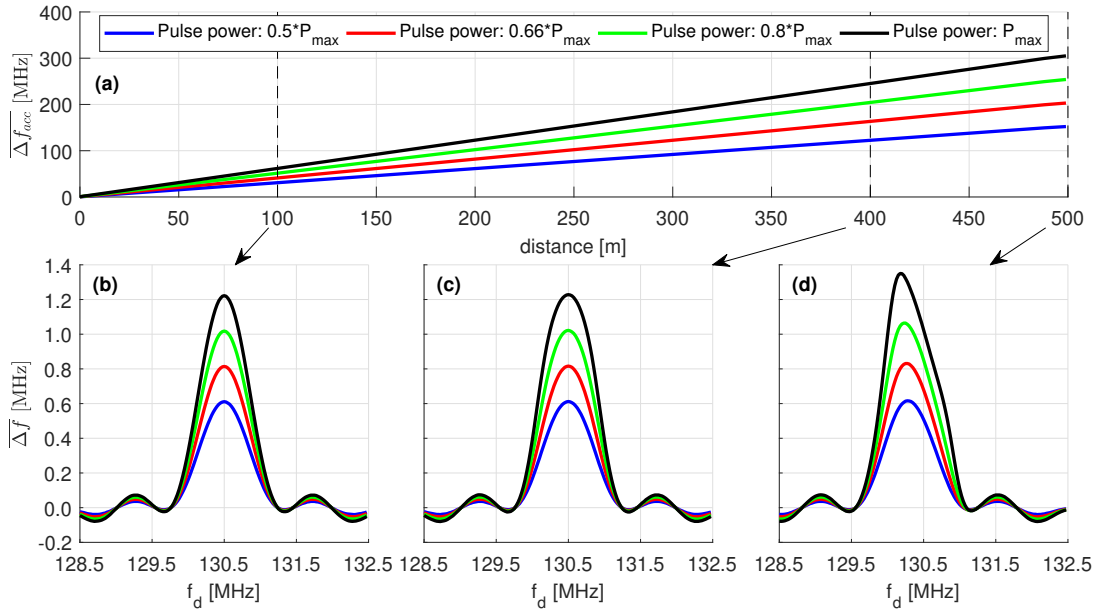


Figure 4.23 – (a) Accumulated frequency shift  $\Delta f_{acc}$  at resonance  $f_d = 130.5$  MHz. Retrieved FSBS resonance with a spatial resolution of 2 m at 100 m (b), 400 m (c) and at fiber end (d).



The results are shown in Fig.4.23. As will be explained in section 4.4.8, the spatial resolution (SR) is to be slightly degraded in this configuration, that is from 80 cm to 2 m. Fig.4.23.(a) shows the accumulated frequency shift  $\overline{\Delta f}_{\text{acc}}$  along the fiber for  $f_d = 130.5$  MHz at different activating pulse powers, ranging from blue (weakest) to black (strongest), corresponding to an accumulated frequency shift going from 150 MHz to 300 MHz, respectively. Fig.4.23.(b), (c) and (d) show the retrieved FSBS resonance at 100 m, 400 m and 500 m, respectively. Note that according to our fiber design, all curves should match between Fig.4.23.(b) and (c), while the resonances in (c) should display an identical shape while exhibiting a slightly lower central frequency.

The simulation yields the following conclusion. For short distance, that is when the accumulated phase modulation induced by FSBS is low, all resonances can be perfectly recovered. After some distance, here exemplified at 400 m, the FSBS resonances turn distorted, and the distortion is more pronounced for higher activating pulse power. This detrimental non-local effect is even more severe at the fiber end, not only due to the extra accumulated distance of 100 m, but also due to the underlying FSBS resonance frequency shift. Overall, the total phase modulation amplitude, which scales as the product between activating pulse power and fiber distance, should be maintained below a certain level to secure safe operating conditions. Here, this corresponds to the lowest activating pulse power, i.e. curves that are drawn in blue.

The numerical simulations performed here enable delimiting a safe zone for the specific experimental setup and fiber used hereafter. While this falls out of the scope of this dissertation, this problem ought to be addressed in depth, in order to draw theoretical limits to the strength of the optical waves launched in the fiber, similar to other distributed optical fiber sensors (DOFS) techniques [34, 89, 90]. The study is expected to be quite complex, as it depends on many parameters that are both fiber and experiment dependent. Note for instance that in our case, the reading pulse width also plays a critical role in the expected amount of distortion because a shorter reading pulse will experience a narrower section of the sinusoidal refractive index modulation (see Fig.4.15), hence the Taylor expansion derived in equations (4.60) and (4.63) will be more accurate. This yet has to be trade-off with the loss of signal in Brillouin optical time-domain analysis (BOTDA) due to a shorter pulse width [31]. With these considerations in mind, we turn our attention to experimental results in polyimide coated fiber.

#### 4.4.8 Fully distributed FSBS sensing in polyimide coated fiber

We present the results of fully distributed FSBS sensing in a 500 m long polyimide coated fiber. The fiber in use has a reduced cladding (diameter of 80  $\mu\text{m}$ ) and is coated with a thin layer of polyimide (10  $\mu\text{m}$ ). Given our reading pulse width (4 ns), a suitable acoustic mode is found around  $f_m \approx 126$  MHz, corresponding to the 3<sup>rd</sup> purely radial mode. The corresponding experimental parameters are synthesized in Table 4.4. Notice that with respect to the previous scenario (see Table 4.3), the activating pulse power has been dropped by a factor  $\sim 3$  in order to



Activating pulse (width/power)	1 $\mu$ s / ~1 W
Reading pulse (width/power)	4 ns / ~1 W
Probe power (per sideband)	~700 mW
$f_{\text{RF}}$ (start/interval/# steps)	10.3 GHz / 8 MHz / 180
$f_d$ (start/interval/# steps)	123.5 MHz / 100 kHz / 50
Averaging	4096

Table 4.4 – Parameters used to measure FSBS in a polyimide-coated single-mode fiber. Optical powers are measured at the FUT input.

prevent the appearance of distortions at the fiber remote end as explicated in section 4.4.7. In addition, FSBS efficiency is slightly lower in polyimide coated fibers than in bare fibers, hence the data was post-processed with a numerical Gaussian filter exhibiting a bandwidth of 50 MHz, yielding a final spatial resolution (SR) of 2 m. The spatial resolution achieved is still outperforming previously reported results, i.e. 100 m of SR in a 1.5 km long polyimide coated fiber [7].

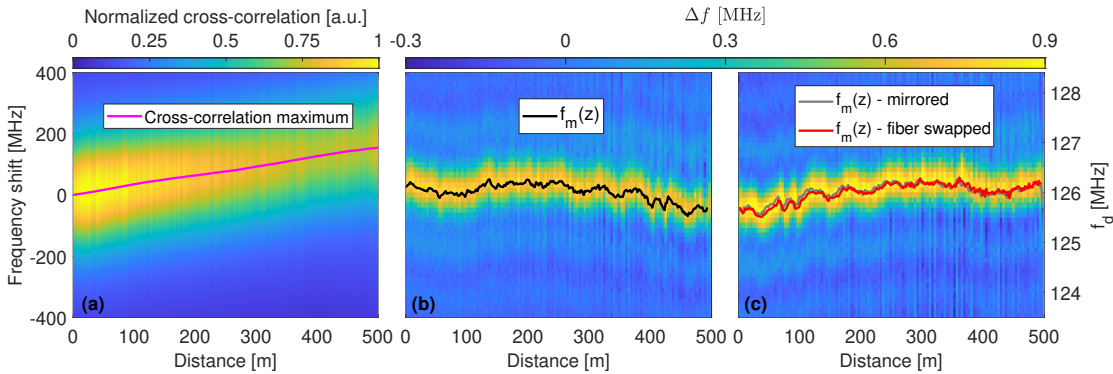


Figure 4.24 – (a) 2-D map of the cross-correlation performed between the Brillouin gain spectra of the fiber with activating pulse turned on and off ( $f_d = 126$  MHz). (b) 2-D map of the retrieved FSBS resonance along the 500 m polyimide coated fiber. (c) Same as in (b) but with swapped fiber ends.

Fig. 4.24.(a) shows the result of the cross-correlation operation, which is explicated in Fig. 4.17, when  $f_d = 126$  MHz and is to be compared to the case of the bare fiber shown in Fig. 4.20.(c). The whole fiber being strongly responsive to FSBS activation, the pulse carrier frequency experiences a continuous frequency shift as it propagates in the fiber, reaching ~160 MHz over ~500 m. Note that this validates that FSBS can be probed over the entire fiber, especially at the fiber beginning, which was not achievable with the previous technique that relied on a broadband BOTDR (see section 4.3.4).

Fig.4.24.(b) reveals the 2-D map of the reconstructed resonance with a SR of 2 m. The black curve denotes the FSBS resonance frequency  $f_m$ , which exhibits variations of  $\sim 0.7\%$  that are attributed to variations in cladding and/or coating diameter. The profile is confirmed to originate from non-uniformities in the fiber rather than from experimental flaws by swapping the fiber ends and repeating the measure, which results are shown in Fig.4.24.(c). Once more, the initially measured profile but swapped (gray) perfectly matches the newly measured one (red), thus confirming our observations.

We now evaluate the results from the perspective of a potential sensing application. To do so, a segment of  $\sim 5$  m near the fiber remote end is immersed in ethanol. Fig.4.25.(a) and (b) show a magnified view of the fiber remote end when the sensing section is exposed to air or is immersed in ethanol, respectively. As anticipated, the signal undergoes a significant amplitude drop due to the broadening of the FSBS resonance as a consequence from enhanced acoustic damping. While not clearly visible from that particular figure, the signal in ethanol remains above the noise floor (see Fig.4.25.(d)), which is once more evaluated based on repeated measurements. The experimental uncertainty on the retrieved frequency shift  $\sigma_{\Delta f}$  is shown in Fig.4.25.(c) to be lower than 0.04 MHz over the entire fiber. The resonances observed within the probing section are shown in Fig.4.25.(d). From numerical simulations (solid line), the equivalent acoustic damping rate in air is found to be equal to  $\Gamma_e = 2\pi \times 240$  kHz. This value is significantly larger than for the case of the bare fiber ( $2\pi \times 80$  kHz), but this outcome is not surprising because 1) the glass-polyimide interface is the source of acoustic loss, and 2) the spatial resolution is larger (2 m compared to 80 cm), hence the variations in the acoustic mode resonant frequency are expected to contribute to a larger extent to the observed resonance broadening.

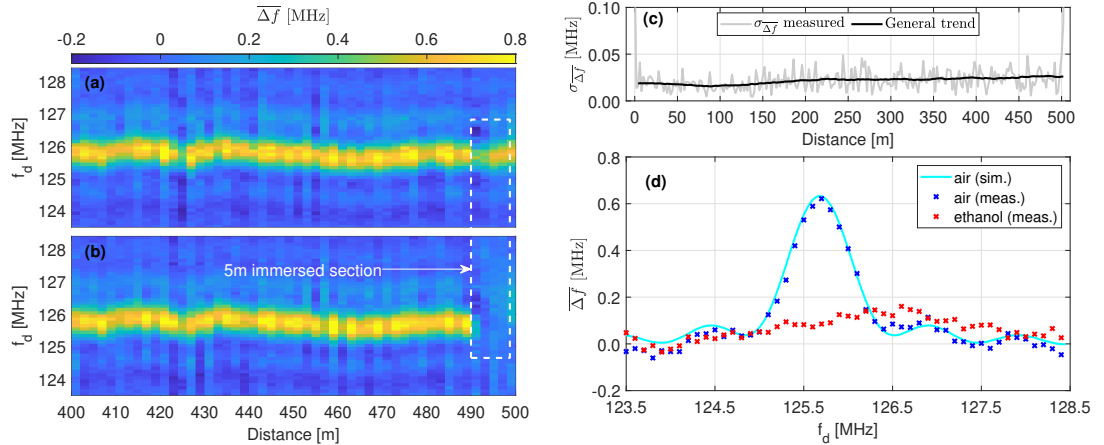


Figure 4.25 – 2-D map of the retrieved FSBS resonance over the last 50 m of sensing fiber when the last  $\sim 5$  m are exposed to air (a) or immersed in ethanol (b). (c) experimental uncertainty with a spatial resolution of 2 m. (d) Retrieved FSBS resonance within the 5 m probing section.

Unfortunately, it was not possible to assign a resonance characterized by a single acoustic

damping parameter to the measured response in ethanol. The reason lies in the sensitivity of the acoustic damping rate to both cladding and/or coating diameter [7, 91], which implies that the measured resonance results from a complicated mix of several individual spectra each exhibiting different central frequencies and damping rates. As will be discussed here after, this feature might severely compromise the accurate evaluation of the liquid damping rate, hence make difficult to distinguish precisely between several fluids with similar acoustic impedances. Nevertheless, the technique presented here is the first, to the best of our knowledge, to enable analysing this phenomenon (FSBS) with such sharp spatial resolution.

### 4.4.9 Discussion

In this section, we presented a novel concept to perform distributed FSBS sensing. The method is mostly interesting owing to the high spatial resolution reached in both types of FSBS sensing, that is 80 cm in bare fiber for remote distributed sensing and 2 m in polyimide coated fiber for fully distributed sensing. The precision of the measurement notably enabled quantifying the changes in the acoustic properties of the fibers under test over their length, that are most likely to originate from dimensional variations. While insightful, these results also raise questions regarding the achievable performances of this type of sensor. Here for instance, it was not possible to provide with a reliable evaluation of the acoustic damping rate of the liquid in which the polyimide coated fiber was immersed. This does not imply that such technique will find no practical application, nor that the accurate determination of liquid via FSBS sensing is not feasible. Yet, it appears that significant added work is required in order to draw definitive conclusions regarding the achievable performance of this emerging branch of distributed optical fiber sensors (DOFS).

To the author's opinion, the main challenge lies in the fiber design, which highly impacts on the sensor performances. With the well-thought aim of achieving proper impedance matching, the use of a thin layer of polyimide of coating might not be the most suitable option, due to the strong sensitivity of certain acoustic modes (both in terms of central frequency and damping rate) to any variation in the fiber (cladding and/or coating) dimension. The different parameters that influence the acoustic behavior of the fiber all intervene in a complex trade-off that includes FSBS efficiency, robustness to dimensional variations as well as sensitivity to the environment acoustic impedance. Moreover, the dedicated interrogating technique is also to be accounted for as an additional variable in this already heavy equation. Here for instance, the use of BOTDA offered several advantages (high SNR, accurate frequency shift evaluation, well-suited sensitivity), while constraining to activate lesser efficient FSBS modes due to limitations inherent to the technique itself (phonon lifetime). To summarize, distributed FSBS sensing is very likely far to have displayed its full potential, and it is the author's hope that the aforementioned study stems plentiful of creative solutions to tackle the many issues yet hindering the potential of this technology.

## 5 Conclusions and Perspectives

Without falling into the pitfall of repeating all presented facts and experimental measurements, it appears quite natural at this stage to recapitulate the major advancements presented in this dissertation in order to draw the logical conclusions of this work and, hopefully, prompt further fruitful and innovative research. This delicate exercise requires to provide with an objective appreciation of one's own work, thus avoiding exaggerating its impact while rightfully acknowledging the advances it brings to the scientific community. In doing so, one should try not only to enumerate the benefits, but also the possible drawbacks and limitations associated to a given technique. In order to preserve a coherent structure with respect to the core material of this thesis, the aforementioned outline is split in two sections, one dealing with the matter of digital signal processing (DSP) while the other treats of forward stimulated Brillouin scattering (FSBS).

### **Digital signal processing**

Digital signal processing (DSP) is omnipresent in research, especially in all fields of physics and engineering that perform measurements by means of various sensing devices. Due to the accessibility to a significant amount of computational power in modern days, algorithms developed within the theory of DSP are routinely implemented and used by researchers and scientists all around the world. To the author's opinion, this crucial step is too often overlooked, as the intricate implications of post-processing any given data are not always known to a sufficient extent. This is perfectly understandable in a field of research such as distributed optical fiber sensing (DOFS), because this cutting-edge technology is already highly demanding in terms of knowledge and understanding of the core complex physical mechanisms it relies on. Nevertheless, DOFS can highly benefit from a better understanding of the theories associated to DSP, as demonstrated multiple times in this dissertation. Here, we restricted the analysis to DOFS that behave as linear time-invariant (LTI) systems, focusing our attention on Brillouin optical time-domain analysis (BOTDA). Although this framework of research might seem narrow, it enabled delivering three complete works, all relying on the concepts of convolution and deconvolution.

First, this thesis established the theoretical limit of the experimental uncertainty reduction brought by any 2-D algorithm on a given BOTDA measurement. The conclusion is that digital filtering brings no additional improvement, provided that the system is fully optimized. While this statement may appear to be disappointing, it came along with substantial knowledge that finally enables to understand *why* it must be so. Additionally, this dissertation provides with various guidelines on how to achieve such optimized state. For instance, and despite the absence of a *net* benefit in terms of performance improvement, digital filtering algorithms might still be used to optimize a given system, e.g. to compensate for a photodetector with a built-in bandwidth that exceeds the targeted spatial resolution of the considered sensor. Far from conveying the message that DSP algorithms are of no use to process the data of BOTDA systems, these techniques yield a high flexibility to the end user, provided that the latter is aware of the fundamental restrictions mentioned here above.

The concept of deconvolution was then used to demonstrate two remarkable applications. First, one shown how to access to the sharp-resolution information hidden in a coarse-resolution BOTDA measurement by making use of simple DSP algorithms based on a well-suited theoretical model. The main advantage of such method is its flexibility, i.e. it makes information at any spatial resolution available, provided that one can afford the unavoidable associated loss in experimental uncertainty. Moreover, and especially for targeted spatial resolutions lower than one meter, the precision reached this way is substantially larger than the one that would be obtained by a direct measurement, hence highlighting the potential of our technique. Nevertheless, the presented algorithm does not operate flawlessly, and yields unwanted distortions at locations where the fiber Brillouin frequency shift experiences rapid changes. While the presence of numerical artifacts in the reconstructed data might be problematic in certain situations, these moderate distortions are very likely to be of negligible importance in most practical cases. In future works, limitations met by conventional BOTDA such as e.g. non-local effects and their impact on the measurement ought to be studied as well for this type of approach.

Finally, the same model enabled to deliver an original implementation of optical pulse coding (OPC). While far from being a novel concept, OPC has been facing many practical implementation issues that, until now, greatly hindered its potential to effectively deliver a substantial performance improvement to various DOFS. Thanks to relying on a simpler and more robust mathematical procedure than other implementations of OPC, the proposed technique circumvents all previously met technical challenges. While achieving similar results in terms of *theoretical* signal-to-ratio enhancement compared to other existing techniques, the developed method secures to meet this theoretical bound without adding to the setup complexity. In other words, the main benefit of the proposed technique lies in its practicality, as it can be readily implemented in most existing setups and immediately improve their capabilities, whereas other techniques are far more cumbersome to implement in any real-life application. As always, one should keep in mind that the proposed method, as well as any form of OPC, suffer from inherent limitations in terms of performance improvement, that one must fully grasp when considering to implement such a system.

---

Overall, the presented work shows the fantastic potential of DSP as a decisive actor in future developments of DOFS. Here, we barely scrapped the surface of this vast field of research, restricting our analysis to systems that behave as linear and time-invariant. The theory of DSP covers yet many exciting topics that might open doors to a whole new world of applications. More specifically, one can point out the many techniques and interrogating schemes that do not behave as linear time-invariant systems, and for which other methodologies ought to be dedicated.

### **Forward stimulated Brillouin scattering**

Forward stimulated Brillouin scattering (FSBS) emerged recently as a promising candidate to diversify the quantities measurable by DOFS. While backward stimulated Brillouin scattering and its associated features have been studied from the perspective of developing sensing applications for many decades, only a few years separate us from the first mention of using FSBS to intentionally measure the acoustic impedance of liquids (*Antman et al.* , 2016 [6]). Naturally, one could not expect for this emerging concept to catch up with more mature DOFS techniques in such short time window, although there has been an abundance of promising publications in recent years (most of which originate from the same group from Bar-Ilan university in Tel-Aviv) that enabled to explain and grasp many intricate concepts inherent to FSBS. Logically, the performances of dedicated developed interrogation procedures remain still unsatisfactory, both in terms of spatial resolution as well as sensing range, which contribute only to a modest number of resolved sensing points.

In this thesis, we took a major step in improving the performances of distributed FSBS sensors. So far, all reported techniques relied on measuring the energy exchange of a multi-tone probe, which exhibits the major limitation of suffering from power fluctuations induced by unwanted non-linear effects, such as four-wave mixing. Moreover, some methods present other flaws, such as a position-dependent SNR as presented in section 4.3. Most issues found in various distributed FSBS sensing schemes were tackled by judiciously impinging a frequency shift on a so called reading pulse from the refractive index modulation induced by FSBS, identical in essence to a serrodyne modulation process. Owing to a better understanding of the harmonic response of FSBS, and especially of the frequency dependent phase-lag contributing to the mechanism, a comprehensive model was assembled, enabling to compare experimental data with semi-analytical solutions based on numerical simulations. Overall, the performances of the proposed technique are excellent, as the spatial resolution reached is far sharper than previously documented. Still, there is a large margin for improvement, both on solving issues related to the dedicated interrogation technique as well as from addressing technical challenges inherent to FSBS itself.

Beginning with the latter, FSBS indeed presents certain characteristics that challenge its accurate evaluation. The most striking one is the dependency of the involved acoustic modes to variations in the dimensions of the corresponding waveguide, namely a bare fiber or a

coated fiber. It turns out that this feature severely complicates the accurate evaluation of the acoustic impedance of the fluid surrounding the fiber in polyimide coated fibers. While this has not been overcome here, it is very likely that the solution lies in a more thoughtful design of the sensing fiber, which so far was driven by the sole need to find a coating material displaying suitable acoustic properties. This alone constitutes an interesting research topic, as the design needs to account for several influences, including possibly the interrogating method to be employed with the aforementioned fiber. Additionally, the accumulative nature of FSBS constrains researchers so far to proceed to a numerical differentiation operation in their data processing routine in order to retrieve the local FSBS response, which unavoidably yields noise enhancement. It is not clear at this stage whether this operation is bound to remain as a consequence from the forward nature of the scattering process, or if a clever technique might be able to circumvent this irritating limiting factor. This is of course worth investigating.

Finally, let us try to enumerate the limitations associated to the method itself. Here, one refers to the serrodyne modulation scheme described in section 4.4. The results reported here indicate that there is a limit to the accumulated phase-modulation process induced by FSBS. More specifically, the total modulation depth might induce spectral distortions on the pulse that complicate the estimation of the underwent frequency shift, hence imposing a limit on the activation of FSBS. This ought to be further analyzed in details, in order to be able to anticipate the optimized activating pulse power to be launched in a given fiber under well defined experimental conditions. Furthermore, while the reading process has been made to a large extent immune to unwanted power fluctuations, the activating pulse (which is decoupled from the reading process) is still sensitive to any unwanted power fluctuation, which would eventually bias the estimation of the frequency shift experienced by the reading pulse. Eventually, and while a conventional BOTDA was used as a position resolved frequency measuring tool, there is no guarantee that this particular technique is the most suited to achieve this task, and other methods based e.g. on reflectometry might perform similarly or even better. With the hope of sparking the creativity of many researchers, the author firmly believes that the setup presented here, although currently outperforming the state-of-the-art, is bound to meet a similar fate in a near future.

# A Solution of the acoustic wave equation in cylindrical coordinates

This appendix is intended to provide the steps necessary to obtain the distribution of acoustic modes in a cylindric rod such as an optical fiber. An emphasis is put on so-called purely radial modes (which are actually longitudinal modes), i.e. one of the two branches of modes which displacement distribution do not vary with the azimuthal coordinate  $\theta$  (the other branch is the family of purely torsional modes).

## A.1 Useful relationships

Before stepping into the resolution of the wave equation in cylindrical coordinates, several useful identities of vector calculus are first provided.

### A.1.1 Problem Geometry

The problem is better tackled in cylindrical coordinates, as pictured in Fig.A.1. The radial extent from the origin is denoted  $r$  while the angle from the x-axis is denoted  $\theta$ . The use of cylindrical coordinates has many computational implications, especially with respect to operations implying the del operator  $\nabla$ . Useful relationships used throughout this document are summarized in the following section.

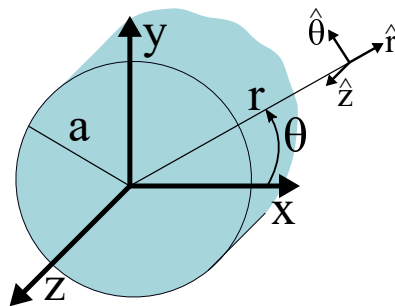


Figure A.1 – Problem geometry in cylindrical coordinates  $(r, \theta, z)$ .



### A.1.2 Nabla operations in cylindrical coordinates

Let  $f$  denote a scalar field, while  $A_r$ ,  $A_\theta$  and  $A_z$  denote the components of a vector field  $\mathbf{A}$ .

$$\text{Gradient: } \nabla f = \frac{\partial f}{\partial r} \hat{\mathbf{r}} + \frac{1}{r} \frac{\partial f}{\partial \theta} \hat{\boldsymbol{\theta}} + \frac{\partial f}{\partial z} \hat{\mathbf{z}} \quad (\text{A.1})$$

$$\text{Divergence: } \nabla \cdot \mathbf{A} = \frac{1}{r} \frac{\partial(r A_r)}{\partial r} + \frac{1}{r} \frac{\partial A_\theta}{\partial \theta} + \frac{\partial A_z}{\partial z} \quad (\text{A.2})$$

$$\text{Curl: } \nabla \times \mathbf{A} = \left( \frac{1}{r} \frac{\partial A_z}{\partial \theta} - \frac{\partial A_\theta}{\partial z} \right) \hat{\mathbf{r}} + \left( \frac{\partial A_r}{\partial z} - \frac{\partial A_z}{\partial r} \right) \hat{\boldsymbol{\theta}} + \frac{1}{r} \left( \frac{\partial(r A_\theta)}{\partial r} - \frac{\partial A_r}{\partial \theta} \right) \hat{\mathbf{z}} \quad (\text{A.3})$$

$$\text{Laplacian: } \Delta f = \frac{1}{r} \frac{\partial}{\partial r} \left( r \frac{\partial f}{\partial r} \right) + \frac{1}{r^2} \frac{\partial^2 f}{\partial \theta^2} + \frac{\partial^2 f}{\partial z^2} \quad (\text{A.4})$$

$$\text{Vector Laplacian: } \Delta \mathbf{A} = \left( \Delta A_r - \frac{A_r}{r^2} - \frac{2}{r^2} \frac{\partial A_\theta}{\partial \theta} \right) \hat{\mathbf{r}} + \left( \Delta A_\theta - \frac{A_\theta}{r^2} + \frac{2}{r^2} \frac{\partial A_r}{\partial \theta} \right) \hat{\boldsymbol{\theta}} + \Delta A_z \hat{\mathbf{z}} \quad (\text{A.5})$$

### A.1.3 Useful vector calculus identities

The following well-known relationships from vector calculus are required to simplify further calculations.

$$\text{Divergence of gradient: } \nabla \cdot \nabla f = \Delta f \quad (\text{A.6})$$

$$\text{Curl of gradient: } \nabla \times \nabla f = \mathbf{0} \quad (\text{A.7})$$

$$\text{Divergence of curl: } \nabla \cdot (\nabla \times \mathbf{A}) = \mathbf{0} \quad (\text{A.8})$$

$$\text{Curl of curl: } \nabla \times (\nabla \times \mathbf{A}) = \nabla (\nabla \cdot \mathbf{A}) - \Delta \mathbf{A} \quad (\text{A.9})$$

$$\text{Laplacian of gradient: } \Delta (\nabla f) = \nabla (\Delta f) \quad (\text{A.10})$$

$$\text{Vector laplacian of curl: } \Delta (\nabla \times \mathbf{A}) = \nabla \times (\Delta \mathbf{A}) \quad (\text{A.11})$$

### A.1.4 Bessel functions properties

The following expressions are given for Bessel functions of the first kind  $J$  although they remain valid for Bessel functions of the second kind  $Y$ .

$$\frac{2n}{\alpha r} J_n(\alpha r) = J_{n-1}(\alpha r) + J_{n+1}(\alpha r) \quad (\text{A.12})$$

$$\frac{2}{\alpha} \frac{dJ_n(\alpha r)}{dr} = J_{n-1}(\alpha r) - J_{n+1}(\alpha r) \quad (\text{A.13})$$

Combining (A.12) and (A.13), the following useful identities may be derived

$$\frac{dJ_n(\alpha r)}{dr} = \frac{n}{r} J_n(\alpha r) - \alpha J_{n+1}(\alpha r) \quad (\text{A.14})$$

$$\frac{dJ_{n+1}(\alpha r)}{dr} = \alpha J_n(\alpha r) - \frac{n+1}{r} J_{n+1}(\alpha r) \quad (\text{A.15})$$

### A.1.5 Strain-displacement relations

Strain-displacement relations are fundamental in the theory of linear elasticity. Let  $U_r$ ,  $U_\theta$  and  $U_z$  denote the components of a vector  $\mathbf{U}$  in cylindrical coordinates. The components of the strain tensor  $\epsilon_{ij}$  are given by

$$\epsilon_{rr} = \frac{\partial U_r}{\partial r} \quad (A.16) \quad \epsilon_{r\theta} = \frac{1}{2} \left[ r \frac{\partial}{\partial r} \left( \frac{U_\theta}{r} \right) + \frac{1}{r} \frac{\partial U_r}{\partial \theta} \right] \quad (A.19)$$

$$\epsilon_{\theta\theta} = \frac{1}{r} \left( \frac{\partial U_\theta}{\partial \theta} + U_r \right) \quad (A.17) \quad \epsilon_{\theta z} = \frac{1}{2} \left[ \frac{\partial U_\theta}{\partial z} + \frac{1}{r} \frac{\partial U_z}{\partial \theta} \right] \quad (A.20)$$

$$\epsilon_{zz} = \frac{\partial U_z}{\partial z} \quad (A.18) \quad \epsilon_{rz} = \frac{1}{2} \left[ \frac{\partial U_r}{\partial z} + \frac{\partial U_z}{\partial r} \right] \quad (A.21)$$

### A.1.6 Stress-strain relations

Similarly to the strain-displacement relation, stress-strain relations are fundamental relationships. They are of particular interest here as the boundary conditions are imposed based on stress. Consider the first and second Lamé parameters  $\lambda$  and  $\mu$ , respectively. The components of the stress tensor  $\sigma_{ij}$  are given by

$$\sigma_{rr} = \lambda \Delta \psi + 2\mu \epsilon_{rr} \quad (A.22) \quad \sigma_{r\theta} = 2\mu \epsilon_{r\theta} \quad (A.25)$$

$$\sigma_{\theta\theta} = \lambda \Delta \psi + 2\mu \epsilon_{\theta\theta} \quad (A.23) \quad \sigma_{\theta z} = 2\mu \epsilon_{\theta z} \quad (A.26)$$

$$\sigma_{zz} = \lambda \Delta \psi + 2\mu \epsilon_{zz} \quad (A.24) \quad \sigma_{rz} = 2\mu \epsilon_{rz} \quad (A.27)$$

where

$$\Delta \psi = \epsilon_{rr} + \epsilon_{\theta\theta} + \epsilon_{zz} \quad (A.28)$$

### A.1.7 Boundary conditions

The following boundary conditions are valid for a free-cylinder. Other types of boundary conditions may have to be specified in different situations, such as e.g. when considering a clad cylinder. Based on Fig. 4.1, the boundary conditions read

$$\sigma_{rr}|_{r=a} = 0 \quad (A.29)$$

$$\sigma_{r\theta}|_{r=a} = 0 \quad (A.30)$$

$$\sigma_{rz}|_{r=a} = 0 \quad (A.31)$$

## A.2 The acoustic wave equation in cylindrical coordinates

We now turn to the solving of the acoustic wave equation in cylindrical coordinates. The steps provided here follow the procedure given in chapter 4 but with significant added details.

### A.2.1 Homogeneous equation

The acoustic wave equation is given by [67, 68, 69]

$$\mu \Delta \mathbf{U} + (\lambda + \mu) \nabla (\nabla \cdot \mathbf{U}) - \rho \frac{\partial^2 \mathbf{U}}{\partial t^2} = \mathbf{0} \quad (\text{A.32})$$

where  $\mathbf{U}$  is the vector displacement field,  $\lambda$  and  $\mu$  are Lamé first and second parameters, respectively, and  $\rho$  is the material density.

### A.2.2 The potentials methods

Before solving (A.32), two potentials are introduced such that

$$\mathbf{U} = \nabla \psi + \nabla \times \Psi \quad (\text{A.33})$$

where  $\psi$  is a dilatational potential (scalar) and  $\Psi$  is an equivoluminal potential (vectorial). In addition, one requires that

$$\nabla \cdot \Psi = F(r, \theta, z, t) \quad (\text{A.34})$$

where  $F(r, \theta, z, t)$  denotes an *arbitrary* function. Although (A.34) is not required to solve (A.32), its introduction will greatly simplify further calculations. Injecting (A.33) into (A.32) yields

$$\begin{aligned} \mu \Delta (\nabla \psi + \nabla \times \Psi) + (\lambda + \mu) \nabla (\nabla \cdot (\nabla \psi + \nabla \times \Psi)) &= \rho \frac{\partial^2 \mathbf{U}}{\partial t^2} \\ \mu \Delta (\nabla \psi) + \mu \Delta (\nabla \times \Psi) + (\lambda + \mu) \nabla (\nabla \cdot (\nabla \psi) + \underbrace{\nabla \cdot (\nabla \times \Psi)}_{=0 \text{ see (A.8)}}) &= \rho \frac{\partial^2 \mathbf{U}}{\partial t^2} \\ \underbrace{\mu \nabla (\Delta \psi)}_{\text{see (A.10)}} + \underbrace{\mu \nabla \times (\Delta \Psi)}_{\text{see (A.11)}} + (\lambda + \mu) \nabla (\Delta \psi) &= \rho \frac{\partial^2 \mathbf{U}}{\partial t^2} \\ \nabla [(\lambda + 2\mu) \Delta \psi] + \mu \nabla \times [\Delta \Psi] \stackrel{(\text{A.33})}{=} \nabla \rho \frac{\partial^2 \psi}{\partial t^2} + \nabla \times \rho \frac{\partial^2 \Psi}{\partial t^2} & \quad (\text{A.35}) \end{aligned}$$

which enables decoupling the contributions from the two potentials  $\psi$  and  $\Psi$  which must satisfy independently

$$V_d^2 \Delta \psi = \frac{\partial^2 \psi}{\partial t^2} \quad (\text{A.36})$$

$$V_s^2 \Delta \Psi = \frac{\partial^2 \Psi}{\partial t^2} \quad (\text{A.37})$$

where  $V_d$  and  $V_s$  are the dilatational waves velocity and the shear waves velocity, respectively, and are defined as

$$V_d = \sqrt{\frac{\lambda + 2\mu}{\rho}} \quad (\text{A.38})$$

$$V_s = \sqrt{\frac{\mu}{\rho}} \quad (\text{A.39})$$

The use of potential enables decoupling the contribution from shear and dilatational waves, such that one must solve (A.36) and (A.37) rather than (A.32).

### A.2.3 The gauge invariance principle

Before proceeding further, one must first take a step back and have another look at equation (A.34), which states that the divergence of the equivoluminal potential  $\Psi$  is equal to a given *arbitrary* scalar function  $F$ . This is true because  $F$  has no influence on the solution of equation (A.32), hence (A.32) is said to be invariant under (A.34), which is also known as the Gauge invariance principle. This can be better understood by looking back at the second step taken into obtaining (A.35), where the following term

$$\nabla(\nabla \cdot (\nabla \times \Psi)) = \mathbf{0} \quad (\text{A.40})$$

is always equal to  $\mathbf{0}$  due to (A.8). However, (A.40) might be rewritten as

$$\begin{aligned} \nabla(\nabla \cdot (\nabla \times \Psi)) &= \\ \Delta(\nabla \times \Psi) + \nabla \times (\nabla \times (\nabla \times \Psi)) &= \\ \nabla \times (\Delta \Psi + \nabla \times (\nabla \times \Psi)) &= \\ \nabla \times (\nabla(\nabla \cdot \Psi)) = \nabla \times (\nabla F) &= \mathbf{0} \end{aligned} \quad (\text{A.41})$$

which holds true for any  $F$  since (A.41) is a fundamental vector calculus identity (A.7). One must therefore keep in mind that any choice we make for  $F$  will result in an identical solution for (A.32).

### A.2.4 Separation of variables

The potentials are assumed to take the form

$$\psi = f(r) \cos(n\theta) \cos(\gamma z - \omega t) \quad (\text{A.42})$$

$$\Psi_r = g_r(r) \sin(n\theta) \sin(\gamma z - \omega t) \quad (\text{A.43})$$

$$\Psi_\theta = g_\theta(r) \cos(n\theta) \sin(\gamma z - \omega t) \quad (\text{A.44})$$

$$\Psi_z = g_z(r) \sin(n\theta) \cos(\gamma z - \omega t) \quad (\text{A.45})$$

where  $\Psi_r$ ,  $\Psi_\theta$  and  $\Psi_z$  are the components of  $\Psi$ ,  $n$  is a positive integer,  $\gamma$  is the propagation constant and  $\omega$  is the angular frequency. First, let us inject (A.42) into (A.36). Using (A.4) one

## Appendix A. Solution of the acoustic wave equation in cylindrical coordinates

---

get

$$V_d^2 \left[ \frac{1}{r} \frac{\partial}{\partial r} \left( r \frac{\partial \psi}{\partial r} \right) + \frac{1}{r^2} \frac{\partial^2 \psi}{\partial \theta^2} + \frac{\partial^2 \psi}{\partial z^2} \right] = \frac{\partial^2 \psi}{\partial t^2}$$

$$\frac{\partial^2 f}{\partial r^2} + \frac{1}{r} \frac{\partial f}{\partial r} + f \left( \alpha^2 - \frac{n^2}{r^2} \right) = 0 \quad (\text{A.46})$$

where

$$\alpha^2 = \frac{w^2}{V_d^2} - \gamma^2 \quad (\text{A.47})$$

Therefore, and provided that  $f(r)$  has to exist at  $r = 0$ ,  $f(r)$  has to take the form

$$f(r) = A J_n(\alpha r) \quad (\text{A.48})$$

where  $A$  is an integration constant and  $J_n$  denote Bessel functions of the first kind. From (A.37) and (A.5) it can be deduced that  $g_z$  obeys to the same equation as  $f$  such that

$$g_z(r) = B_3 J_n(\beta r) \quad (\text{A.49})$$

where  $B_3$  is an integration constant and  $\beta$  is defined as

$$\beta^2 = \frac{w^2}{V_s^2} - \gamma^2 \quad (\text{A.50})$$

The situation is slightly more complex for  $\Psi_r$  and  $\Psi_\theta$ , which must be taken care off simultaneously. First, let us focus on  $\Psi_r$  by working along the  $\hat{\mathbf{r}}$  coordinate in equation (A.37) using (A.5) and following a similar procedure as to establish (A.46)

$$V_s^2 \left[ \frac{1}{r} \frac{\partial}{\partial r} \left( r \frac{\partial \Psi_r}{\partial r} \right) + \frac{1}{r^2} \frac{\partial^2 \Psi_r}{\partial \theta^2} + \frac{\partial^2 \Psi_r}{\partial z^2} - \frac{\Psi_r}{r^2} - \frac{2}{r^2} \frac{\partial \Psi_\theta}{\partial \theta} \right] = \frac{\partial^2 \Psi_r}{\partial t^2}$$

$$V_s^2 \left[ \frac{1}{r} \frac{\partial g_r}{\partial r} + \frac{\partial^2 g_r}{\partial r^2} + \frac{2n}{r^2} g_\theta - \left( \frac{1+n^2}{r^2} + \gamma^2 \right) g_r \right] = -g_r \omega^2$$

$$\frac{\partial^2 g_r}{\partial r^2} + \frac{1}{r} \frac{\partial g_r}{\partial r} + \frac{2n}{r^2} g_\theta + g_r \left( \beta^2 - \frac{1+n^2}{r^2} \right) = 0 \quad (\text{A.51})$$

A very similar development for  $\Psi_\theta$  leads to

$$\frac{\partial^2 g_\theta}{\partial r^2} + \frac{1}{r} \frac{\partial g_\theta}{\partial r} + \frac{2n}{r^2} g_r + g_\theta \left( \beta^2 - \frac{1+n^2}{r^2} \right) = 0 \quad (\text{A.52})$$

Both (A.51) and (A.52) look closely to the well known Bessel equation, except they both present a coupled term proportional to  $g_\theta$  ( $g_r$ ) in the equation of  $g_r$  ( $g_\theta$ ). This can be addressed by

subtracting (A.52) from (A.51), yielding

$$(g_r - g_\theta) \left[ \frac{\partial^2}{\partial r^2} + \frac{1}{r} \frac{\partial}{\partial r} + \beta^2 - \frac{(n+1)^2}{r^2} \right] = 0 \quad (\text{A.53})$$

Similarly, adding (A.51) and (A.52) leads to

$$(g_r + g_\theta) \left[ \frac{\partial^2}{\partial r^2} + \frac{1}{r} \frac{\partial}{\partial r} + \beta^2 - \frac{(n-1)^2}{r^2} \right] = 0 \quad (\text{A.54})$$

Hence, we find the following

$$g_r - g_\theta = 2B_1 J_{n+1}(\beta r) \quad (\text{A.55})$$

$$g_r + g_\theta = 2B_2 J_{n-1}(\beta r) \quad (\text{A.56})$$

where a factor 2 has been left out of the integration constants for later convenience. The gauge invariance principle described in section A.2.3 is now used to simplify the system of equations defined by (A.55) and (A.56). An intuitive justification is that, since ultimately we are searching for a solution of the wave equation (A.32), we should find a vectorial field with three components, hence three integrations constants must be sufficient to determine the solution, whereas the potentials provide four constants. Mathematically, expression (A.34) states that  $F(r, \theta, z, t)$  can be take any form, as it will not impact the solution. Therefore, we define it such that

$$g_r = -g_\theta \quad (\text{A.57})$$

which leads to  $B_2 = 0$  and

$$g_r = B_1 J_{n+1}(\beta r) \quad (\text{A.58})$$

### A.2.5 Displacement, stress and strain

We can now express  $\mathbf{U}$  explicitly using (A.33) as well as the identities (A.1) and (A.3)

$$U_r = \frac{\partial \psi}{\partial r} + \frac{1}{r} \frac{\partial \Psi_z}{\partial \theta} - \frac{\partial \Psi_\theta}{\partial z} = \left[ \frac{\partial f}{\partial r} + \frac{n}{r} g_z + \gamma g_r \right] \cos(n\theta) \cos(\gamma z - \omega t) \quad (\text{A.59})$$

$$U_\theta = \frac{1}{r} \frac{\partial \psi}{\partial \theta} + \frac{\partial \Psi_r}{\partial z} - \frac{\partial \Psi_z}{\partial r} = \left[ -\frac{\partial g_z}{\partial r} - \frac{n}{r} f + \gamma g_r \right] \sin(n\theta) \cos(\gamma z - \omega t) \quad (\text{A.60})$$

$$U_z = \frac{\partial \psi}{\partial z} + \frac{1}{r} \left[ \frac{\partial(r\Psi_\theta)}{\partial r} - \frac{\partial \Psi_r}{\partial \theta} \right] = \left[ -\frac{n+1}{r} g_r - \frac{\partial g_r}{\partial r} - \gamma f \right] \cos(n\theta) \sin(\gamma z - \omega t) \quad (\text{A.61})$$

Before proceeding further, here below are provided some interesting identities of the radial functions of the components of  $\mathbf{U}$ , which naturally follow from equations (A.48), (A.49) and (A.58). In addition, we will denote partial derivative with respect to the radial coordinate  $r$  with a prime, e.g.  $\frac{\partial f}{\partial r} = f'$ . This enables clarifying further computations, as other partial derivatives

## Appendix A. Solution of the acoustic wave equation in cylindrical coordinates

do not show up anymore.

$$f' = \frac{n}{r}f - \alpha A J_{n+1}(\alpha r) \quad (\text{A.62})$$

$$f'' = \left[ \frac{n(n-1)}{r^2} - \alpha^2 \right] f + A \frac{\alpha}{r} J_{n+1}(\alpha r) = \left[ \frac{n^2}{r^2} - \alpha^2 \right] f - \frac{1}{r} f' \quad (\text{A.63})$$

$$g'_z = \frac{n}{r}g_z - \beta B_3 J_{n+1}(\beta r) \quad (\text{A.64})$$

$$g''_z = \left[ \frac{n(n-1)}{r^2} - \beta^2 \right] g_z + B_3 \frac{\beta}{r} J_{n+1}(\beta r) = \left[ \frac{n^2}{r^2} - \beta^2 \right] g_z - \frac{1}{r} g'_z \quad (\text{A.65})$$

$$g'_r = -\frac{n+1}{r}g_r + B_1 \beta J_n(\beta r) \quad (\text{A.66})$$

$$g''_r = \left[ \frac{(n+1)(n+2)}{r^2} - \beta^2 \right] g_r - B_1 \frac{\beta}{r} J_n(\beta r) = \left[ \frac{(n+1)^2}{r^2} - \beta^2 \right] g_r - \frac{1}{r} g'_r \quad (\text{A.67})$$

We apply now the strain-displacement relation (A.16) to compute  $\epsilon_{rr}$ .

$$\begin{aligned} \epsilon_{rr} &= \left[ f'' + \frac{n}{r} \left( g'_z - \frac{g_z}{r} \right) + \gamma g'_r \right] \cos(n\theta) \cos(\gamma z - \omega t) \\ \epsilon_{rr} &= \left[ \left( \frac{n^2}{r^2} - \alpha^2 \right) f - \frac{1}{r} f' + \frac{n}{r} \left( g'_z - \frac{g_z}{r} \right) + \gamma g'_r \right] \cos(n\theta) \cos(\gamma z - \omega t) \end{aligned} \quad (\text{A.68})$$

We then use (A.21) to compute  $\epsilon_{r\theta}$

$$\begin{aligned} \epsilon_{r\theta} &= \frac{1}{2} \left[ \frac{2n}{r} \left( \frac{f}{r} - f' \right) - g''_z + \gamma \left( g'_r - \frac{n+1}{r} g_r \right) - \frac{n^2}{r^2} g_z + \frac{1}{r} g'_z \right] \sin(n\theta) \cos(\gamma z - \omega t) \\ \epsilon_{r\theta} &= \frac{1}{2} \left[ \frac{2n}{r} \left( \frac{f}{r} - f' \right) + g_z \left( \beta^2 - \frac{2n^2}{r^2} \right) + \frac{2}{r} g'_z + \gamma \left( g'_r - \frac{n+1}{r} g_r \right) \right] \sin(n\theta) \cos(\gamma z - \omega t) \end{aligned} \quad (\text{A.69})$$

Finally, we use (A.19) to obtain  $\epsilon_{rz}$

$$\begin{aligned} \epsilon_{rz} &= \frac{1}{2} \left[ -2\gamma f' - \frac{\gamma n}{r} g_z - g''_r - \frac{n+1}{r} g'_r + \left( \frac{n+1}{r^2} - \gamma^2 \right) g_r \right] \cos(n\theta) \sin(\gamma z - \omega t) \\ \epsilon_{rz} &= \frac{1}{2} \left[ -2\gamma f' - \frac{\gamma n}{r} g_z - \frac{n}{r} g'_r + \left( \beta^2 - \gamma^2 - \frac{n(n+1)}{r^2} \right) g_r \right] \cos(n\theta) \sin(\gamma z - \omega t) \end{aligned} \quad (\text{A.70})$$

The stress-strain relations (A.22), (A.25) and (A.27) yield

$$\sigma_{rr} = \left\{ -\lambda(\alpha^2 + \gamma^2)f + 2\mu \left[ \left( \frac{n^2}{r^2} - \alpha^2 \right) f - \frac{1}{r} f' + \frac{n}{r} \left( g'_z - \frac{g_z}{r} \right) + \gamma g'_r \right] \right\} \cos(n\theta) \cos(\gamma z - \omega t) \quad (\text{A.71})$$

$$\sigma_{r\theta} = \mu \left[ \frac{2n}{r} \left( \frac{f}{r} - f' \right) + g_z \left( \beta^2 - \frac{2n^2}{r^2} \right) + \frac{2}{r} g'_z + \gamma \left( g'_r - \frac{n+1}{r} g_r \right) \right] \sin(n\theta) \cos(\gamma z - \omega t) \quad (\text{A.72})$$

$$\sigma_{rz} = \mu \left[ -2\gamma f' - \frac{\gamma n}{r} g_z - \frac{n}{r} g'_r + \left( \beta^2 - \gamma^2 - \frac{n(n+1)}{r^2} \right) g_r \right] \cos(n\theta) \sin(\gamma z - \omega t) \quad (\text{A.73})$$

### A.2.6 Boundary conditions

We now apply the boundary conditions defined by (A.29), (A.30) and (A.31). In order to simplify later calculations, we left out the common terms, i.e. all terms which do not purely depend on the radial coordinate  $r$ . We inject (A.48), (A.49) and (A.58) into (A.22), (A.25) and (A.27), while setting  $r = a$  and group the terms according to the unknown integration constants  $A$ ,  $B_1$  and  $B_3$ . This is quite straightforward, except for  $\sigma_{rr}$  for which we preliminarily highlight the following relationship. We make use of expression (A.38) and (A.39) as well as (A.47) and (A.50) to perform the following operation

$$\begin{aligned}
 -\lambda(\alpha^2 + \gamma^2) - 2\mu\alpha^2 &= -\gamma \frac{\omega^2}{V_d^2} - 2\mu \left( \frac{\omega^2}{V_d^2} - \gamma^2 \right) \\
 -\lambda(\alpha^2 + \gamma^2) - 2\mu\alpha^2 &= -\frac{\omega^2}{V_d^2} (\lambda + 2\mu) + 2\mu\gamma^2 \\
 -\lambda(\alpha^2 + \gamma^2) - 2\mu\alpha^2 &= -\frac{\omega^2}{V_s^2} \mu + 2\mu\gamma^2 \\
 -\lambda(\alpha^2 + \gamma^2) - 2\mu\alpha^2 &= \mu(\gamma^2 - \beta^2)
 \end{aligned} \tag{A.74}$$

The boundary conditions read

$$\begin{aligned}
 \sigma_{rr}|_{r=a} &= A \left\{ \left[ \gamma^2 - \beta^2 + \frac{2n(n-1)}{a^2} \right] J_n(\alpha a) + \frac{2\alpha}{a} J_{n+1}(\alpha a) \right\} \\
 &\quad + B_1 2\gamma \left\{ \beta J_n(\beta a) - \frac{n+1}{a} J_{n+1}(\beta a) \right\} \\
 &\quad + B_3 \frac{2n}{a} \left\{ \frac{n-1}{a} J_n(\beta a) - \beta J_{n+1}(\beta a) \right\}
 \end{aligned} \tag{A.75}$$

$$\begin{aligned}
 \sigma_{r\theta}|_{r=a} &= A \frac{2n}{a} \left\{ \alpha J_{n+1}(\alpha a) - \frac{n-1}{a} J_n(\alpha a) \right\} \\
 &\quad + B_1 \gamma \left\{ \beta J_n(\beta a) - \frac{2(n+1)}{a} J_{n+1}(\beta a) \right\} \\
 &\quad + B_3 \left\{ \left[ \beta^2 - \frac{2n(n-1)}{a^2} \right] J_n(\beta a) - \frac{2\beta}{a} J_{n+1}(\beta a) \right\}
 \end{aligned} \tag{A.76}$$

$$\begin{aligned}
 \sigma_{rz}|_{r=a} &= A 2\gamma \left\{ \alpha J_{n+1}(\alpha a) - \frac{n}{a} J_n(\alpha a) \right\} \\
 &\quad + B_1 \left\{ [\beta^2 - \gamma^2] J_{n+1}(\beta a) - \frac{n\beta}{a} J_n(\beta a) \right\} \\
 &\quad + B_3 \left\{ -\frac{n\gamma}{a} J_n(\beta a) \right\}
 \end{aligned} \tag{A.77}$$



### A.2.7 The matrix form and the frequency equation

Equations (A.75), (A.76) and (A.77) are rewritten in the following form

$$CB = \begin{pmatrix} C_{11} & C_{12} & C_{13} \\ C_{21} & C_{22} & C_{23} \\ C_{31} & C_{32} & C_{33} \end{pmatrix} \begin{pmatrix} A \\ B_1 \\ B_3 \end{pmatrix} = \begin{pmatrix} 0 \\ 0 \\ 0 \end{pmatrix} \quad (\text{A.78})$$

where the coefficients, which are simply repeated from (A.75), (A.76) and (A.77) are

$$C_{11} = \left[ \gamma^2 - \beta^2 + \frac{2n(n-1)}{a^2} \right] J_n(\alpha a) + \frac{2\alpha}{a} J_{n+1}(\alpha a) \quad (\text{A.79})$$

$$C_{12} = 2\gamma \left\{ \beta J_n(\beta a) - \frac{n+1}{a} J_{n+1}(\beta a) \right\} \quad (\text{A.80})$$

$$C_{13} = \frac{2n}{a} \left\{ \frac{n-1}{a} J_n(\beta a) - \beta J_{n+1}(\beta a) \right\} \quad (\text{A.81})$$

$$C_{21} = \frac{2n}{a} \left\{ \alpha J_{n+1}(\alpha a) - \frac{n-1}{a} J_n(\alpha a) \right\} \quad (\text{A.82})$$

$$C_{22} = \gamma \left\{ \beta J_n(\beta a) - \frac{2(n+1)}{a} J_{n+1}(\beta a) \right\} \quad (\text{A.83})$$

$$C_{23} = \left[ \beta^2 - \frac{2n(n-1)}{a^2} \right] J_n(\beta a) - \frac{2\beta}{a} J_{n+1}(\beta a) \quad (\text{A.84})$$

$$C_{31} = 2\gamma \left\{ \alpha J_{n+1}(\alpha a) - \frac{n}{a} J_n(\alpha a) \right\} \quad (\text{A.85})$$

$$C_{32} = [\beta^2 - \gamma^2] J_{n+1}(\beta a) - \frac{n\beta}{a} J_n(\beta a) \quad (\text{A.86})$$

$$C_{33} = -\frac{n\gamma}{a} J_n(\beta a) \quad (\text{A.87})$$

Note that, unfortunately, most of the coefficients found in the references are incorrect. Identical responses are however found in [80]. The coefficients labelled here  $C_{i,j}$  correspond to coefficients  $a^2 C_{3+i,j}$  in [80], where  $i, j = 1, 2, 3$ . Using Cramer's rule, the unknown coefficients are found to be

$$A = \frac{|C_1|}{|C|} \quad (\text{A.88})$$

$$B_1 = \frac{|C_2|}{|C|} \quad (\text{A.89})$$

$$B_3 = \frac{|C_3|}{|C|} \quad (\text{A.90})$$

where the  $C_m$  with  $m = 1, 2, 3$  denote the  $C$  matrix (A.78) where the  $m^{\text{th}}$  column has been replaced by the right-hand side of equation (A.78), that is that column is equal to 0. In that case, it appears obvious that the only way to avoid the trivial solution  $A = B_1 = B_3 = 0$  is to impose the following condition, also known as the frequency equation

$$|C| = 0 \quad (\text{A.91})$$

Equation (A.91) is central in this study, as it imposes certain relationships between the coefficients  $C_{ij}$  of the matrix  $C$ . Depending on the fixed parameters  $\lambda$ ,  $\mu$  and  $\rho$  (which are imposed by the mechanical properties of the material considered) as well as the radius  $a$  of the cylinder, only certain combinations of the free parameters  $n$ ,  $\alpha$ ,  $\beta$ ,  $\gamma$  and  $\omega$  are possible. Of all free parameters,  $n$  plays a particular role and is used to specify distinct families of solutions called modes. For a given  $n$ , i.e. for a given mode family, solutions will be found when one of the Bessel functions in the  $C_{ij}$  coefficients reaches 0. Since Bessel functions are infinitely oscillating, there will be an infinite number of distinct solution for each value of  $n$ . Each solution is often denoted with an integer number  $m$ , which defines the mode order. A given mode specified by  $n, m$  then exhibit a certain dispersion relation which is determined by (A.47) and (A.50), together with (A.91) that relates the angular frequency  $\omega$  to the propagation constant  $\gamma$ .

### A.2.8 Longitudinal-radial modes

We now solely study solutions known as longitudinal-radial modes, which are one of the two families of modes found when  $n = 0$ . This type of modes is fundamental in the study of forward stimulated Brillouin scattering (FSBS), and will therefore be given a special treatment. Setting  $n = 0$  yields

$$C_{11} = [\gamma^2 - \beta^2] J_0(\alpha a) + \frac{2\alpha}{a} J_1(\alpha a) \quad (\text{A.92})$$

$$C_{12} = 2\gamma \left\{ \beta J_0(\beta a) - \frac{1}{a} J_1(\beta a) \right\} \quad (\text{A.93})$$

$$C_{13} = 0 \quad (\text{A.94})$$

$$C_{21} = 0 \quad (\text{A.95})$$

$$C_{22} = \gamma \left\{ \beta J_0(\beta a) - \frac{2}{a} J_1(\beta a) \right\} \quad (\text{A.96})$$

$$C_{23} = \beta^2 J_0(\beta a) - \frac{2\beta}{a} J_1(\beta a) \quad (\text{A.97})$$

$$C_{31} = 2\gamma\alpha J_1(\alpha a) \quad (\text{A.98})$$

$$C_{32} = [\beta^2 - \gamma^2] J_1(\beta a) \quad (\text{A.99})$$

$$C_{33} = 0 \quad (\text{A.100})$$

The matrix  $C$  hence takes the following form

$$\begin{pmatrix} C_{11} & C_{12} & 0 \\ 0 & C_{22} & C_{23} \\ C_{31} & C_{32} & 0 \end{pmatrix} \quad (\text{A.101})$$

## Appendix A. Solution of the acoustic wave equation in cylindrical coordinates

---

which means that the frequency equation (A.91) can be factored as

$$|C| = -C_{23} \begin{vmatrix} C_{11} & C_{12} \\ C_{31} & C_{32} \end{vmatrix} = 0 \quad (\text{A.102})$$

$C_{23} = 0$  yields solutions for purely torsional modes, which are not considered here, because they do not contribute to FSBS [70]. The frequency equation for the family of longitudinal-radial modes is hence given by

$$\frac{2\alpha}{a} J_1(\alpha a) J_1(\beta a) (\beta^2 + \gamma^2) - J_0(\alpha a) J_1(\beta a) (\beta^2 - \gamma^2)^2 - 4\gamma^2 \alpha \beta J_0(\beta a) J_1(\alpha a) = 0 \quad (\text{A.103})$$

Equation (A.103) is central in this analysis, as it defines the particular conditions in terms of momentum (wavevector) and energy (frequency) for which a mode belonging to the family of longitudinal-radial modes will exist. It was determined as early as 1876 [72] by Pochhammer, and independently later on in 1889 [73] by Chree. It can fortunately be further simplified here, as the modes studied here are nearly activated at cutoff, that is their propagation constant is nearly 0.

### A.2.9 Purely radial acoustic modes

Equation (A.103) can be further simplified if we make the following assumption

$$\gamma \approx 0 \quad (\text{A.104})$$

First, let us notice that the matrix  $C$  from equation (A.78) takes the following form

$$\begin{pmatrix} C_{11} & 0 & 0 \\ 0 & 0 & C_{23} \\ 0 & C_{32} & 0 \end{pmatrix} \quad (\text{A.105})$$

hence, its determinant factors out as

$$|C| = -C_{23} C_{11} C_{32} \quad (\text{A.106})$$

Coefficient  $C_{32}$  defines the family of purely longitudinal modes and will not be further inquired here. Coefficient  $C_{11}$  yields

$$\frac{2\alpha}{a} J_1(\alpha a) - \beta^2 J_0(\alpha a) = 0 \quad (\text{A.107})$$

which defines the condition for purely radial modes to exist. Finally, setting  $n = \gamma = 0$  in (A.59) yields the displacement profile of purely radial modes, which only exists along  $\hat{r}$

$$U_r(r, t) = -\alpha A J_{n+1}(\alpha r) \cos(\omega t) \quad (\text{A.108})$$

### A.3 Acoustic modes in a coated fiber

The solution of the acoustic waves in cylindrical coordinates for a clad rod, which corresponds to the case of a coated optical fiber, has been studied in many papers [80, 81, 92]. Here we closely follow the derivation performed in [80] but only provide with the most important results enabling determining the corresponding frequency equation.

#### A.3.1 Displacement field

Consider the cylindrical structure depicted in Fig-A.2 where  $a$  denotes the fiber radius and

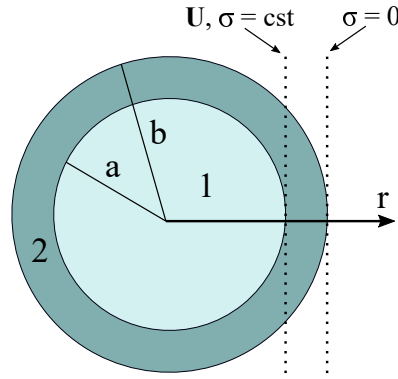


Figure A.2 – Cross-section of a coated fiber.

$b$  is the coating outer radius. Following the notation convention used so far, the potential functions yield

$$\begin{aligned} f^{(i)} &= A_{1i} Z_n(|\alpha^{(i)}| r) + B_{1i} W_n(|\alpha^{(i)}| r) \\ g_r^{(i)} &= A_{2i} Z_{n+1}(|\beta^{(i)}| r) + B_{2i} W_{n+1}(|\beta^{(i)}| r) \\ g_z^{(i)} &= A_{3i} Z_n(|\beta^{(i)}| r) + B_{3i} W_n(|\beta^{(i)}| r) \end{aligned} \quad (\text{A.109})$$

where  $i = 1, 2$  refer to either the fiber or the coating, respectively, and the  $A_{ji}$  and  $B_{ji}$  are integration constants. The functions  $Z_n$  and  $W_n$  denote

$$Z_n = \begin{cases} J_n & \text{if } \alpha^{(i)}, \beta^{(i)} \text{ is real} \\ I_n & \text{if } \alpha^{(i)}, \beta^{(i)} \text{ is imaginary} \end{cases} \quad (\text{A.110})$$

## Appendix A. Solution of the acoustic wave equation in cylindrical coordinates

where  $I_n$  are modified Bessel functions of the first kind and

$$W_n = \begin{cases} Y_n & \text{if } \alpha^{(i)}, \beta^{(i)} \text{ is real} \\ K_n & \text{if } \alpha^{(i)}, \beta^{(i)} \text{ is imaginary} \end{cases} \quad (\text{A.111})$$

where  $Y_n$  and  $K_n$  are Bessel functions of the second kind and modified Bessel functions of the second kind, respectively. The displacements are explicitly given by:

$$U_{r,i} = \left( \frac{\partial f^{(i)}}{\partial r} + \frac{n}{r} g_z^{(i)} + \xi g_r^{(i)} \right) \cos(n\theta) \cos(\xi x + \omega t) \quad (\text{A.112})$$

$$U_{\theta,i} = \left( -n \frac{f^{(i)}}{r} + \xi g_r^{(i)} - \frac{\partial g_z^{(i)}}{\partial r} \right) \sin(n\theta) \cos(\xi x + \omega t) \quad (\text{A.113})$$

$$u_{xi} = \left( -\xi f^{(i)} - \frac{\partial g_r^{(i)}}{\partial r} - (1+n) \frac{g_r^{(i)}}{r} \right) \cos(n\theta) \sin(\xi x + \omega t) \quad (\text{A.114})$$

with  $B_{11} = B_{21} = B_{31} = 0$  [80].

### A.3.2 Frequency equation of purely radial modes

Identically to the case of a bare fiber, the solution of the equation proceeds with the application of appropriate boundary conditions. For a coated fibers, the boundary conditions are

$$U_r^{(1)}|_{r=a} = U_r^{(2)}|_{r=a} \quad (\text{A.115a}) \quad \sigma_{rr}^{(1)}|_{r=a} = \sigma_{rr}^{(2)}|_{r=a} \quad (\text{A.115d}) \quad \sigma_{rr}^{(2)}|_{r=b} = 0 \quad (\text{A.115g})$$

$$U_\theta^{(1)}|_{r=a} = U_\theta^{(2)}|_{r=a} \quad (\text{A.115b}) \quad \sigma_{r\theta}^{(1)}|_{r=a} = \sigma_{r\theta}^{(2)}|_{r=a} \quad (\text{A.115e}) \quad \sigma_{r\theta}^{(2)}|_{r=b} = 0 \quad (\text{A.115h})$$

$$U_z^{(1)}|_{r=a} = U_z^{(2)}|_{r=a} \quad (\text{A.115c}) \quad \sigma_{rz}^{(1)}|_{r=a} = \sigma_{rz}^{(2)}|_{r=a} \quad (\text{A.115f}) \quad \sigma_{rz}^{(2)}|_{r=b} = 0 \quad (\text{A.115i})$$

which yield once more a matrix equation of the form

$$|C_{ij}| = 0 \quad (\text{A.116})$$

where this time  $C$  is  $9 \times 9$ . Note that in [80], the following coefficient is missing

$$C_{83} = K_{21} b |\beta|_1 Z_{n+1}(|\beta|_1 b) - n Z_n(|\beta|_1 b) \quad (\text{A.117})$$

Fortunately, for purely radial modes with  $n = \gamma = 0$ , the general matrix equation (A.116) reduces to

$$\begin{vmatrix} 0 & C_{14} & C_{15} \\ C_{41} & C_{44} & C_{45} \\ C_{71} & C_{74} & C_{75} \end{vmatrix} = 0 \quad (\text{A.118})$$

and the coefficients are

$$C_{14} = 2b |\alpha^{(2)}| Z_1(|\alpha^{(2)} b|) - b^2 (\beta^{(2)})^2 Z_0(|\alpha^{(2)}| b) \quad (\text{A.119a})$$

$$C_{15} = 2b |\alpha^{(2)}| W_1(|\alpha^{(2)} b|) - b^2 (\beta^{(2)})^2 W_0(|\alpha^{(2)}| b) \quad (\text{A.119b})$$

$$C_{41} = \frac{\mu^{(1)}}{\mu^{(2)}} \left[ 2a |\alpha^{(2)}| Z_1(|\alpha^{(2)} a|) - a^2 (\beta^{(2)})^2 Z_0(|\alpha^{(2)}| a) \right] \quad (\text{A.119c})$$

$$C_{44} = -2a |\alpha^{(2)}| Z_1(|\alpha^{(2)} a|) + a^2 (\beta^{(2)})^2 Z_0(|\alpha^{(2)}| a) \quad (\text{A.119d})$$

$$C_{45} = -2a |\alpha^{(2)}| Z_1(|\alpha^{(2)} a|) + a^2 (\beta^{(2)})^2 Z_0(|\alpha^{(2)}| a) \quad (\text{A.119e})$$

$$C_{71} = -a |\alpha^{(1)}| Z_1(|\alpha^{(1)}| a) \quad (\text{A.119f})$$

$$C_{74} = a |\alpha^{(2)}| Z_1(|\alpha^{(2)}| a) \quad (\text{A.119g})$$

$$C_{75} = a |\alpha^{(2)}| W_1(|\alpha^{(2)}| a) \quad (\text{A.119h})$$



## B Distributed FSBS sensing: numerical simulations

The numerical simulations developed in this section aim at providing with a semi-analytical support for the experimental results described in section 4.4. They also serve as the basis to estimate the acoustic damping rate  $\Gamma$  in all related experiments. The numerical simulations presented in the remaining of this document all rely on the model described in the sections 4.2.5 and 4.4.1. Both the propagation of the pulse as well as the extraction of the frequency shift from the acquired data are considered. In addition, the model also accounts for the duration of the activating pulse width. A pseudo-code implementation is provided here below, followed by a more detailed explanation of crucial steps.

- Define activating pulse width:  $\Delta\tau_{\text{act}}$
- Define reading pulse width:  $\Delta\tau_{\text{read}}$
- Define distance axis:  $z$
- Define time axis:  $t$
- Define frequency axis for FSBS:  $f_d$
- Define frequency axis for BOTDA:  $f_{\text{RF}}$
- Define frequency axis for activating pulse spectrum:  $f_{\text{sinc}}$
- Define FSBS resonance profile:  $A_d(z)$ ,  $f_m(z)$  and  $\Gamma(z)$
- Compute fundamental BGS:  $\text{BGS}_{\text{CW}}(f_{\text{RF}})$
- Create normalized sinc profile:  $\text{sinc}(\Delta\tau_{\text{act}} f_{\text{sinc}})$
- Initialize reading pulse:  $p_{\text{read},0}(t) = \text{rect}\left(\frac{t}{\Delta\tau_{\text{read}}}\right)$
- for each  $k$  % Loop scanning through the FSBS frequency  $f_d$ 
  - Initialize empty phase shift profile  $\Delta\phi(t) = 0$
  - for each  $l$  % Loop scanning through the distance axis  $z$ 
    - \* for each  $m$  % Loop scanning the activating pulse spectrum  $f_{\text{sinc}}$ 
      - Current frequency  $f = f_d[k] + f_{\text{sinc}}[m]$



## Appendix B. Distributed FSBS sensing: numerical simulations

- Compute FSBS amplitude and phase response based on theoretical model:  
 $A, \theta = \text{Model}(f, A_d(z[l]), f_m(z[l]), \Gamma(z[l]))$
- Compute local phase shift temporal profile:  
 $\Delta\phi_{\text{loc}}(t) = A * \text{sinc}(\Delta\tau_{\text{act}} f_{\text{sinc}}[m]) * \cos[2\pi(f_m(z[l])t + f_{\text{sinc}}[m]\Delta\tau_{\text{act}}/2 - \theta)]$
- Increment total phase shift profile:  
 $\Delta\phi(t) = \Delta\phi(t) + \Delta\phi_{\text{loc}}(t)$
- end
- \* Impinge phase profile onto reading pulse:  
 $p_{\text{read}, \Delta t} = p_{\text{read}, 0} * \exp(i2\pi\Delta\phi(t))$
- \* Compute pulse power spectral density (via fast Fourier transform) without and with added phase profile:  
 $\hat{p}_{\text{PSD}, 0}(f_{\text{RF}}) = |\text{FFT}(p_{\text{read}, 0}(t))|^2$   
 $\hat{p}_{\text{PSD}, \Delta\phi}(f_{\text{RF}}) = |\text{FFT}(p_{\text{read}, \Delta\phi}(t))|^2$
- \* Convolution with fundamental BGS without and with added phase profile  
 $\text{BGS}_0(f_{\text{RF}}) = \text{BGS}_{\text{CW}}(f_{\text{RF}}) \otimes \hat{p}_{\text{PSD}, 0}(f_{\text{RF}})$   
 $\text{BGS}_{\Delta\phi}(f_{\text{RF}}) = \text{BGS}_{\text{CW}}(f_{\text{RF}}) \otimes \hat{p}_{\text{PSD}, \Delta\phi}(f_{\text{RF}})$
- \* Perform cross-correlation  
 $\text{XCORR}(f_{\text{RF}}) = \text{BGS}_0(f_{\text{RF}}) * \text{BGS}_{\Delta\phi}(f_{\text{RF}})$
- \* Store maximum frequency shift  
 $\overline{\Delta f_{\text{acc}}}(f_d[k], z[l]) = \max_f(\text{XCORR}(f_{\text{RF}}))$
- \* end
- end
- end

The most important part of the implementation described here above lies in the computation of the local phase shift profile denoted as  $\Delta\phi_{\text{loc}}(t)$ . The operation performed actually corresponds to the convolution between the local FSBS resonance and the Fourier transform of the activating pulse gating (i.e. a rectangular function of duration  $\Delta\tau_{\text{act}}$ ). Therefore, the frequency axis  $f_{\text{sinc}}$  should be centered around 0, and spread sufficiently as to represent accurately the spectral content of the activating pulse gating. This way, the newly defined frequency  $f$  scans around the current driving frequency  $f_d$  at each iteration  $m$ . The term  $f_{\text{sinc}}[m]\Delta\tau_{\text{act}}/2$  originates from a time-shifting of the activating pulse of half of its duration in order to place it before the reading pulse on the temporal axis  $t$ . Note that the total phase shift profile  $\Delta\phi(t)$  is incremented all over distance, i.e. it only gets reinitialized to 0 on iterations of the outermost loop (defined by variable  $k$ ). This makes it accumulate as the pulse propagates in the fiber. Note that the operator has a complete freedom over the FSBS resonance profile along the fiber, which can be adjusted at each location by tuning  $A_d(z)$ ,  $f_m(z)$  and  $\Gamma(z)$ . The output value is a 2-D matrix holding the value of the accumulated frequency shift along the fiber at each activating frequency and position  $\overline{\Delta f_{\text{acc}}}(f_d[k], z[l])$ . Numerical differentiation along distance is then required in order to retrieve the local information. While most parameters are easily anticipated, the amplitude profile  $A_d(z)$  is set empirically, in order to replicate the observed frequency shift in the different fibers tested.

## C List of publications

### Journal articles, first author

- S. Zaslawski, Z. Yang, and L. Thévenaz, "On the 2d post-processing of Brillouin optical time-domain analysis", "Journal of Lightwave Technology", vol. 38, no. 14, 2020.
- S. Zaslawski, Z. Yang, and L. Thévenaz, "Distributed optomechanical fiber sensing based on serrodyne analysis", "Optica", vol. 8, no. 3, 2021.

### Journal articles, co-author

- Z. Yang, Z. Li, Simon Zaslawski, Luc Thévenaz and M. A. Soto, "Design rules for optimizing unipolar coded Brillouin optical time-domain analyzers", "Optics Express", vol. 26, no. 13, 2018.
- S. Wang, Z. Yang, S. Zaslawski and Luc Thévenaz, "Short spatial resolution retrieval from a long pulse Brillouin optical time-domain analysis trace", "Optics Letters", vol. 45, no. 15, 2020.
- X. Sun, Z. Yang, X. Hong, S. Zaslawski, S. Wang, M. A. Soto, X. Gao, J. Wu and L. Thévenaz, "Genetic-optimised aperiodic code for distributed optical fibre sensors", "Nature communications", vol. 11, no. 1, 2020.

### Conference papers, first author

- S. Zaslawski, Z. Yang, M. A. Soto and L. Thévenaz, "Impact of Fitting and Digital Filtering on Signal-to-Noise Ratio and Brillouin Frequency Shift Uncertainty of BOTDA Measurements", "26<sup>th</sup> International Conference on Optical Fiber Sensors", OSA, 2018.
- S. Zaslawski, Z. Yang, S. Wang and L. Thévenaz, "Distributed forward stimulated Brillouin scattering measurement using broadband BOTDR", "7<sup>th</sup> European Workshop on Optical Fibre Sensors", SPIE, 2019.

## Appendix C. List of publications

---

- S. Zaslawski, Y. Fu, Z. Yang, K. Markiewicz, L. Szostkiewicz, T. Nasilowski and L. Thévenaz, "Opto-mechanical cross-talk reduction in air-holes multicore fibers", (accepted for oral presentation at the 27<sup>th</sup> international conference on optical fiber sensors, but unfortunately delayed due to the 2020 Covid-19 Pandemic).

### Conference papers, co-author

- X. Sun, Z. Yang, X. Hong, S. Zaslawski, S. Wang, J. Wu and L. Thévenaz, "Boosting the performance of distributed optical fiber sensors based on adaptive decoder", "26<sup>th</sup> International Conference on Optical Fiber Sensors", OSA, 2018.
- Z. Yang, Z. Li, S. Zaslawski, L. Thévenaz, M. A. Soto, "Design rules for Unipolar Unicolor Coded Brillouin Optical Time Domain Analysis", "26<sup>th</sup> International Conference on Optical Fiber Sensors", OSA, 2018.
- S. Wang, Z. Yang, S. Zaslawski and Luc Thévenaz, "Short spatial resolutions retrieval from a long pulse BOTDA trace", "7<sup>th</sup> European Workshop on Optical Fibre Sensors", SPIE, 2019.
- H. Bhatta, S. Zaslawski, Z. Yang, M. Tur and L. Thévenaz, "Performance analysis of the differential pulse-width pair Brillouin optical time domain analysis using the log normalized and linearly normalized gain", "7<sup>th</sup> European Workshop on Optical Fibre Sensors", SPIE, 2019.

## Bibliography

- [1] Brillouin, Léon, “Diffusion de la lumière et des rayons x par un corps transparent homogène - influence de l’agitation thermique”, “*Ann. Phys.*”, vol. 9, no. 17, 1922. [Online]. Available: <https://doi.org/10.1051/anphys/192209170088>.
- [2] A. H. Hartog, An introduction to distributed optical fibre sensors. CRC press, 2017.
- [3] T. Horiguchi and M. Tateda, “Optical-fiber-attenuation investigation using stimulated brillouin scattering between a pulse and a continuous wave”, “*Opt. Lett.*”, vol. 14, no. 8, Apr. 1989. [Online]. Available: <http://ol.osa.org/abstract.cfm?URI=ol-14-8-408>.
- [4] T. Kurashima, T. Horiguchi, H. Izumita, S.-i. Furukawa, and Y. Koyamada, “Brillouin optical-fiber time domain reflectometry”, “*IEICE Transactions on Communications*”, vol. E76-B, no. 4, 1993.
- [5] R. M. Shelby, M. D. Levenson, and P. W. Bayer, “Guided acoustic-wave brillouin scattering”, “*Phys. Rev. B*”, vol. 31, 8 Apr. 1985. [Online]. Available: <https://link.aps.org/doi/10.1103/PhysRevB.31.5244>.
- [6] Y. Antman, A. Clain, Y. London, and A. Zadok, “Optomechanical sensing of liquids outside standard fibers using forward stimulated brillouin scattering”, “*Optica*”, vol. 3, no. 5, May 2016. [Online]. Available: <http://www.osapublishing.org/optica/abstract.cfm?URI=optica-3-5-510>.
- [7] H. H. Diamandi, Y. London, G. Bashan, and A. Zadok, “Distributed opto-mechanical analysis of liquids outside standard fibers coated with polyimide”, “*APL Photonics*”, vol. 4, no. 1, 2019. [Online]. Available: <https://doi.org/10.1063/1.5067271>.
- [8] C. Pang, Z. Hua, D. Zhou, H. Zhang, L. Chen, X. Bao, and Y. Dong, “Opto-mechanical time-domain analysis based on coherent forward stimulated brillouin scattering probing”, “*Optica*”, vol. 7, no. 2, Feb. 2020. [Online]. Available: <http://www.osapublishing.org/optica/abstract.cfm?URI=optica-7-2-176>.
- [9] J. Ballato and P. Dragic, “Glass: the carrier of light - a brief history of optical fiber”, “*International Journal of Applied Glass Science*”, vol. 7, no. 4, 2016. [Online]. Available: <https://ceramics.onlinelibrary.wiley.com/doi/abs/10.1111/ijag.12239>.
- [10] K. Kao and G. Hockham, “Dielectric-fibre surface waveguides for optical frequencies”, “*Proceedings of the Institution of Electrical Engineers*”, vol. 113, 7 Jul. 1966. [Online]. Available: <https://digital-library.theiet.org/content/journals/10.1049/piee.1966.0189>.

## Bibliography

---

- [11] L. Thevenaz, Advanced fiber optics: concepts and technology. 2011.
- [12] T. M. Monro and H. Ebendorff-Heidepriem, "Progress in microstructured optical fibers", *"Annual Review of Materials Research"*, vol. 36, no. 1, 2006. [Online]. Available: <https://doi.org/10.1146/annurev.matsci.36.111904.135316>.
- [13] K. Okamoto, Fundamentals of optical waveguides, I. Elsevier, Ed. Elsevier, 2006.
- [14] G. P. Agrawal, Nonlinear Fiber Optics. Academic Press, 2007.
- [15] R. W. Boyd, Nonlinear Optics. Academic Press, 2008.
- [16] B. Saleh and M. Teich, Fundamentals of Photonics, 3rd Edition. Feb. 2019.
- [17] A. Snyder and J. Love, Optical Waveguide Theory, ser. Science paperbacks. Springer US, 1983. [Online]. Available: [https://books.google.ch/books?id=gIQB%5C\\_hzB0SMC](https://books.google.ch/books?id=gIQB%5C_hzB0SMC).
- [18] D. Marcuse, "Gaussian approximation of the fundamental modes of graded-index fibers", *"J. Opt. Soc. Am."*, vol. 68, no. 1, Jan. 1978. [Online]. Available: <http://www.osapublishing.org/abstract.cfm?URI=josa-68-1-103>.
- [19] L. Landau and E. Lifshitz, Electrodynamics of Continuous Media, 2nd, P. Press, Ed. Robert Maxwell, M.C., 1984, vol. 8.
- [20] I. Fabelinskii, Molecular Scattering of Light. Springer US, 2012. [Online]. Available: <https://books.google.ch/books?id=4aHzBwAAQBAJ>.
- [21] T. Dorfmueller, "Benjamin chu: laser light scattering, basic principles and practice, second edition, academic press, inc., boston 1991, isbn 0-12-174551-1, 343 seiten, preis: \$ 74.50", *"Berichte der Bunsengesellschaft für physikalische Chemie"*, vol. 96, no. 7, 1992. [Online]. Available: <https://onlinelibrary.wiley.com/doi/abs/10.1002/bbpc.19920960722>.
- [22] M. K. Barnoski and S. M. Jensen, "Fiber waveguides: a novel technique for investigating attenuation characteristics", *"Appl. Opt."*, vol. 15, no. 9, Sep. 1976. [Online]. Available: <http://ao.osa.org/abstract.cfm?URI=ao-15-9-2112>.
- [23] P. Healey, "Fading in heterodyne otdr", *"Electronics Letters"*, vol. 20, no. 1, Jan. 1984.
- [24] H. F. Taylor and C. E. Lee, "Apparatus and method for fiber optic intrusion sensing", US Patent 5,194,847, 1993.
- [25] C. V. Raman, "A new radiation [reproduced from indian j. phys., 1928, 2, 387–398]", *"Current Science"*, vol. 74, no. 4, 1998. [Online]. Available: <http://www.jstor.org/stable/24101519>.
- [26] J. Dakin, D. Pratt, G. Bibby, and J. Ross, "Distributed anti-stokes ratio thermometry", *Optical Fiber Sensors*, Optical Society of America, 1985, PDS3. [Online]. Available: <http://www.osapublishing.org/abstract.cfm?URI=OFS-1985-PDS3>.
- [27] J.-C. Beugnot, M. Tur, S. F. Mafang, and L. Thévenaz, "Distributed brillouin sensing with sub-meter spatial resolution: modeling and processing", *"Opt. Express"*, vol. 19, no. 8, Apr. 2011. [Online]. Available: <http://www.opticsexpress.org/abstract.cfm?URI=oe-19-8-7381>.

- 
- [28] M. A. Soto and L. Thévenaz, "Modeling and evaluating the performance of brillouin distributed optical fiber sensors", *"Opt. Express"*, vol. 21, no. 25, Dec. 2013. [Online]. Available: <http://www.opticsexpress.org/abstract.cfm?URI=oe-21-25-31347>.
- [29] M. Alem, M. A. Soto, and L. Thévenaz, "Analytical model and experimental verification of the critical power for modulation instability in optical fibers", *"Opt. Express"*, vol. 23, no. 23, Nov. 2015. [Online]. Available: <http://www.opticsexpress.org/abstract.cfm?URI=oe-23-23-29514>.
- [30] S. Zaslawski, Z. Yang, and L. Thévenaz, "On the 2d post-processing of brillouin optical time-domain analysis", *"Journal of Lightwave Technology"*, vol. 38, no. 14, 2020. [Online]. Available: <https://ieeexplore.ieee.org/document/8961144?arnumber=8961144>.
- [31] M. Alem, M. A. Soto, M. Tur, and L. Thévenaz, Analytical expression and experimental validation of the brillouin gain spectral broadening at any sensing spatial resolution, 2017. [Online]. Available: <https://doi.org/10.1117/12.2267639>.
- [32] T. Horiguchi, T. Kurashima, and M. Tateda, "A technique to measure distributed strain in optical fibers", *"IEEE Photonics Technology Letters"*, vol. 2, no. 5, May 1990.
- [33] T. Kurashima, T. Horiguchi, and M. Tateda, "Distributed-temperature sensing using stimulated brillouin scattering in optical silica fibers", *"Opt. Lett."*, vol. 15, no. 18, Sep. 1990. [Online]. Available: <http://ol.osa.org/abstract.cfm?URI=ol-15-18-1038>.
- [34] L. Thévenaz, S. F. Mafang, and J. Lin, "Effect of pulse depletion in a brillouin optical time-domain analysis system", *"Opt. Express"*, vol. 21, no. 12, Jun. 2013. [Online]. Available: <http://www.opticsexpress.org/abstract.cfm?URI=oe-21-12-14017>.
- [35] A. Dominguez-Lopez, Z. Yang, M. A. Soto, X. Angulo-Vinuesa, S. Martin-Lopez, L. Thevenaz, and M. Gonzalez-Herraez, "Novel scanning method for distortion-free botda measurements", *"Opt. Express"*, vol. 24, no. 10, May 2016. [Online]. Available: <http://www.opticsexpress.org/abstract.cfm?URI=oe-24-10-10188>.
- [36] Z. Yang, Z. Li, S. Zaslawski, L. Thévenaz, and M. A. Soto, "Design rules for optimizing unipolar coded brillouin optical time-domain analyzers", *"Opt. Express"*, vol. 26, no. 13, Jun. 2018. [Online]. Available: <http://www.opticsexpress.org/abstract.cfm?URI=oe-26-13-16505>.
- [37] J. G. Proakis and D. G. Manolakis, Digital signal processing, Principles Algorithms, and Applications, Fourth Edition. Prentice-Hall, Inc., 2007.
- [38] S. J. Orfanidis, Introduction to Signal Processing. Prentice Hall, Inc., 2010.
- [39] S. G. Mallat, A wavelet tour of signal processing, 3rd edition. Academic Press, 2008.
- [40] S. Wang, Z. Yang, M. A. Soto, and L. Thévenaz, "Study on the signal-to-noise ratio of brillouin optical-time domain analyzers", *"Opt. Express"*, vol. 28, no. 14, Jul. 2020. [Online]. Available: <http://www.opticsexpress.org/abstract.cfm?URI=oe-28-14-19864>.

- [41] S. M. Haneef, Z. Yang, L. Thévenaz, D. Venkitesh, and B. Srinivasan, "Performance analysis of frequency shift estimation techniques in brillouin distributed fiber sensors", *"Opt. Express"*, vol. 26, no. 11, May 2018. [Online]. Available: <http://www.opticsexpress.org/abstract.cfm?URI=oe-26-11-14661>.
- [42] E. A. Lee and D. G. Messerschmitt, Digital communication, second edition. Kluwer Academic Publishers, 1994.
- [43] M. A. Soto, J. A. Ramírez, and T. Luc, "Intensifying the response of distributed optical fibre sensors using 2d and 3d image restoration", *"Nature Communications"*, 2016. [Online]. Available: <https://www.nature.com/articles/ncomms10870>.
- [44] H. Wu, L. Wang, Z. Zhao, N. Guo, C. Shu, and C. Lu, "Brillouin optical time domain analyzer sensors assisted by advanced image denoising techniques", *"Opt. Express"*, vol. 26, no. 5, Mar. 2018. [Online]. Available: <http://www.opticsexpress.org/abstract.cfm?URI=oe-26-5-5126>.
- [45] R. W. Schafer, "What is a savitzky-golay filter? [lecture notes]", *"IEEE Signal Processing Magazine"*, vol. 28, no. 4, Jul. 2011.
- [46] S. Wang, Z. Yang, S. Zaslawski, and L. Thévenaz, "Short spatial resolution retrieval from a long pulse brillouin optical time-domain analysis trace", *"Opt. Lett."*, vol. 45, no. 15, Aug. 2020. [Online]. Available: <http://ol.osa.org/abstract.cfm?URI=ol-45-15-4152>.
- [47] A. W. Brown, B. G. Colpitts, and K. Brown, "Distributed sensor based on dark-pulse brillouin scattering", *"IEEE Photonics Technology Letters"*, vol. 17, no. 7, Jul. 2005.
- [48] W. Li, X. Bao, Y. Li, and L. Chen, "Differential pulse-width pair botda for high spatial resolution sensing", *"Opt. Express"*, vol. 16, no. 26, Dec. 2008. [Online]. Available: <http://www.opticsexpress.org/abstract.cfm?URI=oe-16-26-21616>.
- [49] S. M. Foaleng, M. Tur, J. Beugnot, and L. Thevenaz, "High spatial and spectral resolution long-range sensing using brillouin echoes", *"Journal of Lightwave Technology"*, vol. 28, no. 20, Oct. 2010.
- [50] L. Shen, Z. Zhao, C. Zhao, H. Wu, C. Lu, and M. Tang, "Improving the spatial resolution of a botda sensor using deconvolution algorithm", *"Journal of Lightwave Technology"*, vol. 39, no. 7, Apr. 2021.
- [51] M. A. Soto, M. Tur, A. Lopez-Gil, M. Gonzalez-Herraez, and L. Thévenaz, "Polarisation pulling in brillouin optical time-domain analysers", *2017 25th Optical Fiber Sensors Conference (OFS)*, Apr. 2017, pp. 1–4.
- [52] X. Sun, Z. Yang, X. Hong, S. Zaslawski, S. Wang, M. A. Soto, X. Gao, J. Wu, and L. Thévenaz, "Genetic-optimised aperiodic code for distributed optical fibre sensors", *"Nature Communications"*, vol. 11, no. 1, Nov. 2020. [Online]. Available: <https://doi.org/10.1038/s41467-020-19201-1>.
- [53] D. Barton, Radars: Volume 3: Pulse compression. Artech House, Dedham, Massachusetts, USA, 1978.

- 
- [54] J. K. Everard, "Novel Signal Processing Techniques For Enhanced OTDR Sensors", *Fiber Optic Sensors II*, A. M. V. Scheggi, Ed., International Society for Optics and Photonics, vol. 0798, SPIE, 1987, pp. 42–47. [Online]. Available: <https://doi.org/10.1117/12.941083>.
- [55] M. A. Soto, G. Bolognini, F. D. Pasquale, and L. Thévenaz, "Long-range brillouin optical time-domain analysis sensor employing pulse coding techniques", *"Measurement Science and Technology"*, vol. 21, no. 9, Jul. 2010.
- [56] M. A. Soto, S. L. Floch, and L. Thévenaz, "Bipolar optical pulse coding for performance enhancement in botda sensors", *"Opt. Express"*, vol. 21, no. 14, Jul. 2013. [Online]. Available: <http://www.opticsexpress.org/abstract.cfm?URI=oe-21-14-16390>.
- [57] E. K. Sittig and G. A. Coquin, "Visualization of plane-strain vibration modes of a long cylinder capable of producing sound radiation", *"The Journal of the Acoustical Society of America"*, vol. 48, no. 5B, 1970. [Online]. Available: <https://doi.org/10.1121/1.1912255>.
- [58] J. D. Foster and L. M. Osterink, "Thermal effects in a nd:yag laser", *"Journal of Applied Physics"*, vol. 41, no. 9, 1970. [Online]. Available: <https://doi.org/10.1063/1.1659488>.
- [59] S. H. Perlmutter, M. D. Levenson, R. M. Shelby, and M. B. Weissman, "Polarization properties of quasielastic light scattering in fused-silica optical fiber", *"Phys. Rev. B"*, vol. 42, 8 Sep. 1990. [Online]. Available: <https://link.aps.org/doi/10.1103/PhysRevB.42.5294>.
- [60] A. J. Poustie, "Bandwidth and mode intensities of guided acoustic-wave brillouin scattering in optical fibers", *"J. Opt. Soc. Am. B"*, vol. 10, no. 4, Apr. 1993. [Online]. Available: <http://josab.osa.org/abstract.cfm?URI=josab-10-4-691>.
- [61] P. Dainese, P. S. Russell, G. S. Wiederhecker, N. Joly, H. L. Fragnito, V. Laude, and A. Khelif, "Raman-like light scattering from acoustic phonons in photonic crystal fiber", *"Opt. Express"*, vol. 14, no. 9, May 2006. [Online]. Available: <http://www.opticsexpress.org/abstract.cfm?URI=oe-14-9-4141>.
- [62] M. S. Kang, A. Nazarkin, A. Brenn, and P. S. J. Russell, "Tightly trapped acoustic phonons in photonic crystal fibres as highly nonlinear artificial raman oscillators", *"Nature Physics"*, vol. 5, 2009.
- [63] D. M. Chow, Z. Yang, M. A. Soto, and L. Thévenaz, "Distributed forward brillouin sensor based on local light phase recovery", *"Nature communications"*, vol. 9, no. 2990, Jul. 2018. [Online]. Available: <https://www.nature.com/articles/s41467-018-05410-2>.
- [64] G. Bashan, H. H. Diamandi, Y. London, E. Preter, and A. Zadok, "Optomechanical time-domain reflectometry", *"Nature communications"*, vol. 9, no. 2991, Jul. 2018. [Online]. Available: <https://www.nature.com/articles/s41467-018-05404-0>.
- [65] M. Duguay and J. Hansen, "Optical frequency shifting of a mode-locked laser beam", *"IEEE Journal of Quantum Electronics"*, vol. 4, no. 8, Aug. 1968.
- [66] I. Tomita, H. Sanjoh, E. Yamada, and Y. Yoshikuni, "Novel method for generating multiple wavelengths by pulsed serrodyne modulation", *"IEEE Photonics Technology Letters"*, vol. 15, no. 9, Sep. 2003.



- [67] T. R. Meeker and A. H. Meitzler, Guided Wave Propagation in Elongated Cylinder and Plates, W. P. Mason, Ed. Academic Press, 1964.
- [68] L. Landau, E. Lifshitz, A. Kosevich, J. Sykes, L. Pitaevskii, and W. Reid, Theory of Elasticity: Volume 7, ser. Course of theoretical physics. Elsevier Science, 1986. [Online]. Available: <https://books.google.ch/books?id=tpY-VkwCkAIC>.
- [69] P. L. Gould and Y. Feng, Introduction to Linear Elasticity, Fourth Edition. Springer, 2018.
- [70] A. S. Biryukov, M. E. Sukharev, and E. M. Dianov, "Excitation of sound waves upon propagation of laser pulses in optical fibres", *"Quantum Electronics"*, vol. 32, no. 9, Sep. 2002. [Online]. Available: <https://doi.org/10.1070%2Fqe2002v032n09abeh002289>.
- [71] H. H. Diamandi, Y. London, and A. Zadok, "Opto-mechanical inter-core cross-talk in multi-core fibers", *"Optica"*, vol. 4, no. 3, Mar. 2017. [Online]. Available: <http://www.osapublishing.org/optica/abstract.cfm?URI=optica-4-3-289>.
- [72] L. Pochhammer, "Ueber die fortpflanzungsgeschwindigkeiten kleiner schwingungen in einem unbegrenzten isotropen kreiscylinder.", *"Journal für die reine und angewandte Mathematik"*, vol. 1876, no. 81, 1876. [Online]. Available: <https://www.degruyter.com/view/journals/crll/1876/81/article-p324.xml>.
- [73] C. CHREE, "The equations of an isotropic elastic solid in polar and cylindrical coordinates, their solution and application", *"Trans.Camb.Phil.Soc."*, vol. 14, 1889. [Online]. Available: <https://ci.nii.ac.jp/naid/10004966872/en/>.
- [74] Y.-H. Pao and R. D. Mindlin, "Dispersion of Flexural Waves in an Elastic, Circular Cylinder", *"Journal of Applied Mechanics"*, vol. 27, no. 3, Sep. 1960. [Online]. Available: <https://doi.org/10.1115/1.3644033>.
- [75] M. Onoe, H. D. McNiven, and R. D. Mindlin, "Dispersion of Axially Symmetric Waves in Elastic Rods", *"Journal of Applied Mechanics"*, vol. 29, no. 4, Dec. 1962. [Online]. Available: <https://doi.org/10.1115/1.3640661>.
- [76] H. H. Diamandi, Y. London, A. Bergman, G. Bashan, J. Madrigal, D. Barrera, S. Sales, and A. Zadok, "Opto-mechanical interactions in multi-core optical fibers and their applications", *"IEEE Journal of Selected Topics in Quantum Electronics"*, vol. 26, no. 4, Jul. 2020.
- [77] P. B. Nagy, "Longitudinal guided wave propagation in a transversely isotropic rod immersed in fluid", *"The Journal of the Acoustical Society of America"*, vol. 98, no. 1, 1995. [Online]. Available: <https://doi.org/10.1121/1.413702>.
- [78] H. H. Diamandi, Y. London, G. Bashan, and A. Zadok, "Distributed opto-mechanical sensing outside polyimide-coated fiber", *26th International Conference on Optical Fiber Sensors*, Optical Society of America, 2018, FB1. [Online]. Available: <http://www.osapublishing.org/abstract.cfm?URI=OFS-2018-FB1>.
- [79] D. M. Chow and L. Thévenaz, "Forward brillouin scattering acoustic impedance sensor using thin polyimide-coated fiber", *"Opt. Lett."*, vol. 43, no. 21, Nov. 2018. [Online]. Available: <http://ol.osa.org/abstract.cfm?URI=ol-43-21-5467>.

- 
- [80] A. E. Armenakas, "Propagation of harmonic waves in composite circular-cylindrical rods", "The Journal of the Acoustical Society of America", vol. 47, no. 3B, 1970. [Online]. Available: <https://doi.org/10.1121/1.1911965>.
  - [81] R. N. Thurston, "Elastic waves in rods and clad rods", "The Journal of the Acoustical Society of America", vol. 64, no. 1, 1978. [Online]. Available: <https://doi.org/10.1121/1.381962>.
  - [82] Y. Antman, Y. London, and A. Zadok, Scanning-free characterization of temperature dependence of forward stimulated brillouin scattering resonances, 2015. [Online]. Available: <https://doi.org/10.1117/12.2195097>.
  - [83] S. Zaslawski, Z. Yang, and L. Thévenaz, "Distributed optomechanical fiber sensing based on serrodyne analysis", "Optica", vol. 8, no. 3, Mar. 2021. [Online]. Available: <http://www.osapublishing.org/optica/abstract.cfm?URI=optica-8-3-388>.
  - [84] L. M. Johnson and C. H. Cox, "Serrodyne optical frequency translation with high side-band suppression", "Journal of Lightwave Technology", vol. 6, no. 1, Jan. 1988.
  - [85] E. Lichtman, R. G. Waarts, and A. A. Friesem, "Stimulated brillouin scattering excited by a modulated pump wave in single-mode fibers", "Journal of Lightwave Technology", vol. 7, no. 1, Jan. 1989.
  - [86] B. Auld, Acoustic fields and waves in solids, ser. A Wiley-Interscience publication. Wiley, 1973. [Online]. Available: [https://books.google.ch/books?id=%5C\\_2MWAwAAQBAJ](https://books.google.ch/books?id=%5C_2MWAwAAQBAJ).
  - [87] Y. Tanaka and K. Ogusu, "Tensile-strain coefficient of resonance frequency of depolarized guided acoustic-wave brillouin scattering", "IEEE Photonics Technology Letters", vol. 11, no. 7, Jul. 1999.
  - [88] S. Zaslawski, Z. Yang, S. Wang, and L. Thévenaz, "Distributed forward stimulated Brillouin scattering measurement using broadband BOTDR", *Seventh European Workshop on Optical Fibre Sensors*, K. Kalli, S. O. O'Keeffe, and G. Brambilla, Eds., International Society for Optics and Photonics, vol. 11199, SPIE, 2019, pp. 323–326. [Online]. Available: <https://doi.org/10.1117/12.2540011>.
  - [89] E. Geinitz, S. Jetschke, U. Röpke, S. Schröter, R. Willsch, and H. Bartelt, "The influence of pulse amplification on distributed fibre-optic Brillouin sensing and a method to compensate for systematic errors", "Measurement Science and Technology", vol. 10, no. 2, Feb. 1999.
  - [90] A. Dominguez-Lopez, X. Angulo-Vinuesa, A. Lopez-Gil, S. Martin-Lopez, and M. Gonzalez-Herraez, "Non-local effects in dual-probe-sideband brillouin optical time domain analysis", "Opt. Express", vol. 23, no. 8, Apr. 2015. [Online]. Available: <http://www.opticsexpress.org/abstract.cfm?URI=oe-23-8-10341>.
  - [91] G. Bashan, Y. London, H. H. Diamandi, and A. Zadok, "Distributed cladding mode fiber-optic sensor", "Optica", vol. 7, no. 1, Jan. 2020. [Online]. Available: <http://www.osapublishing.org/optica/abstract.cfm?URI=optica-7-1-85>.

## Bibliography

---

- [92] R. N. Thurston, "Elastic waves in rods and optical fibers", "[Journal of Sound and Vibration](http://www.sciencedirect.com/science/article/pii/0022460X9290752J)", vol. 159, no. 3, 1992. [Online]. Available: <http://www.sciencedirect.com/science/article/pii/0022460X9290752J>.

# SIMON ZASLAWSKI

@ simon.zaslowski@gmail.com

+41 78 878 51 59

📍 Chemin de la Prairie 5C, 1007 Lausanne

in linkedin.com/in/simonzaslowski/



## EXPERIENCE

### Doctoral studies

#### Swiss Federal Institute of Technology Lausanne (EPFL)

📅 Mar 2017 - May 2021

📍 Lausanne, Switzerland

#### Group for Fibre Optics (GFO)

- Developed and experimentally demonstrated a theoretical model of the transient behavior of forward Brillouin stimulated scattering (FSBS) in optical fibers under harmonic excitation.
- Demonstrated the use of signal processing methodologies to optimize the performances of distributed optical fiber sensors (DOFS).
- Member of the organizing committee of the 26<sup>th</sup> international conference on optical fibre sensors (500 attendees over 5 days)

### Civil Service

#### Swiss Federal Institute of Technology Lausanne (EPFL)

📅 Oct 2016 - Feb 2017

📍 Lausanne, Switzerland

- Designed laboratory experiments for undergraduate students.

### Unisanté

📅 Jan 2016 - Sep 2016

📍 Lausanne, Switzerland

- Developed informatic tools to assist pharmacists.

## EDUCATION

### Master's Thesis, Industrial Application

#### Omnisens SA

📅 Feb 2015 - Dec 2015

📍 Morges, Switzerland

#### Design of a calibration artifact for Brillouin optical time domain analyzers (BOTDA)

- Developed an industrial solution for the calibration of distributed fiber sensors based on Brillouin scattering.

### Master in Electrical and Electronic Engineering

#### Swiss Federal Institute of Technology Lausanne (EPFL)

📅 Sep 2013 - Feb 2015

📍 Lausanne, Switzerland

- Specialization: Photonics, signal processing

### Minor in Spatial Technologies

#### Laboratoire Temps-Fréquence (LTF)

📅 Sep 2014 - Dec 2014

📍 Neuchâtel, Switzerland

- **Final project:** Frequency stabilized laser system as optical reference for atmospheric CO<sub>2</sub> monitoring.

### Bachelor in Electrical and Electronic Engineering

#### Swiss Federal Institute of Technology Lausanne (EPFL)

📅 Sep 2010 - Aug 2013

📍 Lausanne, Switzerland

- Specialization: Telecommunication, Microwaves Transmission

## SKILLS

### Programming

Matlab

LabVIEW

COMSOL Multiphysics

LaTeX

C++

### Technical Skills

Optical Fiber Sensors

Digital Signal Processing

Instrumentation

Data Analysis

Photonic Devices

Microwave Components

Optical Setup Design & Implementation

## SELECTED PUBLICATIONS

S. Zaslowski et al., On the 2D Post-Processing of Brillouin Optical Time-Domain Analysis, Vol 38 (14), 3723-3736, J. Light. Technol., 2020.

S. Zaslowski et al., Distributed forward stimulated Brillouin scattering measurement using broadband BOTDR, Proc. SPIE, 11199, 2019.

S. Zaslowski et al., Distributed optomechanical fiber sensing based on serrodyne analysis, Vol 8 (3), 388-395, Optica, 2021.

## LANGUAGES

**French** Native, full working proficiency

**English** Full working proficiency

**German** Limited working proficiency

## PERSONAL INTERESTS

Climbing

Piano Playing

Hiking

Scuba Diving

## REFERENCES

Prof. Luc Thévenaz

GFO, Institute of Electrical Engineering, EPFL

@ luc.thevenaz@epfl.ch

📞 +41 21 693 47 74

Dr. Zhisheng Yang

Beijing university of posts and telecommunications, China

@ zhisheng.yang@bupt.edu.cn

📞 +86 138 117 53038

Dr. Etienne Rochat

Omnisens SA, Morges, Switzerland

@ etienne.rochat@omnisens.com

📞 +41 21 510 21 21